Imperial College London
Department of Chemical Engineering

Porous Media Drying and Two-phase Flow Studies Using Micromodels

Ayorinde Kazeem Rufai

January 2019

Submitted in fulfilment of the requirements for the degree of
Doctor of Philosophy in Chemical Engineering of Imperial College London

Abstract

In this thesis, we report an investigation of porous media drying and steady-state two-phase flow behaviour at the pore scale using micromodels based on thin section images of real rocks. Fluid distributions (and the deposition of solid salt in the case of drying) were imaged in real-time using optical microscopy. Computer simulations of the two-phase flow was initially compared to micromodel experiments and then used to predict behaviour in geometries not available in the lab.

We performed evaporation experiments on a 2.5D etched-silicon/glass micromodel based on a thin section image of a sucrosic dolomite carbonate rock at different wetting conditions. NaCl solutions from 0 wt% (deionized water) to 36 wt% (saturated brine) were evaporated by passing dry air through a channel in front of the micromodel matrix. For deionized water in a water-wet model, we observed the three classical periods of evaporation: the constant rate period (CRP) in which liquid remains connected to the matrix surface, the falling rate period (FRP) and the receding front period (RFP), in which the capillary connection is broken and water transport becomes dominated by vapour diffusion. The length of the deionized water CRP was much shorter for a uniformly oil-wet model, but mixed wettability made little difference to the drying process.

For brine systems in water-wet and mixed-wet micromodels, the evaporation rate became linear with the square root of time after a short CRP. Although this appears similar to the RFP for water, salt continued to be deposited at the external surface of the matrix during this period indicating that a capillary connection was maintained. The reduction of evaporation rate appears to be due to the deposited salt acting as a partial barrier to hydraulic connectivity, perhaps allowing dry patches to grow on the evaporating surface. The mechanism causing the square root time behaviour is therefore unlike the case of deionized water where capillary disconnection from the fracture channel is followed by a diffusion controlled process. In completely oil-wet micromodels capillary disconnection prevented salt deposition in the fracture.

The resulting permeability impairment was also measured, for the water-wet model, we observed two regions of a linear downward trend in the matrix and fracture permeability measurements. A similar trend was observed for the mixed-wet systems. However, for the oil-wet systems, fracture permeability only changes slightly even for

360g/L brine, a result of the absence of salt deposits in the fracture caused by the early rupture of the liquid wetting films needed to aid hydraulic connectivity. Overall, matrix permeability for all wetting conditions decreased with increasing brine concentration and was almost total for the 360g/L brine. Furthermore, drying with air was compared with drying with CO_2 gas, with the latter having important applications in CO_2 sequestration processes. We observed that using CO_2 rather than air as carrier gas makes the brine phase somewhat more wetting especially in the deionized water case, with the result that hydraulic connectivity was maintained for longer in the CO_2 case compared to dry-out with air.

Steady-state two-phase flow experiments were also conducted to study the effect of viscosity ratio, flow rate and capillary number on flow regimes and displacement processes using a 2.5D etched-silicon/glass micromodel based on a thin section image of a Berea sandstone rock. Of particular interest here was a new type of pore-scale behaviour, termed dynamic connectivity, previously identified in steady-state two-phase flow experiments in real rocks at the transition to ganglia flow by X-ray tomography. Micromodels have the potential to resolve the dynamics of these displacement processes due to the high speed resolution of optical techniques.

Depending on the mean-size, prevalence, and connectivity of the non-wetting phase, four flow regimes were identified: connected pathway flow (CPF), big ganglia flow (BGF), big-small ganglia flow (BSGF) and small ganglia flow (SGF). These flow regimes move from CPF to SGF as the capillary-viscous balance of the system is altered by increasing the total flow rate of the system. The boundaries of the flow regimes are indistinct, however the domain of the BGF increases (and/or SGF decreases) with a decrease in the viscosity ratio of the system. That is the BGF regime persisted to higher capillary number for the water/squalane system than the water/decane system because it is harder for big blobs to split into smaller blobs at low viscosity ratio.

However, dynamic connectivity was not observed in these micromodel experiments even after replicating the experiments with the same fluid pair (Nitrogen/Deionized water) used in the real porous media experiment. Therefore, we speculate that the constant depth of the micromodel used in this study does not provide a suitable geometry for dynamic connectivity to develop. One potential reason for this is the

compressed range of capillary pressures due to the single etch depth. Hence, a multi-depth non-repeat micromodel was designed based on a single confocal image of a Bentheimer sandstone. Prototypes of small sections of the multi-depth model were produced by 3D printing but it was not possible to fabricate a functioning model due to time constraints.

Simulation was therefore used to explore the multiphase flow behaviour of the new geometry. Initially a Lattice Boltzmann code (developed in another project) was applied to simulate flow in a small region of the single depth geometry and compared to the experimental results as a validation step. The LB model was then used to predict flow behaviour in the multi-depth geometry, however only connected pathway and ganglia flow regimes were seen unambiguously. It is therefore likely that the lack of 3D connectivity rather than capillary pressure limitations prevent the appearance of dynamic connectivity.

Declaration of Originality

I hereby declare that this thesis titled, **Porous Media Drying and Two-Phase Flow Studies using Micromodels**, and the work presented in it are my own, carried out under the supervision of Dr John Crawshaw and Prof Martin Trusler, at the Department of Chemical Engineering, Imperial College London. All published and unpublished materials used in this thesis are appropriately referenced and dully acknowledged respectively.

Ayorinde Kazeem Rufai

Department of Chemical Engineering
Imperial College London
25th January 2019

Copyright Declaration

Ayorinde Kazeem Rufai

Department of Chemical Engineering
Imperial College London
25th January 2019

Acknowledgements

Firstly, I would like to acknowledge GOD ALMIGHTY who has been my source of strength during the course of this postgraduate study and throughout my life.

I would like to express my profound gratitude to my supervisor Dr John Crawshaw, for the continuous support throughout my time at Imperial. John assisted and helped me in pushing the boundaries of my research to a level I never imagined possible. Your words of encouragement spurred me on at a time when I doubted myself. I will also like to express my gratitude to my second supervisor, Prof Martin Trusler, thank you for your guidance and unwavering support. Many thanks to my academic advisor Prof Geoffrey Maitland, for always being available to offer support and guidance when things get knotty. I would also like to thank my former supervisor, Dr Edo Boek, thanks for believing in me.

I would like to thank the Nigerian Federal Government for giving me the opportunity to study at the postgraduate level through its Presidential Special Scholarship for Innovation and Development (PRESSID) scheme funded by the Petroleum Trust Development Fund (PTDF). Many thanks to Dr Iain Macdonald and the Qatar Carbonate and Carbon Storage Research Centre (QCCSRC) for providing the equipment used in this research.

Special thanks to my wonderful wife Sherifat, for her unwavering support throughout the course of my PhD and for the best gift ever - our daughter Zahra. I love you both! Many thanks to my parents and my siblings, for their emotional and spiritual support, for their words of encouragement and endless prayers, for their unshakeable faith in me. Thank you very much!

Finally, I would like to thank my colleagues (Emily, Ibrahim, Christine, Nathan) in the Complex Fluid Group, for their support and stimulating discussions. Without their help in various equipment set-ups and laboratory procedures, this study would not have been possible. Many thanks to Dr Zacharoudiou for the lattice-Boltzmann modelling, Dr Shah for helping with rock polishing and confocal imaging, Mr Gavin Barnes for fabricating the micromodel holder, Ms Bhavna Patel for assisting with booking conference flights and accommodations, my friends (and the Imperial College Nigerian Society) for keeping me sane and sharp with extracurricular activities.

For Zahra… you shall be a shining star!

List of Publications

- A. Rufai and J. Crawshaw, "Micromodel observations of evaporative drying and salt deposition in porous media," *Physics of Fluids*, vol. 29, no. 12, p. 126603, 2017.
- A. Rufai and J. Crawshaw, "Effect of Wettability Changes on Evaporation Rate and the Permeability Impairment due to Salt Deposition," *ACS Earth and Space Chemistry,* vol. 2, no. 4, pp. 320-329, 2018.
- A. Rufai and J. Crawshaw, “Capillary Disconnect During Drying in Model Porous Media at Different Wetting Conditions,” Conference Paper, International Drying Symposium, Valencia, Spain, 2018. (In Print)

Conference Proceedings

- **Poster** presentation at the 2016 AIChE Annual Meeting in San Francisco, California, USA.
  “Capillary disconnect during evaporation in porous media”

- **Oral** presentation at the 2017 Goldschmidt Annual Conference in Paris, France.
  “Experimental studies on evaporative drying and salt deposition in porous media using micromodels”

- **Oral** presentation at the 2018 International Drying Symposium in Valencia, Spain.
  “Capillary disconnect during drying in model porous media at different wetting conditions”

- **Participated** at the 2015 Society of Petroleum Engineers Annual Technical Conference and Exhibition in Houston, Texas, USA.
- **Participated** at the 2015 2nd Biennial CO_2 for EOR as CCUS Conference in Houston, Texas, USA.

Table of Contents

List of Figures

List of Tables

1. Introduction

The industrial revolution heralded an unprecedented economic growth and development of our society. This continuous growth and development are driven by energy, hence, making the demand for energy to continue to increase. The main source of this energy has been fossil fuels, i.e. coal, natural gas and oil. While there are other sources of energy we can tap into, the use of fossil fuels as a source of energy keeps growing in scale mainly because of its high energy density and ease of transportation. The combustion of these fossil fuels, however, leads to an increase in anthropogenic carbon dioxide emissions in the atmosphere, this has been recognised to have an irreversible dangerous effect on our environment causing global warming and essentially leading to adverse climate change [1]. Likewise, the dependency on fossil fuels for our energy demand and economic growth and development cannot be maintained forever as it is a finite source of energy, We will eventually run out of fossil fuels someday in the future! Hence, the need to optimise the production and exploration of the discovered (and yet to be discovered) fossil fuels deposit.

Although, there are several renewable sources of energy i.e. solar, geothermal, biomass and wind, most of our primary energy supply is from fossil fuels. This is because most of these renewable energy sources are not readily available or accessible, or the technology to harness and store them for consumption are not available at the moment. For example; solar energy is essentially only available during sunny daytime hours and wind energy can only be generated when the wind is blowing. This intermittency problem demands adequate storage capacity which is not readily available especially in electricity generation. Also, there is a continuous competition for biomass use from food production. According to a report by the International Energy Agency, 81.3% of our primary energy supply was produced from fossil fuels in 2008 [2]. However, in the 2014 report, it was stated that by the year 2040, fossil fuels will account for around one-quarter of global energy demand, with the remainder from low-carbon fuels. The report also affirms fossil fuels continue to dominate the power sector, although their share of generation declines from 68% in

2012 to 55% in 2040. It is a fact that fossil fuels are a finite source, and a lot of work has been put into developing, improving and optimising other renewable sources of energy. Nonetheless, fossil fuels are still the most viable in the energy mix and our main source of energy for the immediate future, it will be decades before any of the alternative renewable sources of energy become viable enough to replace or displace fossil fuels [1]. Therefore, research to study ways to enhance fossil fuel recovery and the capture and storage of the carbon dioxide emitted from continuous fossil fuel use cannot be overemphasized.

1.1. Carbon Dioxide Emissions and Global Warming

Global warming has become a very divisive topic of discussion especially with the present political atmosphere around the world. While some doubt that the earth's average temperature is indeed increasing, there has been an enormous and overwhelming scientific data to clear any doubt whatsoever that the average global temperature has been steadily increasing since the beginning of the industrial revolution [1, 3, 4]. Much has already been said about global warming, from its causes to it's observed and expected effects on environmental and social systems. Different responses have been proposed in response to global warming, from mitigation (reducing the level of future adverse climate change) to adaptation (planning either in anticipation of or in reaction to future adverse climate change). It has been confirmed that since the early 20th century, earth's mean surface temperature has increased by about 0.8 °C (1.4 °F), and about two-thirds of the increase occurring since 1980 [4].

Greenhouse gases (primarily water vapour, carbon dioxide, methane, nitrous oxide, ozone and Chlorofluorocarbons (CFCs)), are chiefly responsible for this increase in temperature [5]. However, among these several greenhouse gases (GHG), carbon dioxide (CO_2) has the most effect on global warming. Since the beginning of the industrial revolution, anthropogenic carbon dioxide (CO_2) emissions have greatly increased and this has disturbed earth's carbon cycle. The main human activity emitting CO_2 is the combustion of carbon-based fuels or fossil fuels (which are principally wood, natural gas, coal, and oil) largely for energy and transportation. However, there are some major industrial processes that emit a considerable amount of CO_2 like the cement manufacturing industry. Also the effect of deforestation cannot

be overemphasised. In 2012 alone it was estimated that the burning of fossil fuels and extensive clearing of native forests contributed to a 40% increase in the atmospheric concentration of CO_2, from 280 to 392.6 ppm [5].

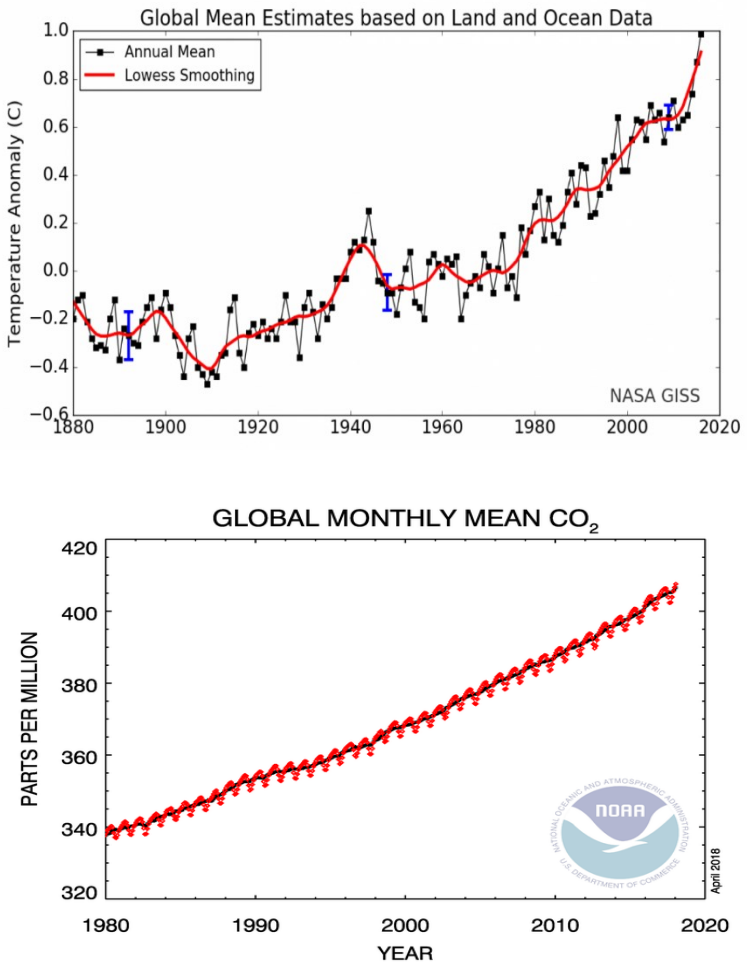

Figure 1.1. (a) The global average land-ocean surface temperature change from 1880 to 2018. (b) The global atmospheric carbon dioxide level from 1980 to 2017.

Figure 1.1a is an illustration of the increase in the global level of atmospheric CO_2 from 1980 to 2017 [6], while figure 1.1b illustrates the corresponding increase in the global average temperature from 1880 to the present year [1, 3]. In the 1890s, the global temperature anomaly was on average slightly below -0.3 °C, with an error range of roughly -0.2 and -0.4 °C. In the 1940s, the global temperature anomaly was on average slightly below +0.1 °C, with an error range of roughly 0.0 and +0.15 °C. In the 2000s, the global temperature anomaly was on average slightly below +0.6 °C, with

an error range of roughly +0.6 and +0.5 °C. According to the 4th assessment report of Intergovernmental Panel on Climate Change (IPCC) 2007, future climate change and associated impacts will vary from region to region around the globe and the effects of an increase in global temperature include a rise in sea levels and a change in the amount and pattern of precipitation, as well as a probable expansion of subtropical deserts.

1.2. Climate Change and Carbon Dioxide Sequestration

With the continued use of fossil fuels as our primary energy source, important and significant steps need to be taken to help stabilize the amount of anthropogenic CO_2 being released into the atmosphere. Since the beginning of the industrial revolution, about 374 billion metric tonnes of CO_2 have been released to the atmosphere mainly from the consumption of fossil fuels and cement production [7, 8]. Approximately half of these fossil fuel CO_2 emissions have occurred since the mid-1980s. Globally, in the year 2011, liquid and solid fuels accounted for 75.5% of the emissions from fossil fuel burning and cement production. In the same year, combustion of gas fuels (e.g., natural gas) accounted for 18.6% (1760 million metric tons of CO_2) of the total emissions from fossil fuels [8]. This reflects a gradually increasing global utilization of natural gas. Figure 1.2 below illustrates the annual global carbon dioxide emissions from burning fossil fuels and from cement production [8]. With the projections showing an increase in the burning of fossil fuel for our energy demands, we expect an accompanying increase in the emission of CO_2 as well.

Hence, it is imperative that procedures are put in place to control man-made CO_2 emissions. Many technologies have been proposed to cut down CO_2 emissions, for example, CO_2 mineralisation technology; an industrial process which permanently fixes the CO_2 into inorganic carbonates for production of carbon compounds or chemicals. CO_2 utilisation technology is another industrial process which uses CO_2 as a feedstock for synthetic applications in chemical and fuel industries [9]. Nonetheless, these technologies cannot reasonably limit the amount of CO_2 emissions because the rate of utilisation is drastically lower than the rate of anthropogenic CO_2 emissions [10-12]. However, one technology that is capable of curtailing the increasing level of CO_2 emissions is carbon capture and storage (CCS) (or simply CO_2 sequestration) [13-16].

CCS is considered to be the main technology available to effectively mitigate CO_2 emissions. Carbon sequestration is the process of capturing and injecting carbon dioxide into suitable geologic formations for long-term storage to mitigate global warming. CCS involves three main processes; the capture of waste CO_2 from large point sources, such as fossil fuel power plants, the transportation of the captured CO_2 to a storage site, and the injection of the captured CO_2 into suitable and secure storage formations [15].

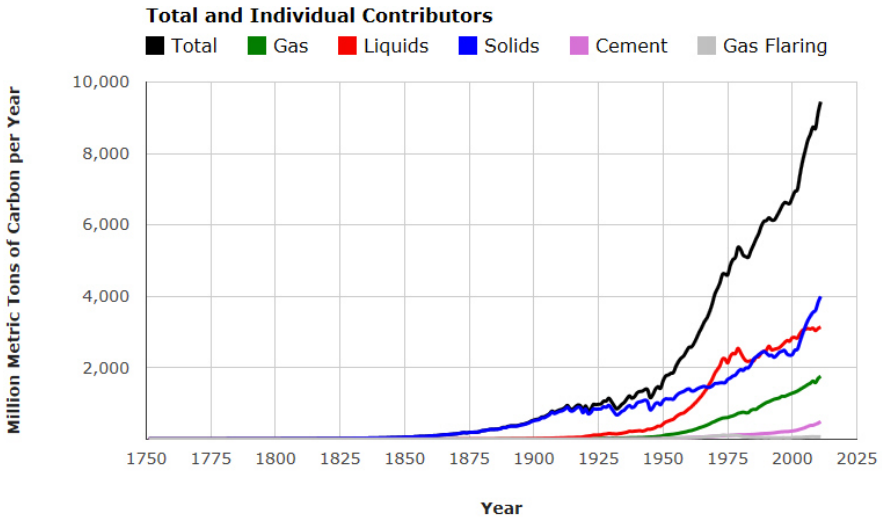

Figure 1.2. Estimate of the Total Carbon Emissions from Fossil Fuel Combustion from 1751 – 2011

Two storage locations have been suggested: geological formations [10, 11, 17] and the deep ocean [10, 18]. However, storage in geological formations is the favoured choice because of the large storage volumes available globally and the security of storage. Possible geological formations suitable for CO_2 storage are depleted oil or gas fields, deep saline aquifers or unmineable coal seams. Before injecting CO_2 into the underground reservoirs, it needs to be compressed into a supercritical or sub-cooled liquid form appropriate for underground storage. However, CO_2 is typically captured in a hot and wet state, i.e. CO_2 in flue gases from a power station is typically captured by dissolution in a solvent, which leaves some water in the CO_2 stream. If the CO_2 is transported in this state, it will cause significant corrosion problems to the pipelines [19-21]. Hence, the CO_2 is dried before transportation in order to avoid

pipeline corrosion and save costs (pipelines that could transport wet CO_2 are quite expensive) [20, 21]. It is the injection of dry CO_2 that motivated the drying experiments aspect of this research. The widely used and most efficient storage method for CO_2 sequestration is the injection into deep saline aquifers or in depleted oil and gas wells. Also, according to the International Energy Agency (IEA), the analyses of CO_2 emissions to be stored in the three underground storage options available are as follows:

I. Deep saline aquifer: 400 – 10,000 Gt CO_2 (20- 500% emissions to the year 2050). These saline aquifers always contain dissolved salt, which leads to salt deposition during dry CO_2 injection [10, 22-24].

II. Depleted oil or gas reservoirs: 920 Gt CO_2 (45% emissions to the year 2050). These oil and gas reservoirs essentially contain a water phase which always contains salt [16, 25], leading to salt deposition during dry CO_2 injection.

III. Unmineable coal beds: 40Gt CO_2 (<2% emissions to the year 2050)

Figure 1.3 shows the geological storage options available for CO2 sequestration [13]. This shows that deep saline aquifer has the largest capacity for CO_2 storage, however, the prediction of migration pathways of CO_2 after injection is crucial and challenging. For this reason, depleted oil or gas fields may be favoured as the storage location because we are already familiar with the geology of such fields and they have a second advantage of enhanced hydrocarbon recovery with CO_2 injection.

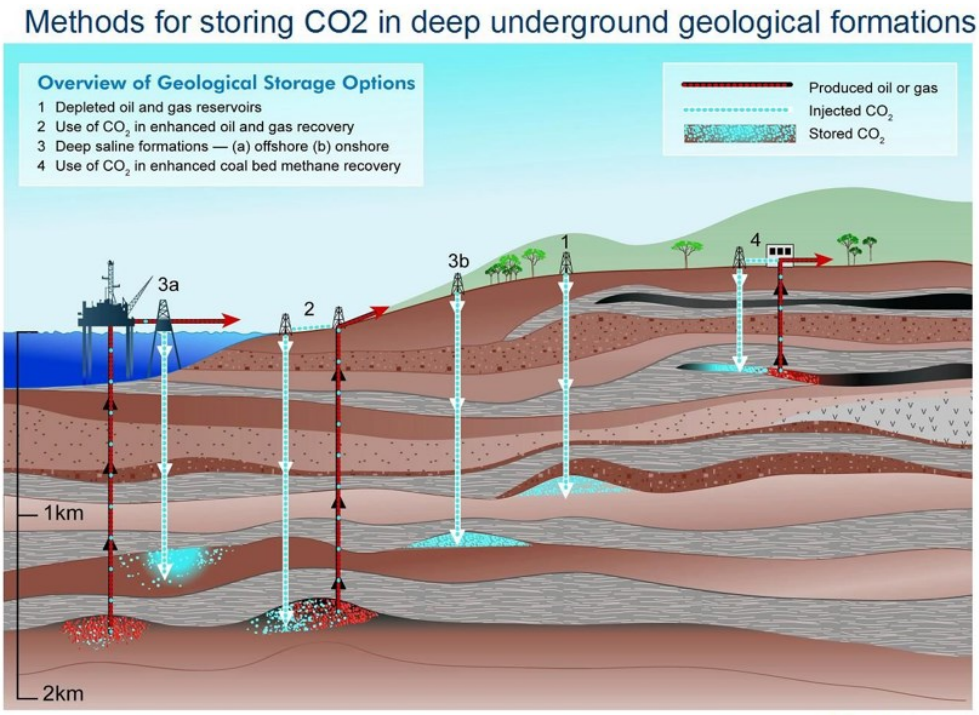

Figure 1.3. Geological storage options for CO_2. Several types of rock formations are suitable for CO_2 storage, including depleted oil and gas fields, deep saline formations and deep, un-mineable coal seams [13].

An obvious concern about storing CO_2 in underground reservoirs is the possibility of the CO_2 seeping through the reservoir sealing formation back into the atmosphere. Hence, the long-term security of the injected CO_2 is imperative. Knowledge of the fundamentals of the interaction between the injected CO_2, the inherent reservoir components and the reservoir sealing formations are very important. CO_2 can be stored for a very long time in these formations by four main mechanisms [16]. The first mechanism is structural or physical (hydrodynamic) trapping. This involves the trapping of injected CO_2 by the high capillary forces and low permeability of the formation cap-rock. Structural trapping is particularly important for early time frames during CO_2 sequestration. The second mechanism is the residual (capillary) trapping of CO_2 within the porous structure of the reservoir. This involves the formation brine surrounding the more buoyant CO_2 as it migrates upwards. The formation brine displaces the injected CO_2 by imbibition leading to an isolated CO_2 phase within the pores of the reservoir [26, 27].

The third storage mechanism is dissolution trapping. This involves the CO_2 dissolving in the in-situ brine in the reservoir making the CO_2-brine mixture much denser. The

denser mixture consequently sinks down into the reservoir keeping the CO_2 securely in place. This mechanism is considered to be a safer way of storing CO_2 with a timescale of up to hundreds of years [28]. The final storage mechanism is geochemical (mineral) trapping, this involves the formation-brine-dissolved CO_2 forming a carbonic acid. The carbonic acid then reacts with the minerals present in the reservoir to precipitate carbonates [29]. This will render the injected CO_2 completely immobile for a very long period of time, hence, the mechanism is considered very attractive for CO_2 sequestration in terms of storage security [30, 31]. All the trapping mechanisms are illustrated in figure 1.4 [32].

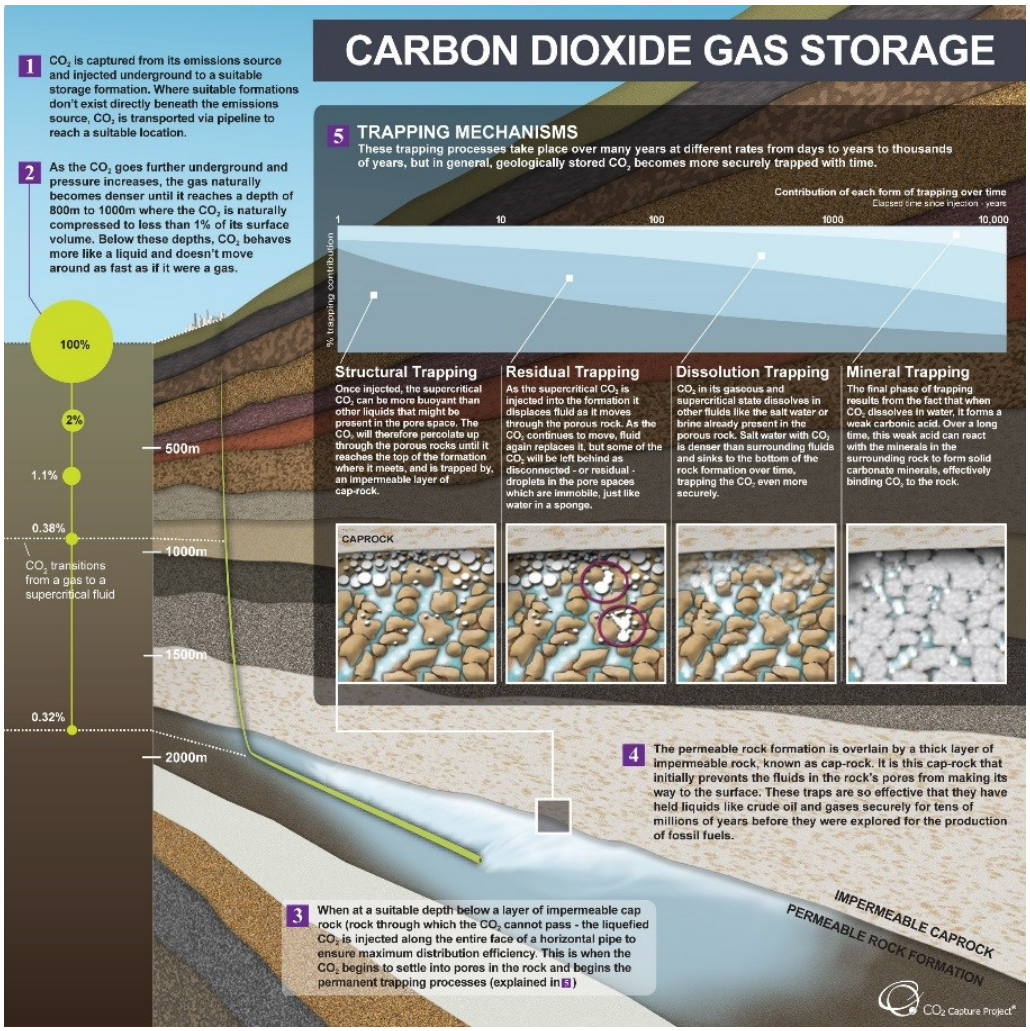

Figure 1.4. An illustration of the different geological storage mechanisms involved in carbon sequestration: structural, residual, dissolution and mineral trapping [32].

The storage capacities of the four trapping mechanisms are shown in tandem in figure 1.5 [33, 34]. Of all these mechanisms, more interest has been placed on understanding residual trapping because trapping is achieved by capillary forces and it is not entirely dependent on the integrity of the cap-rock [27]. Also, isolation of the injected CO_2 is achieved in a relatively short timescale [35-37].

All these trapping mechanisms could be affected by the deposition of salt when dry CO_2 is injected because drying can affect the regions of the reservoir that would be accessed by the dry CO_2 and therefore would have an impact on these mechanisms. All these mechanisms rely on the spatial distribution of CO_2 moving in the reservoir and this can be affected by the deposition of salt in the reservoir.

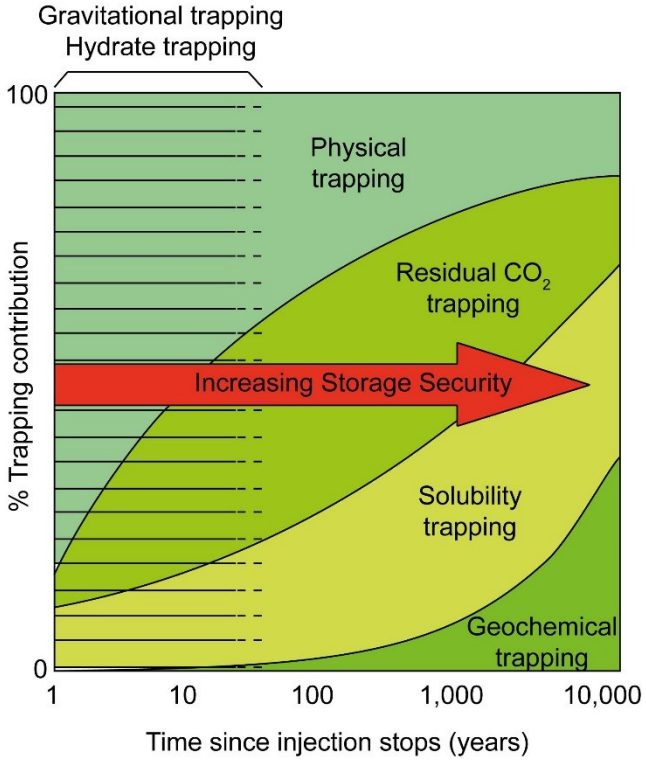

Figure 1.5. The relative security of sequestered CO_2 for various storage mechanisms [33, 34].

1.3. Fossil Fuels and Improved Oil Recovery

Fossil fuels account for more than eighty per cent of global energy production [2, 38-40]. To continue to meet the ever-increasing global demand for energy, exploration and production of crude-oil from fossil fuels must be continuously optimised. Yet, a

large amount of oil remains in the reservoir after primary and secondary recovery processes from most production platforms. Typically, only about thirty-five per cent of the original oil in place (OOIP) is produced before primary and secondary recovery processes becomes economically unreasonable [39-41]. Due to these low recovery percentages, numerous other techniques have been used (and some are still been developed) to improve the yield of oil and gas reservoirs. These tertiary recovery processes are widely regarded as Enhanced Oil Recovery (EOR). Enhanced oil recovery can increase production by up to fifteen per cent using techniques like thermal EOR, chemical EOR, miscible flooding EOR, gas injection EOR or water-alternating-gas (WAG) EOR. Some EOR techniques can raise total oil field recovery to seventy per cent [39, 40].

Out of the many EOR techniques available, the miscible flooding EOR technique using CO_2 is an established technology used widely in oil and gas production; it has an advantage of being able to substitute anthropogenic CO_2 (that would otherwise be emitted into the atmosphere) for EOR. This creates an opportunity for this process to be a climate mitigation strategy, as a significant portion of the CO_2 used in EOR remains in the oil field after oil and gas production ceases. The displacement processes that occur when two immiscible phases flow is at the heart of making reservoir models of oil and gas fields.

1.4. Research Motivation

This study is motivated by two different aspects of multiphase pore-level fluid displacements encountered during CO_2 sequestration and enhanced oil recovery. The first aspect deals with understanding the fundamental physical processes involved in porous media drying in the context of CO_2 sequestration. While the second part aims to shed more light and understanding on the different forces in play during the flow of two immiscible fluids through a porous media.

1.4.1. Drying in Porous Media in the Context of CO_2 Sequestration: Combined Evaporation and Salt Precipitation

During CO_2 injection into an underground reservoir, salt is precipitated which can greatly reduce the permeability and porosity of the reservoir by blocking the pore

bodies and throats in the reservoir formation. These salt depositions happen mainly near the point of injection threatening the entire sequestration process, a process known as wellbore dry-out. This decrease in net injectivity can lead to increased injection costs, reduced carbon efficiency, and reduced CO_2 storage potential. The same phenomenon can also lead to reduced oil recovery. Understanding this blockage process on the pore-scale is imperative for us to be able to enhance and evaluate our carbon sequestration processes. Furthermore, most carbonate reservoirs are known to be fractured systems, this is taken into account in the choice of boundary conditions for this experimental research. The reservoir matrix is full of brine and just above it, there is a very conductive fracture such that when CO_2 is injected, it rapidly fills the fracture and flows across the face of the matrix.

1.4.2. Multiphase Pore-Level Flow Dynamics in Porous Media

A number of important engineering processes involve the flow of two or more immiscible fluids through a porous media of varying complexities, i.e. CO_2 sequestration, enhanced oil recovery, groundwater remediation, and fuel cells fluid separation. The migration path and phase distribution of these fluids during flow depend on different phenomena like the wettability of the porous media, the geometry of the pore space and external hydro-mechanical forces. The use of capillary, viscous and gravity forces to characterize these flows is still not very clear. Our aim is to study these migration pathways at the pore level to further elucidate the dynamics and phase distribution of the different fluids and how we can represent them consistently at the Darcy-scale. We will be investigating the case of co-injection of two immiscible fluids, specifically, we are interested in visualizing rapid processes that take place during these displacement processes using micromodels. For example, an intermittent connections phenomenon was recently reported in immiscible two-phase flow experiment using micro-computed tomography (µ-CT) imaging [42]. However, µ-CT's time resolution is not sufficient to see in detail the dynamics of this intermittent connections. Also, this phenomenon has never been observed in micromodels experiments.

Both aspects of this research are important in ensuring safe, secure and efficient CO_2 storage as well as improved or enhanced oil recovery from underground reservoirs. The experiments are carried out using a range of 2.5D etched silicon micromodels and

a number of different visual imaging suites. The use of micromodels provides the combined advantage of real-time imaging and optical transparency at the pore scale. The advantages of the micromodel for rapid processes motivated the immiscible two-phase flow experiments. These rapid processes have been previously identified in μ-CT experiments but they are not fast enough to adequately resolve it. The micromodel technique has the advantage of being able to capture these rapid processes at high resolution.

1.5. Thesis outline

The remainder of this thesis is divided into seven chapters as follows;

In chapter 2, the background and fundamentals of multiphase flow in porous media will be discussed. Then followed, first by a thorough review of the available literature on evaporation and salt precipitation. This will be followed by a literature review of the pore-level dynamics of multiphase flow in porous media. Chapter 3 describes the materials and methods used in this study. The design and fabrication of the different micromodels used in this study will be discussed. All the imaging techniques used will also be discussed.

Chapters 4 and 5 will present experimental results of the evaporation and salt precipitation aspect of this study while chapter 6 will present experimental results from the pore-level dynamics of multiphase flow in porous media. Chapter 7 will present results on the simulation of the pore-level dynamics of multiphase flow in porous media using the Lattice Boltzmann Method (LBM). Also, the design and manufacture of a new multi-depth non-repeating micromodel will be presented in this chapter. Chapter 8 will present the final conclusions of both aspects of this study and recommendations for future works.

2. Scientific Background and Literature Review

Enhanced oil recovery processes and carbon sequestration in underground reservoirs involves the flow of multiple phases in porous media and in the case of dry CO_2 injection, salt precipitation. To adequately understand these processes, knowledge of the fundamental physics of multiphase flow in porous media is essential. The fundamentals of multiphase flow in porous media will be discussed in this chapter, providing a scientific background to the rest of the thesis. Multiphase dynamics and the different displacement events possible in porous media will be discussed. A comprehensive literature review of experiments and simulations on evaporation and salt deposition in porous media as well as two-phase flow behaviour at the pore scale will be discussed. The application of micromodels in studying multiphase flow dynamics will also be discussed.

2.1. Multiphase Flow in Porous Media

A porous medium is any material that contains voids (pores). Natural materials like reservoir rocks, soil, and man-made ones like cement and ceramics are examples of a porous media. They are characterised by intrinsic properties such as porosity, permeability, wettability and capillary pressure. Knowledge of all these properties is fundamental in investigating how fluid flows at the pore scale. A multiphase fluid consists of two or more immiscible phases with a distinct interface clearly separating them [43]. The fraction of the void space occupied by a particular fluid is known as the saturation of that phase.

2.1.1. Porosity

The porosity is the fraction of the total volume of the porous medium occupied by void space, represented by the symbol ϕ, the porosity is the volume of void space (V_v) in a soil or rock divided by the total or bulk volume (V_b) of the soil. The porosity can also be determined knowing that the bulk volume of the porous structure is made up of the

both the void space and the space taken up by the solid structure (V_s), in this way we can define the porosity of a porous medium to be [44]:

$$\phi = \frac{V_v}{V_b} = \frac{(V_b - V_s)}{V_b} \quad (1)$$

Figure 2.1 shows a schematic of a two-dimensional cross-section of a porous solid, highlighting the different types of pores found in porous media. Porosity can be categorised as total porosity (as defined above) and the effective porosity. Effective or connected porosity is the volume fraction of the porous medium containing connected void spaces through which fluids may flow [45]. In practical applications, only effective porosity is considered, as fluids in isolated pore spaces cannot flow nor be displaced. Henceforth, porosity in this thesis should be taken to mean effective porosity. Mercury intrusion porosimetry (PIV) technique can be used to evaluate the effective porosity of a porous medium while Imaging techniques can be used to estimate the connected and isolated (total) pores of a porous medium.

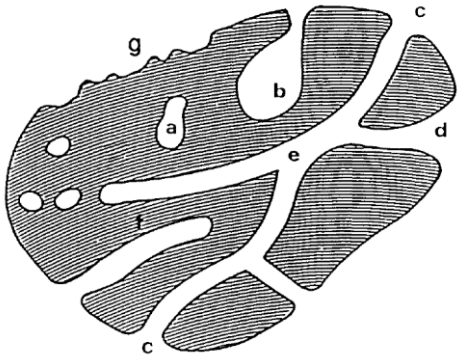

Figure 2.1. A schematic cross-section of a porous medium showing the different types of pores found in porous media, (a) is a closed or isolated pore, (b) & (f) are dead-end pores, (g) is a surface pore and (c), (d) and (e) are 'through' pores (typical interconnected pore network through a porous medium) [46].

2.1.2. Saturation

In oil and gas reservoirs, the oil resides in the void spaces of the porous rock, however, not all the void space is full of hydrocarbons because at the outset brine saturates the porous rock. Hydrocarbons (oil and gas) formed from the chemical transformation of organic matter in deep sediments rises slowly upwards over geological time. The oil

collects under traps, from which it cannot escape, displacing the water that was initially present. However, not all the water can be squeezed out of the rock, some of the water initially present always remains. Saturation is the fraction of the void space occupied by a given phase. The water saturation, S_w is the fraction of the void space of the porous medium occupied by water. The sum of all the phase saturations is, by definition, 1 [45]. That is, the addition of the water saturation, S_w, the oil saturation, S_o, and the gas saturation, S_g equals to 1. ($S_w + S_o + S_g = 1$) . A fully saturated porous medium is one where only a single fluid phase is present, in most cases the aqueous phase or water [45].

2.1.3. Permeability and Relative Permeability

Permeability is defined as the ratio of the flow rate to the pressure gradient within a porous medium, characterized by pore structure and size. The single phase permeability is one of the characteristic parameter measured in any scientific study of a reservoir rock sample. The French scientist, Henry Darcy first proposed the phenomenon in 1986 after his experiments on water flow through sand columns. From the experiments, he was able to generate a linear relationship between flow rate of water and the hydrostatic pressure caused by an upright column of water. These results were used to form the general form of the first proposed Darcy's Law [47, 48]:

$$Q = -\frac{\kappa A}{\mu}(\nabla P - \rho g) \tag{2}$$

where Q is the total discharge (m^3/s) of fluid passing through the porous media, κ is the absolute permeability (m^2) , A is the cross-sectional area (m^2), μ is the dynamic viscosity of the fluid (Pa.s), ρ is the density of the fluid (kg/m^3), g is the gravitational vector (m/s^2), and ∇P is the gradient of the pressure of the fluid (Pa/m). The minus sign in equation (2) indicates that fluid flow is in the opposite direction to increasing pressure, thus, flow is from high to low pressure in a horizontal system. The unit of permeability is the Darcy which is equal to 9.86×10^{-13} m^2 or ≈ 1μm^2 in SI units. Darcy's law has been shown to be derivable from the proper averaging of the steady-state Stokes equation [45, 49], further validating Darcy's observations.

Permeability, as well as porosity, has been found from experiments to vary widely across different reservoir core samples. There are extremely low permeable rocks in the nano-darcy scale to the very high permeable rocks and packed beds on the scale of a few Darcys. Intuitively, one might expect a simple and direct correlation between porosity and permeability for porous media flow. However, this correlation is often ambiguous with many inconsistencies. This is due to the very intricate nature of flow within a porous medium often caused by the pore geometries, the wettability of the pores, tortuosity, etc. Rocks with the same porosity can have permeabilities that are orders of magnitude apart. A conventional way of estimating the permeability of a porous media sample is through the application of a constant pressure gradient across the sample and then measuring the flow rate of the fluid passing through the medium. The permeability of the sample can then be found using equation (3), derived by simplifying equation (2) after integration across the length of the medium and ignoring gravitational effects [50]:

$$\kappa = \frac{q\mu L}{(P_1 - P_2)} \tag{3}$$

with L being the length of the sample, q ($=\frac{Q}{A}$) is the volumetric flux, and P_1 and P_2 being the pressure upstream and downstream of the medium, respectively.

Equations (2) and (3) are only applicable for a single phase flow through a porous medium. In reality, flows in porous media are almost always multi-phasic. Darcy's law can be extended to cases where multiple fluid phases are flowing, each phase is assumed to flow in its own sub-network of the pore space without affecting the flow of the other phases. This extension to the multiphase flow of fluid p is shown in equation (4) [51].

$$q_p = -\frac{\kappa k_{rp}}{\mu}\left(\frac{\delta P}{\delta x} - \rho_p g_x\right) \tag{4}$$

where κ is the absolute permeability of the rock formation, k_{rp} is the relative permeability of phase p. It represents the mobility of the phase as a fraction of what it would be for single-phase flow. This equation is only applicable to flows dominated by

capillary forces at the pore scale, i.e. flows with low Capillary and Bond numbers. Relative permeability is traditionally plotted as a function of the saturation of the material.

All the fundamental physical properties of porous media discussed so far are macroscopic properties, that is, they are influenced by pore structure and are representative of the average behaviour of a sample containing many pores. However, when capillary forces are significant, it is imperative to consider microscopic properties like the wettability and capillary pressure of the porous media [43].

2.1.4. Wettability and Contact Angle

The wetting state of a porous medium is an important microscopic parameter that affects the dynamics of flow at the pore scale. Wettability is the tendency of one fluid to spread on or adhere to, a solid surface in the presence of other immiscible fluids [52]. Wettability refers to the interaction between the fluid and solid phases. In a reservoir, the 'fluid' phase can be water or oil or gas, and the solid phase is the rock mineral grains. Wettability is defined by the contact angle of the fluid with the solid phase. Real-life systems involve multiple fluids (two or more immiscible phases) flowing in porous media, distinct interfaces form between these immiscible phases, across which a pressure difference is present if the interfaces are curved [44]. Figure 2.2 shows a water/air system in a porous medium with the following interfaces; water-solid, water-air and air-solid.

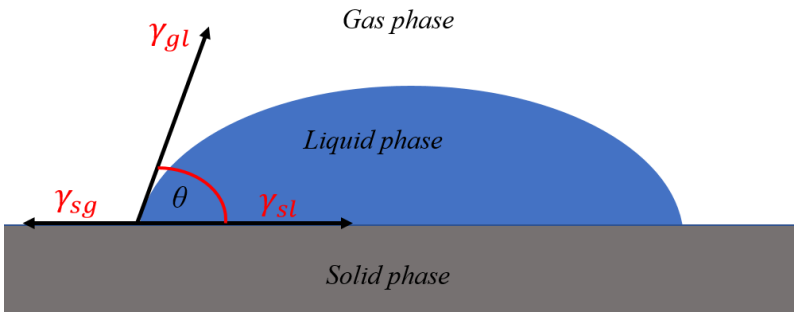

Figure 2.2. Schematic of contact angle (θ) with the respective interfacial tensions: γ_{gl} (gas/liquid), γ_{sg} (solid/gas) and γ_{sl} (solid/liquid).

The interfacial tension between each phase is measured as a force per unit length or energy per unit area. The interfacial tension is, therefore, the energy required to increase the surface area by one unit. These interfacial tensions (i.e. forces of adhesion and forces of cohesion) between the two fluids – the water/air system is described by Young's equation. At equilibrium, the contact angle (θ) illustrated in figure 2.2 can be expressed as:

$$\cos(\theta) = \frac{\gamma_{sg} - \gamma_{sl}}{\gamma_{gl}} \tag{5}$$

where *s, l, g* represents solid, liquid and gas respectively, and $\gamma_{gl,}$ γ_{sg} and γ_{sl} are the interfacial tensions between the gas/liquid, solid/gas and solid/liquid interfaces respectively. The contact angle is conventionally measured through the denser phase that is water for oil/water and gas/water systems and the oil phase for gas/oil systems [44].

From the three-phase system schematic in figure 2.2, when $\theta < 90^o$, the fluid is said to be wetting (water-wet), when $\theta > 90^o$, the fluid is non-wetting, when $\theta = 0$, we have complete wetting and when $\theta = 90^o$, the fluid has neutral wettability. This means that different fluids will have different shapes depending on their hydrophilicity or hydrophobicity. Considering a strongly water-wet solid surface, a fluid which is hydrophilic will have a small contact angle and is considered a 'wetting' fluid – that is it likes to spread over the solid surface. However, a fluid which that is hydrophobic will have a large contact angle, which means its contact angle will be greater than 90^o.

Most clean (surface of the rock in contact with fluids is chemically the same as the bulk composition) rocks are naturally water-wet [45]. Calcite (calcium carbonate, a major component of many carbonate rocks) and quartz (silicon dioxide, a major constituent of many sandstones) are ionically bonded solids with strong inter-atomic interactions resulting in them having large interfacial tensions. However, they also have stronger interaction with water (hydrogen or oxygen) through electrostatic attraction with the surface than with hydrocarbons (which does not allow hydrogen bonding) [45, 53]. This makes the water-solid surface energy less than the oil (or gas)-solid surface energy. Hence, any other fluid (oil or gas) introduced into a water-saturated porous medium will be the non-wetting phase. However, in reality, most

reservoir rocks are not completely water-wet because surface-active components of the oil (like asphaltenes) adhere to the solid surface making it less water-wet [53-55]. Regions not in contact with the surface-active components remain water-wet, hence many oil reservoirs are of mixed-wet configuration – different regions of the pore space have different wettabilities. Hence, the wettability of a reservoir rock is usually determined by the distribution of contact angles in the reservoir rock.

However, in spite of the many and recent advancements in measuring the contact angles of reservoir rocks from pore-scale imaging, these measurements are not routine and often require a detailed level of characterization like pore geometry, flow direction and mineralogy on a pore-by-pore (or even sub-pore) basis [45]. Therefore, it is more common to use macroscopic measurements of capillary pressures to ascertain the wettability of the reservoir rock [56]. Since capillary pressure is not definitively related to contact angle (wettability), quantifying wettability through capillary pressures is a little ambiguous [45]. The Amott indices [57] and the USBM (US Bureau of Mines) index [58] are two of the widely used volume-averaged approaches for quantifying wettability through capillary pressure measurements. These methods define wettability based on the displacement processes that occur during imbibition and drainage (water flooding and oil re-injection cycles) in reservoir rocks.

For the Amott method, the change in saturation is measured during the spontaneous invasion of oil ($\Delta S_{os} = S_o^* - S_{or}$) and during forced injection ($\Delta S_{of} = 1 - S_{wi} - S_o^*$) in a rock sample at the waterflood residual oil saturation (see figure 2.3). This is then followed by a tertiary waterflood, with $\Delta S_{ws} = S_w^* - S_{wi}$ representing the saturation change during the spontaneous imbibition of water and $\Delta S_{wf} = 1 - S_{or} - S_w^*$ representing the change during forced water injection. Hence, $\Delta S_{os} + \Delta S_{of} = \Delta S_{ws} + \Delta S_{wf} = \Delta S_{wt}$ [45].

ΔS_{os} = saturation change for spontaneous oil displacement. S_o is the oil saturation, S_{or} is the residual oil saturation, ΔS_{of} is saturation change for forced oil displacement, S_{wi} is initial water saturation, ΔS_{ws} is the saturation during spontaneous water imbibition, S_w is the water saturation, ΔS_{wf} is the saturation change during forced water injection, ΔS_{wt} is the total saturation change, and the * represents saturation where the capillary pressure is zero.

The Amott water index is defined as

$$I_w = \frac{\Delta S_{ws}}{\Delta S_{wt}} \quad ; \quad 1 \geq I_w \geq 0 \tag{6}$$

While the Amott oil index is defined as

$$I_o = \frac{\Delta S_{os}}{\Delta S_{wt}} \quad ; \quad 1 \geq I_o \geq 0 \tag{7}$$

For water-wet systems, $I_w \approx 1$ and $I_o = 0$, neutral wettability occurs for $I_w \approx I_o \approx 0$, while mixed-wet rocks have $I_w > 0$ and $I_o > 0$. An oil-wet rock has $I_o > 0$ but $I_w = 0$.

Conversely, the USBM index method, measurement of capillary pressures during forced injection for both water and oil is required [45]. It is determined by the ratio of the two areas, A_1 and A_2 in the waterflooding and oil re-injection cycles in figure 2.3, i.e. the area under the secondary (forced) drainage of oil (labelled 5 in figure 2.3) and the water spontaneous imbibition (labelled 2 in figure 2.3), and the area under oil spontaneous invasion (labelled 4 in figure 2.3) and water forced injection (labelled 3 in figure 2.3).

The USBM index is defined as

$$I_{USBM} = \log\left(\frac{A_1}{A_2}\right) \quad ; \quad \infty \geq I_{USBM} \geq -\infty \tag{8}$$

where $A_1 = \int_{S_{wi}}^{1-S_o^*} P_{c2o} dS_w$ and $A_2 = \int_{S_w^*}^{1-S_{or}} P_{cw} dS_w$

where P_{c2o} is the capillary pressure during secondary oil invasion and P_{cw} is the waterflood capillary pressure.

For water-wet systems, $A_1 > A_2$ and a positive index, while oil-wet rocks have $A_1 < A_2$ and a negative index. This characterization makes no account of either water or oil spontaneous imbibition, hence, it cannot differentiate between mixed-wet systems and neutrally systems, $I_{USBM} \approx 0$ in both cases [45]. This limitation makes the USBM index less useful compared to the Amott indices.

Lastly, wettability alteration is known to occur in most porous media, be it oil reservoir rocks, soils or aquifers, although the reason for it differs. In reservoir rocks, wettability (or contact angle) is not a constant throughout the rock, it depends on the surface roughness, the mineralogy of the surface, the oil and brine composition and the temperature and pressure of the reservoir. For aquifers and soils, wettability alteration depends mainly on surfactants' adherence to a solid surface [45].

Contact angle can be characterized as equilibrium, advancing or receding contact angle depending on the flow direction of the fluid on the solid phase. It is an advancing contact angle when the denser phase through which contact angle is measured is the advancing wetting phase (displacing a non-wetting phase). It is receding contact angle when the denser phase through which contact angle is measured is the receding phase (being displaced by the non-wetting phase). The equilibrium contact angle is the angle made when there is no movement in the three-phase system (i.e. no movement of the solid/wetting/non-wetting contact). These three contact angles may all be different for a particular system, the reasons for these are chemical heterogeneities, small-scale surface roughness and wettability alterations described above.

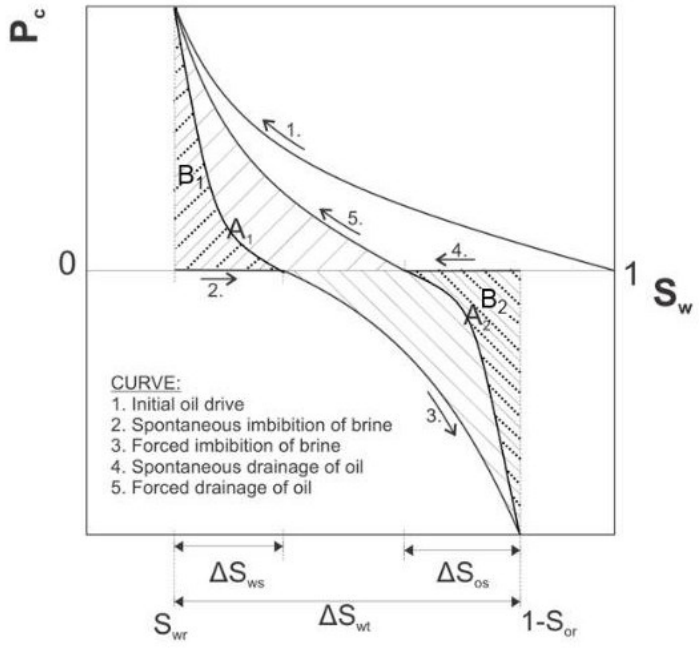

Figure 2.3. Capillary pressure curves for waterflooding and oil re-injection with the definition of Amott and USBM wettability indices [59].

2.1.5. Capillary Pressure

When there are multiple phases present in a porous medium (there will be an interface between the different fluids present), then there exists a pressure difference between them caused by the tension of the separating surface(s). This pressure difference between the two phases is known as the capillary pressure. The capillary pressure represented by P_c is defined as the pressure across the interface between two immiscible phases and can be calculated using the Young-Laplace equation [43, 60]:

$$P_C = P_{NW} - P_W \tag{9}$$

where P_C is the capillary pressure, P_{NW} and P_W are the pressures of the non-wetting and wetting phases, respectively. The non-wetting phase has the higher pressure. In a real porous medium, the local interface within a pore is curved to minimise the surface energy, with two principal radii of curvature, r_1 and r_2 (radii of curvature measured perpendicular to each other) which are related to capillary pressure as [44, 60]:

$$P_C = \gamma\left(\frac{1}{r_1} + \frac{1}{r_2}\right) = 2\frac{\gamma}{r^*} \tag{10}$$

where r^* is the mean radius of curvature and γ is the interfacial tension between the two phases. It has the units of a force per unit length (N/m) or an energy per unit area (J/m^2).

The geometry of a real porous medium is often very irregular with complex pore spaces. Hence, in order to study the fundamentals of multiphase flow in porous media, we often start by looking at very simple idealised structures, from which some qualitative deductions can be made [61]. Capillary tubes are often used to represent a single pore in a porous medium, for a single cylindrical capillary tube with two fluids in equilibrium as illustrated in figure 2.4, the blue arc is the interface between the wetting and the non-wetting phase. The capillary pressure can be expressed in terms of the principal radii of curvature. For enhanced oil recovery and carbon sequestration

operations, capillary pressure measurements can be used to determine which fluid migration pathways are favoured due to pore space geometries (as capillary pressure is dependent on the interfacial tension and the mean radius of curvature) [62].

$$P_C = \frac{2\gamma}{r}\cos(\theta) \tag{11}$$

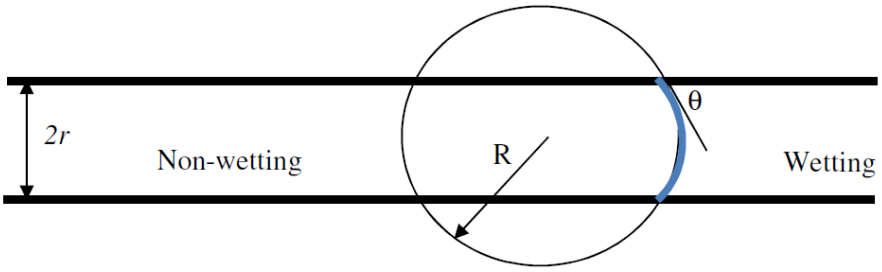

Figure 2.4. Schematic of two immiscible fluids within a capillary tube of radius *r*, where the radius of curvature is $R = \frac{r}{\cos(\theta)}$, where R is the radius of a circle fitted to the curvature of the interface.

2.1.6. Drainage

Consider a porous medium that is water-wet and initially fully saturated with water, then a non-wetting phase (oil) enters the porous medium. If this is done sufficiently slowly then the pressure drop across the oil phase is equal to the capillary pressure. This process is called primary drainage and is the process by which oil migrates from source rock to fill a reservoir (initially fully saturated with water), it is also the same process by which injected CO_2 displaces water (brine) in a storage aquifer [45]. From the Young-Laplace equation (equation (6) and (7)), it can be inferred that the non-wetting phase will preferentially fill the larger pore spaces (in a multi-pore porous medium) because the radius of curvature for the meniscus is larger, thereby resulting in a lower capillary pressure. This means that for a given wetting phase pressure, there is an invasion by a lower non-wetting phase pressure. Subsequent increase in the non-wetting phase pressure will lead to pore spaces with lower radii of curvature to be invaded gradually. Consequently, primary drainage proceeds as a sequence of filling events, accessing progressively smaller pores. An external force (like gravity or

pressure gradient) is needed for the displacement of the wetting phase, displacement events in drainage process only occur by piston-like displacements once the threshold pressure of a particular throat is overcome.

2.1.7. Imbibition

In some sense, imbibition is the opposite of drainage; a wetting fluid invades a porous medium and displaces the non-wetting fluid initially in place. However, unlike the drainage process, imbibition can either be forced (driven by external forces like pressure gradient) or spontaneous (driven by capillary forces). In regards to oil recovery and CO_2 storage, only secondary imbibition is considered, which is the invasion of a wetting phase into a non-wetting phase after primary drainage, that is, there is some wetting fluid already present in the porous medium. Practical examples are seen in water-flooding secondary recovery, where water is injected to displace residual oil in a reservoir. An example of a spontaneous imbibition (also known as capillary imbibition) is when brine displaces stored CO_2 as the CO_2 rises in a storage aquifer [45].

2.2. Evaporative Drying in Porous Media

Evaporation occurs due to vaporization from the surface of a liquid into a gaseous phase that is not saturated with the evaporating substance. Evaporation occurs when there is a change of state from liquid to vapour at a temperature below the boiling point of the liquid. In most cases, the rate of evaporation is limited by the vapour diffusion through the boundary layer close to the interface. Evaporation or drying in porous media is often described as an immiscible displacement process (i.e. a drainage process, as gas is usually the non-wetting phase), involving the removal of a displaced fluid (liquids) from pore spaces by counter-flow in the same pore spaces as the displacing fluid (gas) [63, 64]. The rate of evaporation from a porous medium is also affected by the surface area of the porous media exposed to the drying ‘gas’, the humidity of the drying gas, the speed (flow rate) of the drying gas as well as the temperature of the system. The importance of the knowledge of the drying process in porous media cannot be overemphasized. Its applications are vast including but not limited to the pharmaceutical industry [65, 66], the food industry [67-69], the building

industry [70-73], soil remediation [74, 75], water management in the fuel cell industry [76], the paper and textile industry [77, 78], and most importantly in the context of this study, its use in the recovery process of oil and gas from underground reservoirs [79, 80] and carbon sequestration processes [22, 24, 81-83].

There are two types of boundary conditions usually relevant for porous media drying; the direct injection of dry gas into the porous media matrix (advective drying) and, the flow of dry gas across the surface of the matrix, for example at the surface of the soil or through a fracture channel (diffusive drying). Most experimental or simulation studies on evaporation (or drying) in porous media available in the literature used one or other of these boundary conditions for their investigations. More emphasis will be put on discussing diffusive drying due to the choice of drying application in this study, i.e. fractured systems. Investigation of porous media drying kinetics has generated many studies which has led to much progress being made on measuring the evaporative fluxes in stage-1 and stage-2 evaporation. However, the nature and dynamics of the transition from stage-1 to stage-2 evaporation are still somewhat vague. Three main questions were identified as important in understanding this transition [84]; (i) How the pore size affect distributions affect the transition?, (ii) What determines the duration and abruptness of the transition? (iii) What determines the dynamics of liquid menisci detachment from the surface?

2.2.1. Stages of Evaporation of Pure Water in Porous Media

Evaporation from porous media is a complex multiphase displacement process involving external mass (and energy) transfers (temperature, humidity, surface area and the speed of the drying gas) and internal mass transfers (vapour diffusion, thermal and hydraulic conductivities, and pore space geometry). Hence, the rate of evaporation from porous media is generally limited by atmospheric conditions and pore transport properties [85, 86]. Also, the rate of evaporation is affected by vapour pressure (or relative humidity) at the boundary of the porous medium.

Based on the dynamic interactions of these transfer processes, for an initially completely saturated, water-wet porous medium, the kinetics of isothermal and non-isothermal drying in porous media are typically classified into three stages [85, 87-90]; an early stage of evaporation with a relatively high and constant evaporation rate

known as the Constant Rate Period (CRP) or stage-1 evaporation, followed by a falling and a much lower evaporation rate known as the Receding Front Period (RFP). These stages are connected by a transition stage characterized by a large drop in evaporation rate known as the Falling Rate Period (FRP) [84, 85, 87, 91, 92]. In essence, stage-2 evaporation is a combination of the falling rate period and the receding front period.

I. Stage-1 Evaporation (Constant Rate Period)

For water-wet porous media, stage-1 evaporation is characterized by a relatively high evaporation rate because of the initial high liquid saturation. Due to stronger adhesion of water molecules to the pore wall compared to cohesive forces between water molecules, water is transported via capillarity in the film region leading up to the surface. The gas-filled pore spaces are saturated with water vapour and liquid films cover the pore surface so evaporation can only take place on the exposed surface. This drying period is controlled by external demand [92, 93]. The drying behaviour often conceptualized by stage-1 evaporation is supplied by capillary-induced liquid flow from large pores at the receding drying front supplying fine pores at the evaporating surface [84]. The ability of the capillary transport through corner wetting films to supply evaporative demand during stage-1 evaporation is the reason why the drying porous medium behaves as if it is virtually saturated [91]. This capillary driving force (supplying liquid through the hydraulically connected pores) is the main reason for the constant rate period [94]. Though the name suggests a constant drying rate, however, the drying rate is more accurately described as pseudo-constant rate because it shows a decreasing linear trend as pore corner films (responsible for evaporation by capillarity) thins out [92]. Eventually, the downward gravity and viscous forces overcome the upward capillary driving force at a certain depth of the drying front, disrupting hydraulic continuity with the surface [84, 87, 94]. The disruption of hydraulic continuity marks the end of stage-1 evaporation, and subsequently, liquid menisci move back from the surface to a level below the surface and form a new vaporization plane referred to as the secondary drying front [94].

II. Stage-2 Evaporation (Falling Rate Period and Receding Front Period)

The transition into the secondary drying front marks the onset of stage-2 evaporation, a period characterized by a lower evaporation rate limited by diffusion through the porous media. There is a significant drop in the drying rate due to the receding drying

front as the film region no longer extends up to the surface (a phenomenon called depinning). The falling rate period (FRP) is the transition from the advection to diffusion-dominated evaporation, and the process of diffusion is relatively much slower. During the receding front period (RFP), the film region completely de-pins from the surface of evaporation, cutting the flow of liquid to the surface. The drying rate during this period becomes entirely diffusion dominated as water vapour diffuses slowly towards the surface. The mechanisms for stage-1 and stage-2 evaporation have been experimentally confirmed for homogeneous porous media systems [87], layered porous media systems [95], partially wettable porous media systems [96] and so on.

The main difference between isothermal and non-isothermal porous media drying is the fact that the temperature gradient in the non-isothermal system significantly affects the phase distribution during drying. In the isothermal system, gas displacement of the liquid phase follows the classical invasion percolation pattern with the continuous evaporation of isolated liquid clusters [97]. This leads to a phase distribution characterized by two main regions: a continuously increasing dry zone adjacent to the side opened to the atmosphere and a continuously decreasing two-phase zone where both liquid and gas coexist [89]. However, for the non-isothermal system, due to the dependence of surface tension on temperature (i.e. it is easier for the gas to displace the liquid phase from throats with higher temperature) [90], gas displacement of the liquid phase follows a drying pattern referred to as stabilized invasion pattern [98]. The phase distribution is characterized by three main regions: the continuously increasing dry zone adjacent the side opened to the atmosphere, the continuously decreasing liquid-saturated zone adjacent to the sealed bottom of the porous medium, and a finitely-sized travelling two-phase zone sandwiched between them [89].

2.3. Models for Evaporation of Pure Water from Porous Media

Much advancement has been made in understanding the drying process. For example, drying in porous media can be theoretically described by invasion percolation concepts and it is often modelled as a 2D immiscible displacement [63, 64, 97, 99-102]. However, the dynamics, nature and duration of the stages of evaporation and the nature of the transitions involved in the overall drying process still need more

clarification. Adequate understanding of the transition from stage-1 to stage-2 evaporation and identifying the parameters affecting this transition will enable us to accurately describe and predict the entire drying curve.

For diffusive water drying from a porous medium, initially, the constant rate period persists until water at the surface reached a 'critical water content' [103]. The falling rate period then begins, limited by mass (vapour) transfer through viscous air film at the surface which is then followed by the third period limited by the transport of vapour and liquid through the dry porous media to the surface [103]. The effect of heat fields on porous media (soil) diffusive drying has been studied [104, 105], and it was established that the constant rate period was controlled by atmospheric conditions. The falling rate period was found to be independent of atmospheric conditions and heat fields but limited by transport of water to the surface[105], while the receding front period is controlled by the heat fields [104]. *Le et al. (2009)* [106] suggested that the driving force for evaporation from porous media can be due to mass transfer caused by non-isothermal conditions or simply diffusive transport of volatile species through the pores to a flowing gas stream called pass-over drying (or diffusive drying). Here, the diffusion of gas in porous media controls the overall rate of drying.

However, flow-through drying (advective drying) process can also occur when a gas flows through a porous medium that is partially saturated with liquids [107, 108]. Advective drying processes are particularly different from diffusive drying processes, in that the drying rates are not anymore controlled by diffusion of gas in porous media. Instead, the controlling factor is the compressibility of gas and the transport processes that affect the movement of liquids [106, 107]. That is, the drying rate is controlled primarily by the compressibility of gas and as well as the wicking action of wetting liquids in the porous medium [106].

For diffusive drying, early stages of evaporation from porous media are marked by relatively high evaporation rates supplied by capillary liquid flow from a receding drying front to vaporization surface. At a characteristic drying front depth, hydraulic continuity to the surface is disrupted marking the onset of stage-2 evaporation where a lower evaporative flux is supported by vapour diffusion [84]. A conceptual sketch illustrating the movement of the liquid meniscus from the surface (primary drying front) of a porous medium to a position within the porous medium (secondary drying front) is shown in

figure 2.5 [84]. The receding liquid menisci form a new evaporation surface at a depth below the surface.

While a porous medium with many pores of varying diameters and junction is very complex, drying in single capillary tubes has proven to be useful in gaining more insight of transport phenomena in the porous medium as this can be considered as drying in a single pore (of a complex porous medium). Single capillary tubes are the simplest micromodels available in which multiphase flow studies can be observed on the microscopic scale.

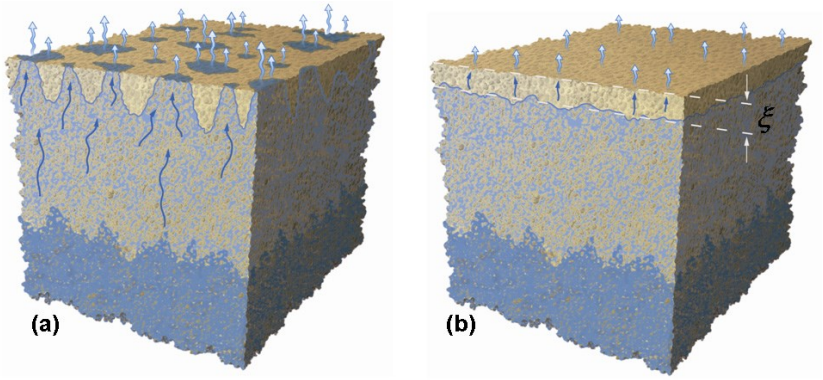

Figure 2.5. An illustration of the movement of the evaporation plane during drying in porous media. (a) A detachment of the liquid meniscus from the surface and pinning to a level below during the transition from stage-1 to stage-2 evaporation. (b) Formation of the secondary drying front at the beginning of stage-2 evaporation. The evaporation is preceded by the capillary flow up to the secondary drying front, vaporization at that level, and vapour diffusion through the dry layer. The depth of the secondary drying front at the onset of stage 2 is related to the maximum tail of the interface between the wet and dry zone [84].

One of the main challenges in predicting evaporation rate and nature of transition in real porous media experiments stems from the effect of liquid films in grooves, crevices, and roughness of the pore space in a porous media. These grooves, crevices and pore wall roughness are however not present in a capillary tube (although roughness can be specifically incorporated and wettability alterations can also be made during the fabrication of a capillary tube). Drying in glass capillary tubes can be used to understand the drying mechanism and process in the porous media [92, 93, 109]. Figure 2.6 is a schematic of drying in a square capillary tube [93, 109]. A comparison of figure 2.5 and 2.6 brings to fore the similarity between drying in a real

porous media and a capillary tube. The meniscus of the capillary tube in figure 2.6 is similar to the drying front in the real porous medium in figure 2.5. Due to the wettability of water, the shape of the meniscus is in a water-wet capillary tube is concave.

The assumption of a flat liquid-vapour interface (flat meniscus) is only relevant in the absence of wetting films which is certainly not typically the case for water in rocks. In model porous media such as a capillary tube, liquid transport to the tube entrance is usually by capillary forces through the wetting films on the corners of the capillary tube. Hence, the geometry of a capillary tube (square or circular) affects the rate of drying. *Chauvet et al. (2009)* [92] demonstrated this with an experiment on drying of organic liquids in square capillary tubes. They compared their results with theoretical values for circular capillary tubes [110].

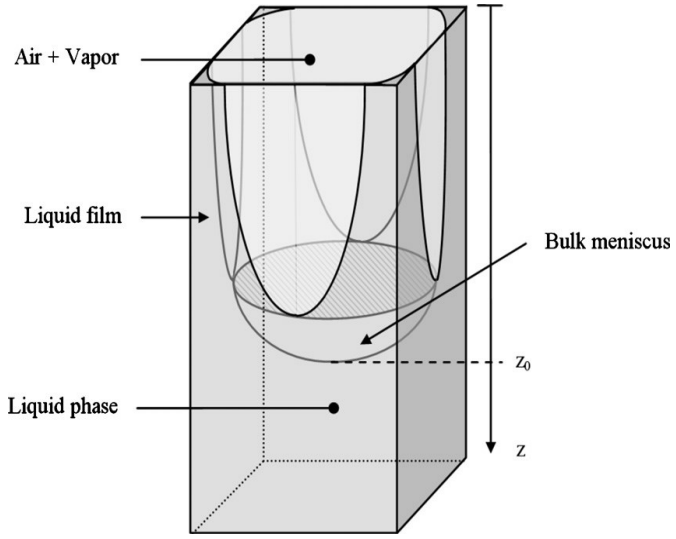

Figure 2.6. Sketch of the thick liquid films in a capillary tube of square cross-section

The results showed that the meniscus drop is significantly faster in the square tube. The evolution of drying of the organic liquids in square and circular capillary tubes is shown in the plot in figure 2.7. The faster evaporation rate for the square capillary tube was described to be due to the fact that circular tubes do not have corners so there are no thick films, therefore, no extra pathways for the liquid to be transported to the tube entrance from the receding bulk meniscus [92, 93]. While the evaporation rate itself is the limiting step during the CRP, the effect of liquid transport through the corner wetting films on the evaporation rate is very important, especially for slow evaporative

processes. The corner wetting films serve to transport the liquid to the surface so that it can evaporate. Hence, drying in square capillary tubes are generally significantly faster than drying in circular capillary tubes. For square capillary tubes, two distinct film regions were observed: the thin films, adsorbed to the walls of the tube and the thick films retained in the corner by capillarity. The corner films provide the transport paths for the liquid between the receding bulk meniscus and the entrance of the capillary tube. The roundness of a capillary tube determines the maximum degree of liquid film extending from the meniscus to the tube entrance, which explains the observations of why evaporation rate of a square capillary tube is faster than a circular one [92, 93].

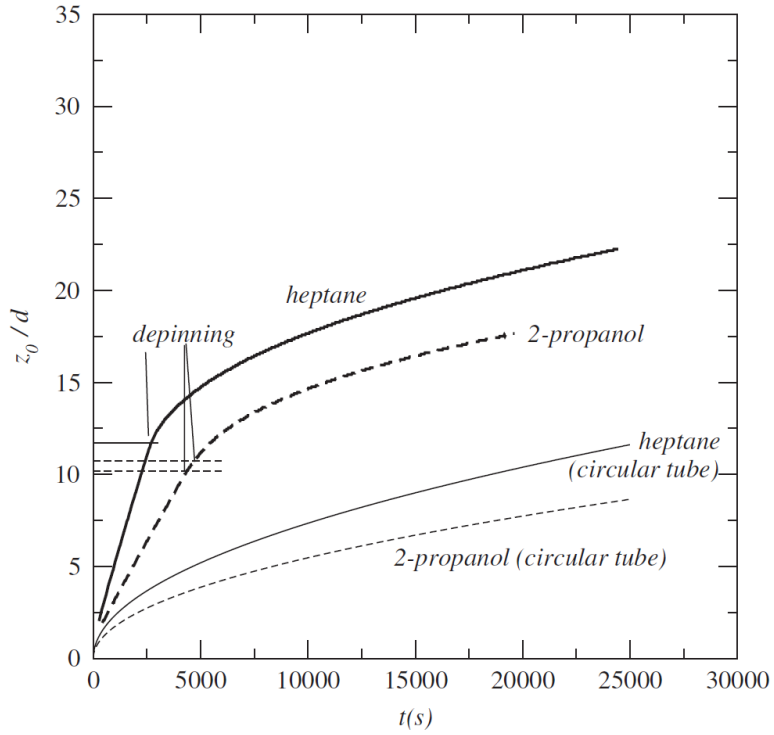

Figure 2.7. Evolution of bulk meniscus position z_0 as a function of time. The thick solid line and the dashed line are for the square tube. The thin solid line and dashed line on the bottom are for a circular tube. The position when the corner liquid films cease to be attached to the tube entrance (depinning) is indicated. The depinning coincides with the CRP-FRP transition and does not occur at the same time in the four corners in the 2-propanol experiment. The two dashed lines indicate the first depinning and when depinning has occurred in the four corners, respectively. Image modified from [92].

Several authors [93, 111-113] have studied film flow along the corners of capillary tubes. A numerical study to show the significant effect of liquid films on the drying rate and phase distribution patterns of a non-volatile liquid in porous media was done by *Yiotis et al. (2005)* [111] in which a remarkable relationship between the ideal single capillary tube and a real porous media was established.

They considered a square capillary tube where the bulk meniscus has just receded leaving liquid films in the four corners in its wake as shown in figure 2.8. The thickness of the film is given as the radius of curvature r, (a function of time and distance) as shown in figure 2.9.

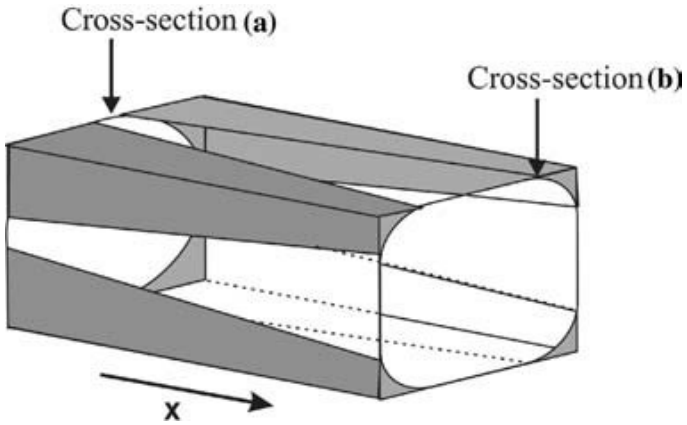

Figure 2.8. Liquid films along the corners of a capillary with square cross-section [111].

From the Young-Laplace equation:

$$P_c = P_g - P_l = \frac{\gamma}{r} \tag{12}$$

Where P_c is the capillary pressure, P_g is the gas phase pressure in the film, P_l is the liquid phase pressure in the film, r is the radius of curvature and γ is the surface tension.

As P_g = 0 (i.e. gas phase pressure variations in the film can be ignored)

Then, the film pressure becomes

$$P_l = \frac{\gamma}{r} \tag{13}$$

From equation (13), it is clear that the pressure of the liquid film is inversely proportional to its thickness. Hence, any gradient in the film thickness along the capillary results in a pressure gradient along the liquid films. Mass transfer (induced by capillary forces) develops along the films from the bulk meniscus cross-section (where the film is thicker, figure 2.9a) to the cross-section at the entrance of the capillary tube (where the film is thinner, figure 2.9b) [111].

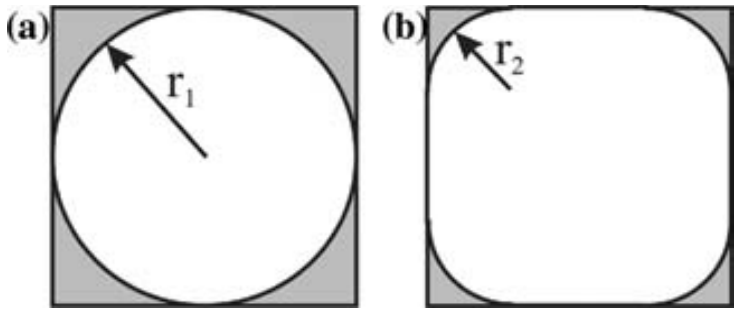

Figure 2.9. Evolution of the film radius that develops at the corners of a capillary with a square cross-section. Cross-section (a) is closer to the bulk liquid phase and the films are thicker than in cross-section (b) [111].

Chauvet et al. (2009) [92] expressed the liquid film flow rate $Q_{(x)}$within each of the corners (based on the results of the classical study done by *Ransohoff and Radke (1988)* [112] on film flow along the corners of long smooth capillaries with polygonal cross-sections) as;

$$Q_{(z)} = \rho_l \frac{\lambda r^4}{\beta \mu}\left(\frac{dP_l}{dx} - \rho_l g\right) \qquad x_f < x < x_0 \qquad (14)$$

Where ρ_l is the liquid density, r is the radius of curvature, μ is the liquid viscosity, λ is the shape factor which depends on the contact angle and β is a dimensionless resistance: x_f is the film tip position ($x_f = 0$ during constant rate drying). *Ransohoff and Radke (1988)* [112] performed calculations on a square capillary and a perfect wetting liquid ($\theta = 0$). They determined the dimensionless resistance β to be equal to 93.5 and the shape factor λ to be $4 - \pi$.

Combining the liquid film flow rate equation (equation (14)) and the modified Young-Laplace equation (equation (13)), we have;

$$Q_{(x)} = \rho_l \frac{\lambda}{\beta\mu}\left(\gamma r^2 \frac{dr}{dx} - r^4 \rho_l g\right) \qquad x_f < x < x_0 \qquad (15)$$

The evaporation flux Q from the liquid films on the four sides of the capillary tube was estimated from mass balance as;

$$4Q = \rho_l d^2 (1 - A_c^*) \frac{dx_o}{dt} \qquad (16)$$

Where $A_c^* = \frac{4\lambda}{3.77^2}$ and as mentioned earlier, shape factor $\lambda = 4 - \pi$.

Wong et al. (1992) [114] computed the area $d^2(1 - A_c^*)$ as the area that is without liquid within the capillary tube at the junction between the bulk liquid meniscus and the corner menisci for a perfectly wetting liquid.

Combining equation (15) and equation (16), we have;

$$(1 - A_c^*) \frac{dx_o}{dt} = 4\frac{\lambda}{\beta\mu}\left(\gamma r^2 \frac{dr}{dx} - r^4 \rho_l g\right) \qquad x_f < x < x_0 \qquad (17)$$

If the liquid bulk meniscus shape is taken to be identical to the quasi-static shape, the capillary pressure can be calculated as $P_c = P_g - P_l = \frac{3.77\gamma}{d}$ which in turn makes $r = \frac{d}{3.77}$ at the boundary condition $x = x_0$ [114].

To determine the evolution of the corner film menisci in-plane curvature, r ($= R$, in figure 2.10) along the film, equation (17) can be solved. Subsequently, the film thickness, *w* can be estimated as $(\sqrt{2} - 1)(r - r_0)$ [92].

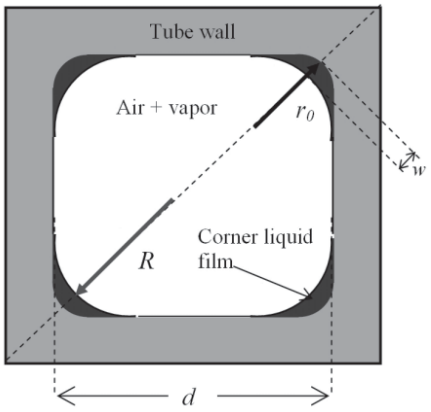

Figure 2.10. Sketch of tube cross section in corner film region, where r_0 is the curvature radius of the rounded corner, $r(=R)$ is the in-plane curvature radius of corner menisci, and w is the corner film thickness [92].

In real porous media drying experiments, the prediction of the movement of the evaporation plane from the surface to within the porous medium is very important. This transition in evaporation stages is sometimes accompanied by a jump in evaporation plane from the surface to a depth below (within the porous medium). The disconnection from the evaporating surface (characteristic jump) is usually as a result of gravitational forces or viscous forces or a combination of both forces. This characteristic jump length, L_C (or ξ in figure 2.5) is determined by a characteristic length of connected clusters at the secondary drying front that obeys a power law with the porous medium's Bond number [84, 87]. The jump (vapour diffusion) length, L_C can be estimated from a modified version of Fick's law as shown in equation (18) [84, 94].

$$E_2 = D\frac{\partial C}{\partial z} = \frac{\theta_a^{2.5}}{\phi} D_{atm} \frac{(C_{sat} - C_\infty)}{L_C} \tag{18}$$

Where E_2 is the evaporation rate at the onset of stage-2, D is the vapour diffusion coefficient in porous media and D_{atm} is the vapour diffusion coefficient in free air. θ_a is the volumetric air content, ϕ is the porosity, L_C is the vapour diffusion length (which equals to the length of the jump at the onset of stage-2). C_{sat} is the saturated water vapour density at the tip of the liquid meniscus after detachment, and C_∞ is the water vapour density above surface.

The characteristic length can be further simplified into the gravity force characteristic length (L_G) and viscous dissipation characteristic length (L_V). The gravitational characteristic length and the viscous characteristic length for a pair of capillaries and a porous medium can be expressed as equation (19) and (20) respectively [87]. The pair of capillaries are hydraulically connected by a permeable interface and initially completely saturated with a liquid before evaporation (see inset of figure 2.11a).

$$L_G = \frac{r_2}{\mathrm{Bo}}\left(\frac{2}{\gamma} - 2\right) \tag{19}$$

$$L_V = \frac{r_2}{\mathrm{Ca}}\left(\frac{2}{\gamma} - 2\right) \tag{20}$$

Where r_2 is the characteristic pore size, Bo is the Bond number, γ is the pore size ratio (i.e. $\frac{r_1}{r_2}$ in the inset of figure 2.11a) and Ca is the capillary number.

In the inset in figure 2.11a, water flows from the drying front to the fine pores at the surface (as indicated by the grey arrows). The characteristic length equals the maximum front depth and is a result of the interplay between capillarity, gravity, and viscous dissipation [87]. In the absence of viscous effect (L_V), the characteristic length (L_C) would grow with decreasing size ratio due to increasing gravitation length (L_G). Due to viscous dissipation the lengths L_V and L_C depend on the evaporation rate that is indicated in parentheses as the ratio between the potential evaporation rate e_0 and the water-saturated hydraulic conductivity K_s [87].

This analysis on characteristics length affecting drying of porous media can be easily extended to a system of hydraulically coupled capillaries as well as to a porous medium represented as a bundle of interacting capillaries [115]. For the vertical pair of capillaries in the inset of figure 2.11a, the gravity characteristic length and the viscous characteristic length can be combined to give equation (21) [87].

$$L_C = \frac{L_G}{\frac{L_G}{L_V} + 1} \tag{21}$$

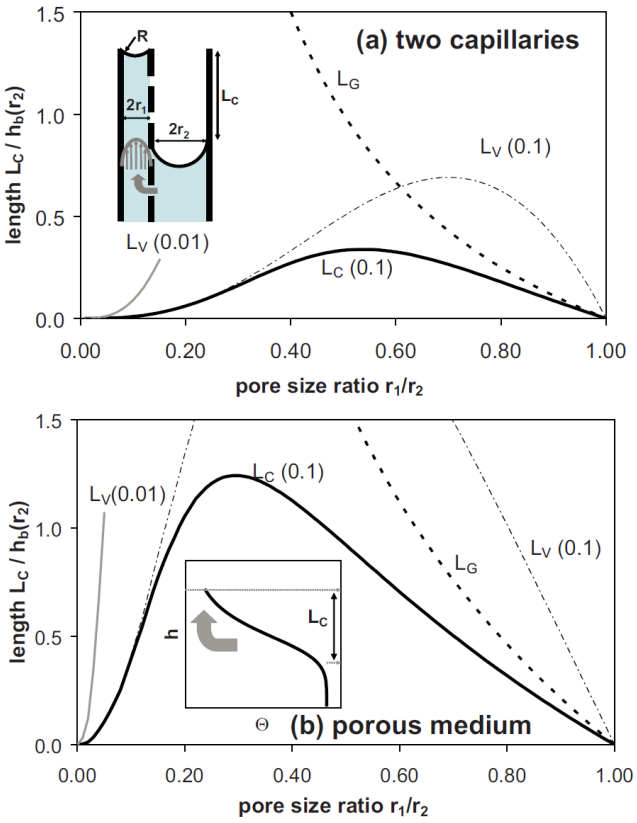

Figure 2.11. Effect of pore size distribution on the characteristic length L_C (end of stage-1) for (a) a pair of hydraulically connected capillaries and (b) a porous medium with hydraulic properties characterized by the Van Genuchten [116] and Mualem [117] models.

2.3.1. Pore Network Models for Drying of Porous Media

Developing models to simulate the drying process of a liquid-saturated porous media has been the focus of many studies in the literature [91, 118]. Macroscopic continuum models with a number of phenomenological coefficients are normally used to investigate porous media drying, however, pore-network models are used to gain more understanding of these phenomenological coefficients at the pore-scale [119]. Pore-network modelling is a useful way of explaining the different processes that take place at the pore scale. This modelling approach is quite useful in studying fluid flow processes in porous media, particularly due to its clear three-dimensional network of interconnected pores (connected by pore throats) representing an easy way to idealize

geometry and topology effects on up-scaled and homogenized petrophysical parameters [120]. There are many studies in the literature that used pore-network models to simulate the drying process [88, 119, 121-124]. A three-dimensional pore network model was used to capture the specific features of drying of porous media under constant external conditions by Bray and Prat (1998) [121]. The constant rate period (CRP) and the presence of dry patches in the porous media was reported to be a direct result of the fractal invasion percolation patterns that characterize capillary forces dominated drying [121].

The two-dimensional pore-network model can also be used to investigate a number of processes that affect isothermal drying in a porous media. The effect of processes like mass transport by gas phase advection and diffusion, viscous flow in liquid and gas phases, and the effects of capillary forces at the gas-liquid interface in the pore throats on the drying process was studied with pore-network models by *Yiotis et al. (2000)* [119]. They used two dimensionless (diffusion based capillary number and Peclet number) and a number of geometrical parameters to characterize the drying process. In the initial stages of drying, the drying front does not usually follow the invasion percolation rules. However, as drying progresses, the drying process changes to one that obeyed the invasion percolation rule [119]. A mechanistic pore-network model was used to simulate drying in two- and three-dimensional pore networks by Segura and Toledo (2005) [124]. They reported that, as drying progresses, transport of liquid was through corner wetting films maintained throughout the porous matrix and the evaporation plane. Capillary forces dominate and the drying process is considered as a modified form of invasion percolation [124]. Thus, pore-network models, together with percolation theories provide a reliable and robust framework for studying drying in porous media. They can be used to predict continuum models parameters and can as well be used as an alternative to solve problems that are otherwise unsolvable by conventional continuum model approaches [88].

2.3.2. Evaporation and Salt precipitation experiments in porous media

Salt crystallization in porous media usually occurs as a result of evaporation-driven supersaturation of salt solution (brine). When the solubility limit of the ionic salt is reached, crystallization can occur both within and outside the porous media. Precipitation of salt crystals within the porous medium is called sub-florescence while

precipitation at the surface of the porous medium is called efflorescence. The distinction between these two phenomena is that primary efflorescence occurs as a limiting case of the crystallization problem within the pores. Efflorescence and sub-florescence are the subjects of active research within the cement and concrete research communities [70-73, 125, 126]. The precipitated salts will deposit at the site of evaporation for large Peclet number and be more widely distributed in the porous medium for small Peclet number, where diffusion can cause supersaturation in a larger region (Peclet number is defined as the ratio of advection to that of diffusion rates of ions in the porous matrix).

An experimental study on drying of a model porous media (glass bead pack) in the presence of dissolved sodium chloride was carried out by *Eloukabi et al. (2013)* [127]. They reported that for sufficiently large-beaded porous media, efflorescence did not significantly affect the drying process and can, in fact, enhance the evaporation rate (when compared with pure water evaporation). However, efflorescence from sufficiently small-beaded porous media was found to greatly limit or block the drying process. There was progressive salt growth at the evaporation plane of the small bead sizes porous media, leading to a compact crust that covered nearly the entire surface evaporation plane. For the large bead sizes porous media, salt grows only in patches at the surface evaporation plane leaving a significant fraction of the surface free of salt crystals [127]. Hence, two types of efflorescence have been identified; crusty efflorescence and patchy efflorescence corresponding to the 'blocking' (small bead packs) and 'enhancing' (large bead packs) drying regime. [127, 128]. The preferential drying of large pores before small pores (capillary effect) is the main reason behind patchy efflorescence for the large bead sizes porous media. The effect of the growth of salt at the evaporating surface and within the porous media on the drying process will be further discussed in chapters 4 and 5.

Two stages can be attributed to the drying kinetics of salt-contaminated porous media; a rapid evaporation period caused by the efflorescence of the aqueous solution and a slow evaporation period connected to the sub-florescence formation [129]. *Shahidzadeh-Bonn et al. (2008)* [130] studied the evaporation and subsequent crystallization of brine (sodium sulphate and sodium chloride) in a square capillary tube, it was concluded that both transport properties in the fluid and interfacial properties of the various crystallization phases would govern the formation of

efflorescence and sub-florescence [130]. Formation of crystals was seen both on the liquid-air interface of the meniscus, within the film region and on the capillary wall at the tube entrance. *Camassel et al. (2005)* [131] also carried out model experiments of sodium chloride precipitation. This was done for both circular and square tube. For the circular tube, only a weakly non-uniform mass fraction of salt and a relatively greater mass fraction were found at the meniscus. However, in contrast to *Shahidzadeh-Bonn et al. (2008),* [130] for the square capillary tube, crystallisation was found at the entrance but not the bulk meniscus due to the thick films at the corners of the tube [131]. Due to the capillary force, the wetting phase tends to be found in the corner when the capillary tube containing saturated solution is in contact with air. Owing to this condition, the evaporation rate was observed to increase much more than what was observed for the circular capillary tube. Hence, they recommended that the film region formation must be accounted for while investigating the effect of drying an ionic solution.

The effect of surfactants on salt crystallization in porous media has been a subject of many studies [132-136]. Recently, *Qazi et al (2018)* [132] studied the effect of surfactants on the evaporation of salt solution from a high-porosity and a low-porosity sandstone porous media. They found that the presence of surfactants in the salt solution does not have any effect on the overall drying kinetics. However, the surfactants act as a modifier for the crystallization of salt, thereby slowing down the evaporation rate at later times due to the formation of a salt crust at the surface, especially for the high-porosity sandstone in which the pores are completely blocked with salt deposition. For CO_2 sequestration processes, precipitation of salts, mainly consisting of halite (NaCl), can be a serious source of a problem during CO_2 injection, this can lead to reductions in porosity and permeability of the reservoir in the vicinity of the wellbore [137, 138]. Changes in porosity do not usually correspond to an equal change in permeability. Nevertheless, models like the Kozeny-Carman grain model [44, 139] and the Verma and Pruess model [140] are often used to describe changes in porosity in relation to the permeability.

Bacci et al. (2011) [137] noted that numerical simulators which couple reservoir chemistry with transport are available; these simulators enable the assessment of the dry-out process occurring during CO_2 injection and estimate changes taking place in the pore space due to salt precipitation. However, these codes all have one limitation

in common: they cannot accurately predict the impact of halite precipitation in field operations as the relationship between changes in porosity and the resulting change in permeability has not yet been defined accurately [141]. Consequently, depending on the reservoir chemistry and pore structure, the change in permeability due to halite precipitation may be significantly different from that measured for the precipitation of other minerals. Hence, it is imperative to conduct a number of laboratory precipitation experiments if reasonable results are to be obtained from numerical simulations [142].

The simulation of supercritical CO_2 injection in a depleted gas reservoir was done with TMGAS TOUGH (multicomponent GASes) using 1D and 2D radial grids by *Giorgis et al. (2007)* [82]. TMGAS TOUGH is a commercial numerical simulator used to simulate the two-phase flow of a gas mixture in equilibrium. The equation of state of water, salt and gas were used to model the CO_2 injection process, while the Verma and Pruess permeability-porosity pore network model [140] was used to capture the effects of salt precipitation on formation permeability and injectivity losses. They reported that salt precipitation around injection wellbores have different behaviours which are mainly dependent on the initial liquid saturation. When the brine has a low mobility, the evaporation front moves with limited precipitation resulting in minor effects on well injectivity. However, when the brine has sufficient mobility, the precipitation front is continuously recharged by the brine flowing to the well due to the capillary pressure gradient driven by the evaporation [82]. Hence, the high mobility brine leads to a much more concentrated precipitation which can strongly reduce the formation permeability.

For CO_2 sequestration in saline aquifers, *Pruess and Muller (2009)* [143] used TOUGH2 (complemented with fluid property module ECO2N) to simulate the fundamentals of evaporation and salt precipitation in saline aquifers during CO_2 storage. The numerical simulations were performed with idealized 1D and 2D radial injection well geometries. Five physical factors were identified to affect drying and salt precipitation during CO_2 sequestration processes in saline aquifers; (a) displacement of formation brine away from the injection well by the injected CO_2, (b) evaporation (dissolution) of formation brine into the injected CO_2 stream, (c) the up-flow of CO_2 due to gravity effects, (d) backflow of formation brine toward the injection point due to capillary pressure gradients that oppose the pressure gradient in the CO_2-rich (‘‘gas’’) phase, and (e) molecular diffusion of dissolved salt [143]. These mechanisms were found to operate on a range of spatial scales. They observed that the counter-flow of

CO_2 and formation brine can significantly increase the salinity of the aqueous phase and can even promote considerable salt precipitation in formations with low dissolved solids. They concluded that injecting a slug of fresh water before injecting CO_2 can reduce salt precipitation and permeability damage near the injection well [143].

Zuluaga et al. (2001) [144] conducted experiments involving the injection of methane into unconsolidated sand packs and consolidated sandstone cores saturated with various salinity brines ranging from 0 to 150 g/l of NaCl under different pressure and temperature conditions. The reduction in permeability in different sets of experiments ranged from 0% for sand-packs saturated with brine with the lowest salinity to 53% for consolidated cores saturated with brine with the highest salinity [144]. These laboratory studies confirmed the possibility of a reduction in permeability due to water vaporisation. However, these results cannot be directly applied to CO_2 injection scenarios since the thermodynamic and flow properties, such as density, viscosity, heat capacity, interfacial tension and reactivity of CO_2 are considerably different than that of methane, which may play a significant role in the vaporisation process [137]. A study involving supercritical CO_2 core flooding experiments on 25% NaCl brine-saturated sandstone cores was done by *Wang et al. (2009)* [145]. Effective permeability to gas measured at the end of the experiment was found to be approximately half of what is expected at similar water saturation for a core without CO_2 exposure [145].

In the experiments involving transport of chloride ion in concrete, by *Puyate et al. (1998)* [125], the total chloride concentration at high Peclet number distinctly shows the formation of a supersaturated region, in the region behind the predicted interfacial position, though the study does not report the extent of solid crystallized salt in the dry region. For a better understanding of this, an experiment on the impact of impact of capillary-driven liquid films on salt crystallization was performed on two sets of Berea sandstone cores by *Le et al. (2009)* [106]. Gravimetric measurements were done on the individual core plugs before and after each experiment of gas flooding to dry conditions, the result showed that the salt mass is greater towards the outer end of the consolidated rock core which was as a result of the solute transport through liquid films [106]. *Peysson et al. (2014)* [22] studied well injectivity during CO_2 storage operations in deep saline aquifers with laboratory experiments while a companion study by *Andre et al.(2014)* [23] used numerical simulation to investigate the same process [22, 23].

During CO_2 injection, initially, water is pushed into the aquifer and two-phase flow immiscible displacement is the main mechanism. Later on, the residual water at the near wellbore might be transferred to the gas phase by thermodynamics, drying (drying rate is proportional to the gas velocity) then becomes the main mechanism controlling water saturation. During drying, dissolved salts in the water are usually carried by capillary forces and often accumulate near the injection surface, ultimately altering the permeability of the system [22]. These experimental observations agree quite well with numerical results [23].

Micro-computed tomography (μ-CT) has been used to study dry-out evolution during supercritical CO_2 injection in porous media [146-148]. *Roels et al. (2014)* [146] experimentally and numerically investigated water-evaporation induced salt precipitation in a Bentheimer sandstone core during CO_2 injection. Their simulation results showed a decline in injectivity due to the accumulation of precipitated salt near the core inlet. This, however, contradicts their experimental results in which neither salt accumulation at the inlet nor injectivity decline was observed. The disparity appears to be as a result of the overestimation of the evaporation of water into the gas phase in the local equilibrium phase partitioning used in the simulator [146]. Also, *Ott et al. (2015)* [148] experimentally investigated the consequences of dry-zone formation in the vicinity of gas injection and production wells using core flood experiments. They showed that under a critical flow rate, salt precipitates with an inhomogeneous spatial distribution due to the transportation of brine and dissolved solids in a counter-current flow upstream where salt will eventually deposits [148]. They also reported a significant impairment in the absolute permeability, however, despite the high accumulation of salt locally, the effective CO_2 permeability increases during all their experiments. Their results were also validated with numerical simulations [148].
More literature review on evaporative drying and salt deposition in real and artificial porous media are presented in chapter 4 and the effect of wettability changes on evaporation and permeability impairment due to salt deposition will be presented in chapter 5.

2.4. Immiscible Two-Phase Flow in Porous Media

The knowledge of the migration path of the fluids in a porous medium under different conditions is important in ensuring secure CO_2 storage and in improving oil recovery.

Individual pore scale events like snap-off displacement, piston-like displacement, and continuum scale phenomena like capillary hysteresis will be introduced in this section. The individual displacement events which can occur for a drainage or imbibition process can be divided into three main categories: snap-off, piston-like and pore body filling events. In the drainage process, the non-wetting fluid invades and advances through the porous medium displacing the wetting fluid in a piston-like manner. That is regions are only filled with non-wetting fluid if they are adjacent to a region that already contains a non-wetting fluid, meaning that both wetting and non-wetting phases remain connected. However, in the imbibition process, all three main displacement events can occur as it is possible for a proportion of the non-wetting phase to fill the pores sequentially (pore-body filling events) or to become trapped by snap-off or by by-passing of regions [45]. These individual displacements events are further explained in the following sub-sections.

In essence, it is very important to understand the inverse relationship between saturation and capillary pressure of the porous medium in order to be able to predict fluid migration and secure CO_2 storage capability.

2.4.1. Snap-Off Displacement

During an imbibition process, it is possible for the wetting phase to trap the non-wetting phase by snap-off or by bypassing. Local in-homogeneities in the pore structure or local capillary pressure can make the invading wetting fluid surrounds and strands a ganglion of non-wetting phase, this is bypassing. However, snap-off is when the wetting phase flows through the wetting layers and fills the narrow region of the pore space in advance of the main wetting phase front. This is made possible because thin wetting films can develop in the corners of the porous medium, and as the pressure in the wetting phase increases, the wetting layer in the corners of the pore space thicken. At a point, the wetting films become unstable and then come together (or in another way, we can say the meniscus between the wetting and the non-wetting phases loses contact with the solid porous medium- an interface can no longer be placed in the pore space) causing the throat to be rapidly filled with the wetting phase [45].

2.4.2. Piston-Like Displacement

This can occur during both drainage and imbibition processes. Both the wetting phase and the non-wetting phase are present within the throat, with the wetting phase located in the corners of the throat. For piston-like displacement to occur during drainage, the non-wetting phase pressure (P_{NW}) must be equal to or greater than that of the wetting phase (P_W). Once the critical pressure ($P_C = P_{NW} - P_W$) is overcome, the non-wetting phase may enter the throat. Piston-like displacement is a reversible process and is dependent on throat dimensions. Piston-like advance is favoured in narrow throats during an imbibition process because the wetting phase prefers the narrow region of the pore space (as can be inferred from the Young-Laplace equation).

2.4.3. Pore Body Filling Events

As mentioned above, piston-like displacement is favoured in narrow throats during an imbibition process, however, it is easier for a wetting phase to fill a pore if more of the surrounding throats are also full of the wetting phase. These events in an imbibition process are dependent on the number of throats connected to the pore that is filled with the non-wetting phase [45]. This dependency hinges on the fact that the largest radius of curvature that can be achieved limits the capillary entry pressure (from the Young-Laplace equation) of a pore body in the system. Therefore, the number and location of throats filled with the wetting phase are important.

2.4.4. Capillary Hysteresis

For the drainage process, given an array of pores, the pores are normally larger than the connecting throats, filling the pores is therefore simple and easy. Throat radius becomes the limiting factor for the invasion of the non-wetting phase. The non-wetting phase next fills the largest radius throat that is connected to a pore already filled with non-wetting phase. This is the process referred to as invasion percolation by Wilkinson and Willemsen in 1983: the pore network is filled in order of size with the constraint that the invading non-wetting phase must be connected to the inlet [45, 101]. However, saturation and capillary pressure have an inverse relationship in porous media. This relationship is best represented by capillary pressure curves as shown in figure 2.12, these curves are shaped in such a way that they are dependent on the displacement history of the system and is known as capillary hysteresis. Each curve represents a

different displacement process and depends on the initial saturation conditions of the porous media. In each case, the phase initially present will be slowly displaced by the other phase.

In the drainage process, the capillary pressure systematically increases with decreasing saturation, until connate water saturation (as depicted by S_{WC} in figure 2.12) is reached after which the saturation will not decrease further even with the continuous increase in capillary pressure. The filling sequence during drainage, therefore, favours pore bodies or pore throats with the lowest capillary pressure because these paths pose the least resistance. In contrast, for the Imbibition process, the capillary pressure decreases with increasing saturation, until the residual saturation level (depicted by as S_{OR} in figure 2.12) is reached. Hence from the Young-Laplace equation, the wetting phase is expected to fill the narrowest downstream throat first, before sequentially filling all other throats in order of increasing throat diameter.

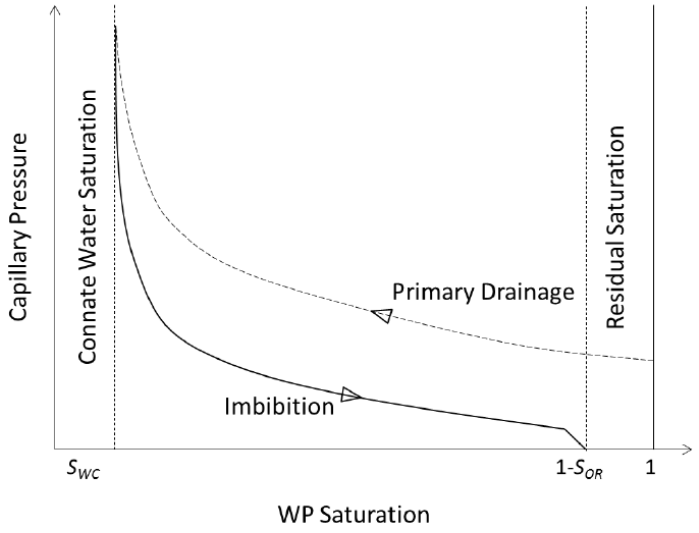

Figure 2.12. Simplified drainage/imbibition capillary pressure curve – during primary and secondary drainage the capillary pressure systematically increases with increasing non-wetting phase saturation to connate water saturation (S_{WC}), whereas the capillary pressure decreases with increasing wetting phase saturation during imbibition to residual saturation (S_{OR}).

In conclusion, displacement events are triggered by the drainage process as well as the imbibition process. These displacement events can be very complex and are dependent on various factors which include but not limited to pore geometry, porous

media properties and location of both the wetting phase and the non-wetting phase within the porous medium. One important point to note is that at a given saturation the capillary pressure for an imbibition process is always lower than that of drainage (primary) process. This is due to contact angle hysteresis, trapping of non-wetting fluids and different displacement mechanisms that occur at the pore scale for the imbibition process [45].

2.5. Displacement Processes and Dynamic Connectivity at the Pore Scale

While the flow of a single fluid is conventionally demonstrated using Darcy's law (equation (2)), the presence of a second immiscible fluid in the pore space will reduce the permeability of the first fluid making Darcy's law (in its's general form) insufficient to model the flow of both fluids. To model two immiscible fluid flow in porous media, a modified Darcy's law is used with a relative permeability term (equation (4)).

Relative permeability is very sensitive and depends on a number of factors such as the flow rates of the two fluids, their viscosities and the proportions of the two fluids. The extension of Darcy's law to include two-phase flow is based on many assumptions and simplifications, the validity of which is now under serious challenge [149]. One of the strong assumptions is that when the two fluids (wetting and non-wetting phase) flow through a porous medium at independently controlled flow rates, the two immiscible fluids each flow under their pressure gradient in static continuous pathways due to the interfacial tension between the two fluids [150-154]. Besides, it is also presumed that when parts of the non-wetting phase disconnect from the main non-wetting phase body, they are immediately isolated and trapped in the pore-space. This would, in turn, imply that isolated non-wetting phase are immobile and their relative permeability becomes zero [149, 155]. This would mean that there is an almost linear relationship between the macroscopic pressure gradients and the fluid flow rates, the proportional coefficients (in this case, the relative permeabilities) should be functions of the corresponding fluid saturation and the structure of the porous medium. Essentially, this implies that the two fluids flow separately, meaning that the flow rate and pressure gradients of each of the fluid can be considered independently using Darcy's law [149]. However, the exact configuration of the two fluids and how this

affects their permeabilities is not very clear. Also, the validity of the assumptions that the fluids flow through connected pathways has been strongly contested [149, 151, 153, 154, 156-159].

Furthermore, the relative permeabilities of the two phases are usually estimated under steady-state conditions and then applied to predict the behaviour of naturally transient (displacement) processes. With the assumption that the instantaneous (though continuously changing) flow mechanisms in the displacing front of the transient flow are similar in spatial and time dimensions to those of the steady-state two-phase flow. This kind of flow decoupling is however not feasible [151, 156]. Another area of confusion on immiscible two-phase flow in porous media is how the system parameters affect the flow rate and relative permeabilities. Specifically, how the capillary number, flow-rate ratio, viscosity ratio, contact angle, dimensionless geometrical (and topological parameters) affect the flow and the relative permeabilities [156]. One of the aims of this PhD research is to specifically study the effect of viscosity ratio, flow-rate ratio and capillary number during steady-state two-phase flow through a 2.5D (two and half-dimensional) micromodel porous media.

2D porous media experiments have been used extensively to study multiphase flow in porous media [60, 149, 156-166]. Chatenever and Calhoun (1952) performed one of the earliest investigations on immiscible two-phase flow in porous media by co-injecting water (wetting phase) and crude oil (non-wetting phase) into bead packs. They reported two types of flow: ‘channel’ flow characterized by the two fluids flowing through the bead pack in separate, stable pathways; and ‘slug’ flow characterized by the flow of isolated small oil ‘slugs’ or (‘globules’) inside a continuous water phase [159]. These results are supported by direct observations in micromodels [167, 168]. Fluid displacement mechanisms were also investigated using a network of capillary ducts as porous media [166]. The results show the presence of both the wetting phase and the non-wetting phase in a duct at the same time with the wetting fluid occupying the corners of the cross-section.

Avraam and Payatakes (1995a) investigated flow regimes and relative permeabilities during steady-state two-phase flow using a model 2D porous network [156]. They concluded that as the flow rates (capillary number) of both phases is increased, the flow behaviour of the non-wetting phase changes from a stable, connected pathway

to the transport of 'ganglia' (oil blobs) in the wetting phase stream. Four different regimes were identified based on the mean size of the mobilized ganglia, droplets' prevalence, and the presence or absence of a stable connected non-wetting phase pathway. These regimes are: Connected Pathway Flow (CPF), Large-Ganglion Dynamics (LGD), Small-Ganglion Dynamics (SGD) and the Drop-Traffic Flow (DTF), and are illustrated in figure 2.13(a) – (d). The flow regimes are dependent on the values of the capillary number, wetting phase saturation and the viscosity ration (while wettability of the porous medium and other physical, geometrical and topological parameters are kept constant) [156].

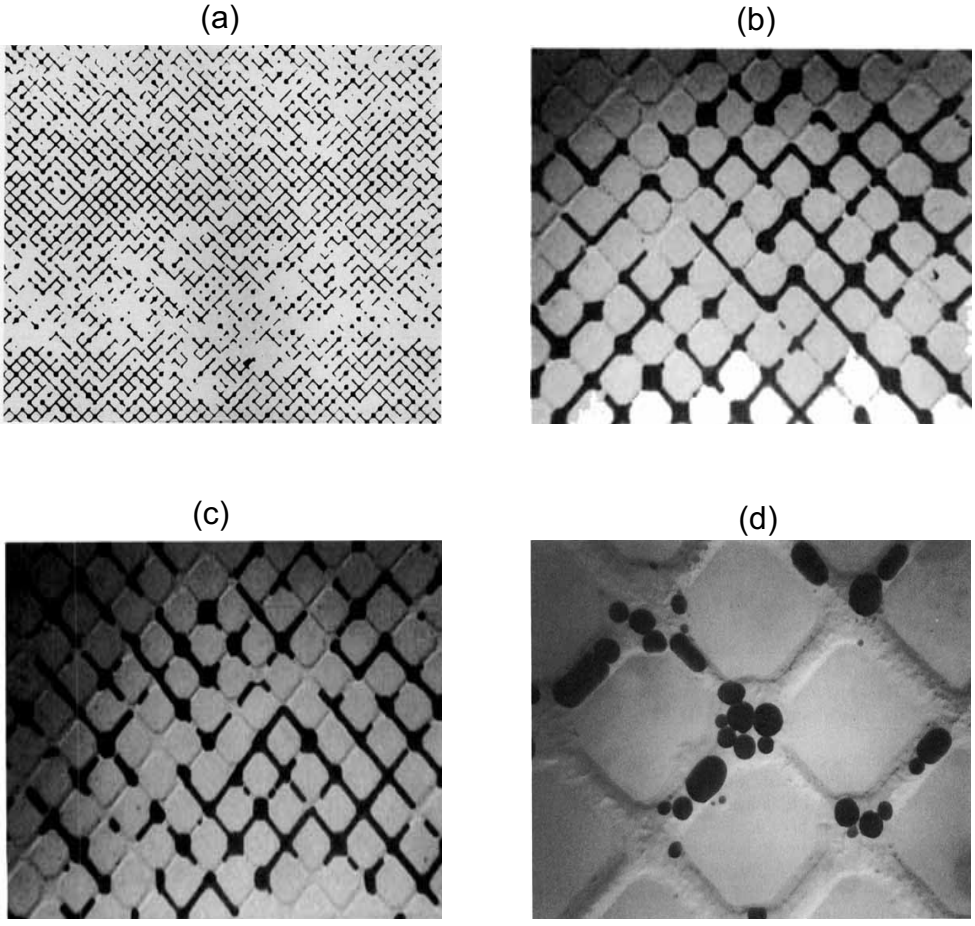

Figure 2.13. Snapshots of flow regimes during the co-injection of two immiscible fluids in a micromodel, (a) connected pathway flow, (b) large-ganglion dynamics, (c) small-ganglion dynamics (c) drop-traffic flow [156].

Similar to the study by Avraam and Payatakes (1995a), a recent experimental study on fluid breakup during simultaneous two-phase flow through a three-dimensional (3D)

bead packs porous medium was done using confocal microscopy for direct visualization [151]. It was concluded that at small flow rates, both the non-wetting phase and the wetting phase flow through stable connected 3D pathways. While, at sufficiently large flow rates, the non-wetting phase breaks up into discrete ganglia in the stream of the wetting phase.

The transition from connected pathway flow to ganglion dynamics was plotted on a state diagram (i.e. non-wetting phase capillary number versus wetting phase capillary number for a range of different flow rates experiments using fluids of different viscosities) as shown in figure 2.14. It was concluded that the transition from connected pathway flow to ganglion dynamics is controlled by the competition between the viscous forces exerted on the flowing non-wetting phase and the capillary forces at the pore scale [151].

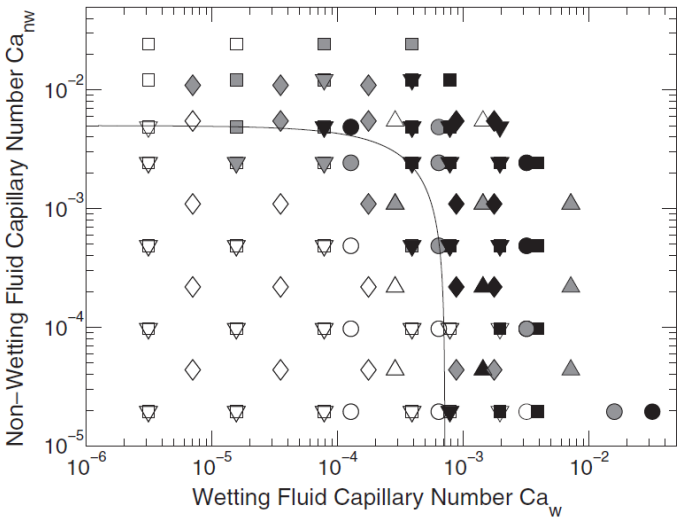

Figure 2.14. The state diagram of the transition from fully connected to broken up flow for simultaneous two-phase flow through a 3D porous medium as a function of Ca_w and Ca_{nw}. Open symbols represent the flow of the non-wetting fluid through a connected 3D pathway, grey symbols represent intermittent breakup of this pathway, and black symbols represent continual breakup of the oil into discrete ganglia, which are advected through the pore space. Each symbol shape represents a different viscosity, bead size, or porous medium cross-sectional area [151].

Studies on two-phase flow experiments using real rocks at the pore-scale was a challenge until the advent of X-ray micro-computed tomography (X-ray μ-CT) [169-

172]. The use of μ-CT in studying fluid flow in porous media is very important, allowing direct imaging of real rock's pore space due to its high spatial resolution (resolution of about 1μm is achievable). Important phenomena like wetting behaviour [173], residual trapping [171] and pore-size distribution [169] can now be observed in real times at reservoir conditions.

Moreover, the intense X-ray beam in fast synchrotron tomography allows even better temporal resolution allowing dynamic pore-scale processes like capillary pressure changes [174], wormhole formations, [174] and Haines jump [170, 175] to be observed and imaged at reservoir conditions. These new advances in pore-scale imaging technology have spurred new pore-scale observations like the non-wetting phase large droplet fragmentation into hundreds of smaller droplets during high capillary number flows in complex carbonate rocks [176] and the quantification of disconnected trapped CO_2 ganglia at low capillary numbers in sandstones [174].

Recently, interesting observations were reported by *Reynolds et al. (2017)* [42] while investigating fluid connectivity during steady-state multiphase flow in a Bentheimer sandstone using nitrogen gas as the non-wetting phase and potassium iodide brine as the wetting phase. They reported a 'new' type of steady-state flow behaviour called 'dynamic connectivity'; a periodical reconnection of pores filled with non-wetting phase like *cars controlled by traffic lights* [42]. A state diagram plot (similar to the one by *Datta et al. (2014)* [151]) was plotted to show the transition from intermittently connected pathway flows to ganglion dynamics as shown in figure 2.15. Prior to their study, this type of flow has never been reported in the literature, probably because the dynamic process is too fast to be observed using μ-CT imaging techniques. Hence, it is imperative to investigate this dynamic intermittent connection-disconnection events through real-time imaging using micromodel techniques.

More literature on two-phase flow experiments and simulations will be reviewed in chapter 6 and 7.

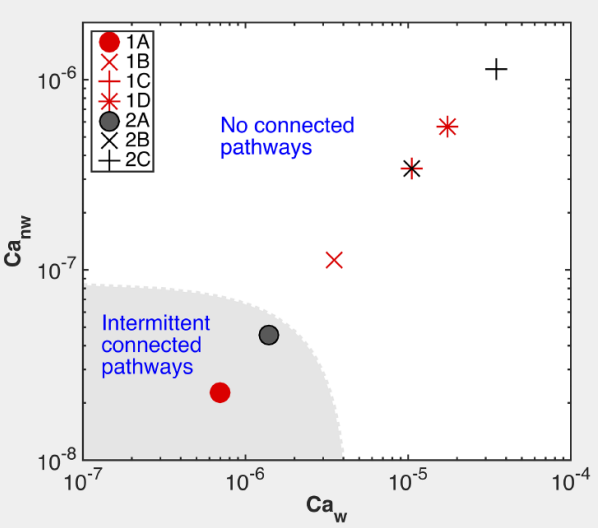

Figure 2.15. The arrangement of the non-wetting phase (as transient connected pathways or as disconnected ganglia) is shown as a function of the wetting and non-wetting phase capillary numbers for a range of constant fractional flow rates experiments [42].

3. Experimental Methods

3.1. Experimental Constraints

Classical laboratory-scale flooding experiments make use of a core sample drilled and shaped from a reservoir rock for studies and collection of recovery data known as core flooding experiments [177]. However, the fundamental physical displacement processes in underground reservoirs occur at the pore-scale, with the smallest structural feature in such reservoirs having dimensions in orders of a micrometre to the millimetre. In order to develop efficient recovery methods and understand CO_2 migration pathways after injection, it is imperative that we understand the underlying physical processes that occur at the pore-scale [178]. Unfortunately, direct visualization of subsurface fluid displacement processes or salt deposition is challenging, requiring the use of either medical- or μ-CT scanners. Yet, these techniques are not able to capture fast dynamic displacement processes in real time [42].

3.2. Micromodels

However, the use of micromodels can overcome some of the challenges associated with experiments in fluid transport in porous rocks. Micromodel devices can be applied in studying different phenomena in a variety of subject areas including geology, biology, chemistry, physics, biochemistry, biomedicine etc. Micromodel systems use fluid flows operating under unusual and unexplored conditions, leading to a new discipline known as microfluidics [179]. *Microfluidics can be defined as the study of flows that are simple or complex, mono- or multiphasic, which are circulating in artificial microsystems* [179]. Hence, the use of micromodels provides a potentially useful tool for the study of multiphase flow at the pore scale. The use of micromodels is very attractive as it offers a real-time imaging since they are usually optically transparent, allowing the use of fast charge-coupled device (CCD) cameras with a high time resolution of (< 0.01s). Also, since micromodels are synthetic systems, one can control

the design and fabrication of the final model to answer specific research questions. Geometry and micromodel properties like roughness, wettability, surface energy and size can be altered, permitting a range of different questions to be investigated and their overall influence on multiphase flow determined. A particularly clear description of micromodels used in multiphase flow in porous media studies was given by Karadimitriou and Hassanizadeh (2012). They described a micromodel as *an idealized, usually two-dimensional representation of a porous medium—a network of connected pores, measuring in the (tens of) microns, through which fluids flow and solutes spread. Moreover, visual observation of the flow of fluids and the movement of colloids or solutes should be possible in a micromodel). Accordingly, a micromodel is typically made of a transparent material that enables visual observation, such as glass or quartz, but it could also be polymeric. The requirement of small pores (<1 mm) is essential for two-phase flow studies because the capillary effects will be otherwise irrelevant. The overall size of a micromodel is typically on the centimetre scale* [160].

3.2.1. A Brief History of Micromodels

Micromodels and microfluidic devices have been around for decades, one of the earliest experiments on flow in porous media using micromodels were performed by Chatenever and Calhoun (1952), with the aim of examining the possibilities for a visual approach in investigations into microscopic mechanisms of fluid behaviour in porous media [159]. They designed and fabricated a micromodel (which was called 'observation flow cell') by placing a single layer of glass spheres between two flat plates. As simple as their model is, the pores within it were very complex making the investigation and understanding of the flow phenomena observed very complicated to explain. However, through the years, with continuous advancement in fabrication technology and imaging technology, more robust micromodel with easy property flexibility have been fabricated [180]. Advances in digital imaging of rock thin-sections, in particular, have enabled micromodel designs to become more and more representative of a real porous medium. With the exception of silicon (or polymer) etching procedures, the general manufacturing component and procedure for manufacturing micromodels still remain the same as those used by Chatenever and Calhoun in 1952.

Subsequently, micromodels have been used to study many processes and applications involving multiphase flow. Examples include displacement mechanisms in multiphase flow [159, 162, 166, 181, 182], effect of specific interfacial area on two-phase flow dynamics [183], measurement of interfacial area and phase saturation [184, 185] solute transport in porous media [186], measurement of relative permeability [149, 187], flow pattern changes with scale of measurement (or fractal dimensions) [188-190], capillary fingering phenomenon [191, 192], the percolation dimension [193], the labyrinth patterns in confined granular–fluid systems [194], fluid flow through a nanometer-scale channel [195] and the study of enhanced oil recovery [60, 164, 196].

3.2.2. Micromodel Geometry and Fabrication

The early micromodels fabricated by Chatenever and Calhoun (1952) consisted of a monolayer of glass beads between two glass flat plates. One disadvantage of their micromodel is the bypass of fluid between the glass plates and the beads. Also, multi-layer glass beads micromodels were not easy to work with due to the difficulty in differentiating the fluid phases involved due to refractive index mismatching. Hence, most of the early micromodels had simple and regular geometry [159, 197, 198]. Later, micromodels of more complex geometry were constructed, especially with the advent of computer-generated micromodel pattern in the 1980s. In a study on a review of micromodels used in multiphase flow experiments by Karadimitriou and Hassanizadeh (2012), four categories of micromodels were identified based on their geometry and topology of the porous medium [160].

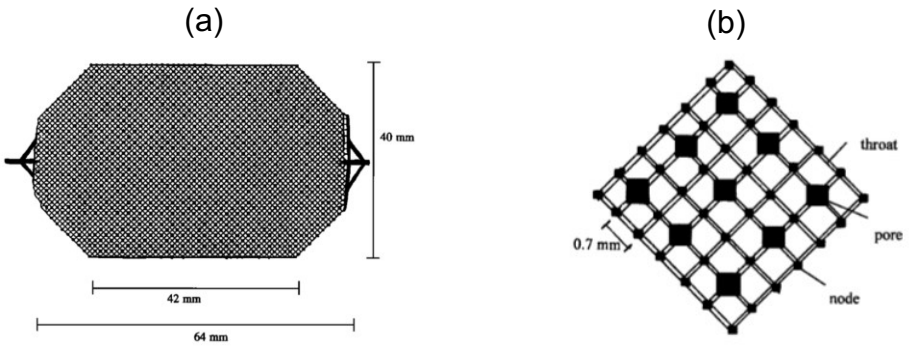

Figure 3.1. (a) An example of a micromodel with a perfectly regular pattern. (b) A magnified part of the micromodel showing the diamond-shaped pores and nodes at intersections [186].

The first category is the perfectly regular models with all pores having the same geometry (i.e. a rhombic or square or rectangular cross-section), same pore width and depth throughout the network. An example of these type of micromodels is shown in figure 3.1. The second category is the partially regular micromodels with pore bodies and pore throats having a regular framework and same cross-sectional shape but varying pores' dimensions. In this category, the pores size distribution determines the permeability of the network [199]. An example of this is shown in figure 3.2.

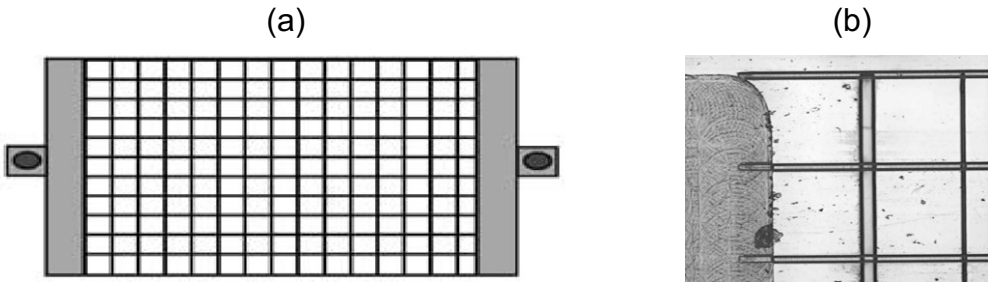

Figure 3.2. (a) An example of a micromodel with a partially regular pattern. (b) A magnified part of the micromodel showing the connection of the pore network with the trough in a corner region [199].

The third category of micromodel geometry is the fractal patterned ones. The fractal patterns can be correlated or uncorrelated, and they often appear to have an entirely random pattern (but are not in reality). The fractal pattern generated networks follow the rules of percolation theory [160]. An example of a fractal pattern is shown in figure 3.3.

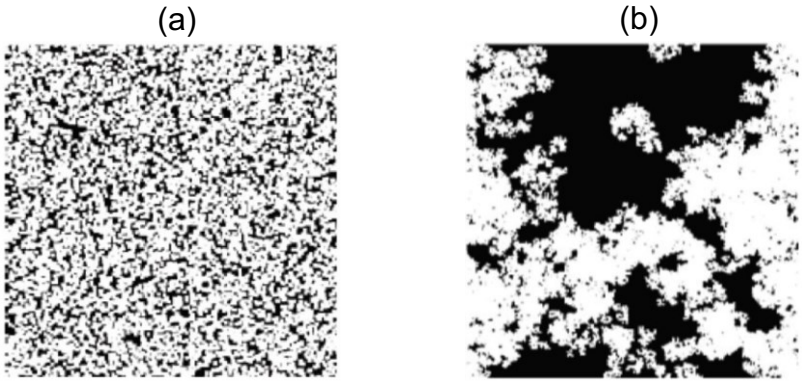

Figure 3.3. (a) An example of a spatially correlated fractal pattern micromodel. (b) The uncorrelated type [200].

Irregular pattern micromodels are the fourth category of micromodel geometry according to Karadimitriou and Hassanizadeh (2012). These type of micromodels lack any spatial correlation and pore bodies are usually randomly positioned in the network domain with sizes computed from a single statistical distribution [194]. An example of this is shown in figure 3.4.

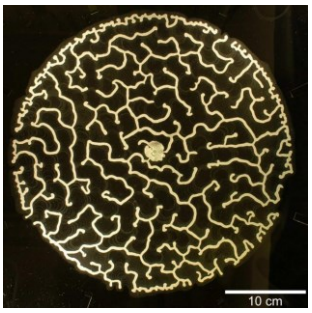

Figure 3.4: An example of an irregular pattern micromodel [194].

However, the micromodels used in this study are based on thin-section images of a sucrosic dolomite rock as an example of a simple carbonate structure and a berea sandstone for the drying experiments and immiscible two-phase flow experiments respectively. The pattern designs were derived from existing rock section images; the dolomite image was from *Knackstedt et al. (2007)* [201] while the berea image was from *Hornbrook et al. (1991)* [202] as shown in figure 3.5. They were however developed and fabricated using the method pioneered by *Hornbrook et al. (1991)* [202] and *Rangel-German and Kovscek (2006)* [203].

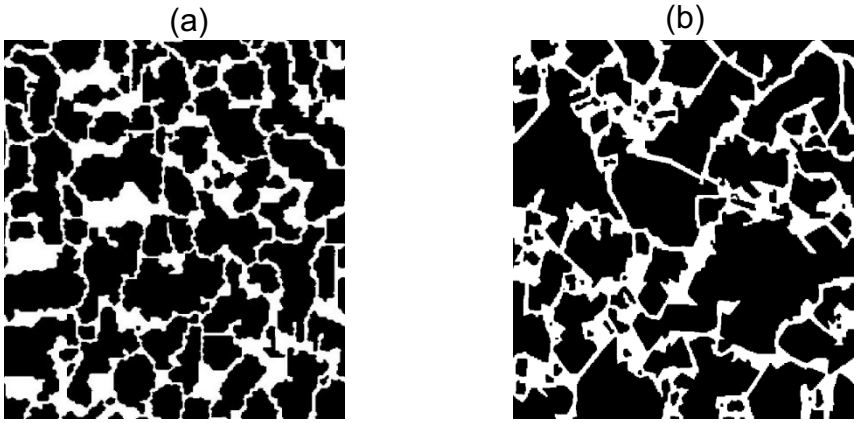

Figure 3.5. Repeat units of the pattern micromodel used in this study (a) Berea sandstone pattern micromodel, and (b) Sucrosic dolomite pattern micromodel [204]. (The pore throats and bodies are the white regions while the black regions are the solid ‘grains’).

In the fabrication of micromodels, it is important that transparent materials are used so as to allow real-time direct visualization of the flow and the fluid distribution in the micromodel network. Examples of materials used in manufacturing micromodels are glass, polymethylmethacrylate (PMMA), silicon, quartz and polydimethylsiloxane (PDMS). Each of these materials has advantages and disadvantages including ease of construction, pressure limitations, mechanical and chemical stability, fabrication time and cost, etching limitations and extent of applicability. Glass micromodels are the most common type of micromodels because unlike PMMA and PDMS, glass micromodels are stiff and rigid, and can withstand temperature changes. They also have well-defined wetting properties, are fairly insensitive to common experimental multiphase flow fluids, and can withstand pressures up to a few hundred kilopascals [160].

PMMA is a good substitute for glass. It is fairly easier and faster to fabricate micromodels using PMMA because it is not as rigid and stiff as glass. However, PMMA (and PDMS) are not insensitive to most fluids used in multiphase flow experiments. Hence, they can absorb or react with these fluids and swell-up, causing the deformation of the micromodel network. Also, PMMA and PDMS are known to deform under relatively high pressure (less than 100kPa), and they have mixed-wettability (and property changes with time) issues as well [160].

Silicon micromodels are quite similar to glass micromodels and they have almost all the advantages of glass micromodels. Also, silicon micromodels can reproduce smaller features and are used to fabricate more “realistic” porous media. However, silicon is translucent and therefore cannot be used to wholly manufacture a micromodel for multiphase flow experiments where direct visual observations are desirable. Hence, silicon micromodels are usually sealed with a transparent material like glass, giving rise to a silicon/glass micromodel. However, unlike the 100% glass micromodels, silicon/glass micromodels are unable to withstand very high pressures. The micromodels used in this research were fabricated from silicon wafers, allowing precise control of the channel geometry and making them very representative of a real reservoir rock.

There are different techniques used in fabricating micromodels, some micromodels are made by lithography methods, some are made using Hele-Shaw flow cell

technique while some are made by etching. Descriptions of these different techniques were reviewed by *Karadimitriou and Hassanizadeh (2012)* [160]. The silicon/glass micromodels used in this research were made using the etching technique. The fabrication procedure of the silicon/glass micromodels followed the procedure established by *Hornbrook et al. (1991)* [202]. The procedure is divided into five essential stages:

Photography. An image of the thin section of the desired porous media is taken at a high enough magnification. The berea sandstone and the sucrosic dolomite carbonate sample were photographed at about 400x magnification. It is important that the image is converted into a white and black (binary) image with no grey scales for subsequent digital manipulation.

Digital Manipulation. Once a satisfactory binary image of the porous media is obtained, the image is digitized at a high enough resolution that no detail of the flow path is lost. The images used in this research were scanned at a resolution of about 2.4 microns/pixel and 2.2 microns/pixel (in the x- and y-axis) for the berea sandstone and the sucrosic dolomite carbonate respectively. After digitization, it is normal for most samples no to have a continuous flow path through the image. Hence, the image is manipulated to ensure the existence of a continuous flow path using any suitable image processing software packages. The images used for the micromodels in this research were altered manually to maintain minimum changes to the flow path.

Image Mask Construction. Once a satisfactory digital image with optimal flow path is obtained, an image is constructed which is used to transfer the flow path image onto a silicon wafer. In constructing the mask, the exact size of the flow path image is determined by defining the height and width of each pixel in the digital image. This single digital image is then mirrored for a particular number of times enough to make up the desired length and width of the micromodel. The smallest pore channel was about 6 microns. Also, at each side of the matrix, a horizontal duct that runs along the whole length of the matrix is fitted in the image mask (these ducts represent fractures as seen in real porous media. The image mask is then used to transfer the image to a silicon wafer.

Image Transfer and Etching. The silicon wafer is then coated with a photoresist material and the coated side is placed in contact with the image mask. Ultraviolet light

is shone through the mask destroying the photo-resist material, resulting in the transfer of the exact flow path image onto the silicon wafer. The exposed portions (i.e. the pore bodies and pore throats) of the silicon wafer are then etched to any desired depth. The micromodels used in this research have a uniform depth of 25 microns.

Micromodel Construction. If needed, the surface of the micromodels is then treated to achieve the desired wettability. Isolation of the flow path is necessary for multiphase flow studies. Hence, the silicon wafer is anodically bonded to a flat glass plate into which the inlets and outlets ports are have been drilled. A schematic of the sucrosic dolomite pattern micromodel and its repeat-unit is shown in the image in figure 3.6. The model matrix size is 2.5 x 1cm^2 etched area with constant etch depth of 25μm. The duct width at each end is 500μm and the matrix grain size ranges between 6-1250μm.

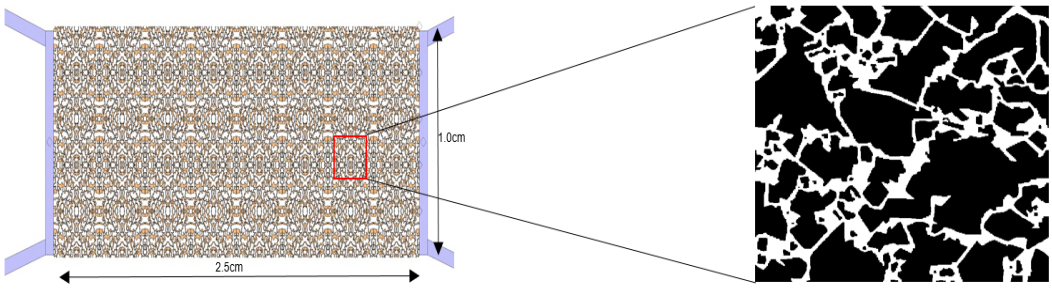

Figure 3.6. Schematic of the sucrosic dolomite pattern micromodel with the repeat-unit shown as an inset.

The micromodels used in this study were fabricated at École Supérieure d'Ingénieurs en Électrotechnique et Électronique [ESIEE (Paris)] by Emily Chapman (2014) [204]. However, the Micromodel holder was designed and fabricated in-house. The micromodel holder (the design specifications are shown in figure 3.7) contains a ledge onto which the fittings are tightened and small O-rings which seal to the model, these O-rings allow the fittings to be fully tightened without breaking the micromodel due to excess pressures at the fittings. Two sets of micromodel holders were fabricated (with the same design specifications), one with aluminium and the other with polyether ether ketone (PEEK).

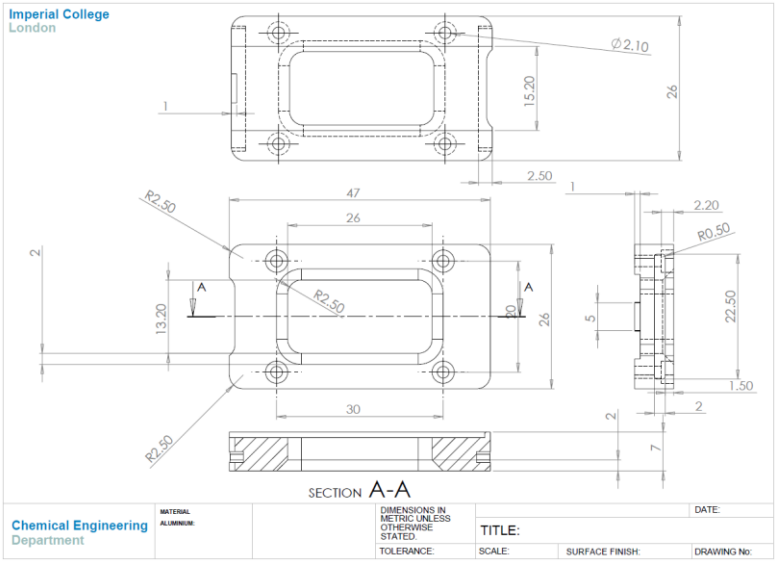

Figure 3.7. Design specifications of the micromodel holder.

Also, the micromodel holder needs to have its own 'holder' to allow easy access to fittings and tubing as well as to ensure the set-up is stable in place. Therefore, a micromodel holder-holder was designed and fabricated in-house for this purpose. The micromodel holder-holder (the design specifications are shown in figure 3.8) was designed to have sufficient space under it so as to allow fittings and tubing for fluid connection pass below it when using the set-up for wide-angle imaging with the DSLR camera. Likewise, it was also designed to fit perfectly onto the slide carrier when inverted on the inverted light microscope for high-resolution imaging.

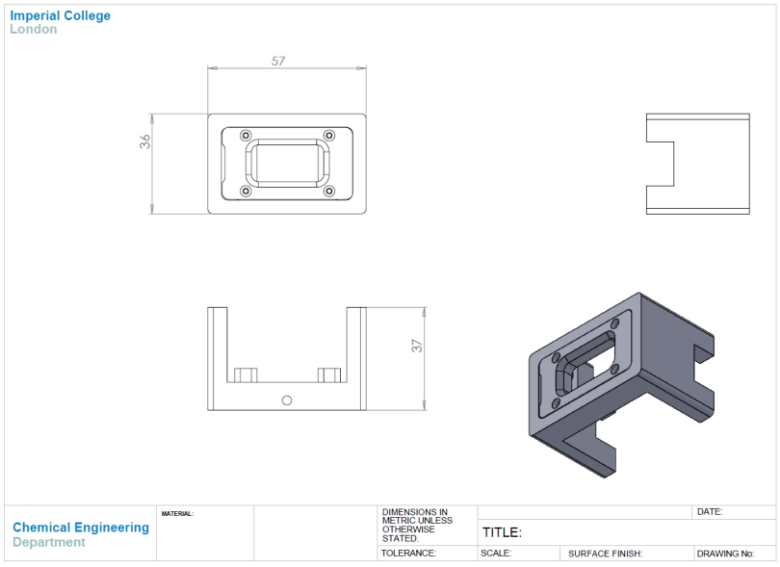

Figure 3.8. Design specifications of the micromodel holder-holder.

3.3. Micromodel Visualization Techniques

One of the main challenges of using micromodels for multiphase flow studies is the ability to observe fluid configurations and arrangement, fluid flow pattern, saturation, and various other features inside pore bodies and pore throats of the micromodel. The type of visualization method used is essential to the outcome of any micromodel experiment. Variables like total pore area, the specific interfacial area, and the average saturation can be estimated for two-phase flow experiments. In micromodel experiments, these variables are measured based on the images or videos taken during or after the experiment. Hence, a high image resolution is needed and for dynamic processes, a high image acquisition rate (or a high-resolution video) is required.

The methods used in observing multiphase flow (static or dynamic process) in micromodel experiments is often categorized into five groups. These are (i) methods making use of fluorescent microscopy, (ii) methods making use of a microscope alone, (iii) methods making use of direct visualization with a camera, (iv) methods making use of microscope along with a camera, and (v) the photo-luminescent volumetric method [160]. All the qualitative experimental results presented in this thesis were acquired by optical imaging techniques. Hence, the methods used in monitoring the multiphase flow for study are direct visualization with a camera and the use of a microscope along with a camera. An inverted light microscope (coupled with a digital camera) and a digital single-lens reflex (DSLR) camera were used in capturing the images and videos used in this study.

3.3.1. Inverted Light Microscope (ILM)

For accurate and high-resolution imaging of the different micromodels used in the experiments, a calibrated inverted light microscope (ILM) was used. A digital camera (AxioCam HSc) and a motorised stage (Mac 6000 system Ludl Electronic Products Ltd) were incorporated into the calibrated ILM (AxioObserver A1.m, Zeiss), this allowed accurate positioning of the micromodels. The ILM has six objective lenses ranging from 2.5X to 50X magnification providing high-quality images from which precise dimensions of the micromodel channel, pore and throat widths can be measured. Details of the objective lenses are given in table 3.1. The ILM is flexible as

both reflected light or transmitted light configurations can be achieved depending on the nature of the micromodel been used. Images were captured by the digital camera (AxioCam HSc) attached to the left side port of the microscope (see figure A.1 in the appendix). Live images of the micromodel positioned on the stage can be viewed through either the eyepiece (figure A.1 in the appendix, component 21) or directly on the PC by running specialist software AxioVision (Version 4.8.1, Zeiss) attached to the microscope via a FireWire cable.

Table 3.1. Details of objective lenses fitted to the ILM.

Magnification	Objective Type	Aperture	FWD	Resolution (μm/pixel)
2.5x	EC Epiplan-Neofluar	0.06 HD* M27	15.1	6.29
5x	EC Plan-Neofular	0.16 Ph**2	18.5	3.09
10x	EC Epiplan-Neofular	0.25 HD	9.0	1.54
20x	EC Plan-Neofular	0.5 Ph2	2.0	0.77
40x	EC Plan-Neofular	0.75 Ph2	0.71	0.38
50x	EC Epiplan-Neofular	0.55 HD DIC***	9.0	0.31

HD – brightfield/darkfield, Ph – phase contrast, DIC – differential interference contrast FWD – free working distance.

The presence of a motorised stage in x- and y directions (with an absolute accuracy of 5μm) allows large mosaic images to be acquired. This enables the whole micromodel to be imaged if required (albeit at long acquisition times) rather than just the limited field of view.

In order to protect the objective lenses, an Aqua-stop II (Zeiss) was installed over the nosepiece to ensure that no fluid came into contact with the objectives. The Aqua-stop II diverts any spillages into a small beaker located off to the side of the microscope.

3.3.2. Digital Single-Lens Reflex (DSLR) Camera

The drying experiments require rapid image acquisition of a larger field of view than what is obtainable on the inverted light microscope. Hence, the digital single-lens reflex (DSLR) camera was used. The DSLR camera (D800E, Nikon, as shown in the images in figure A.2 in the appendix) was combined with a micro-lens (AF-S Micro Nikkor 105 mm, Nikon, as shown in the images in figure A.3 in the appendix) and a

filter Pro1 Digital Close-Up No.3, Hoya). An AC adapter (EH-5b, Nikon) was connected to the camera set-up through a power connector (EP-5B, Nikon) instead of a conventional battery for long continuous image and video capturing. The camera set-up can also be controlled remotely on a desktop computer/laptop computer through a specialized software: Camera Control Pro 2 (version 2.13.0, Nikon). The camera set-up is linked to the computer by a USB cable (UC-E14 USB, Nikon). Just like the inverted light microscope set-up, the DSLR camera set-up can be operated in either transmitted or reflected light as well. However, to use the transmitted light mode, a dimmable halogen backlight (Fibre0Lite, DC-950, Dolan-Jenner) was attached to the lens of the camera. The intensity of the light can be controlled by a separate box attached to the halogen backlight by a fibre-optic cable.

The camera was positioned on an adjustable stand (fabricated in-house) facing vertically downwards onto the micromodel. The stand can be adjusted manually to get the optimal height for the best image acquisition. The DSLR camera was usually operated in Manual setting mode while it is controlled remotely via Camera Control Pro 2. Camera features like the shutter speed, aperture and field of view can be controlled with the software. Also, imaging features like the image type, image storage location, and image formats can be changed with the software. Snapshots and/or videos can be recorded with the DSLR camera set-up; 4288 x 2648 pixel resolution is achievable at up to 8 frames per second (fps). It can also be configured to take images at set time intervals. Comprehensive controls and displays of the DSLR camera and lens are shown in tables A.1 (a-d) and table A.2 respectively in the appendix.

4. Micromodel Observations of Evaporative Drying and Salt Deposition in Porous Media

In this chapter, we employed a water-wet micromodel to study the drying and subsequent salt deposition of a brine saturated porous media. Please note that most parts of this chapter are an edited version of two papers [205, 206], previously published under the Creative Commons License.

4.1. Introduction

Drying of a porous medium is an important process that has motivated many studies, its applications are vast including environmental and industrial applications such as groundwater and soil remediation, food processing and preservation, and geological applications such as carbon sequestration and the recovery of hydrocarbons from underground reservoirs. Two boundary conditions are common; firstly, if dry gas is injected into the pore space it will displace the liquid already saturating the matrix away from the injection surface simultaneously with evaporation [207], secondly if dry gas passes across the face of a porous medium as it would for a surface soil or in gas injection into a fractured formation, the evaporation flux is orthogonal to the main gas flow [87]. We will discuss the second process. In this case, the drying process is characterised by the step-wise gas phase invasion of an initially liquid saturated porous medium. This leads to the formation of a drying front defined as an interface separating the liquid saturated and partially gas-filled domains [87]. Evaporative drying from a porous medium can also be seen as an immiscible displacement process in which a viscous wetting phase (brine) is replaced by a less viscous nonwetting phase (gas) in the pore space [208]. Despite the extensive literature available on the drying process, accurate predictions of the evaporative drying rate and a comprehensive description of the different stages involved in drying are still major challenges, particularly when drying is combined with the deposition of salt.

Generally, three stages of the evaporation of pure water in a porous medium have been clearly described: initially, at high liquid saturation, there is an early stage with a

high and relatively constant evaporation rate (stage-1) followed by a falling and much lower evaporation rate (stage-2) [87, 91, 92, 208, 209]. These stages are connected by a cross-over period characterised by a significant drop in evaporative drying rate [92]. In some literature, the stage-2 period and the cross-over period are described as one period, however, these periods are often classically referred to in sequential order as the constant rate period (CRP), falling rate period (FRP) and receding front period (RFP) [209]. The kinetics of these periods depend on the combination of external and internal mass transfer during the drying process [92]. During the first period, liquid water is still present at the external surface of the matrix and the drying rate is dependent on the external mass transfer to the vapour phase. Dry gas entering the pores to balance the loss of liquid becomes rapidly saturated with water vapour so little evaporation occurs inside the porous medium. The drying rate during this period is constant (or at least pseudo-constant).

$$\frac{dx}{dt} \alpha\, K \tag{22}$$

where x is the distance between the evaporating surface and the bulk liquid. By integrating equation (22), we have $x\ \alpha\ t$. Hence, evaporation varies linearly with time during CRP. During the later stages when the region close to the surface becomes dry the internal mass transfer limits the drying rate and diffusion of water vapour is the dominant process.

$$\frac{dx}{dt} \alpha\, \frac{1}{x} \tag{23}$$

By integrating,

$$\int x dx = \int dt \tag{24}$$

and then,

$$x^2 \alpha\ t \tag{25}$$

The drying rate varies linearly with the square root of time during the later stages of evaporation. In simpler terms, evaporative drying rates in porous media are affected by temperature, surface area, humidity and velocity of drying air (all external mass

transfers) and vapour diffusion, thermal and hydraulic conductivities, pore space geometry (internal mass transfers).

The dynamic interplay of these factors leads to complex interactions between transport processes, boundary conditions, atmospheric conditions and media properties which consequently results in a complex and sometimes ambiguous range of evaporation behaviours [87, 88, 209]. At the onset of evaporative drying, the evaporative demand imposed by atmospheric conditions is balanced by capillarity, i.e. liquid flow through wetting films connecting the evaporative surface to the receding drying front [87, 91, 94, 111]. However, the liquid connections to the drying surface cannot be maintained for long; as the liquid saturation in the region below the drying surface reduces and the size of this region increases, the connecting liquid pathways can no longer provide sufficient flow and capillarity is overcome by viscous (and gravity) effects. This marks the beginning of the receding front period. The motivation for this study was to investigate the impact of salt deposition on this process.

Sub-surface porous media (saline aquifers, oil and gas reservoirs, etc.) naturally contain dissolved mineral salts. Others have salt trapped in them, for instance, salts get trapped in masonry materials during acid rain [210]. The crystallisation/dissolution cycles these salts undergo cause significant damage to the porous building materials used in civil engineering [211-219]. Salt crystallisation in porous media also causes a significant decrease in permeability of underground reservoirs. This decrease in permeability leads to reduced injectivity and possibly storage potential in CO_2 sequestration and reduced oil and gas production from hydrocarbon reservoirs [81].

In addition to the studies on the drying of pure water from porous media, a number of publications address salt crystallisation during evaporation of water from brine in porous media. These studies looked at a variety of factors affecting crystallization in porous media such as wettability [129, 220], 1D systems [127, 215, 221-223], 2D systems [129, 222], relative humidity [224], heterogeneity of the porous media [128, 225, 226] and the effect of confined systems [219, 227, 228]. The distribution (crusty or patchy) [128, 210, 220, 225] and the position (surface salt, efflorescence, or salt precipitation within the matrix, sub-florescence) of the precipitated salt have also been observed [94, 218, 220]. However, a good understanding of the effects of the salt and

its deposited crystals on the different stages of water evaporation in porous media is imperative to mitigate the aforementioned problems caused by salt precipitation.

Lastly, the geometry of a porous medium is often very complex and in order to understand more clearly what takes place, we must begin by looking at very simple patterns, from which some qualitative deductions can be made [61]. Studies on individual capillaries have been shown to be a very important step in gaining more insight into understanding the transport processes in porous media [92, 131, 229, 230]. The evaporation from a capillary bundle, the next simple model of porous media has also been studied [131]. There are a number of evaporation studies in the literature using micromodels [129, 138, 231-233] including very recent ones [234, 235]. These previous studies have used different methods of the injecting the dry gas that provides the driving force for evaporation, depending on the application of the research. Some [138] have chosen to inject directly into the matrix, producing a simultaneous drainage displacement and evaporation process appropriate to the near well-bore dry out occurring during CO_2 storage in an unfractured reservoir or saline aquifer. Others [129, 231-235] flow the drying gas past the outside of the micromodel allowing evaporation through a region of “stagnant air” where diffusion controls the maximum evaporation rate, a process representative of the drying a soil at the surface of the earth.

In this study, we have chosen to continuously flow dry air through a channel adjacent the matrix, thereby maintaining a very low relative humidity at the exposed edge of the matrix throughout the drying process. This is the boundary condition appropriate to a fractured reservoir when dry CO_2 is being injected for carbon storage processes. Therefore, our micromodels were designed to have (fracture) channels on each side of the matrix and the flow rate of dry gas was carefully chosen to maintain a humidity close to zero in the channel while preventing forced advection into the matrix. Choices also need to be made about the geometry of the matrix region of the model and while the previous studies discussed above use synthetic arrays of either capillaries or pillar obstacles, in this study we have decided to use micromodels based on a thin section of sucrosic dolomite, a natural carbonate rock. This study will also be of interest in the increasingly popular field of microfluidics [229, 236].

The use of micromodels allows the visualization of pore scale events in real time using direct imaging and optical microscopy. This is of great advantage as a direct visualisation of transport processes at the pore scale in real porous media is very challenging requiring the use of complex computed tomography scanners. These scanners, however, cannot provide real-time visualization [237, 238]. Hence, the use of optically transparent micromodels as an attractive alternative to real-time visualization (imaging) at the pore scale. Also, since micromodels are synthetic systems, they offer an added advantage of flexibility. The micromodels can be designed (user has a major control on model's wettability, geometry, roughness and so on) to address very specific research questions. In the following section, the characterization of the micromodels used in this study will be presented in more detail.

4.2. Method Development

4.2.1. Micromodels

Micromodels are 2.5D pore networks that allow direct visualization of flows in them through a microscope or other visual imaging technique. The micromodels used in this study are based on thin-section images of a sucrosic dolomite rock [201] as an example of a simple carbonate structure. The pattern designs and manipulations were based on those pioneered by *Hornbrook et al. (1991)* [202] and further developed by *Rangel-German & Kovscek (2006)* [203]. An image of a section of the rock was taken and repeated throughout the micromodel. The image had to be manually manipulated to create a connected pathway for fluid flow. Hence, an image of a small section of the carbonate rock was used and repeated throughout the micromodel for convenience. The micromodels were fabricated from silicon wafers with a glass cover, allowing precise control of the channel geometry and hence a good representation of the original rock thin section [204]. The fabrication procedure follows the procedure pioneered by *Hornbrook et al. (1991)* [202]. SEM images of different sections of the etched micromodel wafer are shown in figure 4.1.

Fluid injection and production are through the ports connected to the ducts that run along the two open edges of the micromodel matrix. These ducts allow one edge of the matrix to be maintained at a low humidity to induce evaporation (representing a fracture in real rock structures). They also allow fluids to flow in and out of the model

during the initial saturation. The model matrix size is 2.5x1cm^2 etched area with constant etch depth of 25μm. The duct width at each end is 500μm and the matrix grain size ranges between 6-1250μm. The average porosity measured from the binarized model image was estimated to be 0.28 and total pore area (excluding vertical channels) is approximately 0.7cm^2. The coordination number varied between 1 and 4, with matrix permeability of about 350mD. The etched silicon surface of the micromodel was oxidised to ensure it is water wet before bonding the glass plate on to the silicon wafer to create an isolated flow path. This was done by heating the silicon wafer on a hotplate at about 315^{o}C for 1 hour. The high air temperature oxidizes the silicon by forming a silicon oxide film, which is water wetting. The oxidation was done during fabrication at ESIEE (Paris).

(a)

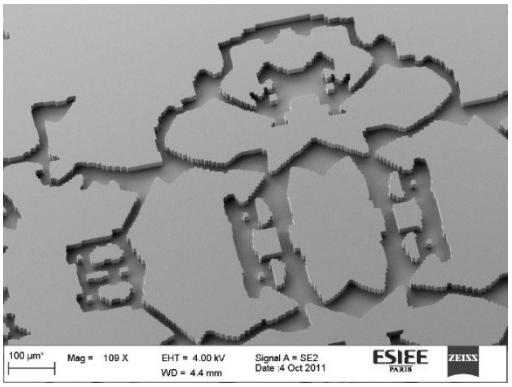

(b)

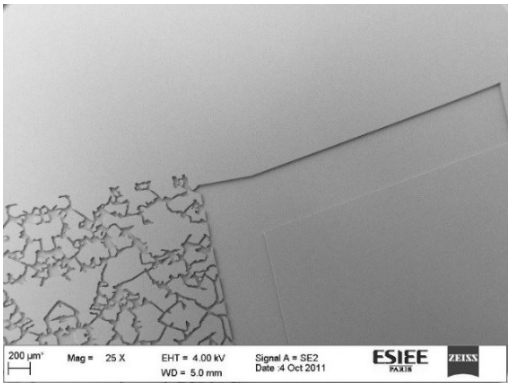

(c)

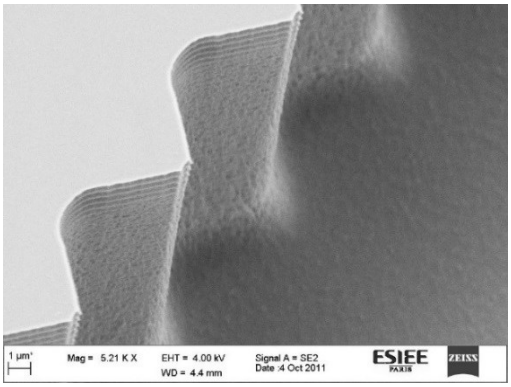

Figure 4.1. SEM images showing different sections of the sucrosic dolomite micromodel wafer at different magnification. (a) Matrix section of the micromodel wafer. (b) Section of the mask showing the inlet/outlet channel, the fracture channel and some matrix. (b) Magnified SEM image of the mask showing the depth of the micromodel.

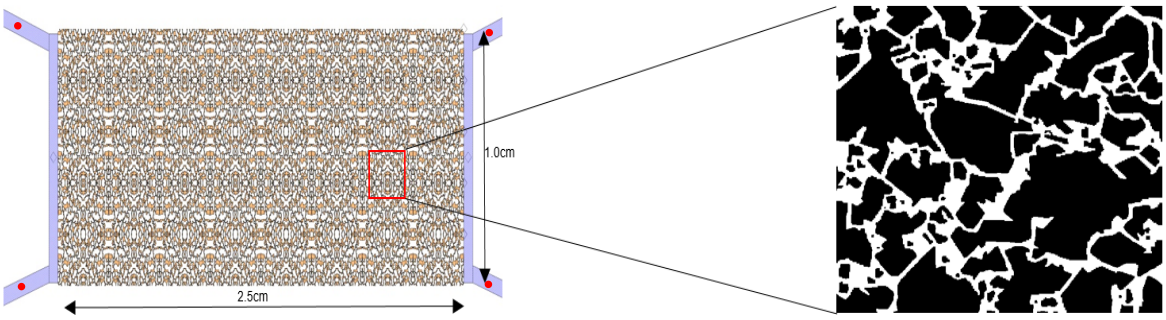

Figure 4.2. Micromodel dimension with the repeated pattern shown as an inset.

The pore-body and throat size distributions, estimated from the equivalent circular diameter and distance across the throats respectively, are shown in the plot in figure 4.3. We employed optical imaging to obtain the images reported in this study. A DSLR (digital single-lens reflex) camera (D800E, Nikon) combined with a macro-lens (AF-S Micro Nikkor 105 mm, Nikon) and filter (Pro1 Digital Close-Up No.3, Hoya) was used to capture images that require a wide field of view and rapid image acquisition. High-resolution images were obtained using an inverted light microscope (AxioObserver A1.m, Zeiss).

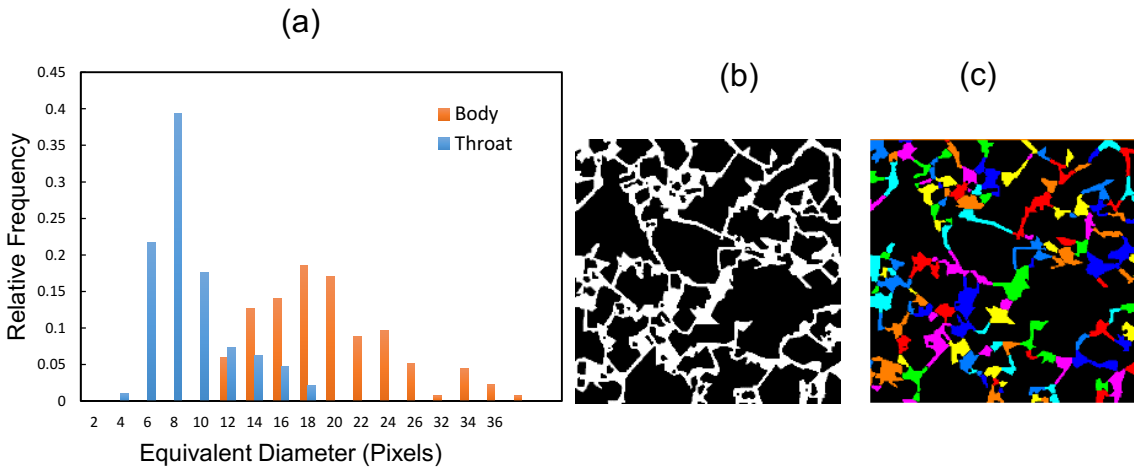

Figure 4.3. (a) Micromodel repeat unit pore-body and throat size distributions in pixels (2.5 µm/pixel), (b) Binary image of the thin section of the sucrosic dolomite mirrored and repeated throughout the micromodel (0.16 X 0.16cm), (c) colour-coded image of the repeat unit showing the separation of pore-body and throats.

4.2.2. Imaging Techniques

The results and images presented in this study were acquired by optical imaging techniques. The DSLR (digital single-lens reflex) camera (D800E, Nikon) set-up was used to capture images that require a wide field of view (see figure 4.4) and rapid image acquisition. For high-resolution imaging of the micromodel, the inverted light microscope (ILM) (AxioObserver A1.m, Zeiss) was used. The ILM was equipped with a number of objectives ranging from 2.5X to 50X magnification providing high-quality images (see figure 4.5) from which precise dimensions of the micromodel channel, pore and throat widths can be measured.

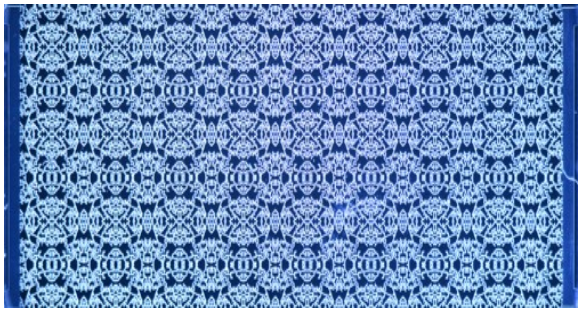

Figure 4.4. Image of an empty micromodel taken with the DSLR camera set-up.

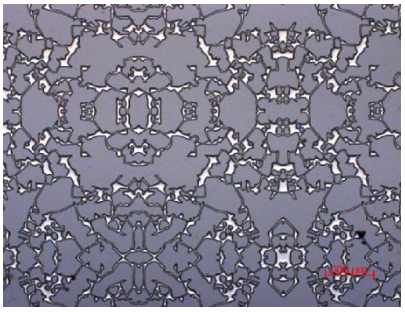

Figure 4.5. Image of a section of the micromodel taken with the ILM.

4.2.3. Experimental Procedure

All experiments were conducted at ambient temperature. Fresh NaCl brine solutions ranging in concentration from 0 wt% to 36 wt% (saturated) were prepared as required for this study. Fluorescein (46960-25G-F, Sigma-Aldrich. 1:700,000 v/v) dye was added to the brine solution for easier phase differentiation. The brine was injected into the micromodel with a 10ml syringe (BD Plasipak, BD300013) using a programmable syringe pump (BS-80000, Braintree Scientific Ltd). The experimental set up with the

inverted light microscope system is shown in figure 4.7a. The micromodel holder designed and fabricated in-house was used to position the model with the injection and production ports.

Initially, 100% brine saturation of the micromodel could not be achieved due to the presence of trapped air bubbles (see figure 4.6b). To mitigate against this, at the start of the experiment the dry micromodel was flushed with CO_2 to displace the air before brine injection. This allowed 100% brine saturation of the model to be achieved due to the solubility of CO_2 in brine. After ensuring model saturation by microscopic inspection, the valves at the four ports were closed and the imaging technique was changed to the DSLR system to obtain images of the entire micromodel matrix.

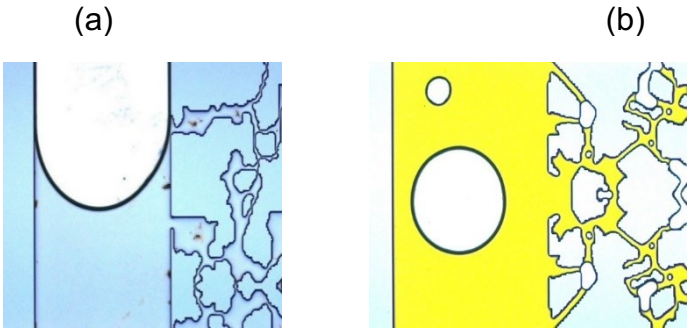

Figure 4.6. (a) The concave meniscus of water in the fracture of the micromodel (proving micromodel is water-wetting). (b) Trapped air bubbles in fluorescein dyed-water in the fracture of the micromodel. (Both images were taken with the ILM).

The DSLR camera was positioned on an adjustable stand, constructed in-house, facing vertically downwards onto the micromodel which was positioned horizontally to eliminate any gravity effects (figure 4.7b). The camera was linked to a personal computer via a USB cable allowing it to be controlled remotely via dedicated software: camera control pro 2 (version 2.13.0, Nikon).

The two ports on the duct at the side of the matrix chosen for evaporation were then opened, one to a dry compressed air-line and the other to the atmosphere to allow the flow of air out of the model. The compressed air pressure was set at 0.5bars which resulted in an air flow rate of approximately 0.3ml/s. The air flow rate was carefully chosen to avoid forced advection into the matrix while, at the same time, maintain the very low humidity boundary conditions in the channel. The humidity was calculated using [239]:

$$g_h = \Theta A\,(x_s - x) \tag{26}$$

where g_h is the amount of evaporated water, Θ (which is equal to 25 + 19v, where v is velocity/flow rate of air above the water surface) is the evaporation coefficient, A is the water surface area, x_s is the humidity ratio in saturated air at the same temperature as the water surface, and x is the humidity ratio in the air. A rough estimation with an air flow rate of 0.3ml/s, an evaporation rate of 4.2 x 10^{-7}cm^3/s, and a surface area of 0.05cm^2 gives a humidity ≈ 9.1 x 10^{-7}.

The drying pattern, the movement of the evaporating front into the matrix and the salt deposition left in its wake, was imaged at different time intervals until complete dry-out. The microvisual data thus obtained was processed and quantitatively analysed as described below.

(a) (b)

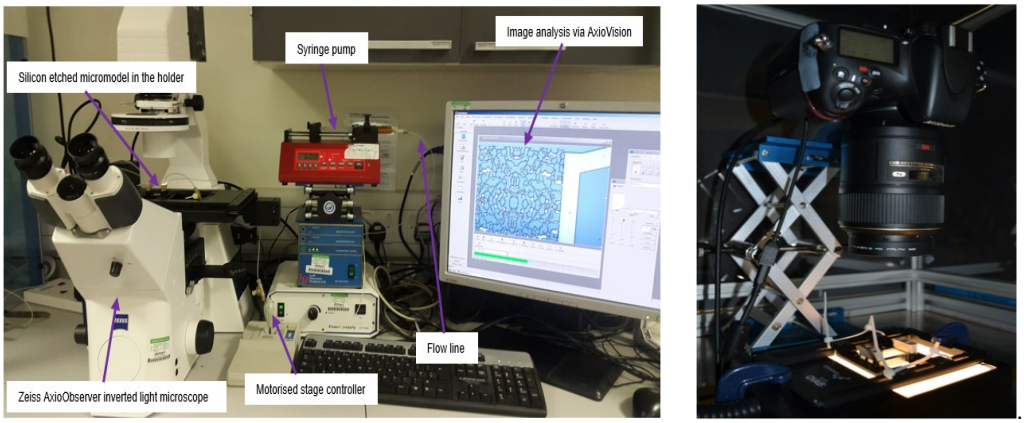

Figure 4.7. The experimental set-up with the (a) ILM and (b) DSLR.

4.2.4. Image Processing

The raw images captured with the DSLR camera were saved in the TIFF format (without compression) to preserve important image qualities and properties. Extracting quantitative data from the images requires some image processing. This was done with ImageJ, an open source software. The images were initially cropped and registered before image segmentation. First, the foreground colour was set to white and the background to black before setting the measurements needed, for example, area, perimeter, and area fraction and so on. The Images were opened in 24-bit (RGB)

format in ImageJ, spatial calibrations were done by scaling the pixel size to an appropriate unit of length (μm) using the known size of the micromodel pattern. The threshold colour plugin was then used to segment the dry pores for subsequent area measurement. Examples of the image segmentation are given below.

Figure 4.8a is a raw image of the micromodel at zero liquid saturation i.e. full of gas and empty of any liquid taken with the DSLR camera set-up before drying starts, the white regions represent empty pore areas while the deep blue regions represent the micromodel solid "grains". Figure 4.8b is the result of segmenting figure 4.8a using ImageJ with the procedure highlighted above, the empty pore regions are now red in colour while the solid "grain" remains the same colour.

(a)

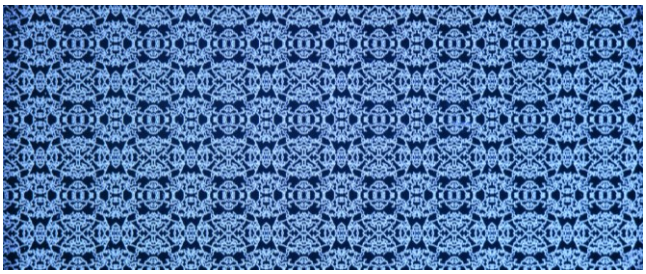

(b)

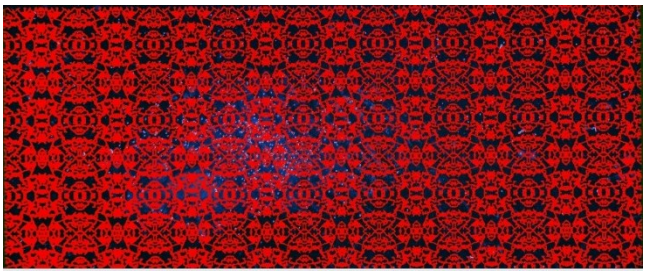

Figure 4.8. (a) Raw image of a micromodel saturated with dyed brine cropped to show only the matrix. (b) Segmented image of a micromodel saturated with brine (measured area are covered in red in ImageJ).

(a)

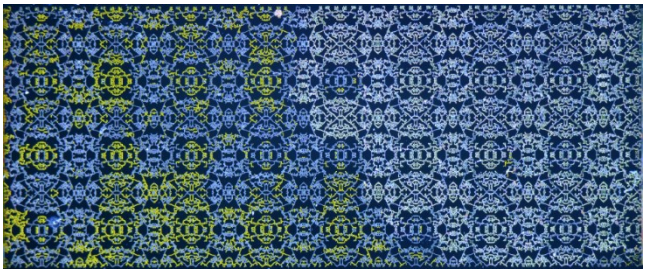

(b)

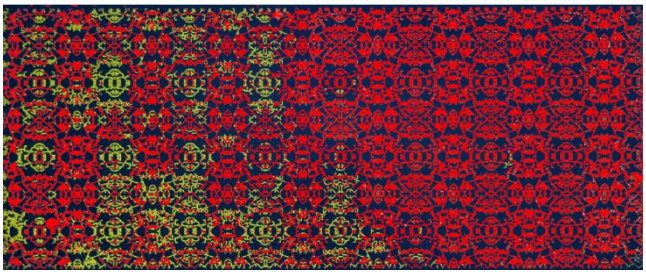

Figure 4.9. (a) Raw image of a micromodel during drying. (b) Segmented image of a micromodel during drying brine (measured area are covered in red in ImageJ).

Similarly, figure 4.9a is a raw image of the micromodel taken sometime during dry-out, the greenish-yellow regions represent pore areas saturated with dyed water (or brine), the white regions represent pore areas that are completely dry, the light blue regions are pore areas empty of liquid but still with liquid film at the corners while the deep blue regions represent the micromodel solid "grains". Figure 4.9b is the result of segmenting figure 4.9a, regions still with liquid phase remain greenish-yellow, dry regions (including dry regions with liquid corner films) are now red in colour while the solid "grain" remains the same colour.

Unfortunately, the pore area containing precipitated salt could not be accurately segmented separately from the dry pore area due to insufficient contrast. Also, a simple mass balance on the brine (the total volume of the salt in the micromodel was calculated before and after dry-out) shows that the salt deposition does not completely fill the entire depth (25 μm) of the micromodel throughout the matrix. This means that there are regions where the pores and throats are only partially blocked after salt deposition. The quantitative data presented in this study are subject to uncertainty in dry pore area measurements. This has been estimated to be $\pm$ 0.02cm^2 from repeat experiments and measurements.

4.3. Results and Discussion

4.3.1. Evaporative Drying of Saturated NaCl brine in a Water-wet Model

The area of the matrix devoid of brine (dry pore area) was measured with the technique laid out in the preceding section. This dry pore area is equivalent to mass lost by evaporation and is plotted as a function of time and the square root of time for 36 wt% Brine (saturated NaCl brine) in figure 4.10 and 4.11 respectively. The very short CRP is shown in figure 4.10, this lasted for approximately 40s for the saturated brine. Also, salt crystals start to deposit at the fracture channel along the outside edge of the porous matrix almost immediately.

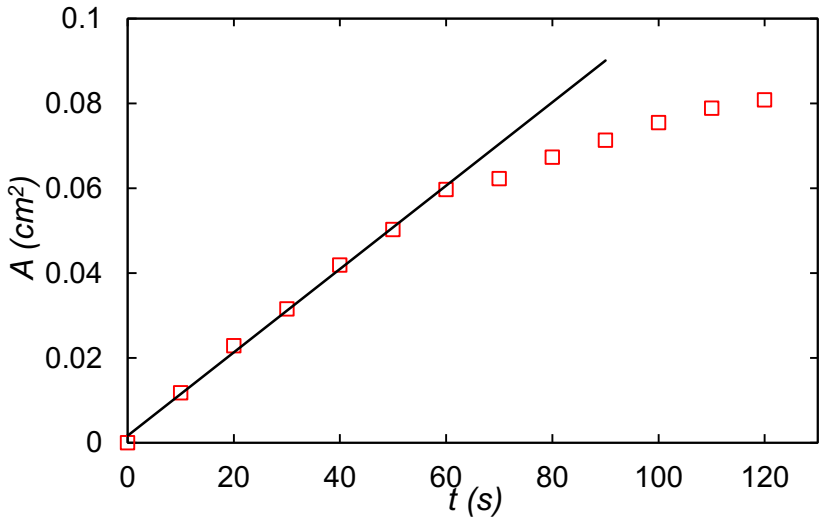

Figure 4.10. Early time plot of dry pore area as a function of time fitted with a linear function.

Drying of brine in a porous media is usually followed by the deposition of salt on the surface of the porous media (efflorescence) or within the porous media (sub-florescence). Brine concentration increases as water is lost to the atmosphere, until the solubility limit is exceeded, resulting in solid salt deposition. Figure 4.11 shows that the evolution of the evaporative drying is linear in the square root of time at all times after the initial deposition of salt. This type of behaviour is usually attributed to a drying process governed by diffusion of vapour through a growing, completely dry region, as is always the case for deionized water evaporation studies. However, salt crystals were found to continue to grow in the fracture channel considerably later after the transition to the slow evaporation, as can be seen in the insets in figure 4.11. This

implies that hydraulic connectivity to the fracture was maintained by wetting films, although these features were too small to be seen directly in the images. Also, this hydraulic connectivity is possible because deposited salt has been found to be both water-wetting and porous [205, 240].

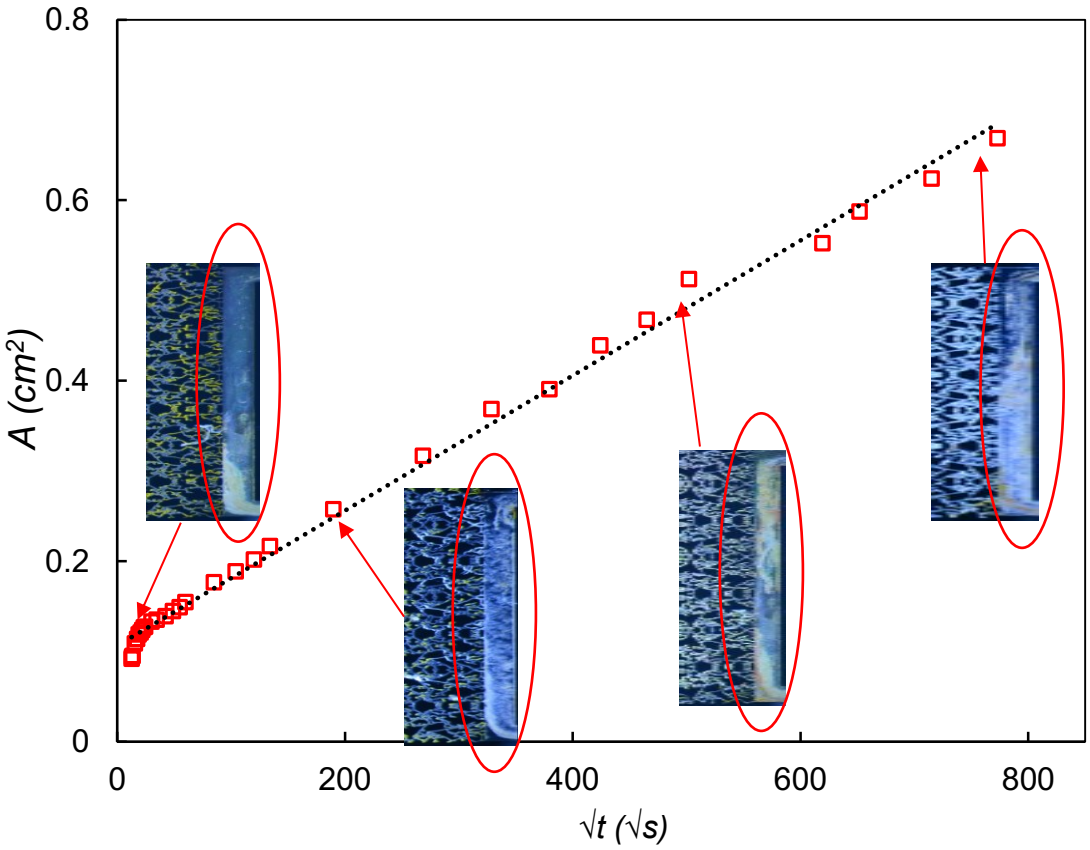

Figure 4.11. The plot of dry pore area as a function of √t for 36 wt% NaCl brine with insets showing precipitated salt crystals at the fracture at different times during drying. Images (a), (b), (c) and (d) with dimensions ~ 0.12cm x 1cm were taken at approximately 60seconds, 10hours, 3days and 7days after the drying starts respectively. The red oval rings highlight the build of salt (white crystals) in the fracture channel.

The relatively high viscosity of saturated NaCl brine (compared to deionized water) provides a higher viscous resistance to mass transfer (liquid flow), and the development of dry solid salt patches in the fracture and matrix close to the fracture due to salt deposits plugging pores, are possible causes for the square root of time behaviour. The size of the dry patches would need to grow proportionally to the mass of brine evaporated to recover a square root of time behaviour. However, the dry

patches cannot be seen directly in the images. An alternative would be to use the differential appearance of salt as the proxy for the evaporating area, but again, this cannot be seen in the images, probably because it is difficult to see crystal growth in the depth direction once some salt has deposited.

4.3.2. Evolution of drying in a water-wet micromodel at different NaCl brine concentrations

Figure 4.12 and 4.13 show the dry pore area as a function of time for different brine concentrations. Three different periods can be seen from the plot of each of the brine concentration. The slope of each of the plot indicates their respective evaporation rates. The rate of evaporation at early times was pseudo-constant for all the brine concentrations measured. This was followed by a transition period, eventually leading to a late time evaporation period with a much smaller slope. For deionized water (0 wt% NaCl), these three periods correspond to the classical periods of evaporation expected from earlier experiments and modelling in porous media drying: the constant rate period (CRP) in which liquid remains connected to the drying surface, the falling rate period (FRP) or transition period, and the receding front period (RFP), in which the capillary connection is broken and water transport becomes dominated by vapour diffusion [87, 92, 109, 207-209, 241, 242].

For the different brine concentrations (12 wt% - 36 wt% NaCl brine), we observed the same trend although the transition from the CRP occurred systematically earlier and at higher liquid saturations as the initial brine concentration was increased. The evaporation rates for the brine solutions during the CRP are lower than that of deionized water, this is expected from the reduction of water vapour pressure in the presence of dissolved ions: the equilibrium vapour pressure above deionized water is 2.49 kPa, significantly higher than 1.88 kPa for saturated brine solution [243]. The observation that the CRP (for deionized water) is actually a period of slowly reducing evaporation rate in porous media drying was first put forward over three decades ago [209]. However, in this study, the evaporation rate of deionized water was seen to remain constant during the initial period.

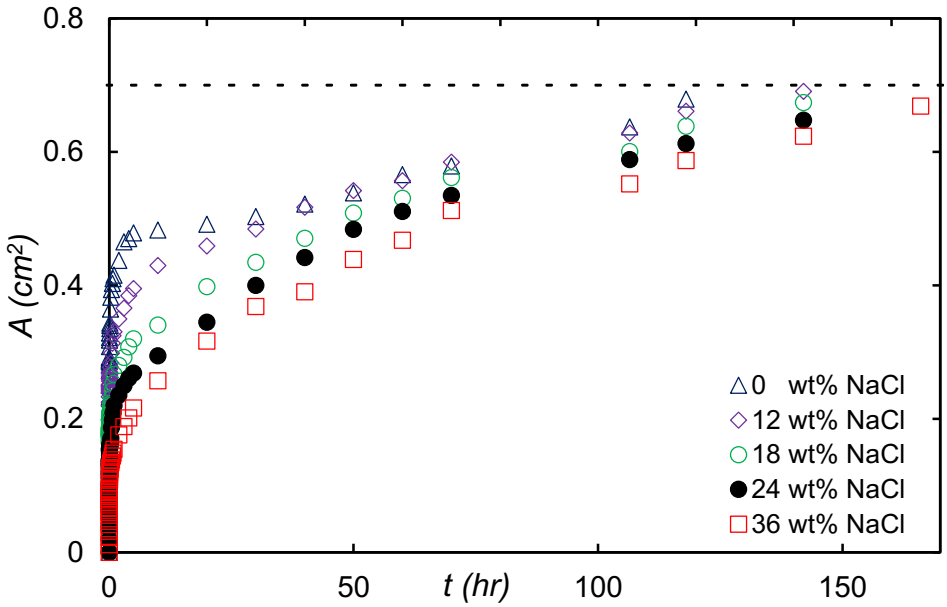

Figure 4.12. Evolution of drying: Dry pore area as a function of time (horizontal black dotted line shows the total pore dry area = 0.7cm2).

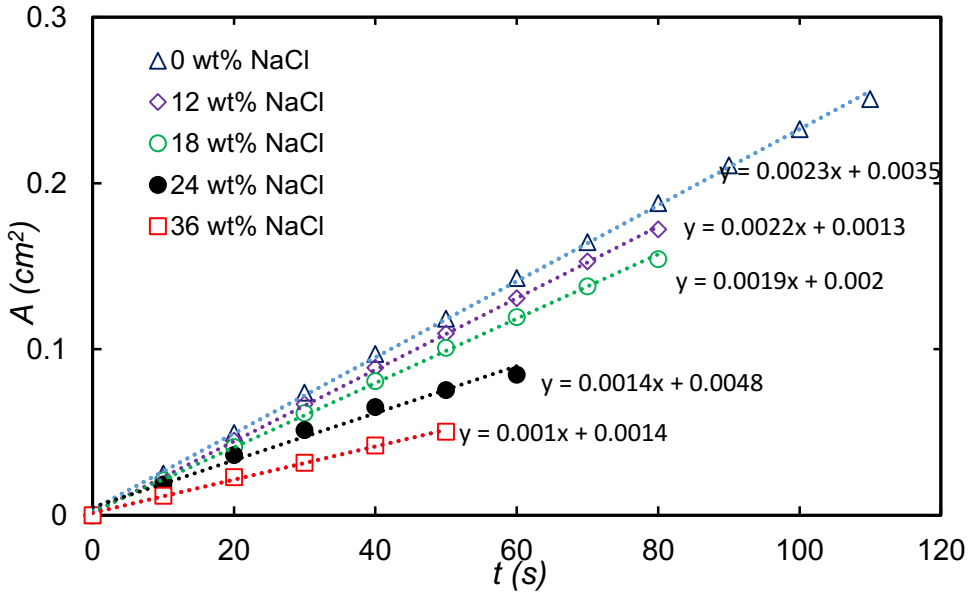

Figure 4.13. Early time dry pore area as a function of time.

According to our vapour pressure theory, the evaporation rate of the different salt concentrations should all become the same just before salt deposition. This is not the case seen in Figure 4.13, the slopes of the CRP decreases with increasing initial salt concentration. To normalize the CRP, we scaled the slopes by the vapour pressures

of their corresponding salt concentration as illustrated in Table 4.1. The slope/vapour pressure for the different salt concentrations are of the same order and approximately the same for 0 wt%, 12 wt% and 18 wt% NaCl brines. The slight difference in the slope/vapour pressure of the 24 wt% and 36 wt% NaCl brines may be attributed to salt deposited at the early time acting as a physical barrier to the liquid phase connectivity.

Table 4.1. Slopes of CRP as a function of vapour pressure for the different NaCl brine concentrations.

Salt Concentration (wt %)	Evaporation Rate (cm^2/min)	Vapour Pressure (kPa)	$\frac{\text{Rate } (\frac{cm^2}{min})}{\text{Vapour Pressure (kPa)}}$
0*	0.0023	3.170	7.3×10^{-4}
12	0.0022	3.091	7.1×10^{-4}
18	0.0019	2.650	6.8×10^{-4}
24	0.0014	2.518	5.6×10^{-4}
36^	0.0010	2.401	4.2×10^{-4}

* deionized water. ^ saturated NaCl brine

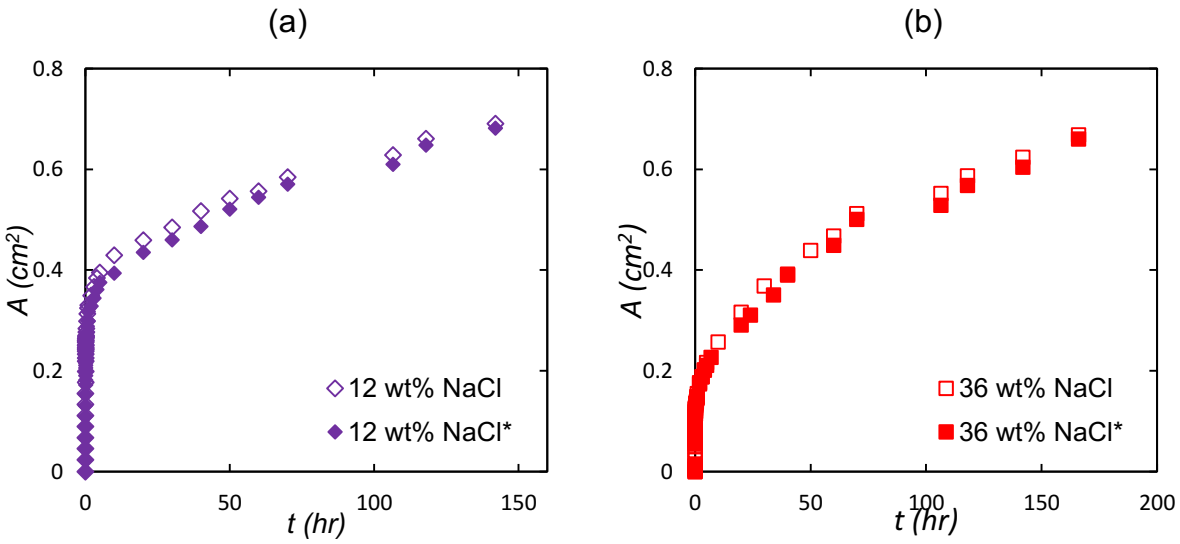

Figure 4.14. Plots to confirm experiment repeatability for12 wt% and 36 wt% NaCl brines.

The repeatability of the experiments was investigated to ensure that the quantitative data obtained from the experiments were reliable. This was done for the 12 wt% and 36 wt% NaCl brines. The results are plotted in figure 4.14a and 4.14b and it showed that the experiments are quite repeatable with only a small negligible deviation. The uncertainty in the dry pore area was estimated to be $\pm$ 0.02cm^2.

4.3.3. Different stages of evaporation during porous media drying

The three periods of evaporation are best illustrated in Figure 4.15, which shows the drying curve as a plot of evaporation rate E (normalised by maximum evaporation rate, E_{max}) as a function of liquid saturation, S. The Evaporation rate E is estimated from $\delta A/\delta t$. The liquid saturation is defined as $S = (A_{max} - A)/A_{max}$, this has been computed to follow the same convention as for real porous medium drying curve. A_{max} is the total pore area which is equal to pore dry area after complete dry-out. The assumptions made in generating these parameters are:

1. *We have neglected possible wetting films still connected to the evaporative surface from the drying front. The dry areas are assumed to be completely dry without any remaining liquid at the corners.*
2. *Liquid filled pore areas are assumed to be completely saturated (this might not be accurate as we can only view the 25μm silicon depth in one direction; from above).*
3. *We have assumed water density is uniform and neglected gravity effects.*

Figure 4.15 gives a clearer picture of the three periods of drying. For deionized water, we observed the three classical periods of evaporation expected, the CRP, FRP and the RFP. The transition from the CRP is at the time (or saturation) at which the drying rate ceases to be almost constant, while the transition from FRP to RFP is marked by the time (or saturation) at which the evaporation rate becomes linear in the square root of time.

Alternatively, we can categorize the drying periods into stage-1 and stage-2 evaporation by plotting the early evaporation rates at ambient conditions (and a relative humidity approximately equal to zero) for 0 wt% NaCl, 18 wt% NaCl brine and 36 wt% NaCl brines in a water-wet micromodel against time as shown in figure 4.16.

The evaporation rates were initially almost constant before a sharp drop after about 2mins for deionized water, 1min for 18 wt% NaCl and almost immediately for saturated NaCl brine. Again, for deionized water, these periods agree to the classical periods of evaporation expected from earlier experiments and modelling in porous media drying: stage-1 evaporation (or the CRP) in which liquid remains connected to the drying surface through capillary forces, and the stage-2 evaporation (a combination of the FRP and the RFP) at which the hydraulic capillary connection to the evaporating surface is broken and water transport becomes dominated by vapour diffusion. From figure 4.16, the same trend of two stages can be seen for the plots of 18 wt% NaCl brine and saturated NaCl brine albeit with different duration for their stage-1 evaporation. The stage-1 evaporation is almost non-existent for the saturated NaCl brine.

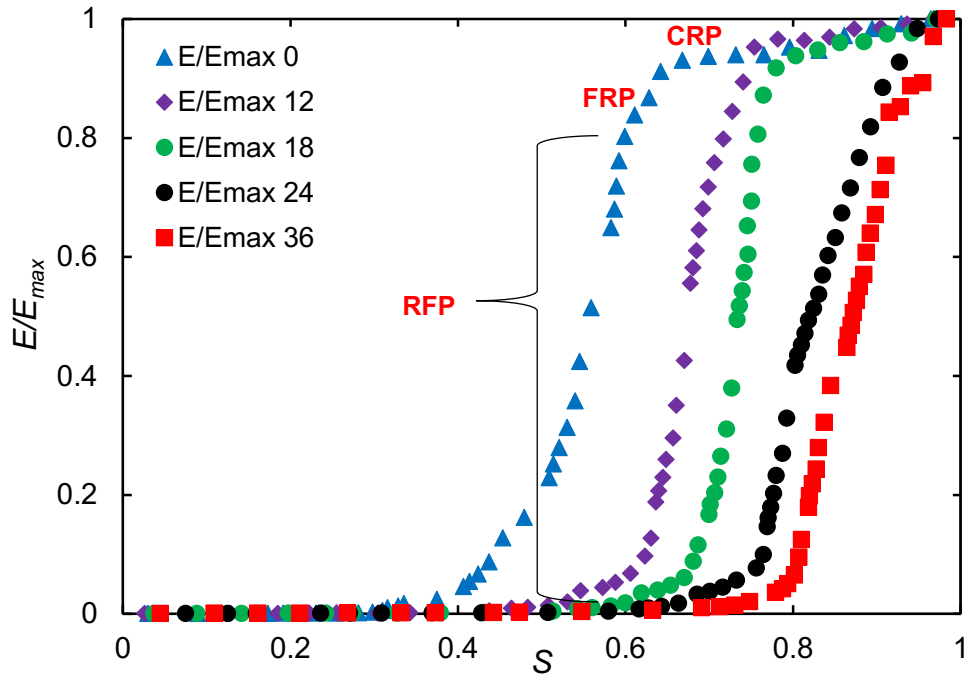

Figure 4.15. Evolution of drying. Evaporation as a function of liquid saturation.

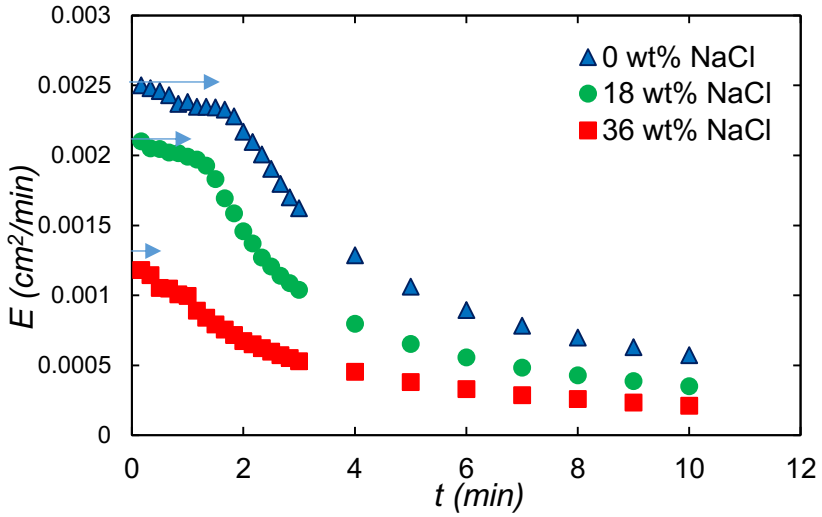

Figure 4.16. Evolution of drying. Evaporation rate as a function of time for the water-wet micromodel (blue arrows signify the extent of the stage-1 evaporation).

For the brines, we observed that the length of the CRP decreased with increasing brine concentration and became almost non-existent for 36 wt% NaCl solution (saturated brine). In the experiments with brine, the dry area of the matrix became linear with the square root of time (Figure 4.17) after the short CRP. However, this is unlikely to be due to capillary disconnection from the surface of the matrix as is usually the case for deionized water drying [92], as the salt crystals continued to be deposited almost exclusively in the duct at the edge of the matrix as seen in the time sequence images in figure 4.18.

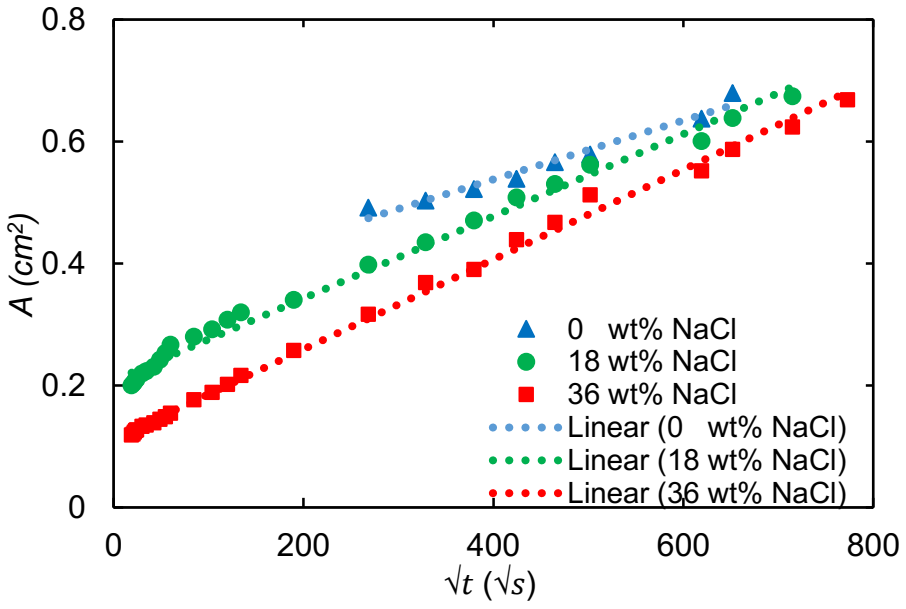

Figure 4.17. Dry pore area as a function of square root of time

We, therefore, contend that the onset of the square root of time drying for brines should not be associated with a receding evaporation front, as is the case for deionized water, as the liquid brine must remain connected to the outer surface of the matrix through wetting films for salt to be deposited there.

For brine systems, the square root of time behaviour started almost immediately after the start of drying (especially for the saturated brine). Therefore, we speculate that the development of dry solid salt patches in the fracture and matrix close to the fracture (plugging the pores and throats), and the relatively high viscosity of saturated NaCl brine (compared to deionized water) which will provide a higher viscous resistance to mass transfer (liquid flow), are possible causes for the square root of time behaviour. Eventually, the hydraulic connectivity to the evaporating surface is broken and the salt concentration deep inside the matrix increases until the solubility limit is exceeded, resulting in solid salt deposition within the matrix. However, this happened much later in the dry-out (approximately during the last 12 hours of an approximately 7-day dry-out period for 36wt% NaCl brine) and the salt crystals are sparsely distributed in the matrix compared to the substantial amount observed in the fracture. This is further explained in the next section.

However, in the experiments done by *Desarnaud et al. (2015)* [219] on the effect of primary and secondary nucleation on contaminated porous media (sandstone) drying, the plot of the intermediate regime (start of stage-2 evaporation) was reported to be exponential in time. They speculated that the evaporation rate decreased as a result of the deposited salt forming a crust on the evaporating surface, thereby decreasing the effective area available for evaporation. That is, the evaporation rate during the FRP is decreases exponentially in time as the area available for drying at the surface decreases. This is similar to the observations reported in this study albeit without the quantitative analysis presented by *Desarnaud et al (2015)* because the deposited salt in this study could not be readily quantified due to imaging technique constraints.

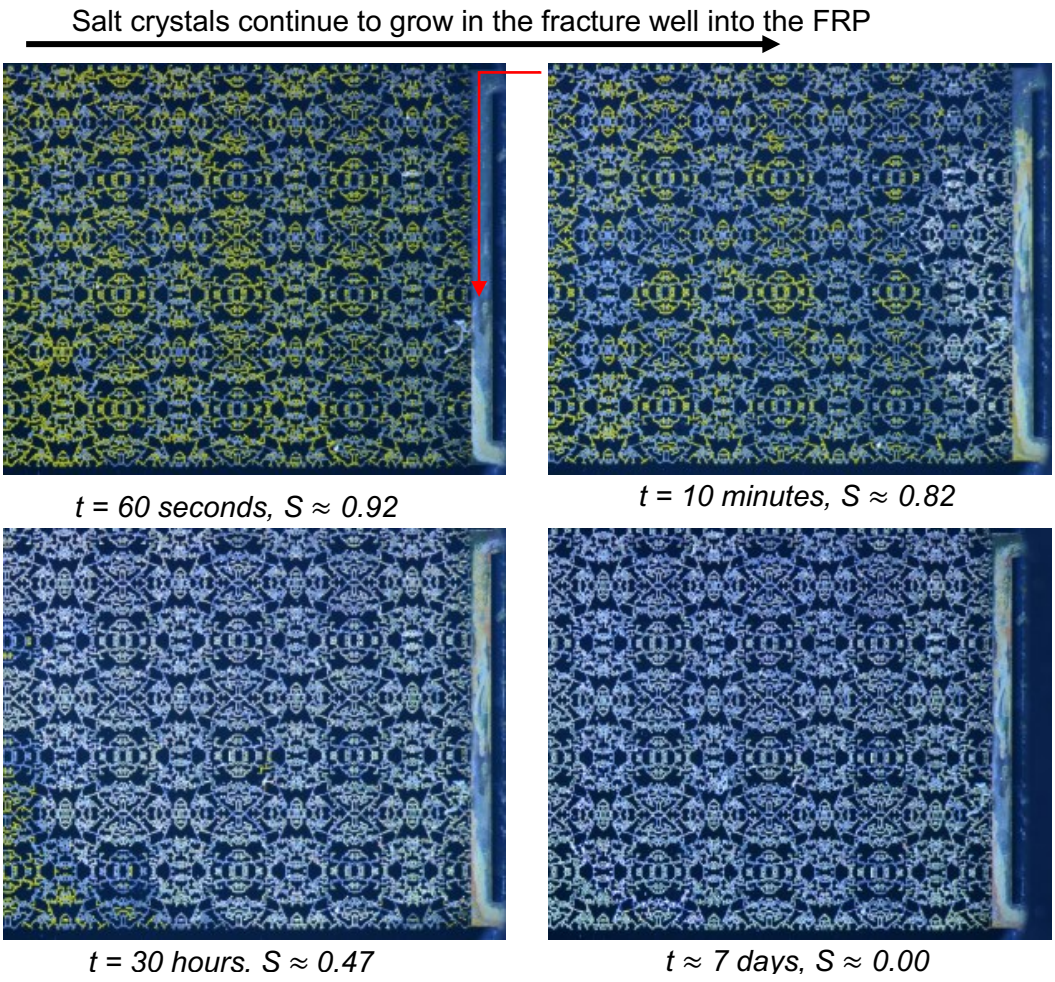

Figure 4.18. Evolution of salt deposit at the fracture for initial salt concentration of 36 wt% NaCl brine at different times during dry-out (the greenish yellow regions represent pore areas saturated with dyed brine, the white and light blue regions represents pore areas that are dry, while the deep blue regions represent the micromodel solid "grains". Salt can be seen growing continuously in the fracture and in the matrix close to the fracture). The red arrow shows the direction of air flow into the fracture.

4.3.4. Combined evaporation and salt precipitation

Evaporation in brine systems is accompanied by salt precipitation. As water is evaporated from the solution, the brine concentration increases until it exceeds the solubility limit, leading to the deposition of solid salt crystals [137, 145]. The achievable degree of supersaturation, *S (= C/C_s, where C is the existing salt concentration, and C_s is the saturation concentration)* may depend on the porous media and there is some evidence from studies in glass capillaries that higher supersaturation can be attained in confinement [227, 228]. Figure 4.19b provides visual evidence for salt precipitation mainly in the evaporating surface and in some pores just below it for a water-wet

micromodel. The greyish dark particles in each of the images are precipitated salt in the evaporating surface (fracture) and in the matrix near the evaporating surface. Figure 4.19c is a zoomed in image of the matrix showing a blocked pore. Nucleation (or the first step in the crystallization process) was observed almost as soon as drying starts for the saturated NaCl brine. The nucleation observed was predominantly heterogeneous, as the crystals formation is aided by the pore wails and grains. The kinetics was governed by the interaction between the pore walls and the brine phase. . As homogeneous nucleation occurs away from surfaces, it will be almost impossible to have homogeneous nucleation in a system under gravity [244]. Although, in our case homogeneous nucleation is possible, the solid (salt crystals) being denser than the liquid will simply sediment when the crystals become large enough to overcome Brownian motion. This would be difficult to distinguish from heterogeneous nucleation at the bottom wall, however preferential accumulation of solid at the (vertical) grain boundaries indicates heterogeneous nucleation.

For saturated brine, we expect the evaporation rate to remain relatively high (although lower than that of deionized water because of the decrease in vapour pressure) since the deposited salt crystals have a similar wettability to that of the clean micromodel. Tests on single NaCl crystals showed that the saturated brine spreads on the dry salt surface. Capillary continuity is maintained for a significant time into the experiment. However, the reverse is what we observe, evaporation rate falls sharply as soon as drying starts and we believe this is due to the appearance of dry patches above the deposited salt at the evaporating surface thereby reducing the surface area available for evaporation.

From Figure 4.17, we see that the drying curve for the 36 wt% NaCl brine (saturated brine) goes into the square root of time ($\sqrt{t}$) regime almost immediately as drying starts. The reason for this immediate transition into the vapour diffusion limited period for saturated brine is likely due to the deposition of salt (which starts almost immediately with drying at this brine concentration) greatly impeding liquid flow to the evaporating surface. See examples in images in Figures 4.19a, 4.19b and 4.19c where salt deposition within the porous media (sub-florescence) and at the surface of the porous media (efflorescence) are clearly highlighted. The higher viscosity of the saturated brine also makes the viscous resistance to liquid flow greater. All these combine to make the evaporation rate fall as soon as drying starts. The entire micromodel showing

the salt deposited at complete dry-out for 18wt% NaCl can be seen in figure 4.19a. In past studies, sub-florescence has been identified to be a major cause of damage to porous media formations.

(a)

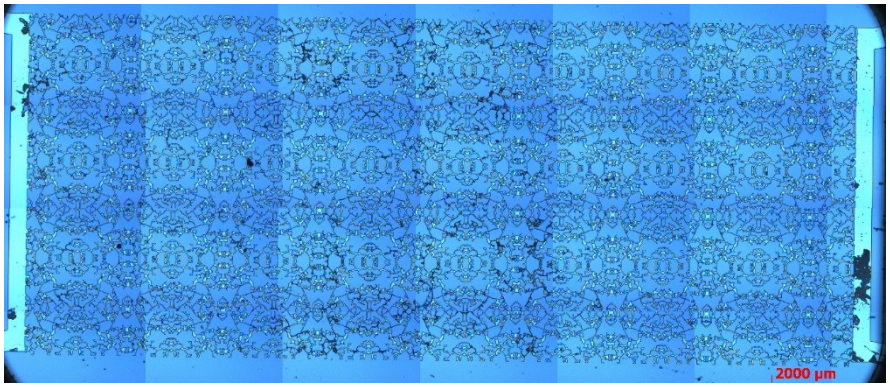

(b)

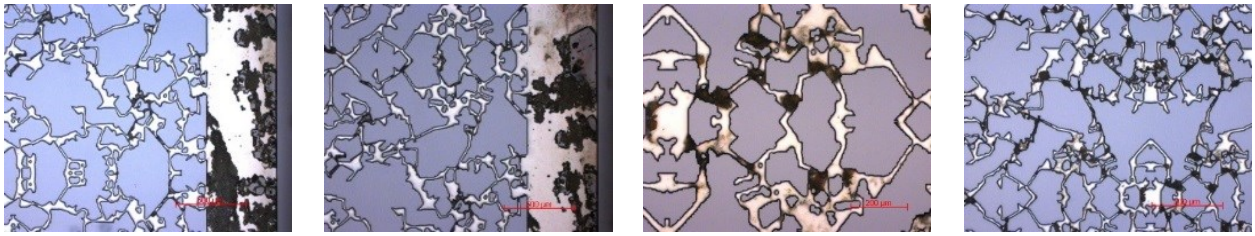

(c)

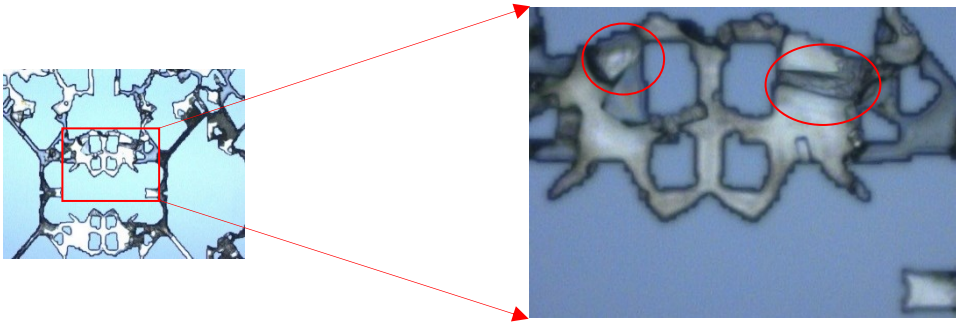

Figure 4.19. The greyish dark particles in each of the images are precipitated salt, (a) Entire micromodel image showing deposited salt in the evaporating surface and in the matrix below at the end of complete drying for 18 wt% NaCl brine (i.e. liquid saturation, S = 0). (b) Images showing deposited salt in the evaporating surface and in the matrix below at the end of complete drying for saturated NaCl brine (i.e. liquid saturation, S = 0). (b) The Zoomed-in image of a pore body blocked by deposited salt for saturated NaCl brine. The red-O rings highlight crystals blocking pore throats and bodies. These high-resolution images were taken with the Inverted Light Microscope.

However, in this study, the growing salt crystals does not exert enough crystallization pressure on the pore walls, high enough to cause any damage. Hence, sub-florescence was not observed to cause any damage to the matrix (and fracture) of the micromodel.

Crystallization pressure depends on the supersaturations reached in the system [245]. The higher the supersaturation reached, the more the crystallization pressure exerted on the walls of the pore, and consequently, the more the damage caused in the porous media. In estimating the supersaturation, some strong assumptions were made as we have no means of directly measuring salt concentration. The high Peclet number (calculated below) indicates that salt concentration will rise steeply close to the site of evaporation. The total amount of water and the dissolved salt remaining in the micromodel at the onset of crystallization was used to calculate the existing salt concentration (C). From this, the supersaturation for the saturated NaCl brine was estimated to be ~1.05. Hence, the pore spaces of the micromodel were not damaged during crystallization. In contrast to a supersaturation of ~1.6 reported in glass capillaries experiment [228]. It was impossible to observe and quantify nucleation rates for the range of salt concentrations studied because of the stochastic nature of nucleation reflected in the large variation in induction times for these systems. The induction time (the time for the first appearance of solid salt for the saturated NaCl solution) was almost instantaneous (~ 5s). For the other range of NaCl concentrations studied, it was difficult to estimate as we do not know when the saturation value is exceeded exactly.

As stated earlier, liquid transport takes place at the evaporating surface through capillarity. Theoretical evidence for this is provided by [222, 223]. This leads to the accumulation of salt at the evaporating surface. As drying continues, there is a gradual increase in brine concentration at the evaporating surface until it becomes precipitated as solid salt. This effect is counterbalanced by a Fickian diffusion process that tends to homogenise the salt profile [45]. Hence, we estimated the Peclet number, Pe at the high and low evaporation rate for the saturated brine experiment using equation (27).

$$Pe = \frac{EL}{W\phi D} \tag{27}$$

E is the evaporation rate (estimated as the pore dry area per unit length and unit time in cm^2/s), L is the length of the micromodel in cm, W is the width of the matrix in cm, ϕ is the model porosity and D is the diffusion coefficient in cm^2/s. For high Peclet number (Pe >> 1), the salt accumulates at the evaporating surface while for low Peclet numbers, diffusion dominates and the deposited salt profile is homogeneous and spreads out in the matrix. From our experiment, the Peclet number for the high evaporation rate period for 36wt % NaCl solution was calculated to be about 260 at ambient conditions, confirming that the advection pulls the brine to the evaporating surface much faster than diffusion could spread dissolved salt in the opposite direction in the matrix. However, for the low evaporation rate (from a liquid saturation of about 0.8 from Figure 4.15), the Peclet number was calculated to be about 10. This is still greater than 1 but much lower than the value for the high evaporation rate period. Therefore, we suggest that diffusion has become relatively stronger and could in fact spread high concentration dissolved salt to some degree against the evaporative flux in the matrix. However, the region of supersaturation probably remains local to the site of evaporation for most of the drying process in these experiments.

4.3.5. Permeability alteration in porous media as a consequence of salt deposition during drying

During the injection of CO_2 in underground reservoirs, solid salt is precipitated as a result of advective drying (and/or a strong water desaturation) of the residual brine in the reservoir. A sizeable proportion of the salt is deposited in the fracture while a much smaller amount is deposited in the matrix close to the fracture. This leads to a decrease in porosity and permeability of the reservoir. We have studied the permeability alteration due to salt precipitation induced by drying for our micromodels.

The permeability changes were measured using two techniques. First, we considered fracture permeability by passing air through fracture (blue arrow in the image in Figure 4.20a), while the ports at the opposite end of the micromodel were closed and the adjacent port open. In this configuration, air flowed in from one port, through the channel and out at the adjacent port, all on the same side of the micromodel. Secondly, we considered matrix permeability by injecting air into the matrix and opening the two ports at the opposite end of the micromodel, but closing the port adjacent to the air

inlet port (see Figure 4.20b). Here, the flow of air was from the inlet port, through the matrix and out at the opposite end ports (see blue arrow in Figure 4.20b).

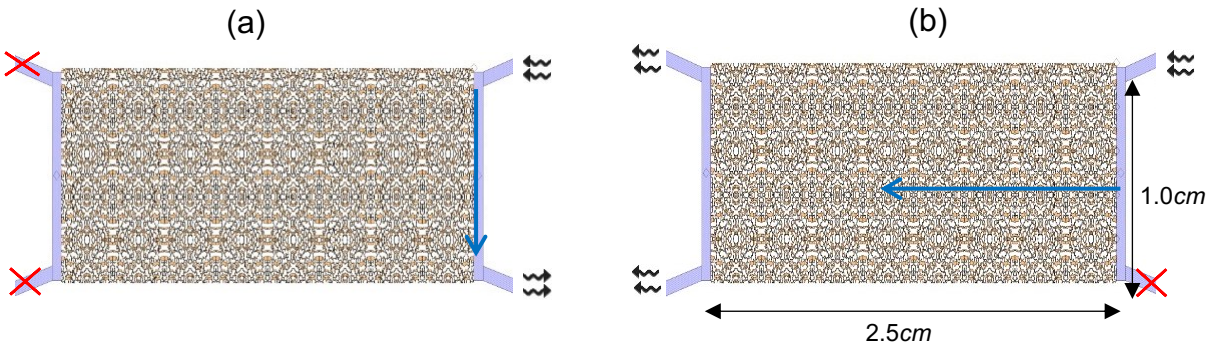

Figure 4.20. Micromodel schematic showing the direction of air flow and the state of the valves at the inlet and outlet ports: (a) fracture permeability measurement (b) matrix permeability measurement.

It should be noted that in the fracture permeability estimation, air can bypass the fracture through the matrix. Also, in the matrix permeability estimation, the pressure drop includes the fracture region of the micromodel. The impact of these issues were not taken into account because the relative size of the matrix and fracture regions, especially for the matrix.

These experimental procedures were carried out on micromodels that have been completely dried of different initial brine concentration at different wetting conditions. Permeability was computed by injecting air at different flow rates and measuring the corresponding pressure difference using Darcy's Law. The two permeabilities were measured after complete drying by injecting air at a known flow rate and measuring the resulting pressure drop first through the matrix and then only through the duct carrying the dry air during the evaporation stage of the experiment. The results are plotted in figure 4.21. We observed two regions (highlighted with red and blue trend lines in figure 4.21a and 4.21b) of a linear downward trend in the matrix and fracture permeability measurements first with the 0 wt% to 18wt% before a sharp decrease and another downward trend from the 24 wt% to the 36 wt% brine. Overall, the matrix permeability, fracture permeability and permeability alteration all decreases with increasing brine concentration and is almost total for the saturated brine concentration (36 wt% brine or 360g/L brine).

Also, we defined permeability alteration as the ratio of final permeability to initial permeability [246, 247] and plotted it as a function of brine concentration for fracture and matrix as plotted in figure 4.21c.

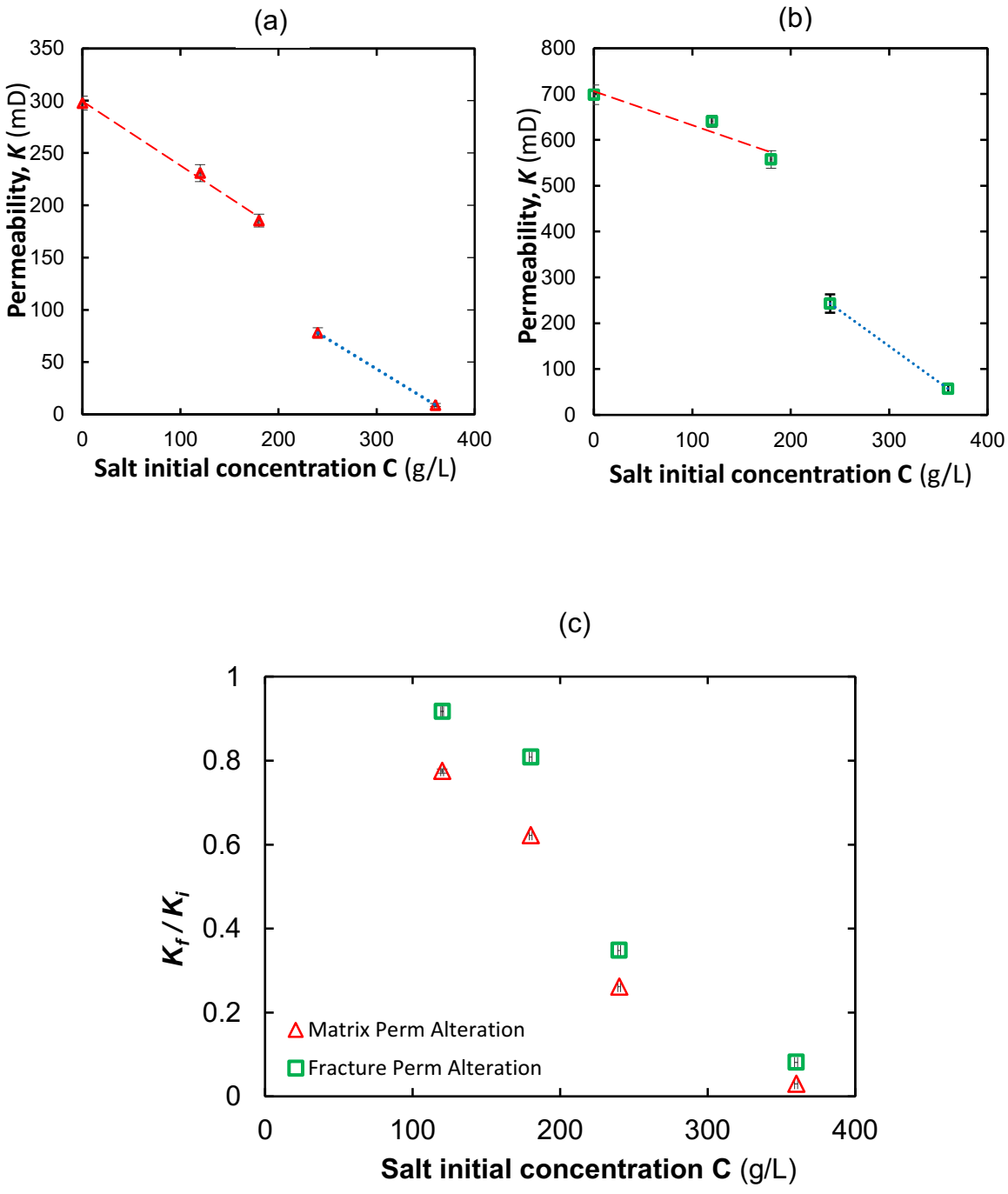

Figure 4.21. Permeability versus Initial salt concentration for the micromodel (a) Matrix (b) Fracture. (c) Permeability alteration versus initial salt concentration for the matrix and fracture.

4.4. Conclusions

The rate of drying has been measured for deionized water in a micromodel based on a thin section image of a sucrosic dolomite rock. The evaporation rate followed the well-established constant rate period at an early time and then a transition to a lower rate becoming linear in the square root of time as the capillary connection to the drying surface was broken and diffusion of water vapour through dry pores starts to dominate.

Drying curves were also measured in the same micromodel for NaCl brine at a range of initial concentrations up to saturation. The shape of the drying curve was superficially similar to that for water, but with a shorter CRP. However, in this case, the break from the constant evaporation rate occurs sooner and is not simply related to liquid depinning from the external surface of the pore space because salt crystals continue to be deposited in the fracture well into the FRP and the wettability of the deposited salt (water wet) is similar to that of the micromodel surfaces. Deposition of salt crystals appears to block liquid paths to the evaporating surface and may lead to the development of dry patches at the surface of the pore space. After a short transition, the brine drying curves were all linear when plotted as the square root of time. Unfortunately, the completely dry regions could not be observed without ambiguity in this experiment due to the presence of wetting films too small to be resolved by the imaging technique used and direct confirmation of this conjecture will be the subject of future work.

The extent of permeability damage, measured after complete drying depended systematically on the initial brine concentration for both the matrix and the duct representing a fracture at the face of the matrix. For saturated brine, the permeability was reduced to almost zero. This would lead to isolations of some regions from CO_2 during CO_2 sequestration. This isolation leads to a decrease in net injectivity, ultimately leading to reduced carbon efficiency and reduced CO_2 storage potential of the reservoir.

5. Effect of Wettability Changes on Evaporation Rate and the Permeability Impairment due to Salt Deposition

The effect of wettability on the drying of porous media is poorly understood especially when the water contains dissolved salts. In this chapter, we report new observations of drying with simultaneous salt deposition in micromodels based on natural rock pore structure at different wetting conditions. The resulting permeability alteration in the porous media was also investigated for different salt concentration. Finally, we compare drying with air and drying with CO_2, with the latter having important applications in CO_2 sequestration processes. Please note that most parts of this chapter are an edited version of a paper [206], previously published under the Creative Commons License.

5.1. Introduction

Oil reservoirs have a wide range of wetting states [248-250] and, given the strong influence of capillary forces, this may have a significant impact on salt deposition during drying. The effect of these different porous media wetting states on the different stages of evaporation and the subsequently deposited salt is not well understood and remains an open problem, especially during the storage of supercritical CO_2 in depleted oil and gas reservoirs. Likewise, to the best of our knowledge, the influence of the composition of the gas carrying water vapour during drying in a salt contaminated porous media, for example drying with air versus drying with CO_2 (as is the case during CO_2 sequestration) has not been studied before.

Understanding the influence of these factors on the pore-scale is essential in order to assess and optimize our carbon sequestration efforts. Hence, we have employed pore scale visualization to investigate evaporative drying and the associated salt deposition of NaCl brine in porous media at different atmospheric and wetting conditions, using a 2.5D etched-silicon/glass micromodel. A new technique for wettability alterations will

be presented and the impairment of permeability due to salt deposition are also presented.

5.2. Experimental Methods

5.2.1. Micromodels and Imaging Techniques

The same micromodel pattern and imaging techniques and used in the previous study (chapter 4) were used in this study. However, since the micromodels were manufactured to be water-wetting. A new technique was used to alter its wettability. The procedure for the technique is explained in the next section.

5.2.2. Micromodel Wettability Alteration Technique

The micromodels are manufactured to be water-wetting. In order to produce mixed-wet micromodels for drying experiments, an alternative technique for wettability alterations of micromodel was developed. Well-established wettability alteration techniques [251, 252] that rely on silane chemistry cannot be used to produce mixed-wet conditions as the silane reacts with the water phase when the model is saturated with both oil and water to generate the appropriate spatial distribution of wetting alteration. Alteration directly with crude oil [248, 253] was also tried, but this rendered the model opaque to visible light. The new technique involves injecting a solution containing silicone caulk (151 Products LTD) (10 v/v %) dissolved in Dodecane (≥ 99%, Sigma-Aldrich) (90 v/v %) into a micromodel initially saturated with water. This ensures that only the surfaces coming into contact with the hydrocarbon phase have wettability alteration, as is the case in oil reservoirs [248, 253]. The micromodel was left to age for 2 days at ambient conditions. After the treatment stage, the micromodel was then completely dried by passing dry compressed air through it after which it was placed in an oven at 60^{o}C for 24hours. A uniformly oil-wet model was also prepared by injecting the silicone solution into a dry model.

After altering the wettability of the micromodel as described in the experimental procedure, the validity of the technique was tested by measuring the contact angle of brine on glass in air using a goniometer (figure 5.1).

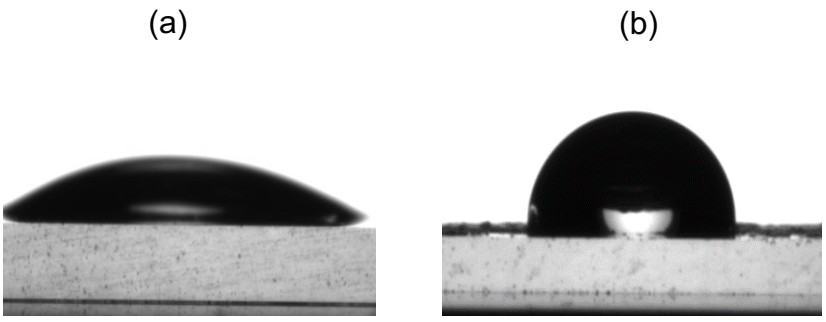

Figure 5.1. Saturated brine (36 wt% NaCl) on glass slide before treatment (Contact angle: ≈ 25°) and after treatment (Contact angle: ≈ 108°).

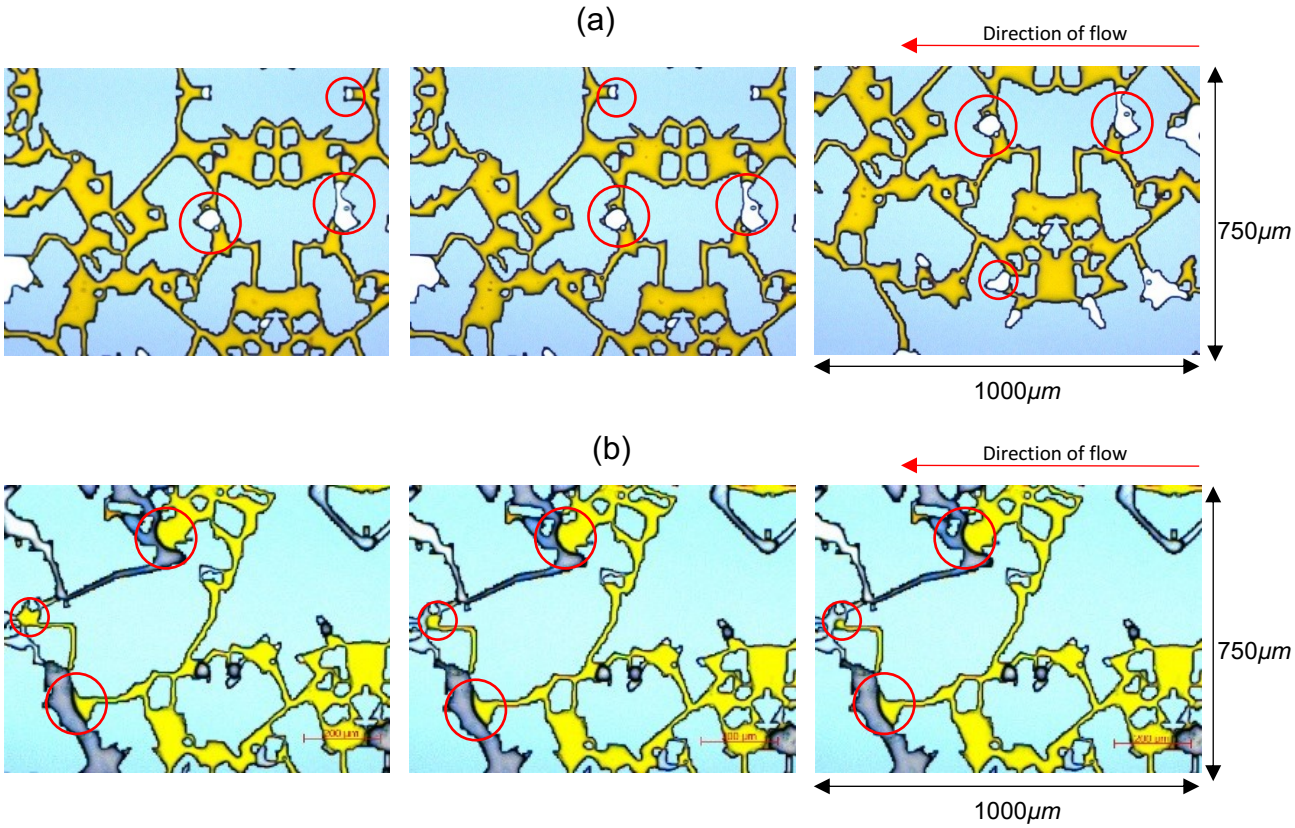

Figure 5.2. (a) Proof of model hydrophilicity before treatment, water invading fonts are concave (invading fonts are highlighted with red rings in the images), (b). Proof of model hydrophobicity, water invading fonts are convex (invading fonts are highlighted with red rings in the images).

The validity of the technique was also tested on the micromodel itself. The meniscus of the invading deionized water (a very low concentration of fluorescein was added to the deionized water for improved visualisation and easier phase differentiation) in the images in figure 5.2b can be seen to be convex during forced imbibition confirming

that the micromodel is no more unlike figure 5.2a which shows the invading deionized water to be concave in a water-wet micromodel.

5.2.3. Experimental Procedure and Image Processing

NaCl brine solutions were prepared freshly in the laboratory at each of the concentrations studied. Fluorescein (46960-25G-F, Sigma-Aldrich. 1:700,000 v/v) was added to each of the NaCl brine solutions for easier phase segmentation. The micromodel was affixed in a holder designed and fabricated in-house. Brine injection into micromodel was by a 10ml syringe (BD Plasipak, BD300013) with a programmable syringe pump (BS-80000, Braintree Scientific Ltd). To prevent the presence of trapped air bubbles, CO_2 gas was first used to flush the air out of the micromodel before injecting the brine solutions.

Subsequently, many pore volumes of the brine solution were continuously injected to flush out the all the CO_2 and the dissolved CO_2-brine system in the micromodel before closing the valves to saturate the micromodel with only brine. This is to ensure that the NaCl brine solution used for drying is essentially free of any dissolved CO_2. After achieving 100% brine saturation of the micromodel (checked with the high-resolution Inverted Light Microscope), the micromodel was placed horizontally (eliminating gravity effects) under the DSLR camera. The DSLR camera is placed on an adjustable stand facing vertically downwards and adjusted to capture the entire micromodel dimension in one image.

The dry gas line (air or CO_2) was attached to one of the inlet ports at the side of the matrix selected for drying while its adjacent port was opened to the atmosphere for continuous flow of dry gas. To ensure evaporative drying, the dry gas pressure was set at 0.5bars, resulting in a low enough flow rate. This was done to maintain very low relative humidity throughout the fracture channel and also circumvent forced advection into the matrix. The evolution of the dry-out was then captured at different time intervals and the movement of the drying front was observed. The images captured were saved in the TIFF format without compression, to obtain some quantitative data from the images, ImageJ was used to calculate the dry pore are (equivalent to mass lost by evaporation) of each of the captured images.

Since the brine was dyed with fluorescein, the dry pore areas are easily distinguishable from the pores still full of brine. Images were cropped and registered before segmentation, then the images were spatially calibrated using the known size of the micromodel pattern before setting the parameters to measure, in this case, “area”. Colour-based thresholding was then used to segment the dry pore areas followed by its area measurement. The procedure for estimating the dry pore area from the images using ImageJ and some examples of this was highlighted in our recent paper [205]. The quantitative data presented in this study are subject to uncertainty in dry pore area measurements. The average error was estimated by conducting repeat experiments and computing the standard deviation of the dry pore area measurement, approximately 0.02cm^2.

5.3. Results and Discussion

5.3.1. Effect of Porous Media Wettability on its Drying Dynamics

The evaporative drying procedure used for the water-wet micromodel was repeated for the mixed-wet and oil-wet micromodel. Figure 5.3 shows the plot of normalised evaporation rate as a function of liquid saturation for the three wetting conditions at different salt concentrations. The classical periods of evaporation for porous media drying: the constant rate period (CRP), the falling rate period (FRP), and the receding front period (RFP) are clearly depicted in figure 5.3. The evaporation rate E is estimated from the change in dry pore area as a function of time while the liquid saturation *S* is taken to be the area fraction of the pore space image occupied by brine. The key assumptions made in calculating the saturation are that pore spaces with liquid are filled and that dry pore areas are completely free of liquid. This allows the equivalence of the area fraction and saturation, which is a volumetric parameter.

All the plots follow a similar trend, a pseudo-constant high evaporation rate period, followed by a sharp fall in evaporation rate to a much slower evaporation rate period depicting the CRP, FRP and the RFP respectively. The depinning which signifies the CRP-FRP transition seem to happen a little early for the mixed-wet micromodel and much earlier for the oil-wet micromodel. Although, earlier experiments provide evidence that evaporation from mixed-wet porous media is slower than that from water-wet media [96, 220, 241, 254]. The reason for this difference between the water-

wet and mixed-wet micromodel is not apparent because we expect the matrix to have oil-wet patches where the micromodel surface came into contact with the oil phase during alteration, but still with water-wet films. Hence, it is expected that the plots for both water-wet and mixed-wet model be very similar, especially if the water-wet corners form a continuous path (maintaining hydraulic connectivity through capillarity) to the evaporating surface. However, the small difference between the water-wet and mixed-wet micromodel is in the continuity of the water-wet regions of the pore space as saturation reduces.

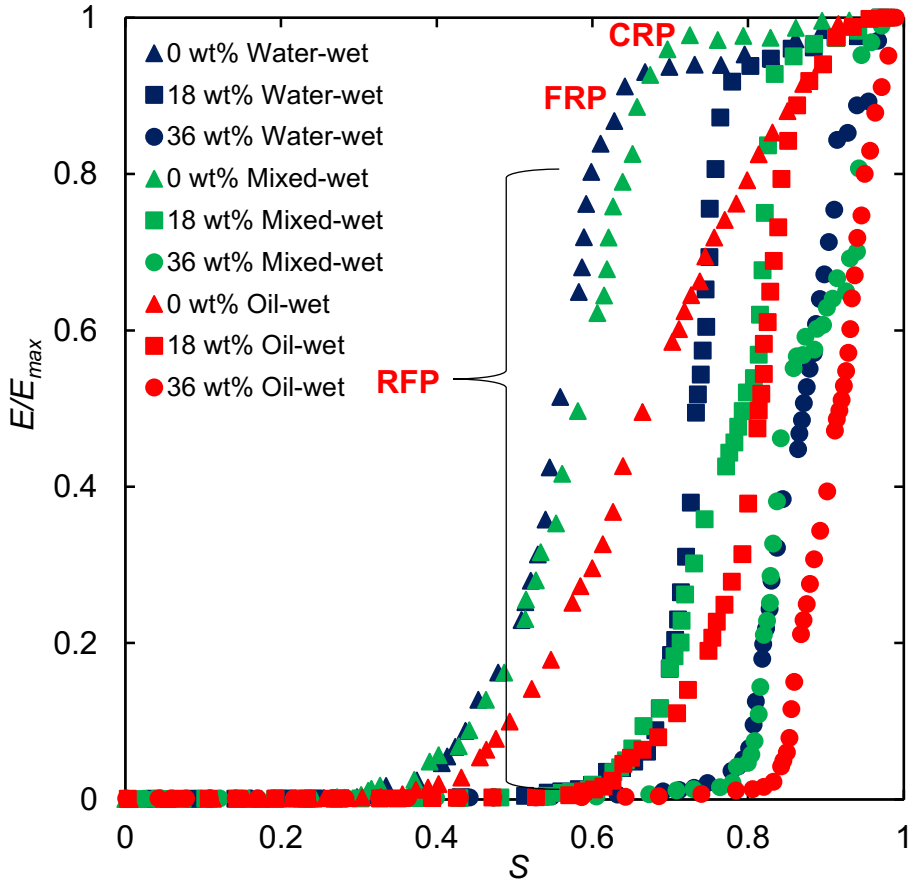

Figure 5.3. Evaporation rate as a function of liquid saturation for the three wetting states.

Likewise, we propose that the reason for the observed difference in the plots in early time as shown in figure 5.4a is due to the presence of oil-wet patches at the evaporating surface. These oil-wet patches at the evaporating surface will reduce the surface area available for evaporation at the surface, which in turn lowers the overall evaporation rate and increases overall drying time. Similarly, from studies of

evaporation of NaCl solution from sand grains porous media of mixed wettability [220], it was observed that the evaporative flux did not change considerably as the percentage of hydrophobic grains increases in the sand packs saturated with NaCl solution. It was concluded that the mixed wettability had little impact on the drying curves in sand packs porous media.

However, for the oil-wet micromodel, the constant rate period (CRP) was much shorter, even for deionized water drying, due to the early depinning as seen in figure 5.3. This is expected since the oil-wet model cannot sustain capillarity at all as there are no wetting films as the contact angle was altered to greater than 90°. The CRP for the saturated brine in the oil-wet micromodel was almost non-existent, with a greatly prolonged FRP over a larger liquid saturation range. For all wetting conditions, in the experiments with brine, the dry area of the matrix became linear with the square root of time after the short CRP, as is shown in Figure 5.4b. In the case of the oil-wet micromodel, this square root of time behaviour is due to capillary disconnect as is usually the case for deionized water drying. For the mixed-wet micromodel, this behaviour is due to a combination of capillary disconnect (it is possible the large flat face of the fracture becomes oil wet after treatment and cannot support water films) and deposited salt in the fracture and matrix acting as a partial barrier to hydraulic connectivity.

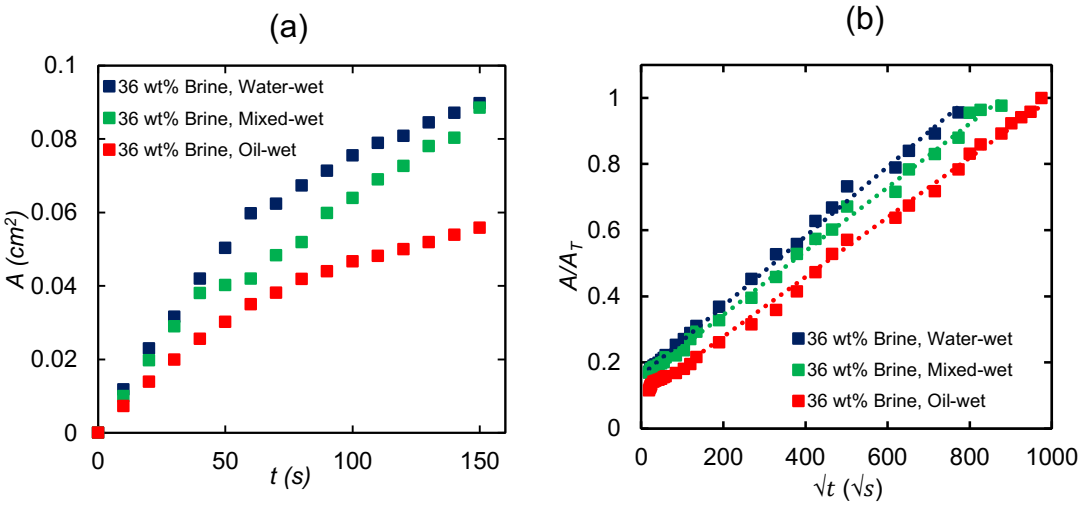

Figure 5.4. (a) Early-time dry area as a function of time and, (b). Dry area (normalised by total pore area) as a function of √t for 36 wt% NaCl brine for the different wetting conditions.

For the water-wet micromodel, it is due to a combination of salt deposition in the fracture and in the matrix greatly impeding hydraulic connectivity to the evaporating surface because the salt crystals continued to be deposited almost preferentially in the fracture above the matrix.

The effect of wettability on the precipitated salt distribution is more pronounced in the oil-wet micromodel. For the mixed-wet micromodel, the precipitated salt pattern was very similar to the water-wet micromodel case, with patchy salt formations in the fracture, again indicating the corner menisci maintained hydraulic connectivity to the fracture well into the falling rate period. This was also confirmed by measuring the contact angle of saturated NaCl brine on a NaCl crystal using the goniometer, the crystal was completely wetting to saturated brine as the brine immediately spreads as soon as it touches the surface of the crystal, giving a contact angle of approximately 0^{o}.

(a)

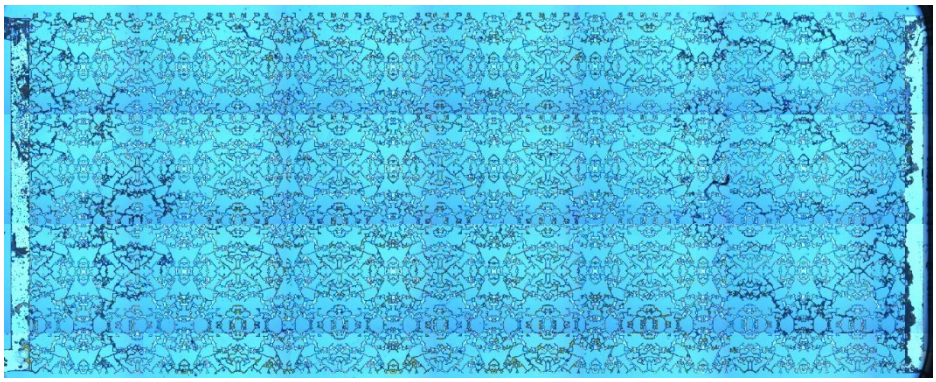

(b) (c) (d)

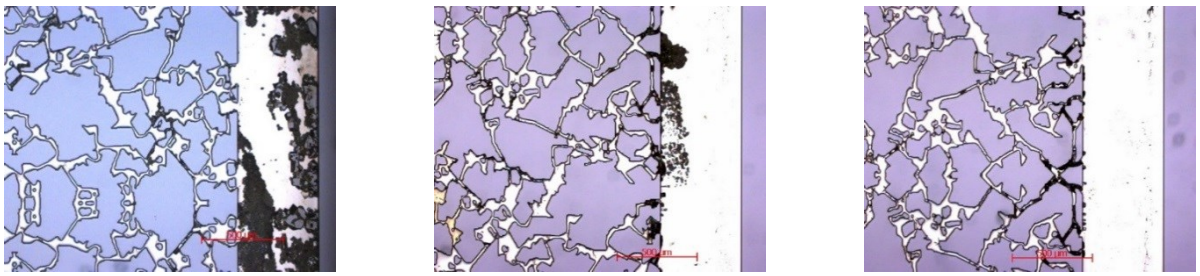

Figure 5.5. Images showing deposited salt in the evaporating surface and in the matrix at the end of complete drying (i.e. liquid saturation = 0) for (a) The entire mixed-wet micromodel, (b) A section of the water-wet micromodel, (c) A section of the mixed-wet micromodel and (d) A section of the oil-wet micromodel.

However, for the oil-wet micromodel, the hydraulic connectivity is broken very early into the drying and we have more patchy salt formations in the fracture as well as more salt precipitation in the matrix than was the case for the water-wet model. This is intuitive as there are no water-wet corners to maintain the capillary flow of liquid to the fracture. Therefore, the evaporation rate drops quickly and most of the salt is precipitated in the matrix. Overall, hydrophobicity in porous media leads to a reduction in capillary movement of water [255].

Drying of salt-contaminated porous media is usually accompanied by solid salt deposition at the evaporating surface (efflorescence) or within the porous media (sub-florescence). The brine concentration increases with the continuous loss of water until the solubility limit is exceeded, leading to solid salt deposition. Less salt was deposited in the fracture channel of the mixed-wet micromodel compared to the water-wet micromodel as seen in the images in Figure 5.5. Further, only a very small amount of salt (probably from the brine solution present in the channel prior to drying) were deposited at the evaporating surface for the oil-wet micromodel. The reason for this is once again due to the absence of wetting films needed to maintain hydraulic connectivity to the surface.

The supersaturation for the saturated NaCl brine was estimated to be ~1.05 for both the water-wet and the mixed-wet systems, and ~1.15 for the oil-wet system. However, this observed difference is likely due to the inability to efficiently observe salt deposition in the matrix (since most of the salt are deposited in the matrix in an oil-wet system) at the resolution of the imaging technique used. Hence, we propose that heterogeneous nucleation started earlier than was observable and the supersaturation value reported for the oil-wet system here is an over-estimate. Also, the size and the amount of salt crystals formed during drying differs for the different wetting states. More and bigger salt crystals were observed in the fracture for the water-wet system because the wetting films maintained hydraulic connectivity to the evaporating surface sustained continuous growth of crystals at the surface. The presence of oil patches in the mixed-wet system was the reason for the prevalence of smaller salt crystals in the fracture (see Figure 5.5a). These oil-patches decreases the effective area available for evaporation as well as crystallization. There are no big salt crystals in the oil-wet micromodels because most of the salt was deposited in the matrix where the diameter of the pores limits the sizes of the salt crystals formed.

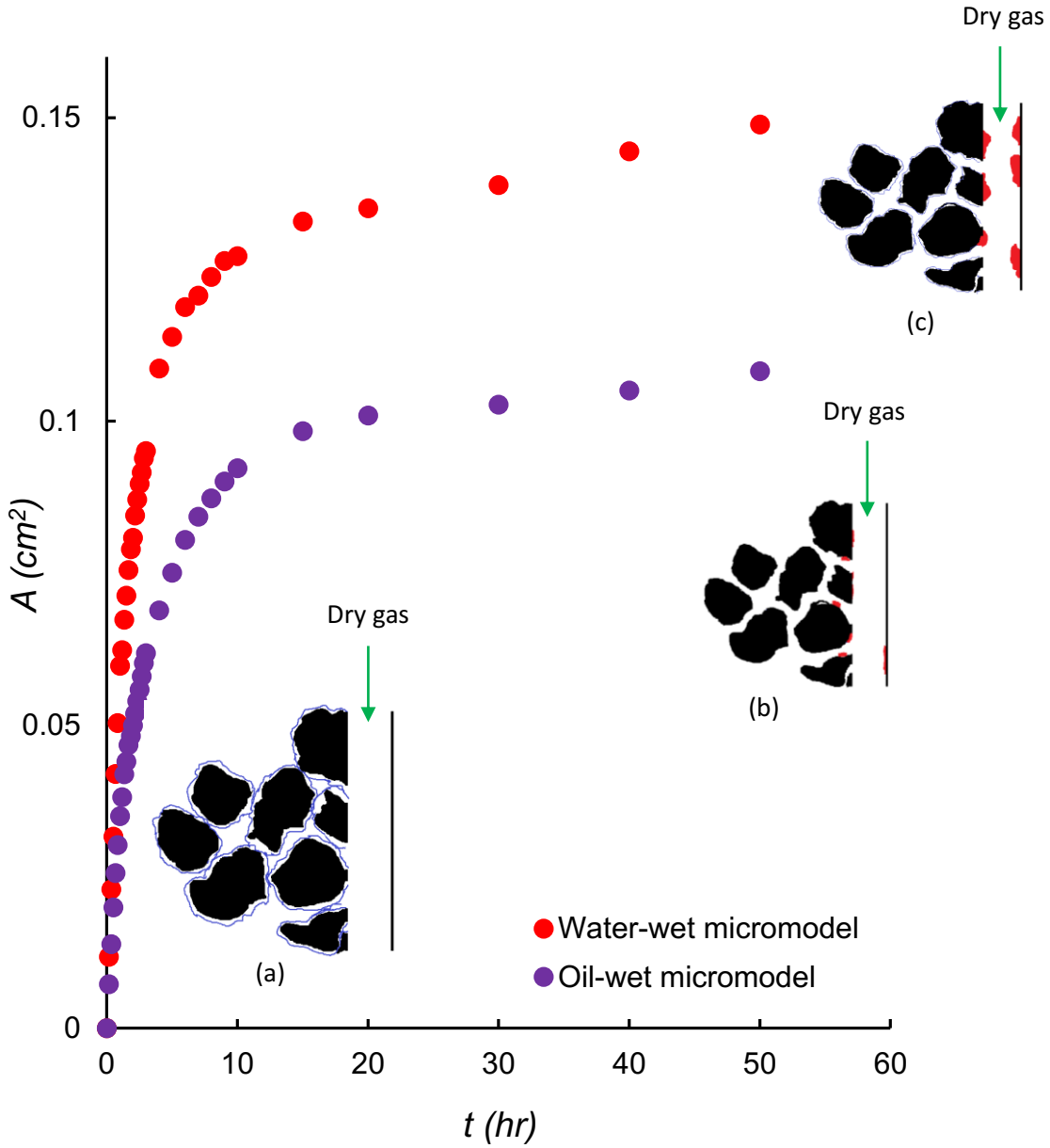

Figure 5.6. Dry pore area as a function of time for a 36 wt% NaCl brine (saturated) solution in a water-wet micromodel and oil-wet micromodel. The inset images are schematic representations of a section of the micromodel (fracture and matrix) at different times. (a) At the onset of drying with fracture full of gas and thick corner wetting films (t ≈ 10s). (b) During drying in an oil-wet micromodel, with little solid salt in fracture and no corner wetting films (t ≈ 30mins). (c) During drying in a water-wet micromodel, with solid salt in fracture and very thin corner wetting films (t ≈ 30mins). Model grains are represented in black, wetting films are indicated in light blue while deposited solid salt is represented in red.

Finally, results of the 36 wt% NaCl brine in a water-wet micromodel and oil-wet micromodel are compared directly in figure 5.6. The schematics show liquid films at

the corners of the micromodel grains percolating at the onset of drying. The thickness of the films decreases as drying continues until no connected pathway remains to the external evaporating surface. For deionized water, this would mark the onset of slower, stage-2, evaporation. However, from our experiment, the corner wetting films persisted after the transition to low evaporation rate, as solid salt continued to build up at the external evaporating surface.

5.3.2. CO_2 Dry-out Versus Air Dry-out

To the best of our knowledge, the similarities and differences in the drying of porous media saturated with brine using air and CO_2 have never been studied in the literature. The latter is particularly important in carbon sequestration process in saline aquifers. The experimental procedure described above was repeated, but instead of injecting dry air, dry CO_2 was injected across the fracture to effect evaporative drying of the brine in the micromodel. The outcome of the dry-out experiment with dry CO_2 was qualitatively very similar to that of dry compressed air as can be seen in figure 5.7. The trends of the different graphs plotted for the two systems were the same. However, there were some noticeable differences in the time it took to achieve complete drying. The CO_2 system dried-out faster than the compressed air system. Also, the CRP for deionized water was much longer for the dry CO_2 system as seen in figure 5.7.

To further highlight this difference, the early time data for both systems were plotted on the same graph in figure 5.8. Clearly, the CRP for the CO_2 systems was longer, although the difference is fairly small for the brines. To investigate this slight difference, the contact angle of deionized water and saturated brine on glass and silicon were measured in air and CO_2 with the preliminary result that the CO_2 atmosphere makes the system slightly more wetting, especially in the deionized water case where the average water contact angle measured in CO_2 was 29^o compared to the average water contact angle of 34^o measured in air, both on silicon. However, this difference of 7^o in the average contact angle cannot be said to be significant enough for the prolonged CRP observed in drying with CO_2. Nevertheless, the difference in the wetting state of the two atmospheric conditions allows hydraulic connectivity to be maintained for slightly longer in the CO_2 case and by extension, the Constant Rate Period (CRP) will be longer than was the case with compressed air.

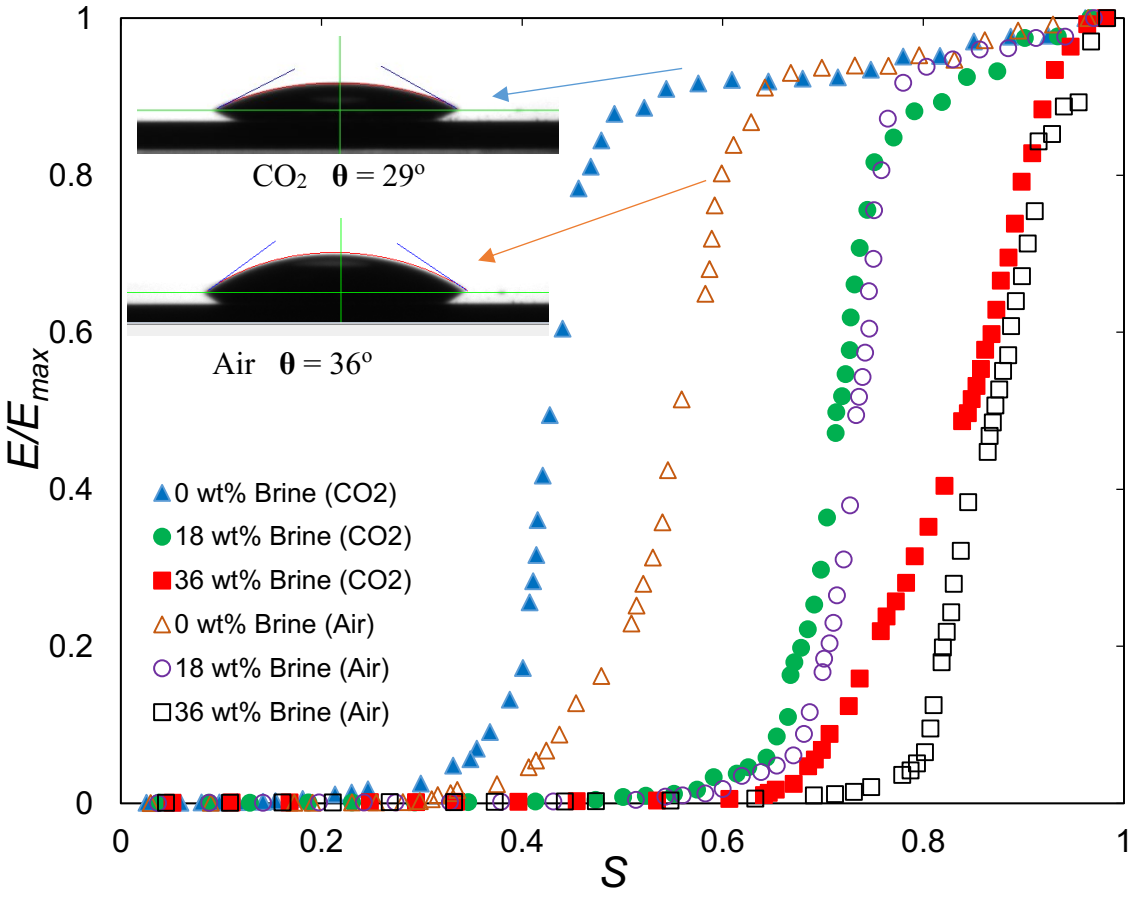

Figure 5.7. Evaporation rate as a function of liquid saturation for deionized water, 18 wt% Brine, and 36 wt% NaCl brine using dry air and CO_2 as the drying medium.

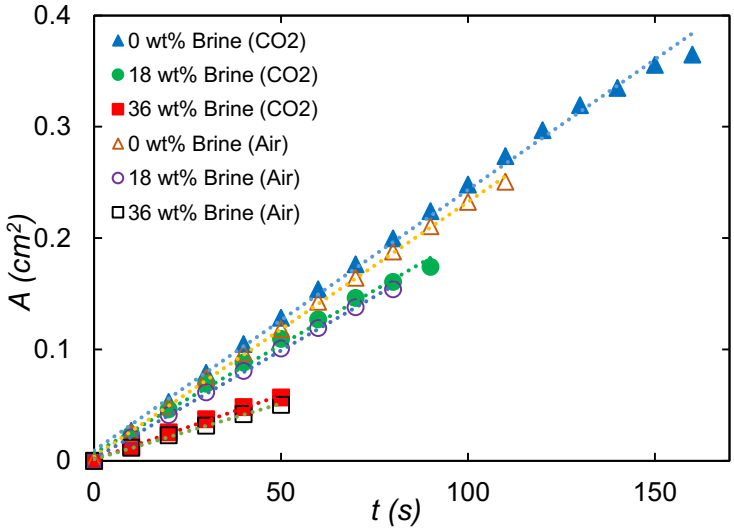

Figure 5.8. Comparison of CRPs for CO_2 and air dry-out, highlighting the difference as a consequence of changes in contact angle under the two systems.

The CO_2 atmosphere will make the corner films more effective in mass transfer of liquid to the evaporating surface, thereby decreasing the overall drying time [109]. The transition from the CRP for the saturated brine appears to depend less on wetting and more on the deposition of salt, so the small change in contact angle has less impact here.

5.3.3. Reduction in Permeability as a result of Salt deposition at Different Porous Media Wetting Conditions

The fracture and matrix permeability alteration (as defined in section 4.3.5 of chapter 4) as a function of initial brine concentration (before drying) at different wetting conditions in figure 5.9. For the water-wet model, we observed two regions of a linear downward trend in the matrix and fracture permeability measurements first with the 120g/L brine to 180g/L brine before a sharp decrease and another downward trend from the 240g/L to the 360g/L brine. A similar trend was observed for the mixed-wet systems. However, for the oil-wet systems, the fracture permeability only changes slightly even for saturated brine (360g/L brine). This is as a result of the absence of salt deposits in the fracture. The absence of salt deposits in the oil-wet is due to the lack of liquid wetting films needed to aid hydraulic connectivity to the fracture. Overall, the matrix permeability for all wetting conditions all decreases with increasing brine concentration and is almost total for the saturated brine concentration (360g/L brine). The practical consequence of this is that, in saline aquifers, salt deposition can lead to a significant decrease in injectivity.

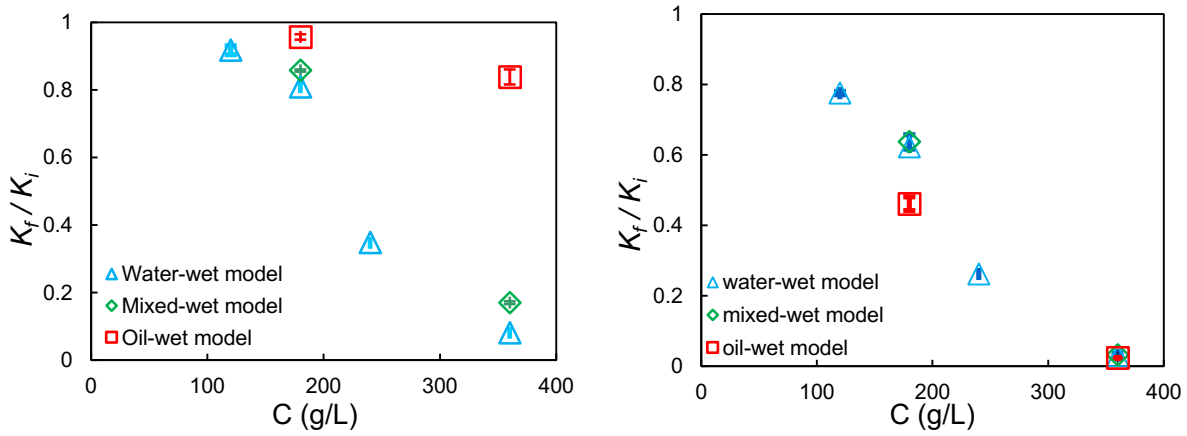

Figure 5.9. Permeability alteration versus initial salt concentration for the (a) fracture and, (b) matrix of the micromodel.

5.4. Conclusion

The impact of the wetting state of the porous media on the drying dynamics was also studied. Two patterns of wettability alteration were obtained by treating the micromodel with a silicone caulk solution. A uniformly oil-wet state was produced by injecting the treatment into a dry micromodel and a mixed wet state, resembling the spatial distribution of wetting in an oil reservoir was produced by injecting the silicone caulk solution into a model already saturated with water. The drying curve for water in the mixed-wet micromodel was very similar to that for the water-wet case, apart from the slightly earlier depinning in the mixed-wet condition. In the oil-wet micromodel, however, the evaporation rate dropped immediately after drying started, probably due to the early loss of hydraulic conductivity for this wetting state. The presence of oil-wet patches on the pore walls at the outer edge of the matrix would also reduce the evaporative flux by reducing the effective (water wetted) surface area available for evaporation and increase overall drying time.

The similarities and difference between air and CO_2 as the drying agent for porous media drying were also studied. The drying curves are quite similar apart from the slightly later depinning in the case of CO_2. This difference was investigated and concluded to be due to the CO_2 system being slightly more water wet than the air system as evident in the contact angle of deionized water under both conditions.

The matrix permeability, at complete dry-out for all wetting conditions, decreases with increasing salt concentration in a similar way. However, for the channel representing a fracture, the permeability decrease for the water-wet and mixed-wet cases was similar, while the fracture permeability for the oil-wet micromodel remained almost constant. This was a result of the absence of salt deposits in the fracture, caused by the lack of liquid wetting films needed to connect liquid brine to a point of evaporation in the fracture.

6. Flow Regimes, Displacement Processes and Dynamic Connectivity at the Pore Scale during Two-phase Flow using Micromodels

In this chapter, we investigate the flow regimes and displacement processes that occur during the steady-state co-injection of a wetting phase and a non-wetting phase using a model porous media. The effect of capillary number and viscosity ratio on the displacement dynamics will also be discussed.

6.1. Introduction

Immiscible two-phase flow through porous media is of great importance for many practical engineering processes such as oil recovery, drying processes, CO_2 sequestration etc. It is imperative that we understand the fundamental physics governing these flows at the different flow regimes. Capillary forces (determined by the interfacial tension and size of the pores) and viscous forces (determined by the flow rate, size of the pores (i.e. shear rate) and viscosity) of the fluid are two of the most important forces used in characterizing two-phase flow regimes and displacement processes in porous media. For example, when viscous forces become significant, displacement processes become governed by the flow field (i.e. they are no longer dominated by the capillary pressure alone), which is ultimately a function of the capillary number (flow rate of the two phases), the viscosities of the fluids (and by extension the viscosity ratio), and their density difference [45].

Generally, the flow of fluids in porous media often occurs through the continuous movement of the individual phases in connected, stable and distinct pathways. However, in some circumstances, the main mechanism of displacement is through the movement of ganglia (non-wetting phase blobs). In porous systems where there are only slight variations in pore-body and pore-throat sizes, ganglion movement becomes important because the capillary pressure difference across a stranded non-wetting phase blob necessary to allow movement through the pore space may be small.

Usually, ganglion movements are observed at high flow rates, i.e. when the capillary number is larger than 0.001 where viscous forces become more important even at the pore scale [45].

The effect of these factors on flow regimes and displacement mechanisms have been an area of active research for more than six decades. The relationship between interface curvature and the consequent capillary pressure was used to rationalise displacement mechanisms by Lenormand and Zarcone (1984) [165]. They studied two-phase displacement mechanisms using water and air in a model porous media. Based on their results, they proposed a displacement formula for pore-body filling events during imbibition. The formula characterizes pore-body feeling events (during imbibition) to be dependent on the number of throats connected to the pore that is filled with the non-wetting phase. They labelled pore-body filling events I1, I2, I3, I4,…..I*n*, where *n* is the number of throats filled with the non-wetting phase [165]. In deriving their I*n* formula, they assumed that the pore body is square and the pore size is the same as its connecting throats. Dodd and Kiel (1959) used Monte Carlo simulations to determine the roles of various parameters (pore-size distribution, network distribution, and number of connections per pore) on the quasi-static capillary pressure desaturation of a wetting liquid from a porous solid matrix [256]. They reported that not only are network models (involving random distributions of selected properties) useful in studying the parameters mentioned above, they are also valuable in characterizing the wettability of porous media with respect to the specified pairs of immiscible fluids saturating the solid [256].

Ganglion movement is also quite important in systems that allow little or no layer flow, such as two-dimensional micromodels. For example, if both oil and water are co-injected in a micromodel, then the phases can only move through the centres of the pore spaces, meaning that ganglion dynamics can be forced through topological constraints [45]. Hence, micromodel layer flow is restricted by the local geometry and therefore both the wetting and the non-wetting phases must flow through separate pore networks, each mostly filled with the transporting phase. That is, a phase can only flow if its network is connected (i.e. above its percolation threshold) across the sample and this is unlikely in porous media with weak spatial correlation. This will eventually result in a transition to ganglia flow at relatively low capillary number compared to real rock systems.

Immiscible two-phase flow in porous media through micromodel observations have been studied extensively by Payatakes and colleagues [149, 156, 157, 257-260]. Avraam and Payatakes (1995a) observed and reported four main flow regimes in their steady-state immiscible two-phase (n-Hexadecane and n-Dodecane as the non-wetting phase and deionized water as the wetting phase) flow experiments using a glass micromodel [156]. The four flow regimes were based on the mean size of the mobilized ganglia, droplets' prevalence, and the presence or absence of a stable connected non-wetting phase pathway. At low flow rates, flow occurs through the movement, break-up and coalescence of ganglia that typically span several pores, called large ganglion dynamics (LGD). By increasing the flow rate, the ganglia becomes smaller with a typical blob size around the size of a single pore, called small ganglion dynamics (SGD). Further increase in the flow rates led to an even smaller ganglia size with several ganglia occupying each pore and throat. This regime is called drop-traffic flow (DTF). However, at the highest flow rates, both phases are forced into an almost parallel and connected flow channel, termed connected pathway flow (CPF) [45, 156]. Other researches have also observed ganglion dynamics in two-phase flow micromodel experiments [158, 261].

The high flow rates at which the connected pathway flow (CPF) regime occurred in the micromodel experiments of Avraam and Payatakes (1995a) is counter-intuitive, according to the conventional description of multiphase flow, it is assumed that connected pathways occur at low flow rates .i.e. at the capillary-controlled limit. However, connected pathway flow at high flow rates was not observed in the micromodel experiments by Lenormand and Zarcone (1984), although their experiment is an unsteady-state displacement of oil by the injecting water (an imbibition process) [165]. Hence, the connected pathway flow observed by Avraam and Payatakes (1995a) is likely to be a consequence of forcing two immiscible fluids through a two-dimensional micromodel [45, 156]. The break-up of ganglia as flow rate increases during the steady-state simultaneous two-phase flow has been confirmed in a three-dimensional sintered bead pack porous media [151]. At sufficiently high flow rates of either the wetting or the non-wetting phases (and/or high flow rates of both phases), ganglion movement is observed, and the regimes are qualitatively similar to those observed by Avraam and Payatakes (1995a). However, the conditions leading to the regimes are different from those in real porous media experiments [169-172],

where connected pathway flow is observed at low flow rates and ganglia dynamics and drop-traffic kind of flow regimes are only observed at high flow rates.

Studies on two-phase flow experiments using real rocks at the pore-scale was a challenge until the advent of X-ray micro-computed tomography (X-ray μ-CT) [169-172]. The use of μ-CT in studying fluid flow in porous media is very important, allowing direct imaging of real rock's pore space due to its high spatial resolution (resolution of about 1μm is achievable). For example, The contributions of capillary forces, viscous forces and the fluid's density differences on both residual saturation and pore-scale morphology of the fluids during two-phase flow has been observed directly by X-ray imaging [262]. However, in two-phase flow experiments involving more complex porous media (real rock cores or 3D systems), displacement is usually capillary-controlled at low capillary numbers (although, this persist to higher capillary numbers than is observed in 2D micromodel porous media) [176]. This is because, unlike the topology constraint in micromodel experiments, the better connectivity of the phases in three dimensions allows connected pathway flow. However, as the capillary number (flow rates) increases, the connected non-wetting phase breaks up into ganglia, with the average size of the ganglia getting smaller and smaller with further increase in flow rates.

Hence, while ganglion movement is possible at low flow rates in two-dimensional micromodels with restricted layer flow [156], advection of trapped clusters in more realistic three-dimensional media are only seen at high flow rates (capillary numbers $\geq 10^{-3}$) [151, 176]. In previous studies [42, 151, 176], the more interesting observation is the presence of small non-wetting phase blobs in the pore space [176] and the periodic connection (and disconnection) of the flow pathways [42, 151] at relatively low flow rates. The periodic connection and disconnection of the non-wetting phase affect the overall fluid distribution, and as a consequence macroscopic parameters like relative permeability and capillary pressure [45]. Flow is no longer through a distinct, stable pathway, but through the temporarily stranded clusters that can reconnect at critical junctions, similar to the movements of cars controlled by traffic lights: *the road network is connected but does not always admit flow* [42, 45]. This flow behaviour was termed 'dynamic connectivity, and although it was reported as a new type of flow behaviour [42], it should be noted that no clear definition of what 'dynamic connectivity'

flow is, was provided. It was described as a flow behaviour where large stable ganglia are intermittently connected and disconnected by a small region between them.

This transient behaviour is yet to be fully understood because the use of three-dimensional pore-scale imaging in investigating displacements process in porous media is still relatively new and the fact that these important dynamic phenomena are usually too fast to be observed using micro-CT imaging techniques. Therefore, in this study we hope to elucidate displacement processes further by investigating these periodic connection-disconnection events through real-time optical imaging using micromodel techniques. For our observations to be attributed to only physical and operational factors, all the experiments in this research were done using the same kind of micromodel porous medium. Although the micromodels are two and a half dimensional network at best, the qualitative aspects of the flow in them are applicable to three-dimensional topologies as well.

6.2. Experimental Methods

6.2.1. Berea Sandstone-patterned Micromodel

The micromodels used in this study are based on thin-section images of a Berea rock as an example of a simple sandstone structure [204]. The pattern designs are already explained in section 4.2.1 of chapter 4. An image of a section (see figure 6.1) of the rock was taken and repeated throughout the micromodel. The image was manually manipulated to create a connected pathway for fluid flow. Hence, an image of a small section of the Berea rock was used and repeated throughout the micromodel for convenience. The Berea pattern is similar to the sucrosic dolomite pattern used in the drying experiments described in Chapter 4 but is closer in structure to the sandstone in which intermittent connectivity was observed [42].

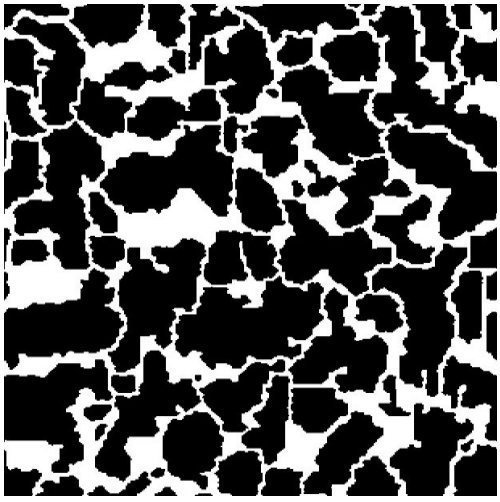

Figure 6.1. Repeated unit of the Berea sandstone used in fabricating the micromodel.

The micromodel matrix size is 2.4 x 0.9 cm^2 etched area with constant etch depth of 25 μm. The coordination number of the pores varies from 2 to 4 and the grains range in size approximately from 10 to 500 μm. The micromodels contain a narrow channel etched along the two edges of the pore network to allow 'uniform' movement of the phases into the fracture. These channels also limit the propagation of slug flow that will otherwise be inevitable if phase injection is directly into the matrix. However, the flow distribution was still not optimal and some slugging was observed. The slug flow propagated for approximately 0.45cm (estimated by eye observations) into the micromodel matrix before the flow settled down to one representative of the matrix geometry only. Hence, all the observations made in these experiments were at least 1cm into the length of the matrix. The narrow channels are 500 μm in width and 25 μm in depth. These channels allow fluid injection and production through holes drilled directly into the glass (used in covering the silicon wafer) at each corner of the micromodel.

The average porosity measured from the binarized model image was estimated to be 0.30 with a matrix permeability of about 350mD. The silicon wafer was treated as described in Chapter 4 to ensure strong water-wetting conditions. The pore-body and throat size distributions of a mirrored repeat unit, estimated from the equivalent circular diameter and distance across the throats respectively, are shown in the plot in figure 6.2. A colour-coded image of a mirrored repeat unit showing the separation of pore-body and throats is shown in figure 6.2b. The capillary pressure distribution for the

repeat pattern is shown in figure 6.2d. The distribution is quite narrow as the constant etch-depth of 25μm (10 pixels) becomes the limiting value for all pores with a diameter higher than the etch-depth. That is, for all the pore-body and pore-throat with a diameter of 12 pixels (30μm) and above, the etch-depth will essentially determine the capillary entry pressure since the capillary pressure is inversely proportional to the pore's mean radius of curvature. This is a clear limitation of a single depth micromodel.

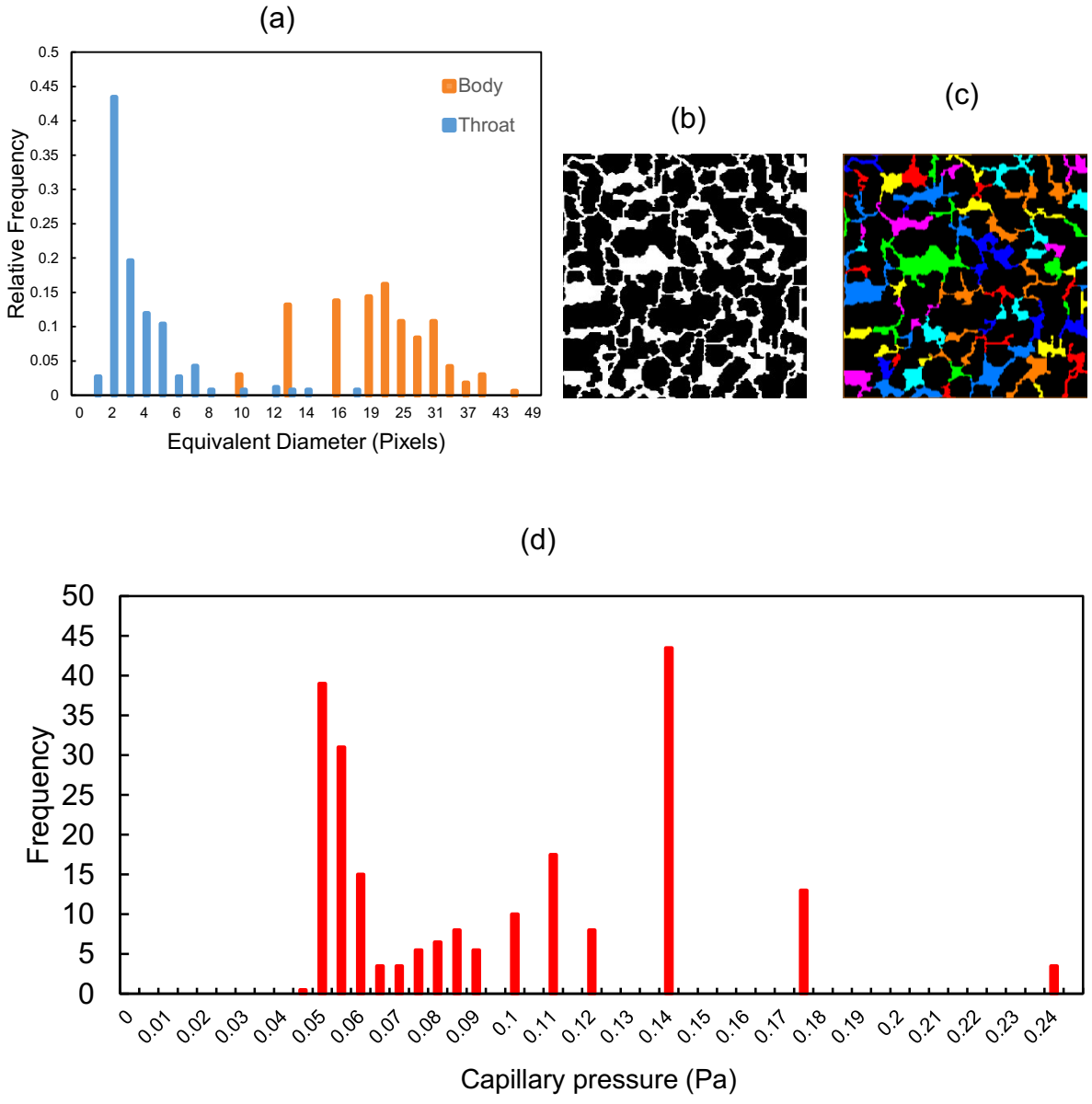

Figure 6.2. (a) Micromodel repeat unit pore-body and throat size distributions in pixels (2.5 μm/pixel), (b) Binary image of the thin section of the Berea sandstone mirrored and repeated throughout the micromodel (0.16 X 0.16cm), (c) colour-coded image of the repeat unit showing the separation of pore-body and throats, (d) the capillary entry pressure distributions of the micromodel repeat unit calculated from the mean radius of curvature (see equation (10) in chapter 2).

An Inverted light microscope (ILM) was used to view fluid movements in the micromodel. The components and working procedure of the microscope have already been explained earlier. Magnifications of 2.5x, 5x, and 10x were used to observe and track the movement of fluids at different fields of view. The 2.5x magnification was used for a larger field of view observation, while the greater magnification of 10x was used to focus on a small number of pores. Live images of the micromodel positioned on the stage were either viewed directly through the eyepiece or on a personal computer (PC) running specialist software AxioVision (Version 4.8.1, Zeiss) attached to the digital camera (AxioCam HSc) on the microscope via a FireWire cable. Images were then captured at predetermined time intervals and dynamic events were recorded with a screen recorder, an open source software.

6.2.2. Experimental Procedure

For all experiments, deionized water was the wetting phase while two different oil phases (decane and squalane) with different viscosities were used as the non-wetting phase. The properties of the fluids are shown in table 6.1. The deionized water was dyed with methyl blue (M6900-50G, Sigma-Aldrich. 1: 700,000 v/v) and the oil phase was dyed with oil red O (O0625-25G, Sigma-Aldrich. 1:200,000 v/v) for easier phase differentiation.

Table 6.1. Oil Phase, Dynamic Viscosity, Viscosity Ratio, and Oil-phase/Water-phase Interfacial Tension

Oil phase	Dynamic viscosity 20°C (cP)	Water to oil viscosity ratio	Interfacial tension (mN/m) (at 20°C)
Decane	0.87	1.10	52.33 ± 0.04
Squalane	22.60	0.04	52.5 ± 0.5

Interfacial tension of water + decane from *Zeppieri et al. (2001)* [263] while the interfacial tension of water + squalane was from *Reichert and Walker (2013)* [264]. The dynamic viscosity of decane is from *Yi Liu et al (2011)* [265] . while that of squalane is from *Harris (2009)* [266].

A vacuum pump was used to remove moisture from the micromodel before each experimental run. Prior to deionized water injection, CO_2 gas was injected into the micromodel to displace air. Since CO_2 is relatively soluble in water, 100% saturation of the micromodel with deionized water is possible. After fully saturating the micromodel with the wetting phase, the oil phase and the wetting phase were then co-injected at different flow rates into the micromodel so the overall process was drainage

(even for experiments where the fractional flow rate was not kept constant, and the flow rate of the wetting phase was much higher than that of the non-wetting phase, still, the initial saturation of the wetting phase will keep decreasing until steady-state is attained). The total flow rates were kept constant until steady state was observed and then changed to a new value. For linear concurrent flow through the micromodel, the production ports on the fracture opposite the inlet port are opened while the valve on the outlet port adjacent to the inlet is closed, as seen in the experimental procedure schematics in figure 6.3. The pressure transducer in the set-up was used to ascertain steady-state conditions by measuring the pressure difference between the flow in the micromodel and the outlet. Experiments were carried out by changing the capillary-viscous force balance by gradually increasing the total flow rate, i.e. from the very low flow rates to large flow rates relative to the micromodel, while keeping the fractional flow constant.

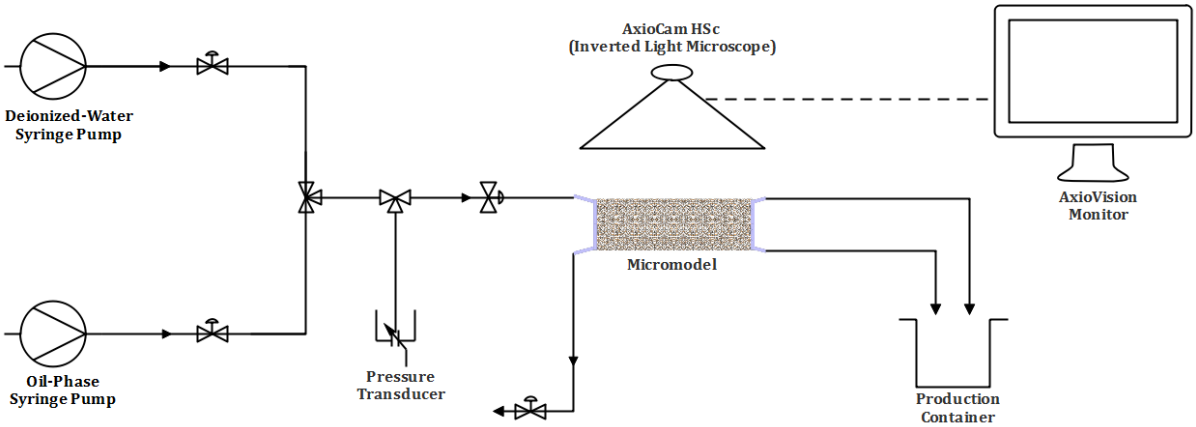

Figure 6.3. Schematic of the flow rig, micromodel and optical microscopy used for the pore-scale co-injection experiments.

The first sets of experiments were conducted at a constant fractional flow rate of 0.5. Other sets of experiments were done at varying fractional flow rates for both deionized water/decane and deionized water/squalane systems. Many identical micromodels were used for the water/decane system and the water/squalane system experiments (i.e. one set of micromodels was used for the water/decane system experiments, and another set of new micromodels was used for the water/squalane experiments). However, the micromodels were cleaned by flushing them with deionized water, followed by acetone and then dried by passing dry air through it after each subset of

experiments. Changes in the wettability of the micromodel will affect the fluid dynamics in them, and these changes can be readily detected. When a wettability change was detected, the micromodel was re-cleaned, and in situations where the problem persisted, the micromodel was discarded, and the experiment was repeated with a new micromodel. Also, tubing connections were washed by the same routine used for the micromodel after each experiment. The wetting phase and non-wetting phase capillary numbers at the different flow rates were calculated using equation (28).

$$Ca_w = \frac{Q_w \, \mu_w}{A\gamma\phi} \tag{28}$$

Where Ca is the capillary number, Q is the flow rate in m^3/s, μ is the dynamic viscosity in *Pa.s*, *A* is the area of the micromodel m^2, γ is the interfacial tension in *mN/m* and ϕ is the porosity of the micromodel, the subscript w represents the wetting phase. The list of experiments at a constant fractional flow rate of 0.5 for deionized water/decane and deionized water/squalane systems are shown in table 6.2 and 6.3 respectively.

Table 6.2. List of experiments for deionized water/decane system at different total flow rates with a constant fractional flow rate (0.5).

Experiment	Total flow rate, Q_T (uL/min)	Water flow rate, Q_w (uL/min)	Decane (Oil) flow rate, Q_{nw} (uL/min)	Wetting phase capillary number, Ca_w	Non-wetting phase capillary number, Ca_{nw}
1	0.2	0.1	0.1	4.73×10^{-7}	4.31×10^{-7}
2	0.4	0.2	0.2	9.45×10^{-7}	8.62×10^{-7}
3	1.0	0.5	0.5	2.36×10^{-6}	2.16×10^{-6}
4	2	1.0	1.0	4.73×10^{-6}	4.31×10^{-6}
5	4	2.0	2.0	9.45×10^{-6}	8.62×10^{-6}
6	10.0	5.0	5.0	2.36×10^{-5}	2.16×10^{-5}
7	20	10.0	10.0	4.73×10^{-5}	4.31×10^{-5}
8	40	20.0	20.0	9.45×10^{-5}	8.62×10^{-5}
9	100	50.0	50.0	2.36×10^{-4}	2.16×10^{-4}
10	200	100.0	100.0	4.73×10^{-4}	4.31×10^{-4}

Table 6.3. List of experiments for deionized water/squalane system at different total flow rates with a constant fractional flow rate (0.5).

Experiment	Total flow rate, Q_T (uL/min)	Water flow rate, Q_w (uL/min)	Squalane (Oil) flow rate, Q_{nw} (uL/min)	Wetting phase capillary number, Ca_w	Non-wetting phase capillary number, Ca_{nw}
1	0.2	0.1	0.1	4.72×10^{-7}	1.07×10^{-5}
2	0.4	0.2	0.2	9.42×10^{-7}	2.13×10^{-5}
3	1.0	0.5	0.5	2.36×10^{-6}	5.31×10^{-5}
4	2.0	1.0	1.0	4.72×10^{-6}	1.07×10^{-4}
5	4.0	2.0	2.0	9.42×10^{-6}	2.13×10^{-4}
6	10.0	5.0	5.0	2.36×10^{-5}	5.31×10^{-4}
7	20.0	10.0	10.0	4.72×10^{-5}	1.07×10^{-3}
8	40.0	20.0	20.0	9.42×10^{-5}	2.13×10^{-3}
9	100.0	50.0	50.0	2.36×10^{-4}	5.31×10^{-3}
10	200.0	100.0	100.0	4.72×10^{-4}	1.07×10^{-2}

6.3. Results and Discussion

6.3.1. Flow Regimes and Displacement Processes

A total of 120 experiments were conducted, 20 (10 each for deionized water/decane system and deionized water/squalane system, see table 6.2 and 6.3 respectively) were done at a constant fractional flow rate and 100 (50 each for deionized water/decane system and deionized water/squalane system, see table A.4 and A.5 in the appendix) were done with a varying fractional flow rate. For each of the experiments, the two phases were not optimally distributed in the channel before going into the matrix, slug flow was observed up to about 20% (approximately 0.45cm, estimated by eye observations) of the length of the matrix (see figure 6.4 below), after which the flow settled down to a state completely controlled by the matrix and not the inlet flow conditions. Therefore, the field of view for observations in these experiments was at least 1cm into the length of the matrix. Also, it took about 1 to 24 hours to achieve ‘steady-state’ (equilibrium) depending on the flow rates of the phases. The equilibrium, in this case, is the dynamic result of the interaction between several viscous and capillary flow phenomena. However, flow is better characterized as *stationary,* in a stochastic sense, rather than as ‘steady-state’ [156]. Nevertheless,

once steady-state (equilibrium) was reached, images of the phase distribution in the micromodels at different pore-scales were captured.

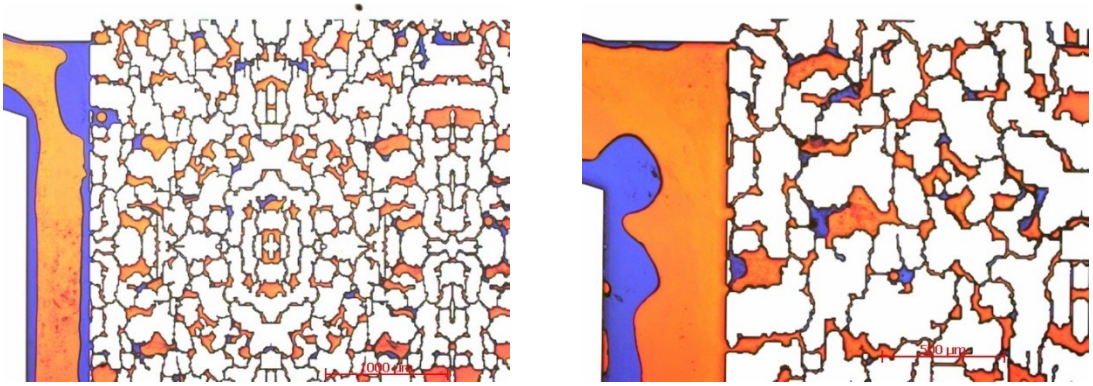

Figure 6.4. Micromodel images of the inlet flow conditions showing the propagation of slug flow in the channel and in the matrix near the channel at 2.5X and 5X magnifications.

In the experiments with relatively high flow rate ($Ca_{nw} > 10^{-6}$ for water/decane system and $Ca_{nw} > 10^{-5}$ for water/squalane system), the non-wetting phase was disconnected while the wetting phase was connected throughout the micromodel. In essence, while the deionized water occupies all corners of the micromodel and flows through continuous pathways, the oil phase breaks down in the deionized water and flows as oil blobs and droplets in the wetting phase – ganglion transport, see figure 6.5.

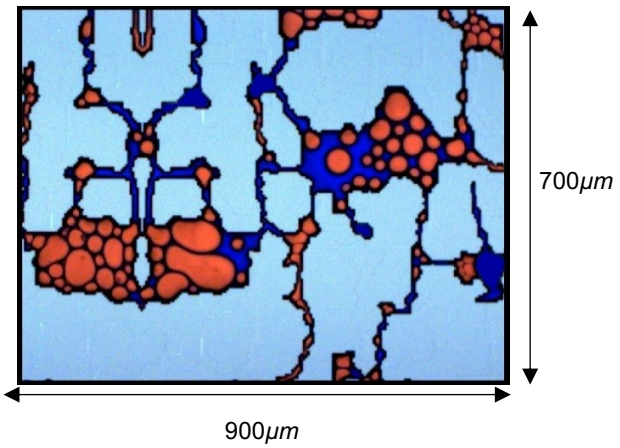

Figure 6.5. Pore-scale image of ganglion transport (decane) within the wetting phase during simultaneous two-phase flow (Ca_{nw} = 2.16 X 10^{-4} and Ca_w = 2.36 X 10^{-4}) in a micromodel with a 10x magnification lens. The oil phase is dyed with Oil Red O while the water phase is dyed with Methyl Blue.

From qualitative observation of the videos of the experiments, different flow regimes can be defined based on the nature of the non-wetting phase dynamics, i.e. the connection (or lack thereof) of the non-wetting phase, and the mean size and prevalence of the non-wetting phase blobs. These flow regimes are: connected pathway flow regime, big ganglia flow regime, big-small ganglia (a mixture of small and big ganglia) flow regime and small ganglia flow regime. The non-wetting phase in the last three regimes (-ganglia regimes) is disconnected and there is no distinct boundary between any neighbouring -ganglia regime as the transition from one -ganglia flow regime to another is gradual. The only distinct boundary is between connected pathway flow regime and the 'disconnected' pathway flow regimes, i.e. the –ganglia regimes.

The connected pathway flow regime was observed at very low total flow rates, in this regime, the oil phase flows in a somewhat connected, unchanging pathways. In some areas, the oil phase may become blocked trying to pass through a tiny throat. However, there is always a connected oil phase pathway in the direction of flow within the area of observation. Figure 6.6 is an example of a connected pathway flow observed in the micromodel. A thin film of the wetting phase is present in all the corners of the pores and throats, although, this cannot be readily seen at the resolution of the images in figure 6.6. Also, in this flow regime, even though the movement of the non-wetting phase is through a connected pathway within the wetting phase, some of the non-wetting phase blobs are cut-off from the flow and trapped.

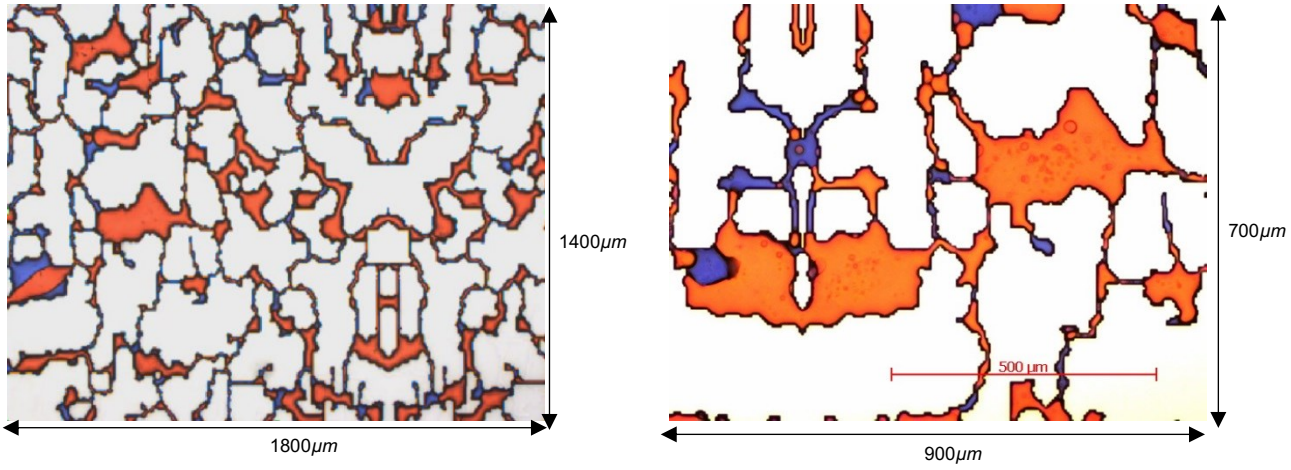

Figure 6.6. 5x and 10X magnification lens image of connected pathway flow regime for water/decane system (Ca_{nw} = 4.31 X 10^{-7} and Ca_w = 4.73 X 10^{-7}).

The big ganglia and the big-small ganglia regimes are quite similar to each other, the difference is the prevalence of oil blobs of smaller mean sizes in the latter. These regimes start to manifest as the total flow rate is increased. First, the oil phase starts to disconnect especially at constrictions, leading to big flowing oil blobs – big ganglia flow regime (figure 6.7a). Then as the total flow rate is increased further, the mean sizes of some of the oil blobs decrease leading to a mixture of big and small ganglia – big and small ganglia flow regime (figure 6.7b). In the big ganglia regime, the flow pathways are still systematic and in order, only that they are no more connected. The distribution of the oil blobs here can be divided into the moving ganglia and the isolated ganglia. There is an intricate interaction between these two classes of oil blobs. Most of the moving big ganglia may become trapped when they get to a tight constriction (or in some rare cases split into smaller ganglia) within the porous medium. Conversely, the big moving ganglia can bump into slower or faster moving ganglia (or even isolated ganglia) and merge to form bigger moving ganglia. However, as the total flow rates are further increased, the rate at which big ganglia split into smaller ganglia at constriction increases leading to a mixture of big and small ganglia. It is important to mention again that the transition from the big-ganglia regime to big-small ganglia regime is very fuzzy.

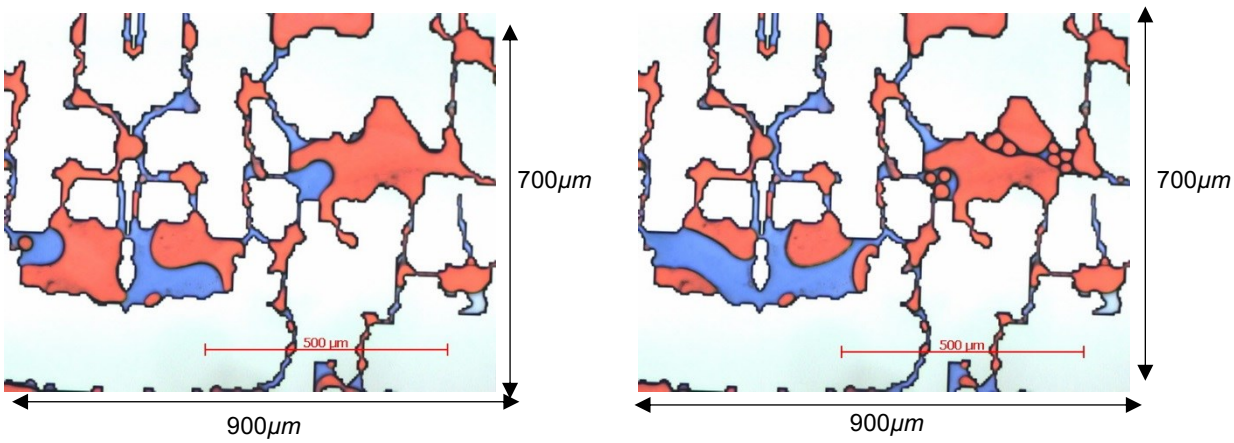

Figure 6.7. 10x magnification lens image of (a) big ganglia flow regime and (b) big-small ganglia flow regime (decane).

Lastly, small ganglia flow regime is observed as the flow rate is further increased (Ca_{nw} > 10^{-5} for water/decane system and Ca_{nw} > 5 x 10^{-4} for water/squalane system). This regime is characterized by the random and rapid movement of small ganglia through

the porous medium. The mean sizes of these ganglia are the smallest, and it is possible to have as many as 20 individual ganglia pass through at the same time as seen in figure 6.5. Occasionally, a few big ganglia are formed by the merging of two small ganglia, however, these big ganglia are very unstable and quickly split back into small ganglia due to the high flow rates.

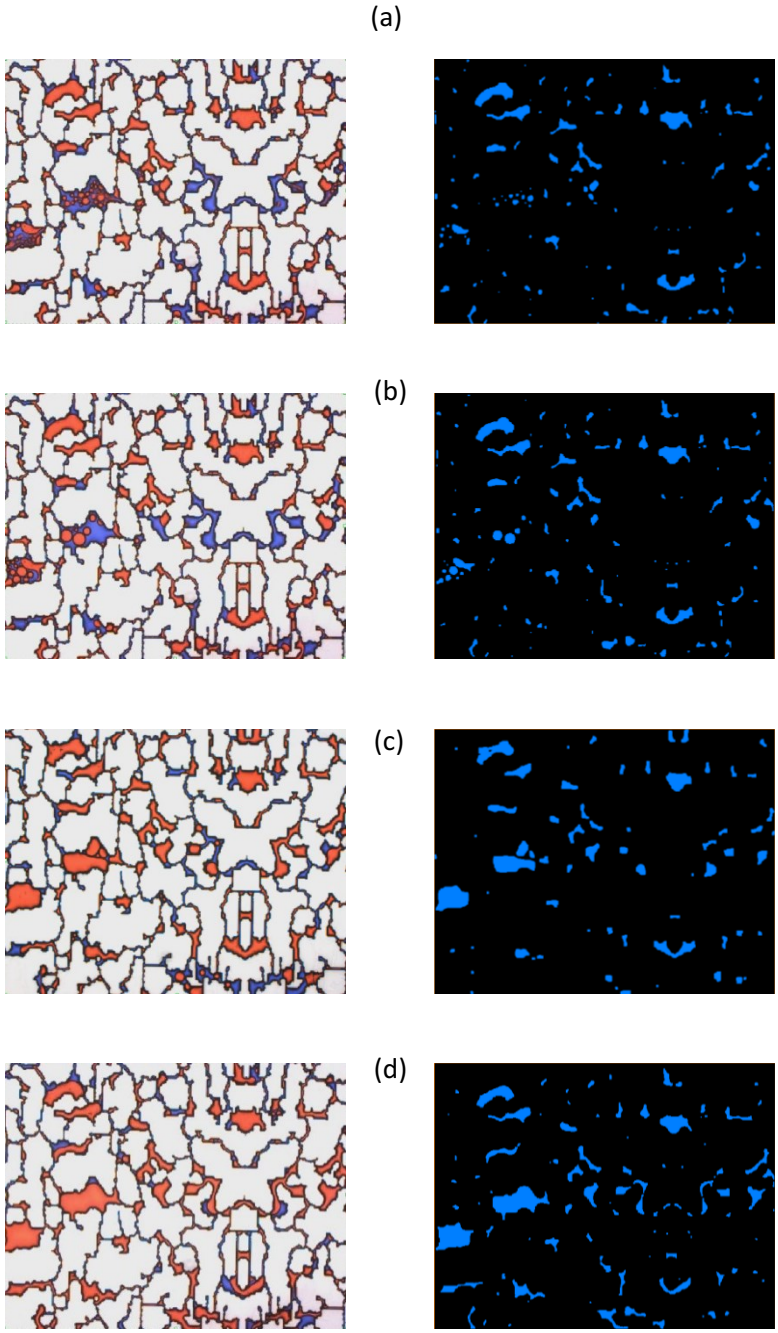

Figure 6.8. Snapshots of each of the regimes and their corresponding segmented image. (a) Small ganglia flow (Ca_{nw} = 8.62 X 10^{-5} and Ca_w = 9.45 X 10^{-5}), (b) big-small ganglia flow (Ca_{nw} = 8.62 X 10^{-6} and Ca_w = 9.45 X 10^{-6}), (c) big ganglia flow (Ca_{nw} = 2.16 X 10^{-6} and Ca_w = 2.36 X 10^{-6}), (d) connected pathway flow (Ca_{nw} = 4.31 X 10^{-7} and Ca_w = 4.73 X 10^{-7}).

Snapshots (and corresponding segmented non-wetting phase images) from the experiments corresponding to the micromodel repeat unit in figure 6.1 are shown in figure 6.8. The image in figure 6.8a is typical of the small ganglia flow (SGF) regime, image in 6.8b is typical of the big-small ganglia flow (BSGF) regime, image in 6.8c is typical of the big ganglia flow (BGF) regime, and image in 6.8d is typical of the connected pathway flow (CPF) regime. Many snapshots (as well as videos) were taken during each of the experiments. These snapshots were processed and the non-wetting phase volumes were segmented out using the interactive thresholding technique on Avizo 9.1 (http://www.vsg3d.com/). These non-wetting phase blobs (ganglia) are shown as light blue in the segmented images. However, due to the low resolution of the raw images over time, and the shadow the pore walls cast on the snapshots, segmenting out the non-wetting phase in very narrow throats was not possible. This is why the segmented image of the connected pathway flow in figure 6.8d appear not to be connected all through even when its corresponding snapshot is connected. Also, live observations at these range of capillary numbers showed that the interfaces had settled down into a stable configuration, even with continuous fluid flow in and out of the micromodel. Hence, there must have been a stable connected pathway for fluid flow.

Furthermore, the ganglia populations in each of the three disconnected (BGF, BSGF and SGF) regimes were analysed and the ganglia-size distribution, estimated from the equivalent diameter using Avizo 9.1 are shown in the plots in figure 6.9. At least 10 random snapshots of each of the regimes were segmented and the equivalent diameter of the oil blobs was estimated. The results were then combined and the distribution for each of the flow regimes was plotted. Figure 6.9a compares the three disconnected regimes directly while figure 6.9b compares the BGF and the SGF. The prevalence of small ganglia in the SGF was high compared to its prevalence in the BGF, and there is a relative balance in the amount of big and small ganglia in the BSGF plot. However, note that the artefacts mentioned above will also result in underestimation of the ganglia sizes for the non-connected regimes. These plots provide quantitative support to the qualitative visual observations already presented.

For all the experiments, it was observed that the mobile oil ganglia seem to follow some preferred paths, these paths are however not permanent and can switch to another path at any time. Also, the flow regimes defined above are similar to those

reported in the micromodel experiments of Avraam and Payatakes (1995a) [156]. However, unlike their study where connected pathway flow regime was observed at high flow rates, our observations here aligned with conventional picture of multiphase flow in porous media where it is assumed that connected pathways flow regime exist only at low flow rates (i.e. in the capillary-controlled limit) [45].

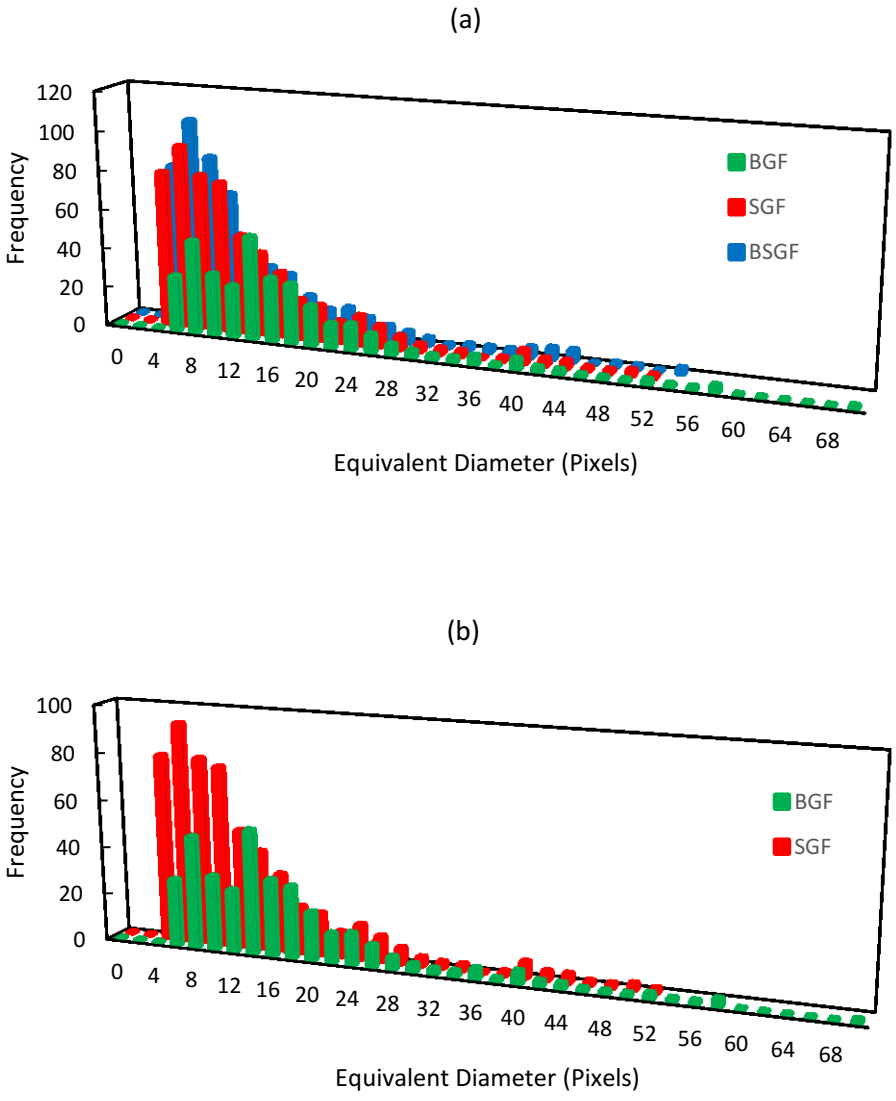

Figure 6.9. Ganglia-size distribution for the disconnected regimes. (a) Comparison of the BGF, the SGF, and the BSGF, (b) comparison of the BGF and the SGF.

This difference might be due to the nature of the micromodel used by Avraam and Payatakes (1995a). While their model is a network of the chamber-and-throat type of

two-dimensional ‘perfectly homogeneous’ micromodel etched in glass, the model here is a 2.5-dimensional micromodel based on a thin section of Berea sandstone etched in silicon and covered with glass. Hence, the connected pathways at a high flow rate in their study may be due to the monotonic nature (all the pore spaces have the same dimensions) of their micromodel favouring the formation of a pathway for one or the other phase. While, the better-connected, more heterogeneous micromodel used in this study will allow more flows in wetting layers.

6.3.2. Water/Decane system vs Water/Squalane system

The effect of the water-to-oil viscosity ratio on the flow regimes and displacement processes was studied by carrying out experiments with two different oil phases with different viscosity. The results discussed in the preceding section were on the water/decane experiments. The same experimental procedure highlighted in section 6.2.2 were repeated for the water/squalane experiment and the observations from the experiments were compared and contrasted with the water/decane system.

There are many similarities between the observations from the two systems. Although, the water/squalane system attained a steady-state much earlier due to its low viscosity ratio. However, the four flow regimes observed in the water/decane system were also observed here and steadily increasing the total flow rate in the systems lead to a disconnection of the oil phase, especially at constrictions. Also, during the big-small ganglia flow regime, smaller blobs coalesce to form big blobs much more than big blobs split into smaller blobs in the water/squalane system essentially leading to more prolonged big ganglia flow regime even as the flow rate is increased. This is because it is harder for big blobs to split at low viscosity ratio. Also, the low viscosity ratio of the water/squalane system makes the overall flow more systematic and orderly compared to the water/decane system that is very chaotic at high flow rates.

The four flow regimes identified in the previous section are represented qualitatively on a state diagram in figure 6.10 and 6.11. Figure 6.10 and 6.11 are state diagrams depicting the transition from connected (systematic) flow to disconnected (random) flow for water/decane and water/squalane systems respectively.

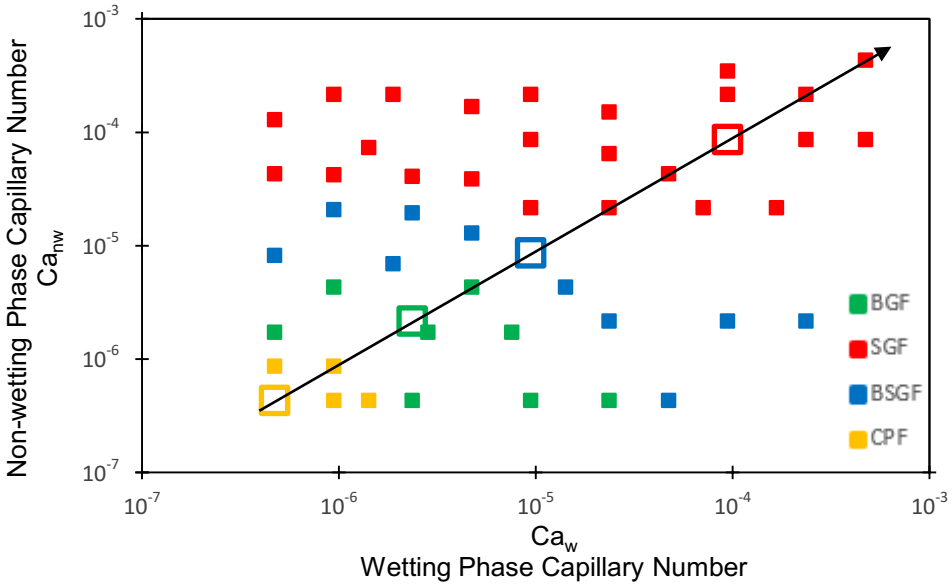

Figure 6.10. State diagram of simultaneous two-phase flow (water/decane system) through a 2.5D porous medium as a function of Ca_w and Ca_{nw}. The curve signifies the transition from connected systematic flow to disconnected random flow. The big yellow, green, blue and red markers correspond to the CPF, BGF, BSGF and SGF images respectively as highlighted in figure 6.7.

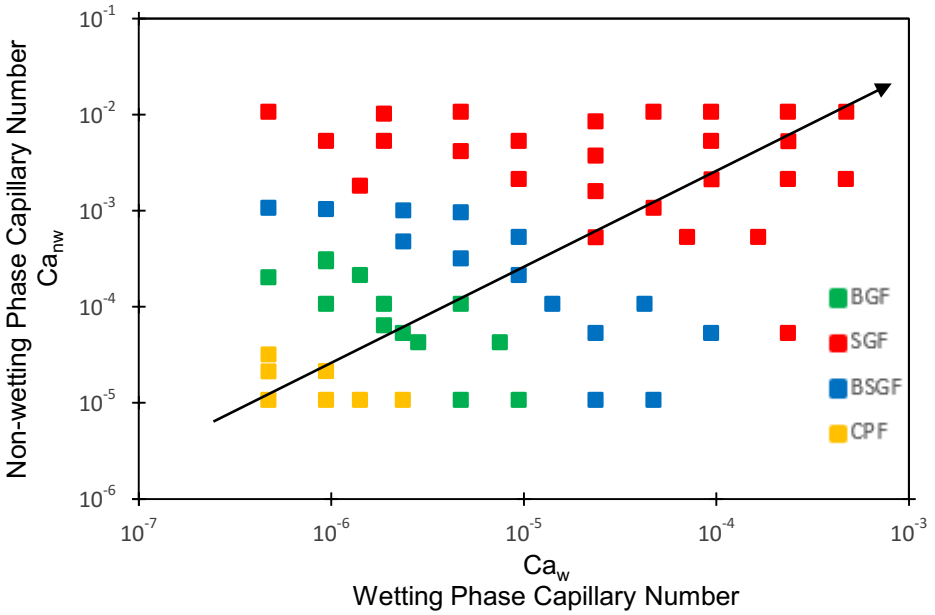

Figure 6.11. State diagram of simultaneous two-phase flow (water/squalane system) through a 2.5D porous medium as a function of Ca_w and Ca_{nw}. The curve signifies the transition from connected systematic flow to disconnected random flow.

(a)

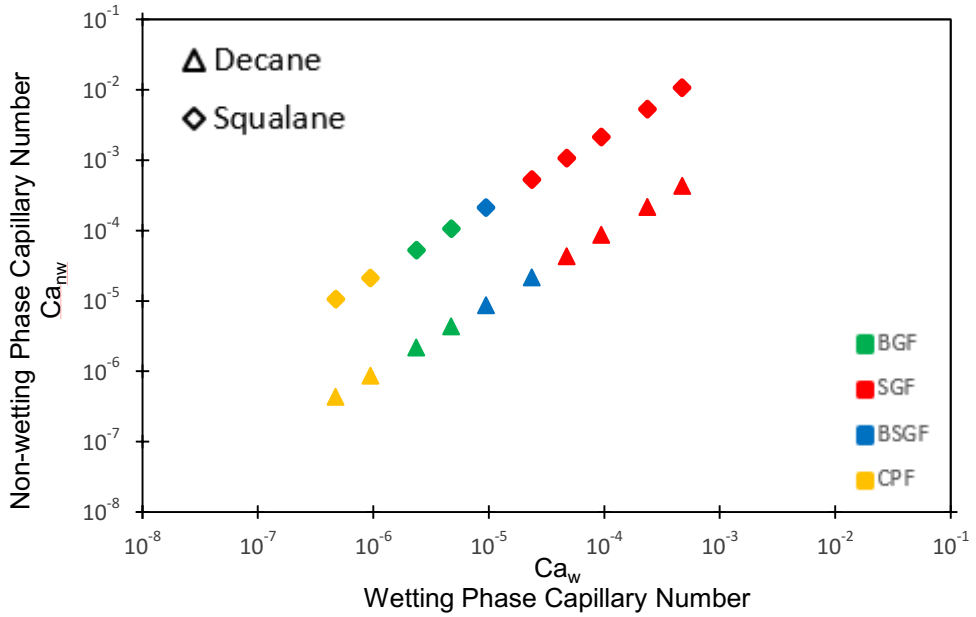

(b)

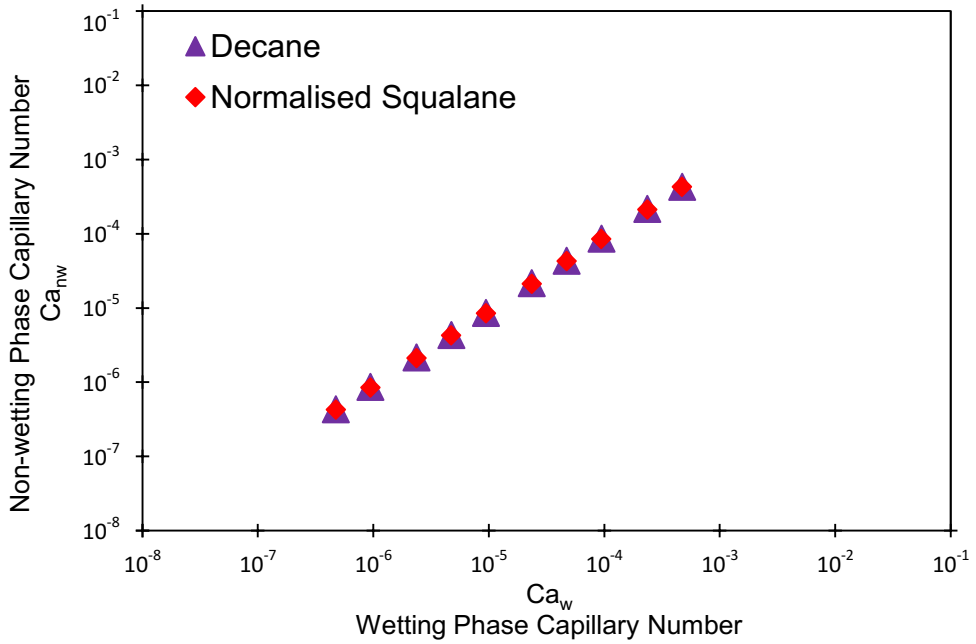

Figure 6.12. State diagram of simultaneous two-phase comparing water/decane system to the water/squalane system. The capillary number for squalane was normalised by the viscosity ratio between squalane and decane.

The small ganglia flow regime domain shifts to higher values of capillary number as the viscosity ratio decreases. This is better shown from the state diagram in Figure 6.12a (In Figure 6.12b, the capillary number for squalane was normalised by the viscosity ratio between decane and squalane) which directly compare the

water/decane and the water/squalane systems. At high viscosity ratio, big oil blobs split more easily to form smaller ones and the small blobs become more prevalent with an increase in capillary number. This is why the small ganglia flow regime starts early ($Ca_{nw} > 10^{-6}$) for the water/decane system. The flow during the CPF and the BGF regimes are systematic and orderly, i.e. the non-wetting phase flow in stable regular pathways. Even during the BGF regime when the non-wetting phase is no longer connected, the big oil blobs flow through unchanging pathways in a well-ordered manner. On the other hand, the flow of the non-wetting phase during the BSGF and the SGF regimes were very random. Oil blobs movements were very erratic and their pathways change often, especially during the SGF regime.

6.3.3. Dynamic fluid connectivity at the pore scale

The stable non-wetting phase connection observed in the connected pathway flow regime at very low flow rates was also reported by *Reynolds et al. (2017)* [42] in their two-phase flow experiments in a Bentheimer sandstone using X-ray imaging. However, at intermediate capillary numbers, before the transition to ganglia flow, the connected pathways in their experiment were unstable and fluctuated in both position and volume over time. This variation in the non-wetting phase pathway at low flow rate was reported to be as a consequence of splitting an initially connected non-wetting phase into two separate large ganglia. However, parts of this disconnected pathway repeatedly connect and disconnect, changing the position of the connected pathway in the pore space [42]. This break-up of the non-wetting phase at low flow rate was also reported in the critical capillary number study of two-phase flow by *Armstrong et al. (2014a)* [267]. Although, the flow of the non-wetting phase in their experiment was neither through a connected pathway nor through moving blobs. Rather, flow was through snap-off and re-connection events causing a fluctuation kind of connectivity, especially close to the percolation threshold of the non-wetting phase [267].

However, these connection-disconnection events (dynamic connectivity) were not observed in our water/decane and water/squalane experiments, probably because of experimental constraint brought about by the two-dimensional nature of the micromodel. The dynamic connectivity was observed by *Reynolds et al. (2017)* [42] was at a non-wetting phase capillary number of 10^{-8} and 10^{-7}, and the wetting phase

capillary number of 10^{-7} and 5 x 10^{-6} (Although, we do not expect the transitions to be at the same capillary numbers in our study since the pore structures are different). These capillary number values were not attainable in our experiments because the micromodel cross-sectional area is too small. Another possibility for this different outcome might be the choice of the two phases (i.e. the large viscosity contrast) or the more realistic better-connected three-dimensional porous media (rock) used by *Reynolds et al. (2017)* [42].

Table 6.4. Phase, Dynamic Viscosity, Viscosity Ratio, and Non-wetting phase/Wetting phase Interfacial Tension

Phase	Dynamic viscosity 20°C (cP)	Wetting phase to non-wetting phase viscosity ratio	Interfacial tension (mN/m)
Potassium Iodide	0.6422		
Nitrogen	0.0208	30.88	64.0

Interfacial tension of potassium iodide + Nitrogen, the dynamic viscosity of both potassium iodide and nitrogen are from *Reynolds et al. (2017)* [42].

Table 6.5. List of experiments for KI/N_2 system at different total flow rates with a constant fractional flow rate (0.5)

Experiment	Total flow rate, Q_T (uL/min)	KI flow rate, Q_w (uL/min)	N_2 flow rate, Q_{nw} (uL/min)	Wetting phase capillary number, Ca_w	Non-wetting phase capillary number, Ca_{nw}
1	0.2	0.1	0.1	2.48 X 10^{-7}	8.03 X 10^{-9}
2	0.4	0.2	0.2	4.96 X 10^{-7}	1.61 X 10^{-8}
3	1.0	0.5	0.5	1.24 X 10^{-6}	4.01 X 10^{-8}
4	2	1.0	1.0	2.48 X 10^{-6}	8.03 X 10^{-8}
5	4	2.0	2.0	4.96 X 10^{-6}	1.61 X 10^{-7}
6	10.0	5.0	5.0	1.24 X 10^{-5}	4.01 X 10^{-7}
7	20	10.0	10.0	2.48 X 10^{-5}	8.03 X 10^{-7}
8	40	20.0	20.0	4.96 X 10^{-5}	1.61 X 10^{-6}
9	100	50.0	50.0	1.24 X 10^{-4}	4.01 X 10^{-6}
10	200	100.0	100.0	2.48 X 10^{-4}	8.03 X 10^{-6}

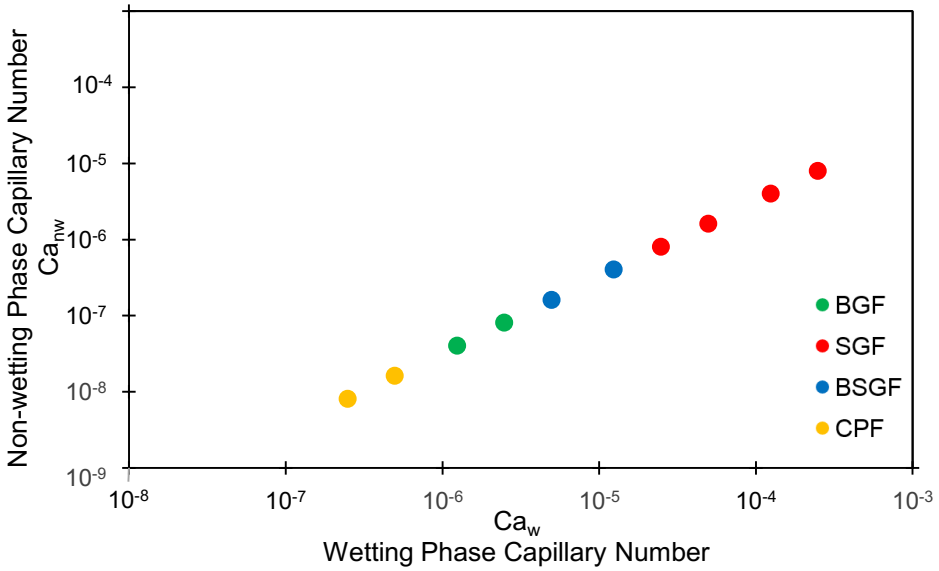

Figure 6.13. State diagram of simultaneous two-phase flow (KI/N_2 system) through a 2.5D porous medium as a function of Ca_w and Ca_{nw}.

Therefore, the former reason was investigated by using the same pair of fluids used in the *Reynolds et al. (2017)* [42] experiment, i.e. 1.5mol.kg^{-1} potassium iodide (KI) brine as the wetting phase and air (N_2) as the non-wetting phase. The properties of these fluids and the list of experiments at a constant fractional flow rate of 0.5 are shown in table 6.4 and 6.5 respectively.

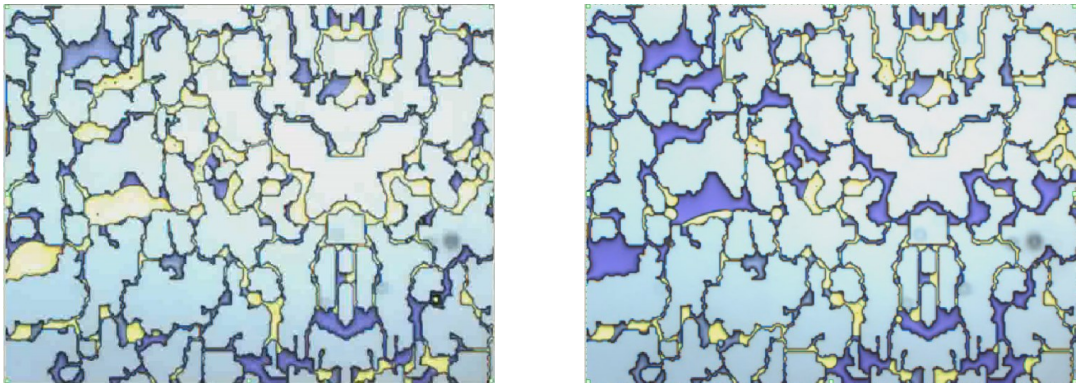

Figure 6.14. 5x magnification lens image of (a) connected pathway flow regime (Ca_{nw} = 8.03 X 10^{-9} and Ca_w = 2.48 X 10^{-7}) and (b) disconnected -ganglia flow regime (Ca_{nw} = 1.61 X 10^{-8} and Ca_w = 4.96 X 10^{-5}). The non-wetting phase, N_2 is colourless (although it appeared as yellow in the images) while the wetting phase, KI is blue (dyed with Methyl Blue).

Some of the images from the KI/N_2 system experiment are shown in figure 6.14. The quantitative results (the state diagram for the KI/N_2 is shown in figure 6.13) from the experiments were similar to those of the water/decane and water/squalane systems. The four flow regimes earlier described were identified albeit with fewer ganglia in the –ganglia flow regimes due to the large viscosity contrast. However, the dynamic connectivity phenomenon was still not observed in this system. Therefore, it can be concluded that the viscosity contrast alone was not the cause of the dynamic events reported by *Reynold et al. (2017)* [42].

6.4. Conclusion

The co-injection of a wetting phase and a non-wetting phase at steady-state was studied experimentally in a transparent Berea sandstone patterned micromodel using visual imaging. The capillary-viscous balance of the flow was altered by increasing the total flow rate of the system in a step-wise manner, while the geometrical and topological parameters of the model porous medium were kept constant. Also, a pair of different viscosity oil phases and Nitrogen gas (N_2) as the non-wetting phase were used to investigate the effect of viscosity ratio on the flow regimes. The micromodel used for all the experiments are water-wetting and the flow history in all the experiments was drainage.

The flow dynamics at the pore-scale (and/or Darcy-scale) and the flow regimes were observed under steady-state conditions. During the co-injection of the wetting phase and non-wetting phase, the non-wetting phase is disconnected in the form of oil blobs while the wetting phase is connected throughout the porous medium by a combination of connected pathways and corner wetting films. Although disconnected, especially at high flow rates, the non-wetting phase flow mainly through the movement of ganglia. On the Darcy scale, the non-wetting phase flow is often chaotic and random, while the flow seems more uniform on the macroscopic scale.

Based on the connectivity, the mean-size and prevalence of the non-wetting phase blobs for all the fluid pair studied, four main flow regimes have been identified, i.e. connected pathway flow regime, big ganglia flow regime, big-small ganglia flow regime and small ganglia flow regime. The mean size of the ganglia corresponds to the

capillary number values of the system, hence the flow regimes move from the connected pathway to small ganglia as the total flow rate is steadily increased. The domain of the big ganglia flow regime increases (and/or small ganglia flow regime decreases) with a decrease in the viscosity ratio of the system. Also, the boundaries of neighbouring flow regimes are indistinct and each regime slowly changes into its neighbour as the flow rate was changed.

The dynamic non-wetting phase connectivity reported in two-phase flow experiments in real 3D porous media (rocks) was not observed in this micromodel experiments even after replicating the experiment with the fluid pair used in the real porous media experiment. It is also possible that the constant etch depth of the micromodel used in this study does not provide a range of entry capillary pressures large enough for the fluids for the dynamic connectivity to occur, i.e. the micromodel is not representative enough of a well-connected three-dimensional porous media. Therefore, it would be important to design and fabricate an improved micromodel with multiple depths to further study this phenomenon. It will be equally important to elucidate this dynamic connectivity phenomenon using computer simulations. Hence, the design of the multi-depth micromodel, as well as the computer simulation of flow during steady-state two-phase co-injection using Lattice Boltzmann Methods (LBM), will be discussed in the next chapter.

7. Lattice Boltzmann Simulation of Dynamic Connectivity at the Pore Scale during Two-phase Flow, and the Design of a Multi-depth Micromodel

To complement the experimental study in chapter 6, in this chapter, we used computer simulations to study the displacement dynamics that occur during steady-state two-phase flow in a geometry reproducing a part of the experimental micromodel and also a new, multi-depth geometry that could not be fabricated in time for this project. We also laid out the design of a multi-depth micromodel that could be applied to further study displacement dynamics in model porous media in the future.

7.1. Introduction

The many applications of multiphase flow in porous media have been mentioned in the experimental study in the previous chapter. Here, we use computer simulations to further investigate and validate the observations reported in the previous chapter. There are three main reasons to use computer simulations to study a process: First, it can provide access to parameters that are impractical, or impossible, to obtain in the experiments such as the spatial pressure field around an event. Secondly, it can be used to explore behaviour in synthetic geometries not available in laboratory experiments. Thirdly, it can be used to further validate experimental observations. In chapter 6 it was concluded that one of the reasons why there was a discrepancy between observations in natural rocks and the results from our micromodel experiments was because of the micromodel's single depth. Therefore, it's a good idea to repeat the experiments with a multi-depth micromodel.

There is also a section in this chapter on how to design and fabricate a physical multi-depth non-repeat pattern micromodel. However, fabrication of the complete physical model was not possible in the time available for experiments and only prototypes of small regions of the model were produced. Hence, we cannot rely only on the

experimental observations in chapter 6 to bridge the knowledge gap in our understanding of the dynamic processes that occur in the subsurface especially at the pore-scale. This is why we are using computer simulations to complement, enhance and extend the parameter space investigated in our efforts to better understand multiphase flow in porous media. There are basically two ways to compute fluid flow in porous media: there is a direct modelling approach and there is an approach based on network modelling [172].

Direct modelling approaches (computational fluid dynamics (CFD) models) simulate flow processes by computing flow and transport mainly using Cartesian grids derived from binarised three-dimensional images. Examples of this modelling approach are the technique known as the lattice Boltzmann method (LBM) and the volume of fluid technique [268-271]. Also, there are other direct numerical simulations like finite element type and finite volume type that are not built on Cartesian grids but on unstructured meshes. This approach has the advantage of retaining as much information as possible on the geometry of the pore space but at the cost of extensive computing time and limited system size. On the other hand, network modelling approaches simulate flow by first extracting an ideal topological representative network from the original image before analytically computing flow and transport through the bonds of the network. The first network models were constructed more than six decades ago using the similarity between a random resistor network and flow in porous media [197]. Other examples of this modelling approach are grain-based pore-network modelling [272], pore-network models based on the resolution of the macroscopic reactive transport equation between the nodes of the network [120], and pore-network models based on two-dimensional micromodel laboratory experiments [163].

These two modelling methods both have advantages and disadvantages which will not be extensively discussed here. For a broad review of fluid flow and transport modelling at the pore scale, refer to *Blunt et al. (2013)* [172]. However, since our aim is to simulate a dynamic process, a direct numerical simulation approach will be used for this study. This is because the majority of the mathematical network models are quasi-static models (with no explicit representation of time), where only the order of pore fillings are calculated and the fluid interfaces are assumed to be static. Although, dynamic network models do exist, however, they all involve radical simplification of the

geometry used to represent the pore space, so, given that we do not know the origin of the dynamic intermittent connectivity events, they are not suitable for our study. Therefore, the lattice Boltzmann method, a direct dynamic modelling approach will be used to simulate the fluid flow and transport in this study.

7.2. Lattice Boltzmann Method for Fluid Flows

The lattice-Boltzmann method (LBM) is a numerical system for simulating fluid flow and transport in porous media. The LBM is particularly effective in simulating multiphase flow applications involving interfacial dynamics, thermodynamics and complex geometries and boundaries [269]. While most traditional numerical models are based on the discretization of macroscopic continuum equations, the lattice-Boltzmann method is based on microscopic models and mesoscopic kinetic equations. In essence, the lattice-Boltzmann method uses simplified kinetic models that include important microscopic and mesoscopic processes in order for the macroscopic averaged properties to obey the desired macroscopic equations. This is based on the fact that macroscopic dynamics are usually independent of the underlying details in microscopic physics and are also a collection of the behaviour of many microscopic particles in the flow. For a comprehensive look at the fundamentals of the lattice-Boltzmann theory and lattice-Boltzmann method for fluid flow, refer to Succi (2001) and Chen and Doolen (1998) [269, 273].

The lattice-Boltzmann method can be used to investigate a wide range of phenomena encountered in the multiphase flow in porous media. For example, Boek and colleagues have used the LBM on a variety of multiphase flow investigations including; two-dimensional lattice-Boltzmann simulations were used to investigate viscous fingering of two immiscible fluids using the Shan-Chen model [67], Haines jumps dynamics and capillary filling [268], reactive transport [274], and fluid flow in two-dimension micromodels [275, 276]. While there are many approaches to using LBM for direct simulation of two-phase flow in porous media, the approach used in this study is the Free Energy Lattice Boltzmann Method.

7.2.1. The Free Energy Lattice Boltzmann Method

The free energy lattice Boltzmann method is an extension of the numerical approach first introduced by *Swift et al. (1995)* [277]. The free energy LBM's algorithm belongs to a class of hydrodynamic models, known as *diffuse interface models* [278, 279], where the fluid-fluid interface has a finite size [279, 280]. Typically, in a square cross-section, around 15 lattice units are used to represent the minimum pore space to allow the interface to obtain the correct curvature [279]. Far away from a contact line, the method solves the hydrodynamic equations of motion of the fluid, i.e. the Navier-Stokes equations and the continuity equation, using a multiple-relaxation time methodology. The codes used for the simulation were written and compiled by Ioannis Zacharoudiou (a post-doctoral researcher in my research group). For a detailed review of the lattice Boltzmann method, refer to Ioannis' PhD thesis [281].

7.3. Results and Discussion

7.3.1. Single-depth geometry simulations using LBM

The simulation was done on one repeat unit geometry of the Berea-pattern micromodel (described in chapter 6) mirrored once in the direction of flow. This was the maximum geometry volume on which it was practical to do the simulations. Computing flow in the whole experimental geometry using the lattice Boltzmann method simulations was too computationally expensive. For example, it took approximately two months for the low capillary number (Ca_{nw} = 8.6 X 10^{-7} and Ca_w = 3.7 X 10^{-7}) simulation to reach breakthrough, running on two P100 Graphics Processing Units (GPUs). The capillary entry pressure of the pores was correctly resolved by doing preliminary simulations. The minimum throat of the simulation geometry was found to be 8 by 50 lattice units to allow the interface between the two phases to bend and obtain a curvature that matches the theoretical prediction of the entry pressure. Two reservoirs are added on each side of the matrix for uniform fluid injection and production. To prevent slug flow conditions at the inlet, the two phases were injected at a number of alternating points in the inlet reservoir as shown in figure 7.1. The total points totalled 38200 in number in the Y*Z direction (1528 in the y-direction and 25 in the z-direction). This minimised slug flow to approximately 0.05cm (~ 14% of the total length of the matrix) into the matrix even for the lowest flow rate

experiments. A periodic boundary condition was imposed on the edges of the matrix while there is continuous flow into the matrix from the inlet reservoir, and outflow from the outlet reservoir.

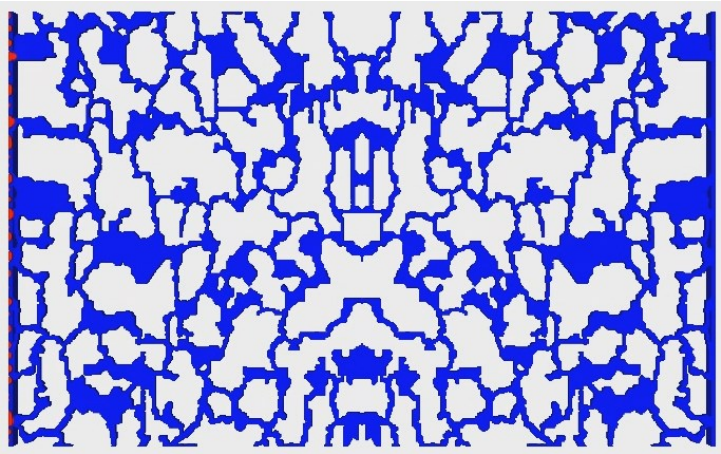

Figure 7.1. Snapshot of simulation geometry showing the alternating point source phase injections into the inlet reservoir. The wetting phase is water (blue) and the non-wetting phase is decane (red).

The wetting and non-wetting phase pair for the simulation is deionized water (in blue) and decane (in red) respectively, and the porous media is water-wetting, with a contact angle of 30^{o} and a depth of 25um (corresponding to 50 lattice units). More explicit information on the lattice Boltzmann parameters used to represent the fluids is explained in sections 3.2, 3.3, and 4.1 of Ioannis' PhD thesis [281]. Just like in the experiment, the pore space was initially filled with water, followed by co-injection of both phases at a constant fractional flow rate of 0.5. A snapshot from one of the videos from the simulation is shown in figure 7.2. Views from different angles from a subsection of the snapshot are blown out to highlight the three-dimensional nature of the flow, as well as the curvature of the invading non-wetting phase at the interface in a pore filled with the wetting phase. Comparing the simulation results with the experimental results presented in the previous chapter, the flow regimes and displacement processes in the experiment are well matched in the simulation.
Simulations were run with an initial inlet velocity ranging from 2.5 x 10^{-6} to 5 x 10^{-4} m^3/s for both the wetting phase and the non-wetting phase.

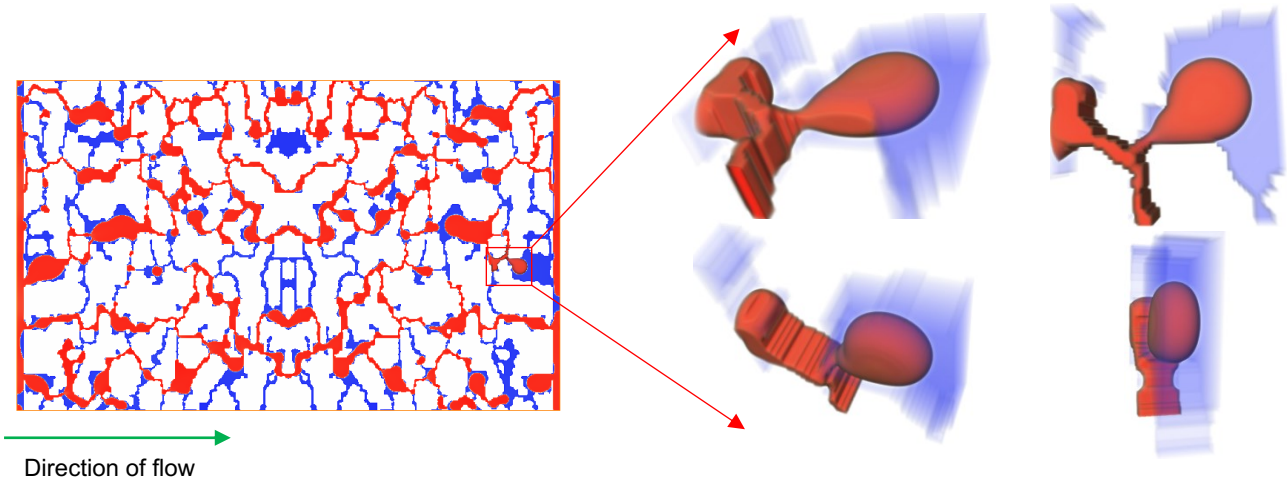

Figure 7.2. A snapshot of one of the videos from the simulation, with a blow-out of the invading phase. The wetting phase is water (blue) and the non-wetting phase is decane (red).

The average velocity of each of the phase after the saturation of both phases converges was then used to compute the capillary number of both phases. Based on the connectivity of the non-wetting phase and the mean size, and prevalence of the non-wetting phase; four flow regimes were identified in the simulation as well, depending on the initial inlet velocity of both phases. These comparison with the experimental results presented in the previous chapter validates the lattice Boltzmann simulation. However, the prevalence of small ganglia in the small ganglia flow regime is much lower in the simulation. This is because the free energy lattice Boltzmann method used to simulate the flow is a diffuse interface method, where the sharp-interface formulation is replaced with a continuous variation of an order parameter over a finite-sized interfacial region. The interface (transition from phase 1 to 2) has a finite size of about 5 lattice units. Therefore, one must be careful in directly comparing the simulation to the laboratory experiment where this transition takes place at a much smaller length scale. One way of resolving this problem would be to increase the system size so that the ratio of the interface width to the characteristic length scale of the system (e.g. average throat diameter) becomes very small (ideally < 1/10). In practice, this would further increase the computational load of the simulation.

Another reason for the low amount of small ganglia in the simulation result of the small ganglia flow regime is that in the lattice Boltzmann method (whether phase-field methods or diffuse interface methods), the energy balance does not favour the formation of small ganglia. The flow evolves to decrease the overall free energy of the

system, but the volume of each phase is not strictly conserved. This leads to a problem: the small ganglia formed will dissolve in the surrounding majority phase, as the system prefers to pay a small penalty cost associated with the dissolution of the smaller droplet (and the consequent shift in the value of concentration away from the equilibrium value) rather than having an increased energy by introducing new interfaces.

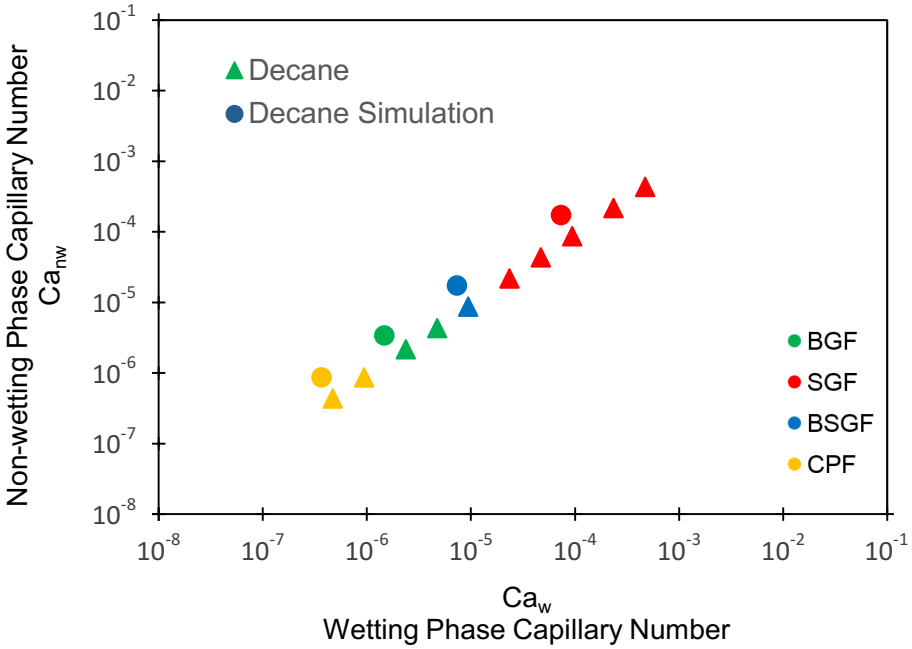

Figure 7.3. State diagram of simultaneous two-phase comparing the lattice Boltzmann simulation results to the experimental results for water/decane system.

A direct comparison of the simulation and laboratory experimental results from chapter 6 are presented on the state diagram in figure 7.3. The offset in the capillary states between the simulation and experiment is due to the different definitions of the capillary number used in their computations. While the laboratory experimental values were computed using average velocity based on injection flow rates and porosity, the simulation values were computed using the actual average fluid velocity as measured in the simulations (this is not readily accessible in the laboratory experiment). Also, snapshots from the simulation videos are directly compared with the corresponding videos from the experiment (experimental snapshots are from figure 6.8) as shown in figure 7.4. The dynamic connectivity phenomena were not readily observed in the

simulations in the range of capillary number explored. Also, the capillary number range of the transition between flow regimes is similar in both simulation and laboratory experiment.

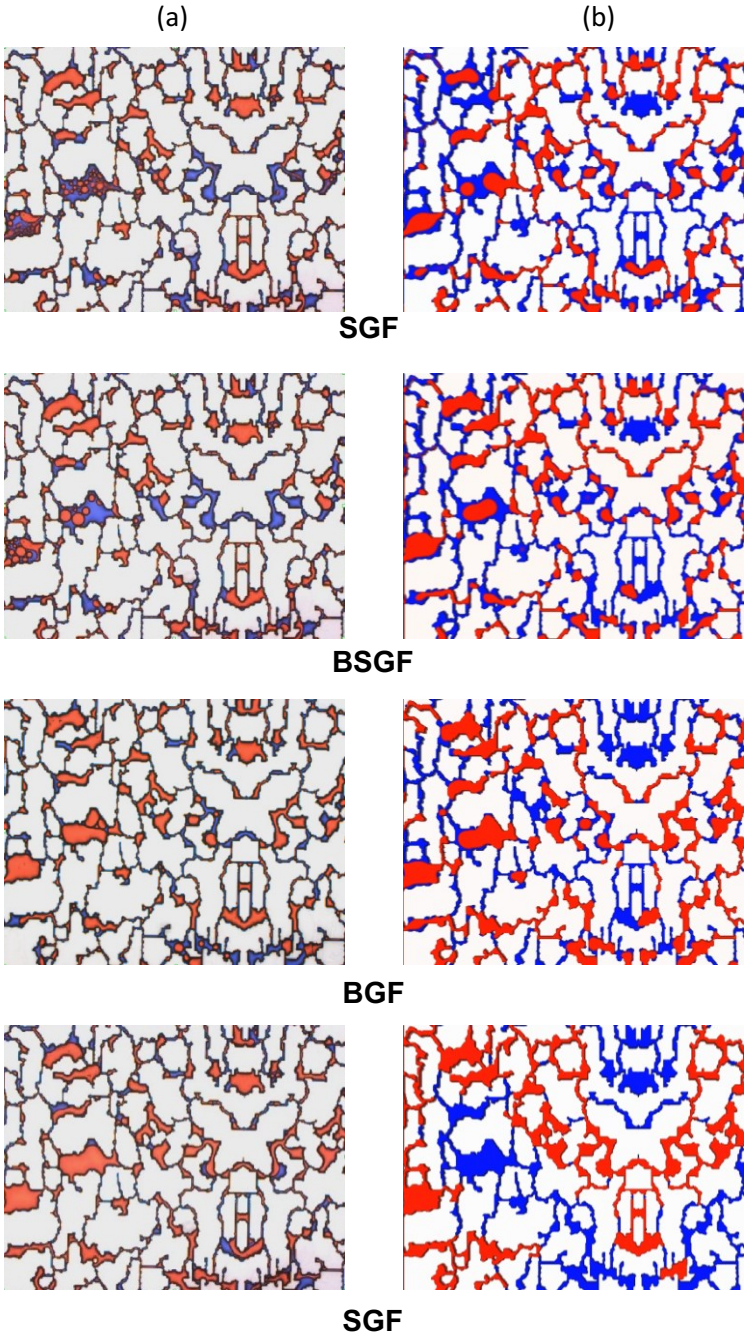

Figure 7.4. Snapshots of each of the flow regimes from (a) laboratory micromodel experiments, (b) lattice Boltzmann computer simulations, CPF (Ca_{nw} = 8.6 X 10^{-7} and Ca_w = 3.7 X 10^{-7}), BGF (Ca_{nw} = 3.4 X 10^{-6} and Ca_w = 1.48 X 10^{-6}), BSGF (Ca_{nw} = 1.72 X 10^{-5} and Ca_w = 7.39 X 10^{-6}), and SGF (Ca_{nw} = 1.72 X 10^{-4} and Ca_w = 7.39 X 10^{-5}).

At high capillary numbers (small ganglia flow, SGF), there are only a few small droplets of the non-wetting phase in the simulation. This is a known artefact of the lattice Boltzmann simulation technique used as already explained above [280]. However, even at low capillary number (connected pathway regime, CPF), the phases are more segregated in the simulation than in the laboratory experiment, i.e. spatial distributions of the phases at low capillary number are quite different. The main reason for this is because the simulation was done on a single-mirrored repeat unit of the micromodel matrix. That is, the simulation geometry was chosen to represent a section of the physical micromodel with an identical geometry. However, in the physical micromodel, the section of the geometry where the camera is focused on is surrounded on all sides by more and more geometry. In the simulations, the geometry is a single-mirrored repeat unit bounded on both sides by a reservoir. Hence, the boundary conditions are different. However, that aside, the transition between flow regimes were still happening in the same way, and the capillary number range that falls between a particular flow regime is similar in both simulation and laboratory experiment.

7.3.2. Multi-depth geometry simulations using LBM

Comparison of the results from the computer simulations in the single-depth geometry to the results of the laboratory experiment in the single-depth micromodel validates the lattice Boltzmann simulation. Therefore, the lattice Boltzmann simulation was used to predict the behaviour of the flow in a multi-depth model, since a physical multi-depth micromodel could not be fabricated in time for this research. The single-depth pore space geometry was redesigned into a multi-depth geometry in Avizo 9.1. The pore spaces were eroded twice by 16 pixels each time and three depths of 16μm, 32μm and 48μm were assigned to the pore spaces, depending on the distance from the pore walls. All pore spaces with a diameter greater than 64μm will have three depths, and the deepest section will be the centre of the pore space with a depth of 48μm. An intermediate depth (32μm) surrounds the deepest section of the pore space, followed by a depth of 16μm in the region adjacent to the wall. The initial geometry of the whole pore space is shown in figure 7.5a, after one erosion, the remaining geometry is shown in figure 7.5b and next erosion leaves only the largest pore spaces as shown in figure 7.5c. The multi-depth geometry is shown in figure 7.6 with a blow-out of a section

clearly showing the three depths. Arrows of different colours are used to highlight the three depths; red arrow = 48μm, green arrow = 32μm, and yellow arrow = 16μm.

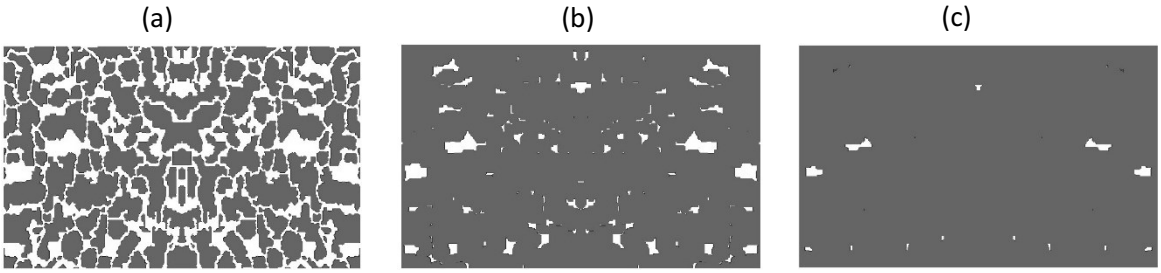

Figure 7.5. Images of the multi-depth geometry showing the (a) the pore spaces with three depths, (b) the pore spaces (with two depths) left after one erosion and, (c) the pore spaces (with one depth) left after the second erosion.

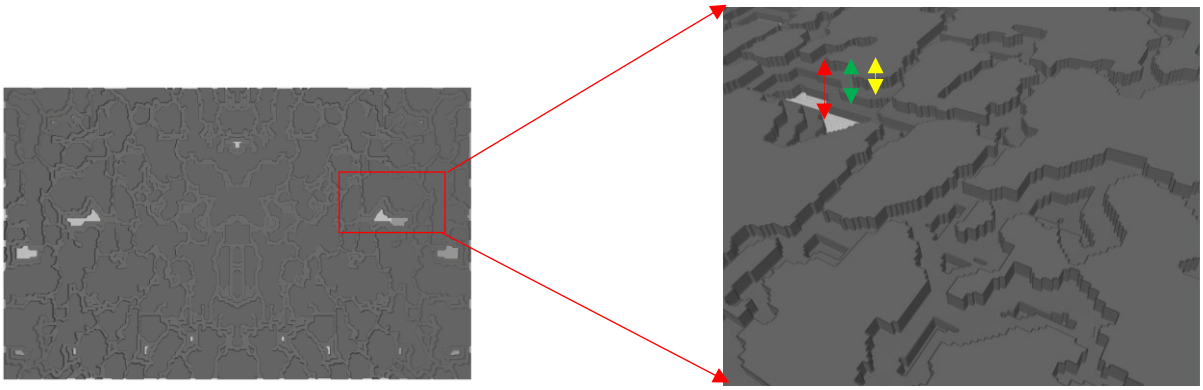

Figure 7.6. A snapshot of the multi-depth geometry, with a blow-out of a section, clearly showing the three depths.

The simulation procedure for the single-depth geometry was repeated for the multi-depth geometry with the same flow and boundary conditions. The multi-depth nature of the can be seen in the blow-out image in figure 7.7. The blow-out image is an underside of a section of the geometry that has three depths. The observations from the multi-depth geometry simulation were very similar to the single-depth geometry simulation presented in the previous section. The flow regimes and displacement processes are shown in the images in figure 7.8. However, there are some events in the intermediate inlet velocity flow rate simulation (Ca_{nw} = 2.7 X 10^{-6} and Ca_{w} = 1.42 X 10^{-6}), i.e. the big ganglia flow regime, that were close to being the dynamic connectivity events.

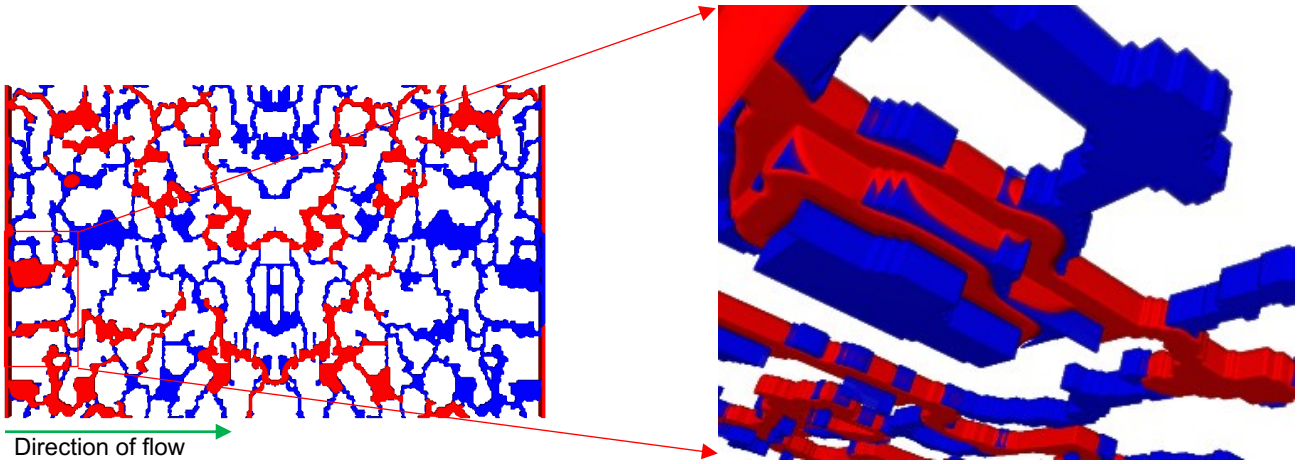

Figure 7.7. A snapshot of one of the videos from the simulation, with an underside blow-out of a section of the geometry, clearly showing the three depths of the pore space. The wetting phase is deionized water (blue) and the non-wetting phase is decane (red).

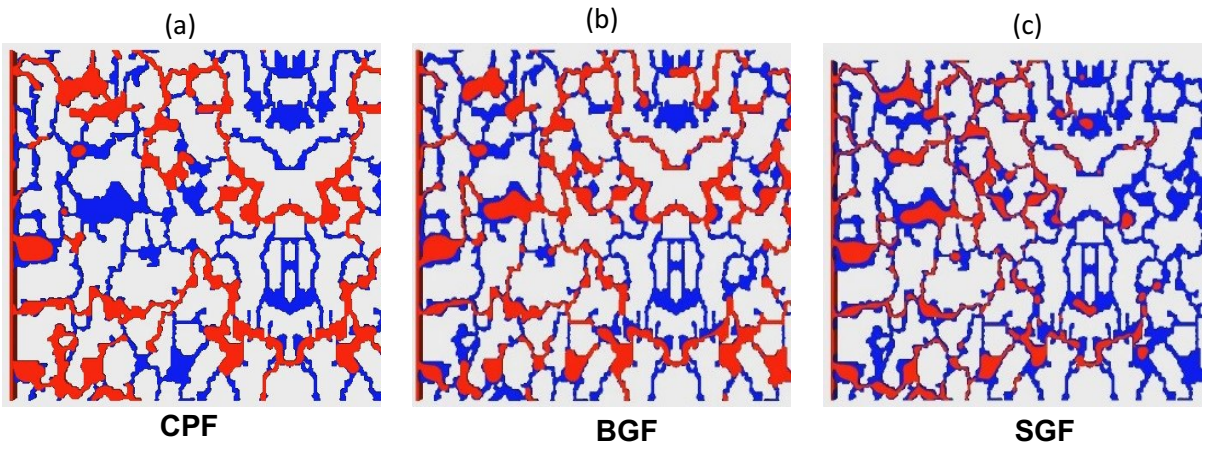

Figure 7.8. Snapshots of different flow regimes for the multi-depth geometry simulations CPF (Ca_{nw} = 8.1 X 10^{-7} and Ca_w = 2.9 X 10^{-7}), BGF (Ca_{nw} = 2.7 X 10^{-6} and Ca_w = 1.42 X 10^{-6}), and SGF (Ca_{nw} = 1.16 X 10^{-4} and Ca_w = 7.33 X 10^{-5}).

Since there is no clear definition of these dynamic connectivity events, a clear distinction between the ganglia flow regime and the connection-disconnection events cannot be made. A time sequence snapshot from the intermediate inlet velocity flow rate simulation is shown in figure 7.9. Two fairly stable ganglia, connecting and disconnecting at a small region (the region highlighted with a black circle in the snapshots) between them can be seen. This is not quite the same as the large stable blobs, bridged by an intermittent small volume of fluid reported in the literature [42].

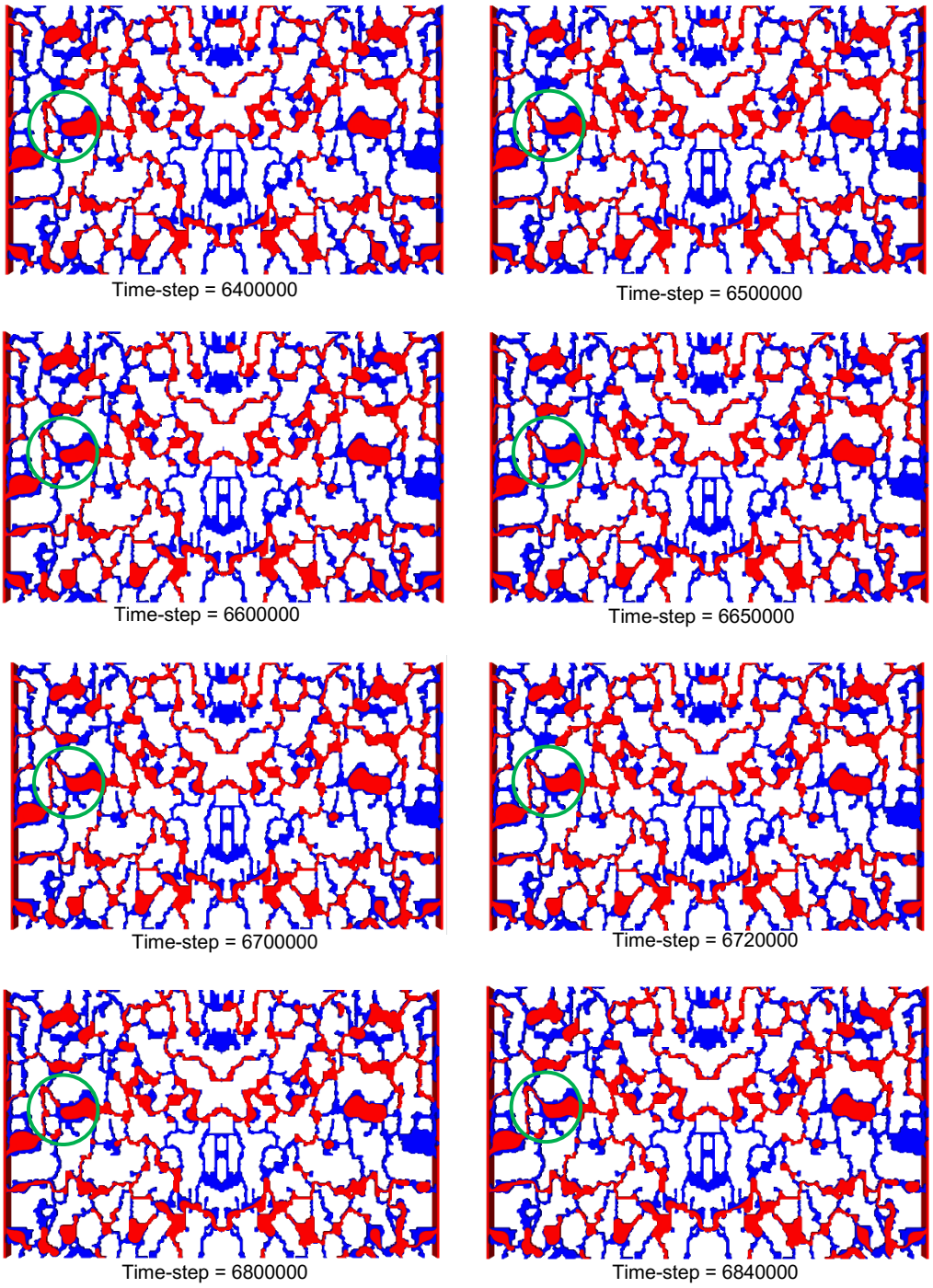

Figure 7.9. Time sequence snapshots of the intermediate inlet velocity simulation, regions of what appeared to be 'dynamic connectivity' are highlighted with green circles.

Therefore, our observation of transition straight to ganglia flow from connected pathway flow (CPF) in the laboratory experiment, the single-depth geometry LB simulations, and the multi-depth geometry LB simulations, is consistent. We cannot,

however, categorically assert that what is observed in the intermediate velocity simulation of the multi-depth geometry is the same as the dynamic connectivity reported in real rock experiments [42]. Hence, we propose that the dynamic connectivity phenomena have more to do with the better 3D connectivity of the real rocks against the micromodels.

7.4. Design of a Multi-depth Micromodel

A Bentheimer sandstone rock sample of dimensions 2.7 by 1.2cm was used for the design of the new non-repeat, multi-depth micromodel. Confocal laser scanning microscopy (CLSM)) was used to image the rock sample. However, before imaging with a confocal microscope, the sample needs to undergo some preparation. The pore space of the rock sample was vacuum impregnated with a low-viscosity, slow-curing epoxy doped with fluorescent Epodye. The impregnated rock sample was then ground and finely polished using the standard abrasive-polishing technique to obtain an optically planar surface. The Bentheimer rock sample, the Cast n' Vac 100 vacuum impregnation unit, the epoxy-impregnated sample, and the Buehler Auto-Met 300 automatic grinder and polisher are shown in the images in figure 7.10. More details on sample preparation can be found here [282, 283].

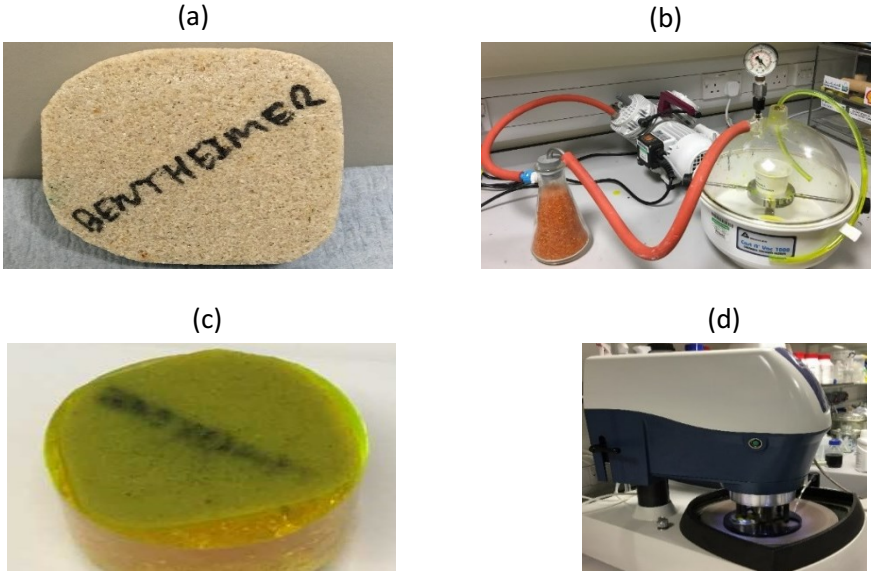

Figure 7.10. (a) The Bentheimer sandstone rock sample, (b) the Cast n' Vac 100 vacuum impregnation unit, (c) the epoxy-impregnated rock sample and, (d) the automatic grinding and polishing machine.

After polishing, the sample was then imaged with the confocal microscope, the raw image of the sample is shown in figure 7.11a, the raw image was then binarized using ImageJ, where the grey-scale values correlate to average atomic number values that provide contrast between the rock grains and the epoxy-filled regions. The black pixels represent corresponds to the rock grains while the white pixels represent the epoxy-filled pore throats and bodies in the binarized image in figure 7.11b. The binarised two-dimensional (2D) image was then modified by hand to erase areas of incomplete epoxy-impregnation. Unlike a 3D system, there is a lack of pore connectivity in a 2D image. Therefore, in order to preserve the porosity, permeability, and connectivity between the 2D image and a 3D system, isolated pores were connected by hand.

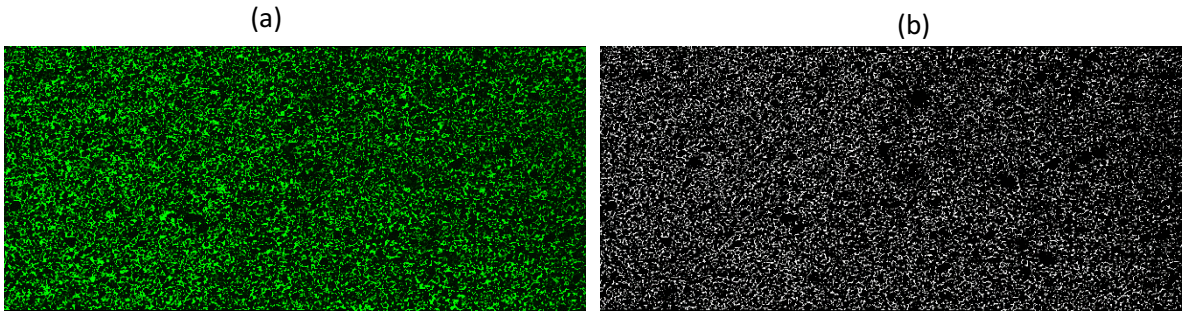

Figure 7.11. (a) The raw confocal image of the Bentheimer sandstone, (b) the binarized image.

The porosity was calculated to be about 16% in Image J, the grain size ranges from 10 to 1500μm, pore size ranges from 8 to 200μm, while the coordination number is between 1 and 5. The pore body size distributions of the matrix region are shown in figure 7.12b.

Vertical channels were added along the entire length of the inlet (injection) and outlet (production) sides of the micromodel. These channels enhance flow into the matrix by providing a linear boundary condition instead of a pointy boundary condition. There are many levels of branching at the inlet ports to break down the different phases before discharging into the fracture, see figure 7.12a. This is to ensure the oil and water enter the matrix as if they had come from another pore space similar in size to the pore spaces in the matrix.

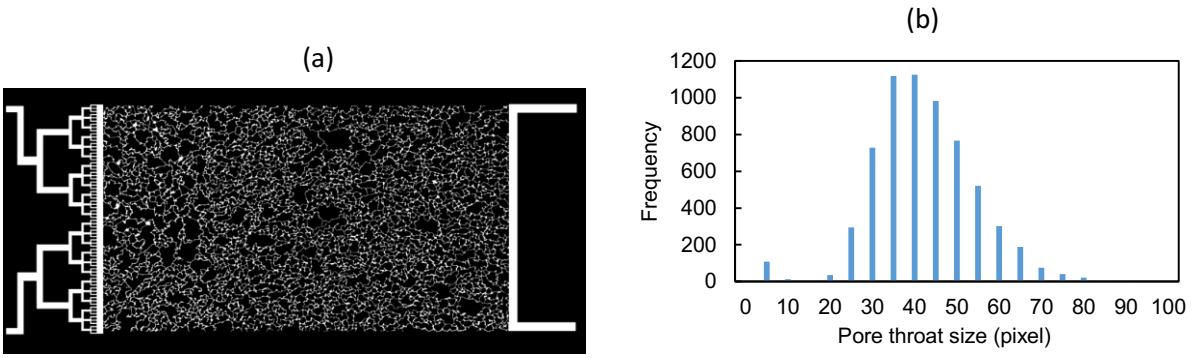

Figure 7.12. (a) The final 2D micromodel design, (b) the pore-size distributions of the micromodel.

To fabricate the micromodel, three depths, each of 10μm was chosen for the micromodel. The multiple depths will give the micromodel a wide range of capillary pressures better representative to simulate a real rock porous media than a single-depth micromodel. A small section of the micromodel, shown in figure 7.13a, was cut-out to be manufactured as a test sample.

Two different ways of fabricating the test sample were explored; the traditional etching method and fabrication by 3D printing. Both methods have relative advantages and disadvantages. While the traditional etching method is best for mass and long production runs, 3D printing is best for small, one-off production runs. Traditional etching method also offers a high material selection, unlike 3D printing where the material selection is much spaser. It is also important to mention that 3D printing does not always produce a perfect finish, surfaces of 3D printed items are not as smooth as surfaces of items manufactured by traditional etching methods. However, 3D printing will most probably improve in the future, and most of its disadvantages highlighted here will be remediated.

Since the intention was to fabricate a small section of the micromodel as a test sample, a high-resolution Nanoscribe 3D printer (Photonic Professional GT, resolution ~ 400nm) in the Computing Department was used for this purpose. An .STL file of the micromodel was generated in ImageJ from which a section of it was cut out to be printed as a test sample, see figure 7.13a. A screenshot of the .STL file of a smaller section of the test sample to be printed is shown in figure 7.13b, highlighting the multiple depths in 3D as read by the Nanoscribe's software. The test sample was printed using IP-Dip photoresist (from Nanoscribe) on a glass substrate. The glass slide has a thin a layer of ITO (Indium Tin Oxide) to find the interface between the

substrate and the resist. The printed structure was then cured with ultraviolet (UV) light. The printing of the test sample took about an hour and a half (30 minutes for setup, 30 minutes for printing, and another 30 minutes for developing), costing £186 (at £124 per hour).

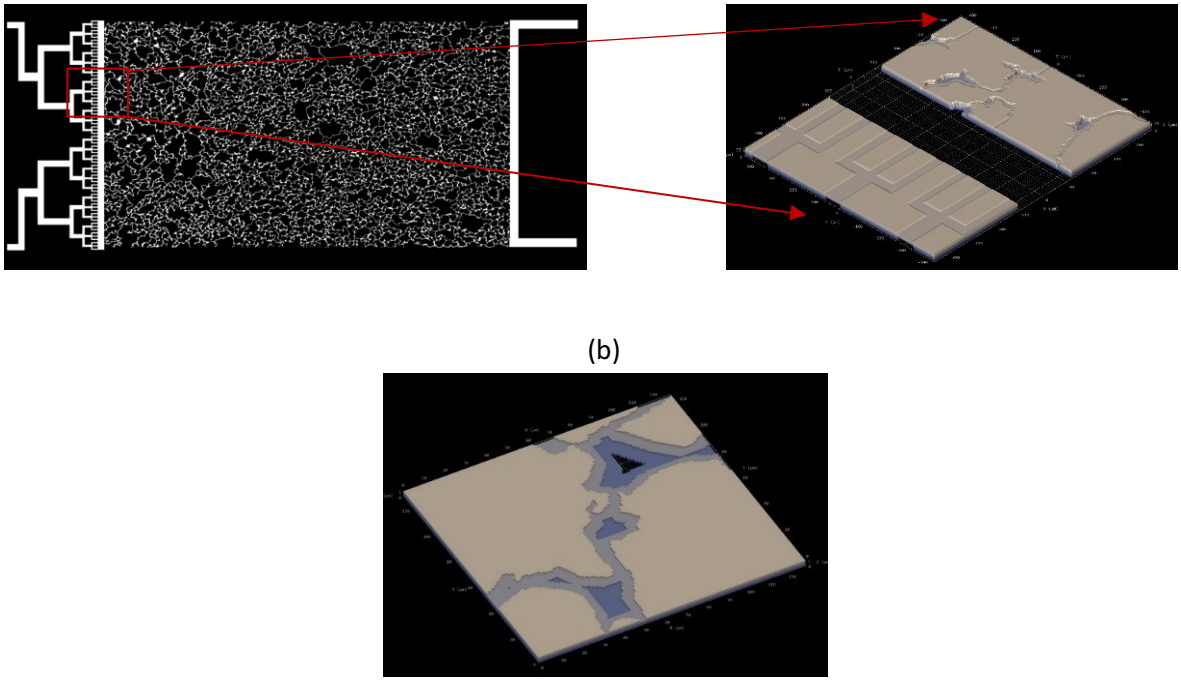

Figure 7.13. (a) A 2D binarised confocal image of the micromodel and a screenshot of the Nanoscribe's rendering of a section of the micromodel to be printed as a test, (b) the multiple depths are better highlighted here.

After printing, some validation checks were done on it using optical microscopy, scanning electron microscope (SEM) and vertical scanning interferometry (VSI), see the images in figure 7.14. Using the VSI imaging technique, the dimensions of the test sample were found to be off on the z-axis (the depths), the height (depth) of the test micromodel does not add up to 30µm. Since the test sample was printed using the *shell and scaffolding* method of the Nanoscribe 3D printer. And given the transparent nature of the test sample and the tiny features printed, this can interfere with light in unexpected ways, thus, we can't rule out optical interference for this discrepancy. Consequently, the sample was coated to block light and analysed with SEM imaging technique. The test sample looks much better in SEM than it did with VSI, so the problem must have been the transparency of the resist coupled with the fact that VSI

is an optical technique. However, from the SEM images, there appear to be lines on the large flat regions at regular intervals dividing the image into regular rectangles. These lines appear as a result of stitching this 'large' structure together because, in order to print at a reasonable rate, the sample was broken down to blocks of volume of 200μm^{-3} that overlap slightly to make the full, solid structure.

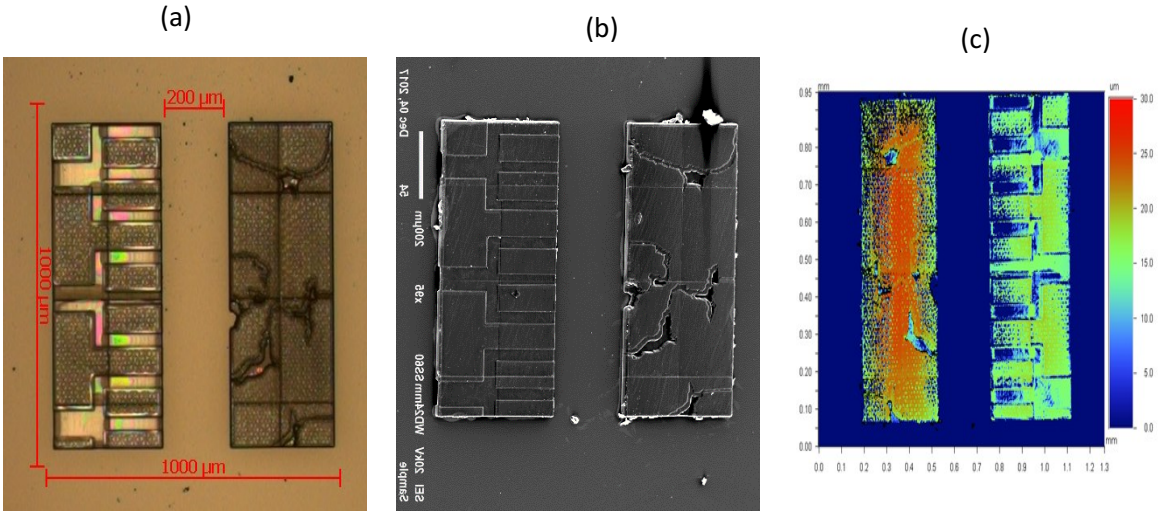

Figure 7.14. The micromodel test sample image with (a) inverted light microscope (ILM), (b) a scanning electron microscope (SEM), and (c) a vertical scanning interferometry (VSI).

After printing the test sample; to create an isolated flow path suitable for multiphase flow studies, a transparent cover will need to be attached to seal the face of the printed model. Hence, a large solid region around the pattern will be needed in order to make the seal with the cover. This will be prohibitively time-consuming with the Nanoscribe Photonic Professional GT. Because of the 3D printing artefacts, and due to the high time and money costs of 3D printing the entire micromodel (even without the large solid region needed to provide a coverslip, the entire micromodel is estimated to take about 48hours to print), it will be better to use established traditional micromodel manufacturing method of polymer etching. However, the 3D printing approach of fabricating microfluidic devices is promising and will be further explored in future work.

7.5. Conclusions

The laboratory experiment results presented in the previous chapter and the free energy lattice Boltzmann method (LBM) simulations presented in this chapter give similar transitions between flow regimes. However, the dynamic connectivity could not be readily and conclusively observed even after using a multi-depth geometry to run the simulation. This implies that the lack of conclusive dynamic connectivity in these experiments is the result of the 2D connectivity of the micro model rather than the restricted capillary pressure ratio between the pore bodies and throats although more work would be needed to definitively answer this question.

Also, we designed a multi-depth non-repeat micromodel based on a confocal image of Bentheimer sandstone rock. The multiple depths offer an extended range of capillary pressures, more representative of natural rock porous media. Apart from its microfluidics applications, this will be particularly useful in studies to understand the fundamental physical displacement processes encountered in multiphase flow in porous media." The use of 3D printing appears to be a promising approach to producing micro models with more flexibility as to geometry. However further development of the technique is required for it to be a practical approach for structures with micron resolution resembling rocks.

8. Conclusions and Future Work

A suite of micromodel experiments has been used to investigate fundamental multiphase flow phenomena at the pore scale. Two processes were considered; drying in micromodels representing fractured rocks where the fracture is maintained at low humidity and immiscible fluid displacement events during steady-state co-injection into the porous matrix. Fluid flow (and subsequent solid deposition in the case of the drying experiments) in optically transparent micromodels was imaged and observed in real-time using optical microscopy. The micromodels were based on thin section images of real rocks. All the experiments were conducted at ambient temperatures and pressures. Lattice Boltzmann simulations, initially compared to the experiments, were used to further study the dynamics of simultaneous two-phase flow in porous media in geometries unavailable in the lab. The conclusions, recommendations, and possible future work are presented below.

8.1. Conclusions

8.1.1. Drying in Porous Media in the Context of CO_2 Sequestration: Combined Evaporation and Salt Precipitation

Most previous evaporation experiments using artificial porous media have focused on single capillaries or sand packs. Here, the evaporative drying of brine and the associated salt deposition at different wetting conditions was investigated using a 2.5D etched-silicon/glass micromodel (based on a thin section image of a sucrosic dolomite carbonate rock). NaCl solutions from 0 wt% (deionized water) to 36 wt% (saturated brine) were evaporated by passing dry gas (air or CO_2) through a channel in front of the micromodel matrix (evaporative drying).

For deionized water, the three classical periods of evaporation were observed: the constant rate period (CRP) in which liquid remains connected to the matrix surface, the falling rate period (FRP) and the receding front period (RFP), in which the capillary connection is broken and water transport becomes dominated by vapour diffusion. The

length of the deionized water CRP was much shorter for a uniformly oil-wet model as a consequence of the early breaking of the liquid connection to the external surface of the matrix, but mixed wettability made little difference to the drying process as the liquid remained connected through the water wet corners of the micromodel.

For brine systems at all wetting conditions, the dry area became linear with the square root of time after a short CRP. However, unlike the case of deionized water which is due to capillary disconnection from the fracture channel, this is due to the deposited salt at the evaporating surface. Although the deposited salt does not completely block liquid transport to the surface because the deposited salt is porous. However, the area available for evaporation at the surface decreases with time due to continuous salt deposition. We can only infer the position of the evaporation by the appearance of salt, but we were not able to analyse this in enough detail to develop a model for the square root of time behaviour. We conjecture that the square root of time behaviour is due to the reduction of the wetted area where evaporation is happening, although this could not observe this directly.

For the water-wet model, two regions of a linear downward trend in the matrix and fracture permeability measurements after complete drying were observed as a function of initial brine concentration. A similar trend was observed for the mixed-wet systems. However, for the oil-wet micromodels, the fracture permeability only changes slightly even for 360g/L (saturated NaCl) brine, a result of the absence of salt deposits in the fracture, caused by the early rupture of the liquid wetting films needed to transport dissolved salt to the site of deposition. Overall, the matrix permeability decreased with increasing brine concentration for all wetting conditions and was almost total for the 360g/L brine. Finally, using CO_2 rather than air as carrier gas makes the liquid phase slightly more wetting, especially in the deionized water case, with the result that hydraulic connectivity was maintained for longer in the CO_2 case, compared to dry-out with air.

8.1.2. Multiphase Pore-Level Flow Dynamics in Porous Media

Since most pore-scale displacement processes are fast, and therefore, hard to capture with μ-CT techniques, direct optical visualization using a 2.5D micromodel based on a thin image of a Berea sandstone was used to investigate immiscible two-phase flow behaviour in porous media at steady state. The effect of viscosity ratio, flow-rate ratio

and capillary number on the flow regimes were investigated. More importantly, a new type of flow regime termed “dynamic connectivity” reported [42] in real rocks, at the boundary between stable connected pathway flow and ganglia transport was investigated. For most of the experiments, deionized water was used as the wetting phase while two different oil phases (Decane and Squalane) with different viscosities were used as the non-wetting phase.

For both systems (water/decane and water/squalane), at low flow rates, both phases flow in connected, unchanging pathways within the area of observation. This flow regime is known as connected pathway flow (CPF). By steadily increasing the total flow rates of the system, the (non-wetting) oil-phase starts to disconnect especially at constrictions, leading to big flowing oil blobs, termed big ganglia flow (BGF). At this stage, the non-wetting phase pathways are still stable but flow is by ganglia in some places. A further increase in the total flow rate leads to a decrease in the mean size of the oil ganglia, a mixture of big and small oil blobs is formed at this stage, termed big-small ganglia flow (BSGF). The big-small ganglia flow regime is particularly unique because as some small blobs coalesce to form big blobs, some big blobs are splitting into smaller blobs at constrictions, and these two processes are happening simultaneously and randomly within the area of observation. Increasing the total flow rate even further leads to the creation of smaller oil blobs (ganglia) that move rapidly and randomly through the micromodel. This flow regime is termed small ganglia flow (SGF). The low viscosity ratio of the water/squalane system makes the system attain steady state earlier and the overall flow is more systematic and orderly compared to the water/decane system.

The free energy lattice Boltzmann computer simulations were used to further investigate the dynamic connectivity phenomenon. A small fraction of the micromodel (a single-mirrored repeat unit of the micromodel) geometry was used for the simulations because simulation using the entire micromodel geometry was too computationally expensive. This led to a mismatch of boundary conditions between the simulations and the laboratory experiments. However, the results of the simulations in the single-mirrored repeat unit of the micromodel qualitatively matches what was observed in the laboratory experiments. The flow regimes were similar, and the transition between flow regimes occurred at similar capillary numbers.

Recently, a new flow regime (termed dynamic fluid connectivity) was reported in the literature from steady-state two-phase flow experiments in a Bentheimer sandstone [42]. This phenomenon has never been reported in any micromodel multiphase flow experiment (including this study), possibly because most micromodels have a single depth, and this means they have a restricted range of capillary pressures. Hence, we designed a new multi-depth micromodel (the multiple depths offer a wide range of capillary pressures representative enough to simulate a real rock porous media) to study this phenomenon (using lattice Boltzmann simulations). The results are however inconclusive as we do not readily observe the dynamic connection/disconnection events. We propose that the dynamic connectivity phenomenon have more to do with the better three-dimensional connectivity of the real rocks against the micromodels.

8.2. Recommendations

When trying to alter the wettability of a micromodel to be used for flow studies in which one of the fluids is water, the new technique reported in Chapter 5 should be used. This is because well-established wettability alteration techniques that rely on silane chemistry cannot be used because the silane will react with the water phase. Wettability alteration with crude oil cannot be used as well because this technique will render most parts of the micromodel opaque, making it impossible to observe flow processes in the porous system.

Regarding the new multi-depth micromodel fabrication, with the technology available presently, the cost of 3D printing of the whole micromodel designed in Chapter 7 is very high. Also, a technique for bonding the transparent cover to the printed micromodel would need to be developed. Hence, the conventional micromodel fabrication technique of etching silicon or glass micromodel materials is recommended for producing a multi-depth micromodel.

8.3. Future work

A major result of the drying experiment presented in this study is that the current explanations in the literature for a lengthy period in which the mass lost to evaporation is linear in the square root of time are not consistent with our micromodel observations

of the drying of brine. We speculate that an alternative mechanism is the development of growing dry patches on the outer surface of the porous medium. However, these could not be observed directly and we, therefore, did not develop a rigorous model base on this conjecture. It is trivial to write down a model leading to the square root time behaviour, a dry patch area that grows directly proportionately to the mass lost to evaporation would produce the desired result, but such a basis requires more direct evidence and that would be the subject of future work. A better spatial and time resolution imaging technique could be incorporated into the experimental set-up to provide more direct evidence of the growth of the outer surface dry patch. Obtaining a high-quality image is essential, but it might still not be adequate enough to directly observe the evaporation occurring from very thin films of liquid. It would be a good idea to seek some other parameter such as temperature that reveals the location of the evaporation without needing to resolve sub-micron films of liquid which are very difficult to see optically. The spatial distribution of small temperature changes on the evaporation surface could be observed by thermal imaging as a proxy for the location of evaporation.

Furthermore, an important motivation for the drying experiments is its application to the water desaturation and subsequent salt deposition that occur during CO_2 sequestration. Hence, it will be more realistic to perform experiments at reservoir conditions, and with saline aquifer brines and not just NaCl brine. The impact of salt precipitation on the permeability of the reservoir can be further tested on a larger scale for better optimization of the CO_2 sequestration process. One more possibility for future work would be to investigate the impact of an oil phase on the drying process. Also, the influence of the deposited salt (and surfactants) on the interfacial tension of the system would be interesting to investigate. There are conflicting reports in the literature on how the presence of salt affects the interfacial tension of a water-hydrocarbon system. Some reports that the presence of salt lowers the interfacial tension [284, 285] while some claim it increases the interfacial tension of the system [286, 287] . Thus, it would be important to shed more light on this relationship between and interfacial tension in a water/hydrocarbon system. This would complement the wettability study done here and have relevance for CO_2 EOR applications. A micromodel could be brought to residual oil saturation through a cycle of initial saturation with brine, the drainage with oil phase, and finally water imbibition before

starting the drying process and observing how the presence of a non-wetting oil phase impacts the transport of brine and evaporation.

Four flow regimes were identified in the two-phase co-injection experiments. These regimes were qualitatively validated by computer simulations using the free energy lattice Boltzmann method. However, more quantitative data from laboratory experiments and computer simulations are needed to accurately characterize these regimes. Also, the dynamic fluid connectivity phenomenon observed in real porous media experiments was not readily observed in our micromodel experiments, probably due to the single depth of the micromodel limiting the range of possible capillary entry pressures of the pores. This makes the micromodel less representative of a real porous media. A better-connected multi-depth non-repeat pattern micromodel has already been designed based on a confocal image of a Bentheimer sandstone. However, this new 'three-dimensional' micromodel is still restricted in 3D and only adds the multiple depth pore bodies. A new micromodel with more realistic 3D connectivity could be developed but this would probably require refractive index matching of all the phases to enable fast optical observations.

Finally, more complementary core scale experiments that will explore more rocks of different types and more flow conditions should be used to determine how general the dynamic connectivity event is. Likewise, more computer simulations can be used to further investigate the phenomenon. Simulations on a real 3D geometry (perhaps the CT scan of the rock sample used in the experiment in the literature [42]) could be used to further investigate the dynamic connectivity event.

References

[1] J. Gale *et al.*, "IPCC Special Report on Carbon Dioxide Capture and Storage, Working Group III of the Intergovernmental Panel on Climate Change," ed: Cambridge University Press, Cambridge, UK, 2005.

[2] H. Khatib, "Iea world energy outlook 2011—A comment," *Energy policy,* vol. 48, pp. 737-743, 2012.

[3] T. F. Stocker *et al.*, "Climate change 2013: the physical science basis. Intergovernmental panel on climate change, working group I contribution to the IPCC fifth assessment report (AR5)," *New York,* 2013.

[4] N. R. Council, *Advancing the science of climate change*. National Academies Press, 2011.

[5] T. Blasing and S. Jon, "Current greenhouse gas concentrations," *Updated February,* 2005.

[6] P. Tans and R. Keeling, "Trends in atmospheric carbon dioxide," *NOAA/ESRL & Scripps Institute of Oceanography, http://www. esrl. noaa. gov/gmd/ccgg/trends/(January 2012),* 2014.

[7] T. Boden, G. Marland, and R. Andres, "Global, regional, and national CO2 emissions," ed, 2009.

[8] T. Boden, Marland, G, Andres, RJ,. (2015). *Global, regional, and national CO2 emissions*.

[9] E. Alper and O. Y. Orhan, "CO2 utilization: Developments in conversion processes," *Petroleum,* vol. 3, no. 1, pp. 109-126, 2017.

[10] S. Bachu and J. Adams, "Sequestration of CO2 in geological media in response to climate change: capacity of deep saline aquifers to sequester CO2 in solution," *Energy Conversion and management,* vol. 44, no. 20, pp. 3151-3175, 2003.

[11] S. Bachu, "Sequestration of CO2 in geological media: criteria and approach for site selection in response to climate change," *Energy conversion and management,* vol. 41, no. 9, pp. 953-970, 2000.

[12] H. Herzog, E. Drake, and E. Adams, "CO Capture, Reuse, and Storage Technologies," Citeseer1997.

[13] I. P. o. C. Change. (2013, 13 April). *Methods for storing CO2 in deep underground geological formations.* Available: https://www.ipcc.ch/publications_and_data/graphics/jpg/large/Figure%20TS-07.jpg

[14] J. D. Figueroa, T. Fout, S. Plasynski, H. McIlvried, and R. D. Srivastava, "Advances in CO2 capture technology—the US Department of Energy's Carbon Sequestration Program," *International journal of greenhouse gas control,* vol. 2, no. 1, pp. 9-20, 2008.

[15] J. Orr, "Modelling of ocean storage of CO2---The GOSAC study," *Report PH4/37, International Energy Agency, Greenhouse Gas R&D Programme, Cheltenham, UK,* 2004.

[16] S. M. Benson and F. M. Orr, "Carbon dioxide capture and storage," *Mrs Bulletin,* vol. 33, no. 4, pp. 303-305, 2008.

[17] S. Bachu, "Screening and ranking of sedimentary basins for sequestration of CO 2 in geological media in response to climate change," *Environmental Geology,* vol. 44, no. 3, pp. 277-289, 2003.

[18] K. S. Lackner, "A guide to CO2 sequestration," *Science,* vol. 300, no. 5626, pp. 1677-1678, 2003.

[19] I. Cole, D. Paterson, P. Corrigan, S. Sim, and N. Birbilis, "State of the aqueous phase in liquid and supercritical CO2 as relevant to CCS pipelines," *International Journal of Greenhouse Gas Control,* vol. 7, pp. 82-88, 2012.

[20] I. S. Cole, P. Corrigan, S. Sim, and N. Birbilis, "Corrosion of pipelines used for CO2 transport in CCS: is it a real problem?," *International Journal of Greenhouse Gas Control,* vol. 5, no. 4, pp. 749-756, 2011.

[21] L. Carter, *Capture and storage of CO2 with other air pollutants*. IEA Clean Coal Centre, 2010.

[22] Y. Peysson, L. André, and M. Azaroual, "Well injectivity during CO2 storage operations in deep saline aquifers—Part 1: Experimental investigation of drying effects, salt precipitation and capillary forces," *International Journal of Greenhouse Gas Control,* vol. 22, pp. 291-300, 2014.

[23] L. André, Y. Peysson, and M. Azaroual, "Well injectivity during CO2 storage operations in deep saline aquifers–Part 2: Numerical simulations of drying, salt deposit mechanisms and role of capillary forces," *international journal of Greenhouse Gas Control,* vol. 22, pp. 301-312, 2014.
[24] M. Azaroual *et al.*, "Behaviour of the CO2 injection well and the near wellbore during carbon dioxide injection in saline aquifers," in *TOUGH Symposium 2012*, 2012, p. Session V: Carbon Dioxide Storage II.
[25] A.-M. O. Mohamed, M. El Gamal, and A. Y. Zekri, "Effect of salinity and temperature on water cut determination in oil reservoirs," *Journal of Petroleum Science and Engineering,* vol. 40, no. 3-4, pp. 177-188, 2003.
[26] Y. Tanino and M. J. Blunt, "Capillary trapping in sandstones and carbonates: Dependence on pore structure," *Water Resources Research,* vol. 48, no. 8, 2012.
[27] R. Juanes, E. Spiteri, F. Orr, and M. Blunt, "Impact of relative permeability hysteresis on geological CO2 storage," *Water resources research,* vol. 42, no. 12, 2006.
[28] R. Qi, T. C. LaForce, and M. J. Blunt, "Design of carbon dioxide storage in aquifers," *International Journal of Greenhouse Gas Control,* vol. 3, no. 2, pp. 195-205, 2009.
[29] E. H. Oelkers, S. R. Gislason, and J. Matter, "Mineral carbonation of CO2," *Elements,* vol. 4, no. 5, pp. 333-337, 2008.
[30] W. Gunter, B. Wiwehar, and E. Perkins, "Aquifer disposal of CO 2-rich greenhouse gases: extension of the time scale of experiment for CO 2-sequestering reactions by geochemical modelling," *Mineralogy and Petrology,* vol. 59, no. 1-2, pp. 121-140, 1997.
[31] S. Bachu, W. Gunter, and E. Perkins, "Aquifer disposal of CO2: hydrodynamic and mineral trapping," *Energy Conversion and management,* vol. 35, no. 4, pp. 269-279, 1994.
[32] C. C. Project. (2014, 13 April). *Carbon Dioxide Gas Storage* Available: https://www.co2captureproject.org/media/3_CCP_infographic.jpg
[33] S. Benson *et al.*, "Underground geological storage," *IPCC special report on carbon dioxide capture and storage,* pp. 195-276, 2005.
[34] U. o. Southampton. (13 April). *CO2 trapping method performance*. Available: https://www.southampton.ac.uk/oes/research/projects/geological_storage_of_co2_into_oceanic_crust.page
[35] S. M. Benson and D. R. Cole, "CO2 sequestration in deep sedimentary formations," *Elements,* vol. 4, no. 5, pp. 325-331, 2008.
[36] S. T. Ide, K. Jessen, and F. M. Orr Jr, "Storage of CO2 in saline aquifers: Effects of gravity, viscous, and capillary forces on amount and timing of trapping," *International Journal of Greenhouse Gas Control,* vol. 1, no. 4, pp. 481-491, 2007.
[37] M. A. Hesse, F. M. Orr, and H. Tchelepi, "Gravity currents with residual trapping," *Journal of Fluid Mechanics,* vol. 611, pp. 35-60, 2008.
[38] V. Alvarado and E. Manrique, "Enhanced oil recovery: an update review," *Energies,* vol. 3, no. 9, pp. 1529-1575, 2010.
[39] R. G. Miller and S. R. Sorrell, "The future of oil supply," ed: The Royal Society, 2014.
[40] A. Muggeridge *et al.*, "Recovery rates, enhanced oil recovery and technological limits," *Phil. Trans. R. Soc. A,* vol. 372, no. 2006, p. 20120320, 2014.
[41] I. Sandrea and R. Sandrea, "Global Oil Reserves-1: Recovery factors leave vast target for EOR technologies," *Oil and gas journal,* vol. 105, no. 41, p. 44, 2007.
[42] C. A. Reynolds, H. Menke, M. Andrew, M. J. Blunt, and S. Krevor, "Dynamic fluid connectivity during steady-state multiphase flow in a sandstone," *Proceedings of the National Academy of Sciences,* vol. 114, no. 31, pp. 8187-8192, 2017.
[43] F. A. Dullien, *Porous media: fluid transport and pore structure*. Academic press, 2012.
[44] J. Bear, *Dynamics of fluids in porous media*. Courier Corporation, 2013.
[45] M. J. Blunt, *Multiphase flow in permeable media: A pore-scale perspective*. Cambridge University Press, 2017.

[46] J. Rouquerol *et al.*, "Recommendations for the characterization of porous solids (Technical Report)," *Pure and Applied Chemistry,* vol. 66, no. 8, pp. 1739-1758, 1994.
[47] P. G. Nutting, "Physical analysis of oil sands," *AAPG Bulletin,* vol. 14, no. 10, pp. 1337-1349, 1930.
[48] R. Wyckoff, H. Botset, M. Muskat, and D. Reed, "The measurement of the permeability of porous media for homogeneous fluids," *Review of Scientific Instruments,* vol. 4, no. 7, pp. 394-405, 1933.
[49] S. Whitaker, "Flow in porous media I: A theoretical derivation of Darcy's law," *Transport in porous media,* vol. 1, no. 1, pp. 3-25, 1986.
[50] A. RP40, "Recommended practices for core analysis," *Feb,* 1998.
[51] M. Muskat and M. W. Meres, "The flow of heterogeneous fluids through porous media," *Physics,* vol. 7, no. 9, pp. 346-363, 1936.
[52] E. Crain, *Crain's petrophysical handbook*. Spectrum 2000 Mindware Limited, 2002.
[53] P. Chiquet, D. Broseta, and S. Thibeau, "Wettability alteration of caprock minerals by carbon dioxide," *Geofluids,* vol. 7, no. 2, pp. 112-122, 2007.
[54] S. Saraji, L. Goual, and M. Piri, "Adsorption of asphaltenes in porous media under flow conditions," *Energy & Fuels,* vol. 24, no. 11, pp. 6009-6017, 2010.
[55] K. Jarrahian, O. Seiedi, M. Sheykhan, M. V. Sefti, and S. Ayatollahi, "Wettability alteration of carbonate rocks by surfactants: a mechanistic study," *Colloids and Surfaces A: Physicochemical and Engineering Aspects,* vol. 410, pp. 1-10, 2012.
[56] W. Anderson, "Wettability literature survey-part 2: Wettability measurement," *Journal of petroleum technology,* vol. 38, no. 11, pp. 1,246-1,262, 1986.
[57] E. Amott, "Observations relating to the wettability of porous rock," 1959.
[58] E. C. Donaldson, R. D. Thomas, and P. B. Lorenz, "Wettability determination and its effect on recovery efficiency," *Society of Petroleum Engineers Journal,* vol. 9, no. 01, pp. 13-20, 1969.
[59] S. Strand, "Wettability alteration in chalk-A Study of Surface Chemistry," *University of Stavanger: Dr. Ing. Thesis,* 2005.
[60] J. S. Buckley, "Multiphase displacements in micromodels," *Interfacial Phenomena in Petroleum Recovery,* vol. 36, pp. 157-189, 1991.
[61] C. Marle, *Multiphase flow in porous media*. Éditions technip, 1981.
[62] R. R. Berg, "Capillary pressures in stratigraphic traps," *AAPG bulletin,* vol. 59, no. 6, pp. 939-956, 1975.
[63] T. Shaw, "Drying as an immiscible displacement process with fluid counterflow," *Physical Review Letters,* vol. 59, no. 15, p. 1671, 1987.
[64] M. Sahimi, "Flow phenomena in rocks: from continuum models to fractals, percolation, cellular automata, and simulated annealing," *Reviews of modern physics,* vol. 65, no. 4, p. 1393, 1993.
[65] R. H. Walters, B. Bhatnagar, S. Tchessalov, K.-I. Izutsu, K. Tsumoto, and S. Ohtake, "Next generation drying technologies for pharmaceutical applications," *Journal of pharmaceutical sciences,* vol. 103, no. 9, pp. 2673-2695, 2014.
[66] K. Sollohub and K. Cal, "Spray drying technique: II. Current applications in pharmaceutical technology," *Journal of pharmaceutical sciences,* vol. 99, no. 2, pp. 587-597, 2010.
[67] X. D. Chen and A. S. Mujumdar, *Drying technologies in food processing*. John Wiley & Sons, 2009.
[68] A. Gharsallaoui, G. Roudaut, O. Chambin, A. Voilley, and R. Saurel, "Applications of spray-drying in microencapsulation of food ingredients: An overview," *Food Research International,* vol. 40, no. 9, pp. 1107-1121, 2007.
[69] S. J. Babalis and V. G. Belessiotis, "Influence of the drying conditions on the drying constants and moisture diffusivity during the thin-layer drying of figs," *Journal of food Engineering,* vol. 65, no. 3, pp. 449-458, 2004.

[70] P. Fonseca and G. Scherer, "An image analysis procedure to quantify the air void system of mortar and concrete," *Materials and Structures,* vol. 48, no. 10, pp. 3087-3098, 2015.
[71] Z. P. Bazant and W. Thonguthai, "Pore pressure and drying of concrete at high temperature," *ASCE J Eng Mech Div,* vol. 104, no. 5, pp. 1059-1079, 1978.
[72] Z. Bažant and L. Najjar, "Drying of concrete as a nonlinear diffusion problem," *Cement and Concrete Research,* vol. 1, no. 5, pp. 461-473, 1971.
[73] G. W. Scherer, "Drying, shrinkage, and cracking of cementitious materials," *Transport in Porous Media,* vol. 110, no. 2, pp. 311-331, 2015.
[74] J. Farifteh, F. Van der Meer, C. Atzberger, and E. Carranza, "Quantitative analysis of salt-affected soil reflectance spectra: A comparison of two adaptive methods (PLSR and ANN)," *Remote Sensing of Environment,* vol. 110, no. 1, pp. 59-78, 2007.
[75] P. Conte, A. Agretto, R. Spaccini, and A. Piccolo, "Soil remediation: humic acids as natural surfactants in the washings of highly contaminated soils," *Environmental pollution,* vol. 135, no. 3, pp. 515-522, 2005.
[76] F. Barbir, "PEM fuel cells," in *Fuel Cell Technology*: Springer, 2006, pp. 27-51.
[77] P. Zhao, S. Ge, D. Ma, C. Areeprasert, and K. Yoshikawa, "Effect of hydrothermal pretreatment on convective drying characteristics of paper sludge," *ACS Sustainable Chemistry & Engineering,* vol. 2, no. 4, pp. 665-671, 2014.
[78] H. K. Ozturk, "Energy usage and cost in textile industry: A case study for Turkey," *Energy,* vol. 30, no. 13, pp. 2424-2446, 2005.
[79] A. Fakhru'l-Razi, A. Pendashteh, L. C. Abdullah, D. R. A. Biak, S. S. Madaeni, and Z. Z. Abidin, "Review of technologies for oil and gas produced water treatment," *Journal of hazardous materials,* vol. 170, no. 2-3, pp. 530-551, 2009.
[80] W. Kleinitz, M. Koehler, and G. Dietzsch, "The precipitation of salt in gas producing wells," in *SPE European formation damage conference*, 2001: Society of Petroleum Engineers.
[81] N. Muller, R. Qi, E. Mackie, K. Pruess, and M. J. Blunt, "CO2 injection impairment due to halite precipitation," *Energy procedia,* vol. 1, no. 1, pp. 3507-3514, 2009.
[82] T. Giorgis, M. Carpita, and A. Battistelli, "2D modeling of salt precipitation during the injection of dry CO 2 in a depleted gas reservoir," *Energy Conversion and Management,* vol. 48, no. 6, pp. 1816-1826, 2007.
[83] M. Zeidouni, M. Pooladi-Darvish, and D. Keith, "Analytical solution to evaluate salt precipitation during CO2 injection in saline aquifers," *International Journal of Greenhouse Gas Control,* vol. 3, no. 5, pp. 600-611, 2009.
[84] N. Shokri and D. Or, "What determines drying rates at the onset of diffusion controlled stage-2 evaporation from porous media?," *Water Resources Research,* vol. 47, no. 9, 2011.
[85] J. Van Brakel, "Mass transfer in convective drying," 1980.
[86] N. Shokri, "Pore-scale dynamics of salt transport and distribution in drying porous media," *Physics of Fluids,* vol. 26, no. 1, p. 012106, 2014.
[87] P. Lehmann, S. Assouline, and D. Or, "Characteristic lengths affecting evaporative drying of porous media," *Physical Review E,* vol. 77, no. 5, p. 056309, 2008.
[88] M. Prat, "Recent advances in pore-scale models for drying of porous media," *Chemical engineering journal,* vol. 86, no. 1-2, pp. 153-164, 2002.
[89] N. Vorhauer, Q. Tran, T. Metzger, E. Tsotsas, and M. Prat, "Experimental investigation of drying in a model porous medium: influence of thermal gradients," *Drying Technology,* vol. 31, no. 8, pp. 920-929, 2013.
[90] F. Plourde and M. Prat, "Pore network simulations of drying of capillary porous media. Influence of thermal gradients," *International Journal of Heat and Mass Transfer,* vol. 46, no. 7, pp. 1293-1307, 2003.
[91] G. W. Scherer, "Theory of drying," *Journal of the American Ceramic Society,* vol. 73, no. 1, pp. 3-14, 1990.

[92] F. Chauvet, P. Duru, S. Geoffroy, and M. Prat, "Three Periods of Drying of a Single Square Capillary Tube," *Physical Review Letters,* vol. 103, no. 12, p. 124502, 09/16/ 2009.
[93] F. Chauvet, P. Duru, and M. Prat, "Depinning of evaporating liquid films in square capillary tubes: Influence of corners' roundedness," *Physics of Fluids,* vol. 22, no. 11, p. 112113, 2010.
[94] N. Shokri, P. Lehmann, and D. Or, "Critical evaluation of enhancement factors for vapor transport through unsaturated porous media," *Water resources research,* vol. 45, no. 10, 2009.
[95] N. Shokri, P. Lehmann, and D. Or, "Evaporation from layered porous media," *Journal of Geophysical Research: Solid Earth,* vol. 115, no. B6, 2010.
[96] N. Shokri, P. Lehmann, and D. Or, "Characteristics of evaporation from partially wettable porous media," *Water Resources Research,* vol. 45, no. 2, p. W02415, 2009.
[97] M. Prat, "Percolation model of drying under isothermal conditions in porous media," *International Journal of Multiphase Flow,* vol. 19, no. 4, pp. 691-704, 1993.
[98] M. Prat and F. Bouleux, "Drying of capillary porous media with a stabilized front in two dimensions," *Physical Review E,* vol. 60, no. 5, p. 5647, 1999.
[99] L. Xu, S. Davies, A. B. Schofield, and D. A. Weitz, "Dynamics of drying in 3D porous media," *Physical review letters,* vol. 101, no. 9, p. 094502, 2008.
[100] I. Tsimpanogiannis, Y. Yortsos, S. Poulou, N. Kanellopoulos, and A. Stubos, "Scaling theory of drying in porous media," *Physical Review E,* vol. 59, no. 4, p. 4353, 1999.
[101] D. Wilkinson and J. F. Willemsen, "Invasion percolation: a new form of percolation theory," *Journal of Physics A: Mathematical and General,* vol. 16, no. 14, p. 3365, 1983.
[102] J. Page, J. Liu, B. Abeles, H. Deckman, and D. Weitz, "Pore-space correlations in capillary condensation in Vycor," *Physical review letters,* vol. 71, no. 8, p. 1216, 1993.
[103] T. K. Sherwood, "The drying of solids—I," *Industrial & Engineering Chemistry,* vol. 21, no. 1, pp. 12-16, 1929.
[104] J. R. Philip, "Evaporation, and moisture and heat fields in the soil," *Journal of meteorology,* vol. 14, no. 4, pp. 354-366, 1957.
[105] S. Idso, R. Reginato, R. Jackson, B. Kimball, and F. Nakayama, "The three stages of drying of a field soil1," *Soil Science Society of America Journal,* vol. 38, no. 5, pp. 831-837, 1974.
[106] D. Le, H. Hoang, and J. Mahadevan, "Impact of capillary-driven liquid films on salt crystallization," *Transport in porous media,* vol. 80, no. 2, pp. 229-252, 2009.
[107] J. Mahadevan, M. M. Sharma, and Y. C. Yortsos, "Flow-through drying of porous media," *AIChE journal,* vol. 52, no. 7, pp. 2367-2380, 2006.
[108] P. Coussot, "Scaling approach of the convective drying of a porous medium," *The European physical journal B-condensed matter and complex systems,* vol. 15, no. 3, pp. 557-566, 2000.
[109] M. Prat, "On the influence of pore shape, contact angle and film flows on drying of capillary porous media," *International journal of heat and mass transfer,* vol. 50, no. 7, pp. 1455-1468, 2007.
[110] J. Stefan, "On Equilibrium and Motion, Especially Diffusion in Gas Mixtures," *Ger.), Stizungsber. Akad. Wiss. Wien,* vol. 63, no. 2, pp. 63-124, 1871.
[111] A. Yiotis, A. Stubos, A. Boudouvis, I. Tsimpanogiannis, and Y. Yortsos, "Pore-network modeling of isothermal drying in porous media," *Transport in Porous Media,* vol. 58, no. 1, pp. 63-86, 2005.
[112] T. Ransohoff and C. Radke, "Laminar flow of a wetting liquid along the corners of a predominantly gas-occupied noncircular pore," *Journal of colloid and interface science,* vol. 121, no. 2, pp. 392-401, 1988.
[113] D. Zhou, M. Blunt, and F. Orr Jr, "Hydrocarbon drainage along corners of noncircular capillaries," *Journal of colloid and interface science,* vol. 187, no. 1, pp. 11-21, 1997.
[114] H. Wong, S. Morris, and C. Radke, "Three-dimensional menisci in polygonal capillaries," *Journal of Colloid and Interface Science,* vol. 148, no. 2, pp. 317-336, 1992.

[115] T. Metzger and E. Tsotsas, "Influence of pore size distribution on drying kinetics: A simple capillary model," *Drying Technology,* vol. 23, no. 9-11, pp. 1797-1809, 2005.
[116] M. T. Van Genuchten, "A closed-form equation for predicting the hydraulic conductivity of unsaturated soils 1," *Soil science society of America journal,* vol. 44, no. 5, pp. 892-898, 1980.
[117] Y. Mualem, "A new model for predicting the hydraulic conductivity of unsaturated porous media," *Water resources research,* vol. 12, no. 3, pp. 513-522, 1976.
[118] O. Plumb, "Transport phenomena in porous media: modeling the drying process," ed: Marcel Dekker, Inc., New York, 2000, pp. 755-785.
[119] A. G. Yiotis, A. Stubos, A. Boudouvis, and Y. C. Yortsos, "A 2-D pore-network model of the drying of single-component liquids in porous media," *Advances in Water Resources,* vol. 24, no. 3, pp. 439-460, 2001.
[120] L. Algive, S. Bekri, and O. Vizika, "Pore-network modeling dedicated to the determination of the petrophysical-property changes in the presence of reactive fluid," *SPE Journal,* vol. 15, no. 03, pp. 618-633, 2010.
[121] Y. Le Bray and M. Prat, "Three-dimensional pore network simulation of drying in capillary porous media," *International journal of heat and mass transfer,* vol. 42, no. 22, pp. 4207-4224, 1999.
[122] M. Prat, "Pore network models of drying, contact angle, and film flows," *Chemical Engineering & Technology,* vol. 34, no. 7, pp. 1029-1038, 2011.
[123] T. Metzger, A. Irawan, and E. Tsotsas, "Isothermal drying of pore networks: Influence of friction for different pore structures," *Drying Technology,* vol. 25, no. 1, pp. 49-57, 2007.
[124] L. A. Segura and P. G. Toledo, "Pore-level modeling of isothermal drying of pore networks accounting for evaporation, viscous flow, and shrinking," *Drying Technology,* vol. 23, no. 9-11, pp. 2007-2019, 2005.
[125] Y. Puyate, C. Lawrence, N. Buenfeld, and I. McLoughlin, "Chloride transport models for wick action in concrete at large Peclet number," *Physics of fluids,* vol. 10, no. 3, pp. 566-575, 1998.
[126] G. W. Scherer, "Crystallization in pores," *Cement and Concrete research,* vol. 29, no. 8, pp. 1347-1358, 1999.
[127] H. Eloukabi, N. Sghaier, S. B. Nasrallah, and M. Prat, "Experimental study of the effect of sodium chloride on drying of porous media: The crusty–patchy efflorescence transition," *International Journal of Heat and Mass Transfer,* vol. 56, no. 1-2, pp. 80-93, 2013.
[128] S. Veran-Tissoires and M. Prat, "Evaporation of a sodium chloride solution from a saturated porous medium with efflorescence formation," *Journal of Fluid Mechanics,* vol. 749, pp. 701-749, 2014.
[129] H. Eloukabi, N. Sghaier, M. Prat, and S. Ben Nassrallah, "Drying experiments in a hydrophobic model porous medium in the presence of a dissolved salt," *Chemical Engineering & Technology,* vol. 34, no. 7, pp. 1085-1094, 2011.
[130] N. Shahidzadeh-Bonn, S. Rafaı, D. Bonn, and G. Wegdam, "Salt crystallization during evaporation: impact of interfacial properties," *Langmuir,* vol. 24, no. 16, pp. 8599-8605, 2008.
[131] B. Camassel, N. Sghaier, M. Prat, and S. B. Nasrallah, "Evaporation in a capillary tube of square cross-section: application to ion transport," *Chemical engineering science,* vol. 60, no. 3, pp. 815-826, 2005.
[132] M. J. Qazi, D. Bonn, and N. Shahidzadeh, "Drying of Salt Solutions from Porous Media: Effect of Surfactants," *Transport in Porous Media,* pp. 1-14, 2018.
[133] M. J. Qazi, R. W. Liefferink, S. J. Schlegel, E. H. Backus, D. Bonn, and N. Shahidzadeh, "Influence of Surfactants on Sodium Chloride Crystallization in Confinement," *Langmuir,* vol. 33, no. 17, pp. 4260-4268, 2017.
[134] J. Chen, J. D. Ormes, J. D. Higgins, and L. S. Taylor, "Impact of surfactants on the crystallization of aqueous suspensions of celecoxib amorphous solid dispersion spray dried particles," *Molecular pharmaceutics,* vol. 12, no. 2, pp. 533-541, 2015.

[135] C. Rodriguez-Navarro, E. Doehne, and E. Sebastian, "Influencing crystallization damage in porous materials through the use of surfactants: experimental results using sodium dodecyl sulfate and cetyldimethylbenzylammonium chloride," *Langmuir,* vol. 16, no. 3, pp. 947-954, 2000.
[136] A. Sonin, T. Palermo, and A. Lubek, "Effect of a dispersive surfactant additive on wetting and crystallisation in a system: water-oil-metal substrate. Application to gas hydrates," *Chemical Engineering Journal,* vol. 69, no. 2, pp. 93-98, 1998.
[137] G. Bacci, A. Korre, and S. Durucan, "Experimental investigation into salt precipitation during CO2 injection in saline aquifers," *Energy Procedia,* vol. 4, pp. 4450-4456, 2011.
[138] M. Kim, A. Sell, and D. Sinton, "Aquifer-on-a-Chip: understanding pore-scale salt precipitation dynamics during CO 2 sequestration," *Lab on a Chip,* vol. 13, no. 13, pp. 2508-2518, 2013.
[139] E. W. Bolton, A. C. Lasaga, and D. M. Rye, "Long-term flow/chemistry feedback in a porous medium with heterogenous permeability; kinetic control of dissolution and precipitation," *American Journal of Science,* vol. 299, no. 1, pp. 1-68, 1999.
[140] A. Verma and K. Pruess, "Thermohydrological conditions and silica redistribution near high-level nuclear wastes emplaced in saturated geological formations," *Journal of Geophysical Research: Solid Earth,* vol. 93, no. B2, pp. 1159-1173, 1988.
[141] S. Hurter, J. G. Berge, and D. Labregere, "Simulations for CO2 injection projects with compositional simulator," in *Offshore Europe*, 2007: Society of Petroleum Engineers.
[142] S. Hurter, D. Labregere, and J. Berge, "Simulations of dry-out and halite precipitation due to CO2 injection," in *AGU Fall Meeting Abstracts*, 2007.
[143] K. Pruess and N. Müller, "Formation dry-out from CO2 injection into saline aquifers: 1. Effects of solids precipitation and their mitigation," *Water Resources Research,* vol. 45, no. 3, p. W03402, 2009.
[144] E. Zuluaga, N. Munoz, and G. Obando, "An experimental study to evaluate water vaporisation and formation damage caused by dry gas flow through porous media," in *International Symposium on Oilfield Scale*, 2001: Society of Petroleum Engineers.
[145] Y. Wang, E. Mackie, J. Rohan, T. Luce, R. Knabe, and M. Appel, "Experimental study on halite precipitation during CO2 sequestration," in *International Symposium of the Society of Core Analysts held in Noordwijk, The Netherlands*, 2009, pp. 27-30.
[146] S. M. Roels, H. Ott, and P. L. Zitha, "μ-CT analysis and numerical simulation of drying effects of CO2 injection into brine-saturated porous media," *International Journal of Greenhouse Gas Control,* vol. 27, pp. 146-154, 2014.
[147] H. Ott and S. Oedai, "Wormhole formation and compact dissolution in single-and two-phase CO2-brine injections," *Geophysical Research Letters,* vol. 42, no. 7, pp. 2270-2276, 2015.
[148] H. Ott, S. Roels, and K. De Kloe, "Salt precipitation due to supercritical gas injection: I. Capillary-driven flow in unimodal sandstone," *International Journal of Greenhouse Gas Control,* vol. 43, pp. 247-255, 2015.
[149] D. Avraam and A. Payatakes, "Flow mechanisms, relative permeabilities, and coupling effects in steady-state two-phase flow through porous media. The case of strong wettability," *Industrial & engineering chemistry research,* vol. 38, no. 3, pp. 778-786, 1999.
[150] W. Rose, "Richards' assumptions and Hassler's presumptions," *Transport in Porous Media,* vol. 6, no. 1, pp. 91-99, 1991.
[151] S. S. Datta, J.-B. Dupin, and D. A. Weitz, "Fluid breakup during simultaneous two-phase flow through a three-dimensional porous medium," *Physics of Fluids,* vol. 26, no. 6, p. 062004, 2014.
[152] M. M. Honarpour, *Relative permeability of petroleum reservoirs*. CRC press, 2018.
[153] M. Leverett, "Capillary behavior in porous solids," *Transactions of the AIME,* vol. 142, no. 01, pp. 152-169, 1941.
[154] L. A. Richards, "Capillary conduction of liquids through porous mediums," *physics,* vol. 1, no. 5, pp. 318-333, 1931.

[155] M. Honarpour and S. Mahmood, "Relative-permeability measurements: An overview," *Journal of petroleum technology,* vol. 40, no. 08, pp. 963-966, 1988.
[156] D. Avraam and A. Payatakes, "Flow regimes and relative permeabilities during steady-state two-phase flow in porous media," *Journal of Fluid Mechanics,* vol. 293, pp. 207-236, 1995.
[157] D. Avraam and A. Payatakes, "Generalized relative permeability coefficients during steady-state two-phase flow in porous media, and correlation with the flow mechanisms," in *Multiphase Flow in Porous Media*: Springer, 1995, pp. 135-168.
[158] K. T. Tallakstad *et al.*, "Steady-state two-phase flow in porous media: statistics and transport properties," *Physical review letters,* vol. 102, no. 7, p. 074502, 2009.
[159] A. Chatenever and J. C. Calhoun Jr, "Visual examinations of fluid behavior in porous media-part i," *Journal of Petroleum Technology,* vol. 4, no. 06, pp. 149-156, 1952.
[160] N. Karadimitriou and S. Hassanizadeh, "A review of micromodels and their use in two-phase flow studies," *Vadose Zone Journal,* vol. 11, no. 3, p. 0072, 2012.
[161] C. Zhang, M. Oostrom, T. W. Wietsma, J. W. Grate, and M. G. Warner, "Influence of viscous and capillary forces on immiscible fluid displacement: Pore-scale experimental study in a water-wet micromodel demonstrating viscous and capillary fingering," *Energy & Fuels,* vol. 25, no. 8, pp. 3493-3505, 2011.
[162] L.-C. Chang, J.-P. Tsai, H.-Y. Shan, and H.-H. Chen, "Experimental study on imbibition displacement mechanisms of two-phase fluid using micro model," *Environmental Earth Sciences,* vol. 59, no. 4, p. 901, 2009.
[163] V. Joekar Niasar, S. Hassanizadeh, L. Pyrak-Nolte, and C. Berentsen, "Simulating drainage and imbibition experiments in a high-porosity micromodel using an unstructured pore network model," *Water resources research,* vol. 45, no. 2, 2009.
[164] A. A. Keller, M. J. Blunt, and A. P. V. Roberts, "Micromodel observation of the role of oil layers in three-phase flow," *Transport in Porous Media,* vol. 26, no. 3, pp. 277-297, 1997.
[165] R. Lenormand and C. Zarcone, "Role of roughness and edges during imbibition in square capillaries," in *SPE annual technical conference and exhibition*, 1984: Society of Petroleum Engineers.
[166] R. Lenormand, C. Zarcone, and A. Sarr, "Mechanisms of the displacement of one fluid by another in a network of capillary ducts," *Journal of Fluid Mechanics,* vol. 135, pp. 337-353, 1983.
[167] F. F. Craig, *The reservoir engineering aspects of waterflooding*. HL Doherty Memorial Fund of AIME New York, 1971.
[168] A. E. Scheidegger, "The physics of flow through porous media," 1974.
[169] D. Wildenschild and A. P. Sheppard, "X-ray imaging and analysis techniques for quantifying pore-scale structure and processes in subsurface porous medium systems," *Advances in Water Resources,* vol. 51, pp. 217-246, 2013.
[170] S. Berg *et al.*, "Real-time 3D imaging of Haines jumps in porous media flow," *Proceedings of the National Academy of Sciences,* vol. 110, no. 10, pp. 3755-3759, 2013.
[171] M. Andrew, B. Bijeljic, and M. J. Blunt, "Pore-scale imaging of trapped supercritical carbon dioxide in sandstones and carbonates," *International Journal of Greenhouse Gas Control,* vol. 22, pp. 1-14, 2014.
[172] M. J. Blunt *et al.*, "Pore-scale imaging and modelling," *Advances in Water Resources,* vol. 51, pp. 197-216, 2013.
[173] K. Singh, B. Bijeljic, and M. J. Blunt, "Imaging of oil layers, curvature and contact angle in a mixed-wet and a water-wet carbonate rock," *Water Resources Research,* vol. 52, no. 3, pp. 1716-1728, 2016.
[174] M. Andrew, H. Menke, M. J. Blunt, and B. Bijeljic, "The imaging of dynamic multiphase fluid flow using synchrotron-based X-ray microtomography at reservoir conditions," *Transport in porous media,* vol. 110, no. 1, pp. 1-24, 2015.

[175] R. T. Armstrong, H. Ott, A. Georgiadis, M. Rücker, A. Schwing, and S. Berg, "Subsecond pore-scale displacement processes and relaxation dynamics in multiphase flow," *Water resources research,* vol. 50, no. 12, pp. 9162-9176, 2014.
[176] T. Pak, I. B. Butler, S. Geiger, M. I. van Dijke, and K. S. Sorbie, "Droplet fragmentation: 3D imaging of a previously unidentified pore-scale process during multiphase flow in porous media," *Proceedings of the National Academy of Sciences,* vol. 112, no. 7, pp. 1947-1952, 2015.
[177] N. Hadia, L. Chaudhari, A. Aggarwal, S. K. Mitra, M. Vinjamur, and R. Singh, "Experimental and numerical investigation of one-dimensional waterflood in porous reservoir," *Experimental Thermal and Fluid Science,* vol. 32, no. 2, pp. 355-361, 2007.
[178] N. S. K. Gunda, B. Bera, N. K. Karadimitriou, S. K. Mitra, and S. M. Hassanizadeh, "Reservoir-on-a-Chip (ROC): A new paradigm in reservoir engineering," *Lab on a Chip,* vol. 11, no. 22, pp. 3785-3792, 2011.
[179] P. Tabeling, *Introduction to microfluidics*. Oxford University Press on Demand, 2005.
[180] W. Yun, C. M. Ross, S. Roman, and A. R. Kovscek, "Creation of a dual-porosity and dual-depth micromodel for the study of multiphase flow in complex porous media," *Lab on a Chip,* vol. 17, no. 8, pp. 1462-1474, 2017.
[181] I. Jafari, M. Masihi, and M. Nasiri Zarandi, "Experimental study on imbibition displacement mechanisms of two-phase fluid using micromodel: Fracture network, distribution of pore size, and matrix construction," *Physics of Fluids,* vol. 29, no. 12, p. 122004, 2017.
[182] J.-D. Chen and D. Wilkinson, "Pore-scale viscous fingering in porous media," *Physical review letters,* vol. 55, no. 18, p. 1892, 1985.
[183] N. Karadimitriou, S. Hassanizadeh, V. Joekar-Niasar, and P. Kleingeld, "Micromodel study of two-phase flow under transient conditions: Quantifying effects of specific interfacial area," *Water Resources Research,* vol. 50, no. 10, pp. 8125-8140, 2014.
[184] D. Chen, L. J. Pyrak-Nolte, J. Griffin, and N. J. Giordano, "Measurement of interfacial area per volume for drainage and imbibition," *Water Resources Research,* vol. 43, no. 12, 2007.
[185] D. Crandall, G. Ahmadi, D. H. Smith, and G. Bromhal, "Direct, dynamic measurement of interfacial area within porous media," National Energy Technology Lab.(NETL), Pittsburgh, PA, and Morgantown, WV (United States). In-house Research2010.
[186] Y. M. Corapcioglu, S. Chowdhury, and S. E. Roosevelt, "Micromodel visualization and quantification of solute transport in porous media," *Water resources research,* vol. 33, no. 11, pp. 2547-2558, 1997.
[187] L.-C. Chang, H.-H. Chen, H.-Y. Shan, and J.-P. Tsai, "Effect of connectivity and wettability on the relative permeability of NAPLs," *Environmental geology,* vol. 56, no. 7, pp. 1437-1447, 2009.
[188] R. Lenormand, "Fractals in the natural sciences-Flow through porous media: limits of fractal patterns," *Proc. R. Soc. Lond. A,* vol. 423, no. 1864, pp. 159-168, 1989.
[189] R. Lenormand, "Applications of fractal concepts in petroleum engineering," *Physica D: Nonlinear Phenomena,* vol. 38, no. 1-3, pp. 230-234, 1989.
[190] R. Lenormand and C. Zarcone, "Invasion percolation in an etched network: measurement of a fractal dimension," *Physical review letters,* vol. 54, no. 20, p. 2226, 1985.
[191] C. Cottin, H. Bodiguel, and A. Colin, "Drainage in two-dimensional porous media: From capillary fingering to viscous flow," *Physical Review E,* vol. 82, no. 4, p. 046315, 2010.
[192] Y. Wang *et al.*, "Experimental study of crossover from capillary to viscous fingering for supercritical CO2–water displacement in a homogeneous pore network," *Environmental science & technology,* vol. 47, no. 1, pp. 212-218, 2012.
[193] S. Van Der Marck and J. Glas, "Pressure measurements during forced imbibition experiments in micro-models," *European journal of mechanics. B, Fluids,* vol. 16, no. 5, pp. 681-692, 1997.
[194] B. Sandnes, H. Knudsen, K. Måløy, and E. Flekkøy, "Labyrinth patterns in confined granular-fluid systems," *Physical review letters,* vol. 99, no. 3, p. 038001, 2007.

[195] J.-T. Cheng and N. Giordano, "Fluid flow through nanometer-scale channels," *Physical review E,* vol. 65, no. 3, p. 031206, 2002.
[196] R. T. Armstrong and D. Wildenschild, "Investigating the pore-scale mechanisms of microbial enhanced oil recovery," *Journal of Petroleum Science and Engineering,* vol. 94, pp. 155-164, 2012.
[197] I. Fatt, "The network model of porous media," 1956.
[198] W. Nuss and R. Whiting, "Technique for reproducing rock pore space," *AAPG Bulletin,* vol. 31, no. 11, pp. 2044-2049, 1947.
[199] C. Tsakiroglou and D. Avraam, "Fabrication of a new class of porous media models for visualization studies of multiphase flow processes," *Journal of materials science,* vol. 37, no. 2, pp. 353-363, 2002.
[200] J. T. Cheng, L. J. Pyrak-Nolte, D. D. Nolte, and N. J. Giordano, "Linking pressure and saturation through interfacial areas in porous media," *Geophysical Research Letters,* vol. 31, no. 8, 2004.
[201] M. Knackstedt *et al.*, "Pore scale analysis of electrical resistivity in complex core material," *Proc. Of the Soc. Core Analysts, Calgary, Canada,* 2007.
[202] J. Hornbrook, L. Castanier, and P. Pettit, "Observation of foam/oil interactions in a new, high-resolution micromodel," in *SPE Annual Technical Conference and Exhibition*, 1991: Society of Petroleum Engineers.
[203] E. Rangel-German and A. Kovscek, "A micromodel investigation of two-phase matrix-fracture transfer mechanisms," *Water resources research,* vol. 42, no. 3, 2006.
[204] E. M. Chapman, "Microfluidic visualisation and analysis of multiphase flow phenomena at the pore scale," 2014.
[205] A. Rufai and J. Crawshaw, "Micromodel observations of evaporative drying and salt deposition in porous media," *Physics of Fluids,* vol. 29, no. 12, p. 126603, 2017.
[206] A. Rufai and J. Crawshaw, "Effect of Wettability Changes on Evaporation Rate and the Permeability Impairment due to Salt Deposition," *ACS Earth and Space Chemistry,* vol. 2, no. 4, pp. 320-329, 2018.
[207] H. Ott, S. M. Roels, and K. de Kloe, "Salt precipitation due to supercritical gas injection: I. Capillary-driven flow in unimodal sandstone," *International Journal of Greenhouse Gas Control,* vol. 43, pp. 247-255, 2015/12/01/ 2015.
[208] N. Shokri, P. Lehmann, and D. Or, "Liquid-phase continuity and solute concentration dynamics during evaporation from porous media: Pore-scale processes near vaporization surface," *Physical Review E,* vol. 81, no. 4, p. 046308, 04/13/ 2010.
[209] J. Van Brakel, "Mass transfer in convective drying," *Advances in Drying,* vol. 1, pp. 217-267, 1980.
[210] N. Shahidzadeh-Bonn, S. Rafaï, D. Bonn, and G. Wegdam, "Salt crystallization during evaporation: impact of interfacial properties," *Langmuir,* vol. 24, no. 16, pp. 8599-8605, 2008.
[211] C. Rodriguez-Navarro and E. Doehne, "Salt weathering: influence of evaporation rate, supersaturation and crystallization pattern," *Earth surface processes and landforms,* vol. 24, no. 3, pp. 191-209, 1999.
[212] D. Everett, "The thermodynamics of frost damage to porous solids," *Transactions of the Faraday society,* vol. 57, pp. 1541-1551, 1961.
[213] A. Goudie and H. A. Viles, *Salt weathering hazard*. Wiley, 1997.
[214] G. W. Scherer, "Stress from crystallization of salt," *Cement and concrete research,* vol. 34, no. 9, pp. 1613-1624, 2004.
[215] H. Huinink, L. Pel, and M. v. A. Michels, "How ions distribute in a drying porous medium: A simple model," *Physics of fluids,* vol. 14, no. 4, pp. 1389-1395, 2002.
[216] M. Steiger, "Crystal growth in porous materials—I: The crystallization pressure of large crystals," *Journal of crystal growth,* vol. 282, no. 3-4, pp. 455-469, 2005.
[217] N. Shahidzadeh-Bonn, J. Desarnaud, F. Bertrand, X. Chateau, and D. Bonn, "Damage in porous media due to salt crystallization," *Physical Review E,* vol. 81, no. 6, p. 066110, 2010.

[218] V. N. Wong, R. C. Dalal, and R. S. Greene, "Salinity and sodicity effects on respiration and microbial biomass of soil," *Biology and fertility of soils,* vol. 44, no. 7, pp. 943-953, 2008.
[219] J. Desarnaud, H. Derluyn, L. Molari, S. de Miranda, V. Cnudde, and N. Shahidzadeh, "Drying of salt contaminated porous media: effect of primary and secondary nucleation," *Journal of Applied Physics,* vol. 118, no. 11, p. 114901, 2015.
[220] M. Bergstad and N. Shokri, "Evaporation of NaCl solution from porous media with mixed wettability," *Geophysical Research Letters,* vol. 43, no. 9, pp. 4426-4432, 2016.
[221] S. Veran-Tissoires, M. Marcoux, and M. Prat, "Discrete salt crystallization at the surface of a porous medium," *Physical review letters,* vol. 108, no. 5, p. 054502, 2012.
[222] N. Sghaier and M. Prat, "Effect of efflorescence formation on drying kinetics of porous media," *Transport in Porous Media,* vol. 80, no. 3, pp. 441-454, 2009.
[223] L. Guglielmini, A. Gontcharov, A. J. Aldykiewicz Jr, and H. A. Stone, "Drying of salt solutions in porous materials: intermediate-time dynamics and efflorescence," *Physics of Fluids,* vol. 20, no. 7, p. 077101, 2008.
[224] S. Gupta, H. P. Huinink, M. Prat, L. Pel, and K. Kopinga, "Paradoxical drying of a fired-clay brick due to salt crystallization," *Chemical Engineering Science,* vol. 109, pp. 204-211, 2014.
[225] F. Hidri, N. Sghaier, H. Eloukabi, M. Prat, and S. B. Nasrallah, "Porous medium coffee ring effect and other factors affecting the first crystallisation time of sodium chloride at the surface of a drying porous medium," *Physics of Fluids,* vol. 25, no. 12, p. 127101, 2013.
[226] U. Nachshon, N. Weisbrod, M. I. Dragila, and A. Grader, "Combined evaporation and salt precipitation in homogeneous and heterogeneous porous media," *Water Resources Research,* vol. 47, no. 3, 2011.
[227] A. Naillon, P. Duru, M. Marcoux, and M. Prat, "Evaporation with sodium chloride crystallization in a capillary tube," *Journal of Crystal Growth,* vol. 422, pp. 52-61, 2015.
[228] J. Desarnaud, H. Derluyn, J. Carmeliet, D. Bonn, and N. Shahidzadeh, "Metastability limit for the nucleation of NaCl crystals in confinement," *The journal of physical chemistry letters,* vol. 5, no. 5, pp. 890-895, 2014.
[229] T. M. Squires and S. R. Quake, "Microfluidics: Fluid physics at the nanoliter scale," *Reviews of modern physics,* vol. 77, no. 3, p. 977, 2005.
[230] J. Stefan, "On the equilibrium and movement of gas mixtures, in particular diffusion," *Sitzungsber. Kais. Akad. Wiss. Wien,* vol. 63, pp. 63-124, 1871.
[231] N. Vorhauer, Y. Wang, A. Kharaghani, E. Tsotsas, and M. Prat, "Drying with formation of capillary rings in a model porous medium," *Transport in Porous Media,* vol. 110, no. 2, pp. 197-223, 2015.
[232] J. B. Laurindo and M. Prat, "Numerical and experimental network study of evaporation in capillary porous media. Drying rates," *Chemical engineering science,* vol. 53, no. 12, pp. 2257-2269, 1998.
[233] J. B. Laurindo and M. Prat, "Numerical and experimental network study of evaporation in capillary porous media. Phase distributions," *Chemical engineering science,* vol. 51, no. 23, pp. 5171-5185, 1996.
[234] C. Chen, P. Duru, P. Joseph, S. Geoffroy, and M. Prat, "Control of evaporation by geometry in capillary structures. From confined pillar arrays in a gap radial gradient to phyllotaxy-inspired geometry," *Scientific Reports,* vol. 7, no. 1, p. 15110, 2017.
[235] P. Fantinel, O. Borgman, R. Holtzman, and L. Goehring, "Drying in a microfluidic chip: experiments and simulations," *Scientific Reports,* vol. 7, no. 1, p. 15572, 2017.
[236] G. Karniadakis and A. Beskok, "Micro flows: fundamentals and simulation. 2002," ed: New York, NY: Springer Verlag, 2002.
[237] P. van Hemert, E. S. J. Rudolph, and P. L. Zitha, "Micro Computer Tomography Study of Potassium Iodide Precipitation in Bentheimer Sandstone Caused by Flow-through CO 2 Drying," *Energy Procedia,* vol. 37, pp. 3331-3346, 2013.

[238] S. M. Roels, H. Ott, and P. L. Zitha, "μ-CT analysis and numerical simulation of drying effects of CO 2 injection into brine-saturated porous media," *International Journal of Greenhouse Gas Control,* vol. 27, pp. 146-154, 2014.
[239] (2004, 24/06). *Evaporation from a Water Surface.* . Available: https://www.engineeringtoolbox.com/evaporation-water-surface-d_690.html
[240] S. Shokri-Kuehni, T. Vetter, C. Webb, and N. Shokri, "New insights into saline water evaporation from porous media: Complex interaction between evaporation rates, precipitation and surface temperature," *Geophysical Research Letters,* 2017.
[241] N. Shahidzadeh-Bonn, A. Azouni, and P. Coussot, "Effect of wetting properties on the kinetics of drying of porous media," *Journal of physics: condensed matter,* vol. 19, no. 11, p. 112101, 2007.
[242] A. Yiotis, A. Boudouvis, A. Stubos, I. Tsimpanogiannis, and Y. Yortsos, "Effect of liquid films on the drying of porous media," *AIChE Journal,* vol. 50, no. 11, pp. 2721-2737, 2004.
[243] R. Robinson, "The vapour pressures of solutions of potassium chloride and sodium chloride," *Trans. R. Soc. New Zealand,* vol. 75, no. 2, pp. 203-217, 1945.
[244] X. Liu, "Heterogeneous nucleation or homogeneous nucleation?," *The Journal of Chemical Physics,* vol. 112, no. 22, pp. 9949-9955, 2000.
[245] C. W. Correns, "Growth and dissolution of crystals under linear pressure," *Discussions of the Faraday society,* vol. 5, pp. 267-271, 1949.
[246] Y. Peysson, "Permeability alteration induced by drying of brines in porous media," *The European Physical Journal-Applied Physics,* vol. 60, no. 2, p. 24206, 2012.
[247] Y. Peysson, B. Bazin, C. Magnier, E. Kohler, and S. Youssef, "Permeability alteration due to salt precipitation driven by drying in the context of CO2 injection," *Energy Procedia,* vol. 4, pp. 4387-4394, 2011.
[248] A. S. Al-Menhali and S. Krevor, "Capillary Trapping of CO2 in Oil Reservoirs: Observations in a Mixed-Wet Carbonate Rock," *Environmental Science & Technology,* vol. 50, no. 5, pp. 2727-2734, 2016/03/01 2016.
[249] T. Austad and D. C. Standnes, "Spontaneous imbibition of water into oil-wet carbonates," *Journal of Petroleum Science and Engineering,* vol. 39, no. 3, pp. 363-376, 2003/09/01/ 2003.
[250] N. Kasiri and A. Bashiri, "Wettability and Its Effects on Oil Recovery in Fractured and Conventional Reservoirs," *Petroleum Science and Technology,* vol. 29, no. 13, pp. 1324-1333, 2011/05/03 2011.
[251] J. W. Grate *et al.*, "Silane modification of glass and silica surfaces to obtain equally oil-wet surfaces in glass-covered silicon micromodel applications," *Water Resources Research,* vol. 49, no. 8, pp. 4724-4729, 2013.
[252] P. Esmaeilzadeh, M. T. Sadeghi, Z. Fakhroueian, A. Bahramian, and R. Norouzbeigi, "Wettability alteration of carbonate rocks from liquid-wetting to ultra gas-wetting using TiO 2, SiO 2 and CNT nanofluids containing fluorochemicals, for enhanced gas recovery," *Journal of Natural Gas Science and Engineering,* vol. 26, pp. 1294-1305, 2015.
[253] A. M. Alhammadi, A. AlRatrout, K. Singh, B. Bijeljic, and M. J. Blunt, "In situ characterization of mixed-wettability in a reservoir rock at subsurface conditions," *Scientific Reports,* vol. 7, p. 10753, 2017.
[254] O. Chapuis and M. Prat, "Influence of wettability conditions on slow evaporation in two-dimensional porous media," *Physical review E,* vol. 75, no. 4, p. 046311, 2007.
[255] M. Sahimi, *Flow and transport in porous media and fractured rock: from classical methods to modern approaches*. John Wiley & Sons, 2011.
[256] C. G. Dodd and O. G. Kiel, "Evaluation of Monte Carlo methods in studying fluid–fluid displacements and wettability in porous rocks," *The Journal of Physical Chemistry,* vol. 63, no. 10, pp. 1646-1652, 1959.
[257] M. M. Dias and A. C. Payatakes, "Network models for two-phase flow in porous media part 2. motion of oil ganglia," *Journal of Fluid Mechanics,* vol. 164, pp. 337-358, 1986.

[258] M. M. Dias and A. C. Payatakes, "Network models for two-phase flow in porous media Part 1. Immiscible microdisplacement of non-wetting fluids," *Journal of Fluid Mechanics,* vol. 164, pp. 305-336, 1986.
[259] A. Payatakes, "Dynamics of oil ganglia during immiscible displacement in water-wet porous media," *Annual Review of Fluid Mechanics,* vol. 14, no. 1, pp. 365-393, 1982.
[260] A. Payatakes, K. Ng, and R. Flumerfelt, "Oil ganglion dynamics during immiscible displacement: Model formulation," *AIChE Journal,* vol. 26, no. 3, pp. 430-443, 1980.
[261] K. T. Tallakstad, G. Løvoll, H. A. Knudsen, T. Ramstad, E. G. Flekkøy, and K. J. Måløy, "Steady-state, simultaneous two-phase flow in porous media: An experimental study," *Physical Review E,* vol. 80, no. 3, p. 036308, 2009.
[262] E. H. Kimbrel, A. L. Herring, R. T. Armstrong, I. Lunati, B. K. Bay, and D. Wildenschild, "Experimental characterization of nonwetting phase trapping and implications for geologic CO 2 sequestration," *International Journal of Greenhouse Gas Control,* vol. 42, pp. 1-15, 2015.
[263] S. Zeppieri, J. Rodríguez, and A. López de Ramos, "Interfacial tension of alkane+ water systems," *Journal of Chemical & Engineering Data,* vol. 46, no. 5, pp. 1086-1088, 2001.
[264] M. D. Reichert and L. M. Walker, "Interfacial tension dynamics, interfacial mechanics, and response to rapid dilution of bulk surfactant of a model oil–water-dispersant system," *Langmuir,* vol. 29, no. 6, pp. 1857-1867, 2013.
[265] Y. Liu, R. DiFoggio, K. Sanderlin, L. Perez, and J. Zhao, "Measurement of density and viscosity of dodecane and decane with a piezoelectric tuning fork over 298–448 K and 0.1–137.9 MPa," *Sensors and Actuators A: Physical,* vol. 167, no. 2, pp. 347-353, 2011.
[266] K. R. Harris, "Temperature and pressure dependence of the viscosities of 2-ethylhexyl benzoate, bis (2-ethylhexyl) phthalate, 2, 6, 10, 15, 19, 23-hexamethyltetracosane (squalane), and diisodecyl phthalate," *Journal of Chemical & Engineering Data,* vol. 54, no. 9, pp. 2729-2738, 2009.
[267] R. T. Armstrong, A. Georgiadis, H. Ott, D. Klemin, and S. Berg, "Critical capillary number: Desaturation studied with fast X-ray computed microtomography," *Geophysical Research Letters,* vol. 41, no. 1, pp. 55-60, 2014.
[268] I. Zacharoudiou and E. S. Boek, "Capillary filling and Haines jump dynamics using free energy Lattice Boltzmann simulations," *Advances in water resources,* vol. 92, pp. 43-56, 2016.
[269] S. Chen and G. D. Doolen, "Lattice Boltzmann method for fluid flows," *Annual review of fluid mechanics,* vol. 30, no. 1, pp. 329-364, 1998.
[270] D. Koroteev *et al.*, "Direct hydrodynamic simulation of multiphase flow in porous rock," *Petrophysics,* vol. 55, no. 04, pp. 294-303, 2014.
[271] I. Lunati and P. Jenny, "Multiscale finite-volume method for compressible multiphase flow in porous media," *Journal of Computational Physics,* vol. 216, no. 2, pp. 616-636, 2006.
[272] P.-E. Øren and S. Bakke, "Process based reconstruction of sandstones and prediction of transport properties," *Transport in porous media,* vol. 46, no. 2-3, pp. 311-343, 2002.
[273] S. Succi and S. Succi, *The lattice Boltzmann equation: for fluid dynamics and beyond*. Oxford university press, 2001.
[274] E. S. Boek, I. Zacharoudiou, F. Gray, S. M. Shah, J. P. Crawshaw, and J. Yang, "Multiphase-flow and reactive-transport validation studies at the pore scale by use of lattice Boltzmann computer simulations," *SPE Journal,* vol. 22, no. 03, pp. 940-949, 2017.
[275] E. S. Boek and M. Venturoli, "Lattice-Boltzmann studies of fluid flow in porous media with realistic rock geometries," *Computers & Mathematics with Applications,* vol. 59, no. 7, pp. 2305-2314, 2010.
[276] I. Zacharoudiou, E. M. Chapman, E. S. Boek, and J. P. Crawshaw, "Pore-filling events in single junction micro-models with corresponding lattice Boltzmann simulations," *Journal of Fluid Mechanics,* vol. 824, pp. 550-573, 2017.
[277] M. R. Swift, W. Osborn, and J. Yeomans, "Lattice Boltzmann simulation of nonideal fluids," *Physical review letters,* vol. 75, no. 5, p. 830, 1995.

[278] P. Seppecher, "Moving contact lines in the Cahn-Hilliard theory," *International journal of engineering science,* vol. 34, no. 9, pp. 977-992, 1996.
[279] V. M. Kendon, M. E. Cates, I. Pagonabarraga, J.-C. Desplat, and P. Bladon, "Inertial effects in three-dimensional spinodal decomposition of a symmetric binary fluid mixture: a lattice Boltzmann study," *Journal of Fluid Mechanics,* vol. 440, pp. 147-203, 2001.
[280] E. S. Boek, "Pore scale simulation of flow in porous media using lattice-Boltzmann computer simulations," in *SPE Annual Technical Conference and Exhibition*, 2010: Society of Petroleum Engineers.
[281] I. Zacharoudiou, "Viscous fingering and liquid crystals in confinement," 2012.
[282] S. Shah, J. Crawshaw, and E. Boek, "Three-dimensional imaging of porous media using confocal laser scanning microscopy," *Journal of microscopy,* vol. 265, no. 2, pp. 261-271, 2017.
[283] S. Shah, J. Crawshaw, and E. Boek, "Preparation of microporous rock samples for confocal laser scanning microscopy," *Petroleum Geoscience,* vol. 20, no. 4, pp. 369-374, 2014.
[284] T. Al-Sahhaf, A. Elkamel, A. Suttar Ahmed, and A. Khan, "The influence of temperature, pressure, salinity, and surfactant concentration on the interfacial tension of the n-octane-water system," *Chemical Engineering Communications,* vol. 192, no. 5, pp. 667-684, 2005.
[285] E. Ruckenstein and I. Rao, "Interfacial tension of oil—brine systems in the presence of surfactant and cosurfactant," *Journal of colloid and interface science,* vol. 117, no. 1, pp. 104-119, 1987.
[286] B.-Y. Cai, J.-T. Yang, and T.-M. Guo, "Interfacial tension of hydrocarbon+ water/brine systems under high pressure," *Journal of chemical & engineering data,* vol. 41, no. 3, pp. 493-496, 1996.
[287] S. Bamberger, G. V. Seaman, K. Sharp, and D. E. Brooks, "The effects of salts on the interfacial tension of aqueous dextran poly (ethylene glycol) phase systems," *Journal of Colloid and Interface Science,* vol. 99, no. 1, pp. 194-200, 1984.

Appendix

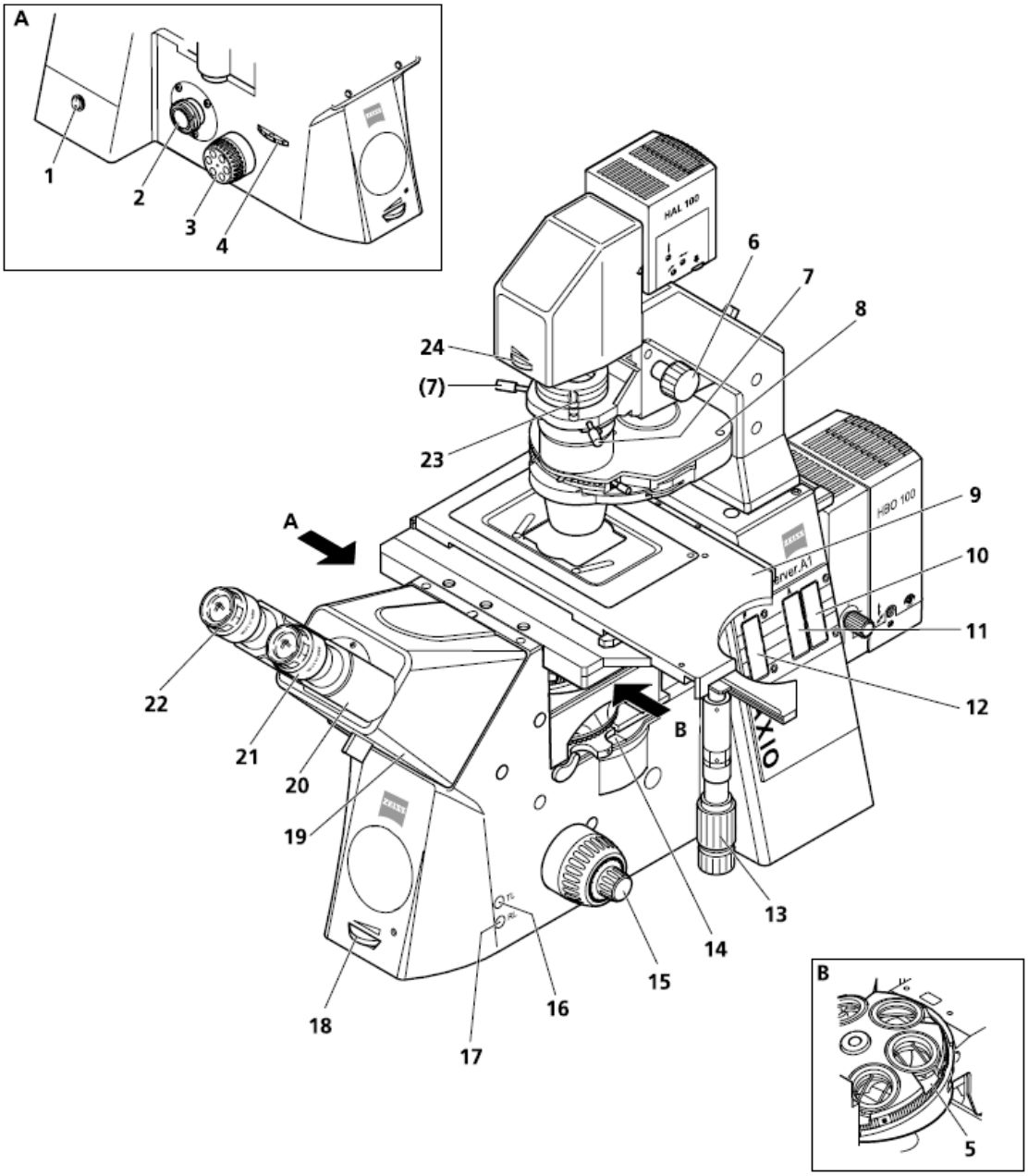

Figure A.1. Schematic of the Zeiss AxioObserver A1.m inverted light microscope.

Table A.1. Components and Controls of the ILM from figure 3.6.

1	On/Off switch	13	Drive knobs for controlling XY positioning of the mechanical stage
2	Left side port	14	Reflector turret
3	Coarse/fine focus drive (left side) with fine drive, flat[1]	15	Focus drive coarse/fine (right side)[1]
4	Light path switching control (left side port)	16	TL button for switching the transmitted light halogen illuminator on and off
5	Objective nosepiece	17	RL button for switching the reflected light shutter (fluorescence) on and off[3]
6	Vertical adjustment knob for condenser	18	Halogen illumination intensity control
7	Condenser centring screw	19	Binocular tube
8	Condenser	20	Binocular section of the binocular tube
9	Microscope stage	21	Eyepiece
10	3-position filter slider slot (diameter 25 mm)	22	Eyepiece adjustment ring
11	Slot for iris stop slider as reflected light aperture stop of FL attenuator[2]	23	Polarizer with 2-position filter changer or 3-position filter changer
12	Slot for iris stop slider as reflected light luminous-field stop[2]	24	Luminous-field stop control

[1] The positions are reversed on the microscope, [2] Not in use, [3] Not in use - reflected light controlled by the external control box.

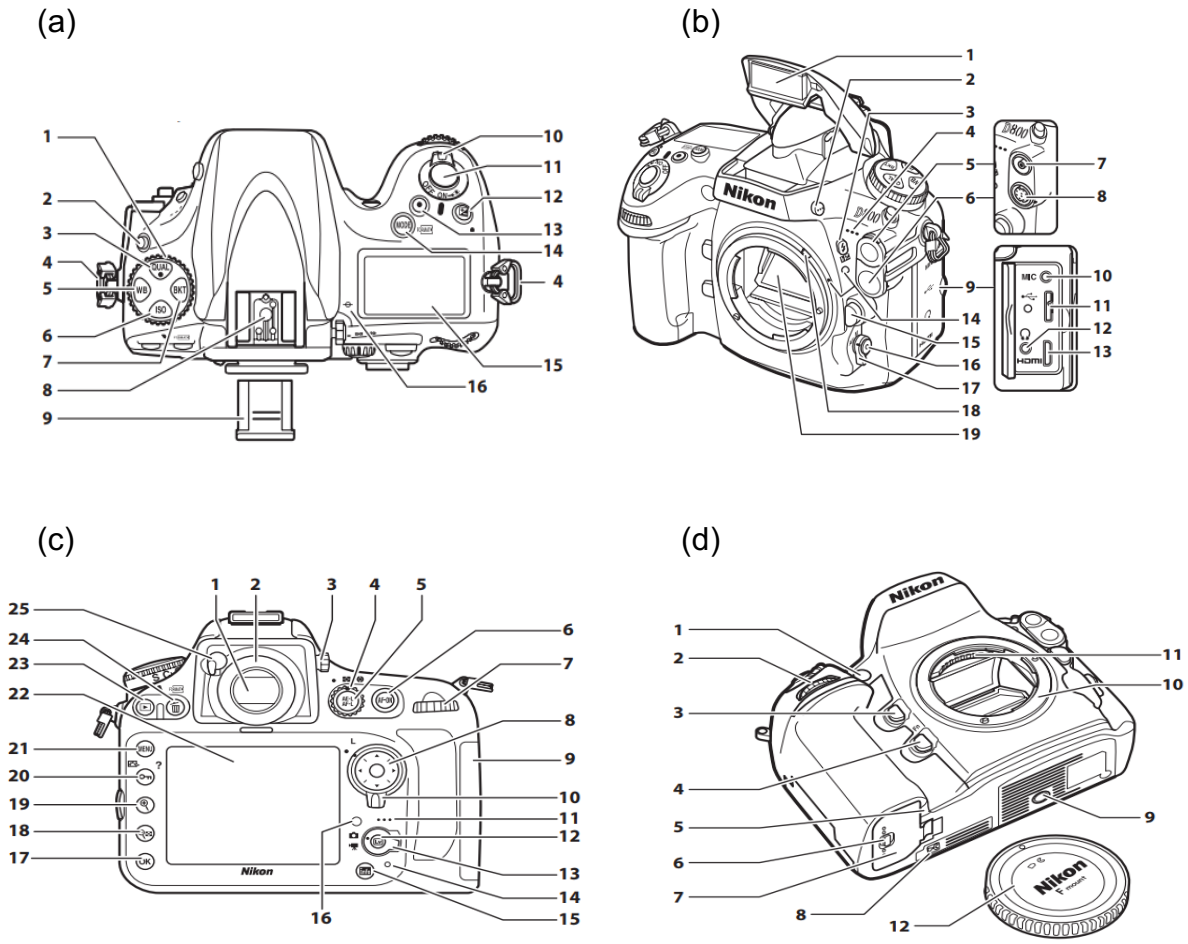

Figure A.2. Schematics of the Nikon D300E Digital Single-Lens Reflex (DSLR) Camera.

Table A.2a. DSLR Camera Controls and Displays (a).

1	Release mode dial	9	Accessory shoe cover
2	Release mode dial	10	Power switch
3	QUAL button	11	Shutter-release button
4	Eyelet for camera strap	12	Exposure compensation button
5	WB button	13	Movie-record button
6	ISO button	14	Mode/Format button
7	BKT button	15	Control panel
8	Accessory shoe	16	Focal plane mark

Table A.2b. DSLR Camera Controls and Displays (b).

1	Built-in flash	11	USB connector
2	Flash pop-up button	12	Headphone connector
3	Flash mode button	13	HDMI mini-pin connector
4	Built-in microphone	14	Mounting index
5	Flash sync terminal cover	14	Lens release button
6	Ten-pin remote terminal cover	16	AF-mode button
7	Flash sync terminal	17	Focus-mode selector
8	Ten-pin remote terminal	18	Meter coupling selector
9	Connector cover	19	Mirror
10	Connector for external microphone		

Table A.2c. DSLR Camera Controls and Displays (c).

1	Viewfinder	14	Memory card access lamp
2	Viewfinder eyepiece	15	Info button
3	Diopter adjustment control	16	Ambient brightness sensor
4	Metering selector	17	OK button
5	AE/AF button	18	Thumbnail button
6	AF-ON	19	Playback zoom-in button
7	Main command dial	20	Protect/Picture control button
8	Multi selector	21	Menu button
9	Memory card slot cover	22	Monitor
10	Focus selector lock	23	Playback button
11	Speaker	24	Forward/delete button
12	Live view button	25	Eyepiece shutter lever
13	Live view selector		

Table A.2d. DSLR Camera Controls and Displays (d).

1	AF-assist illuminator	7	Battery-chamber cover
2	Sub-command dial	8	Contact cover for optional battery
3	Depth-of-field preview button	9	Tripod socket
4	Function button	10	Lens mount
5	Power connector button	11	CPU contacts
6	Battery-chamber cover latch	12	Body cap

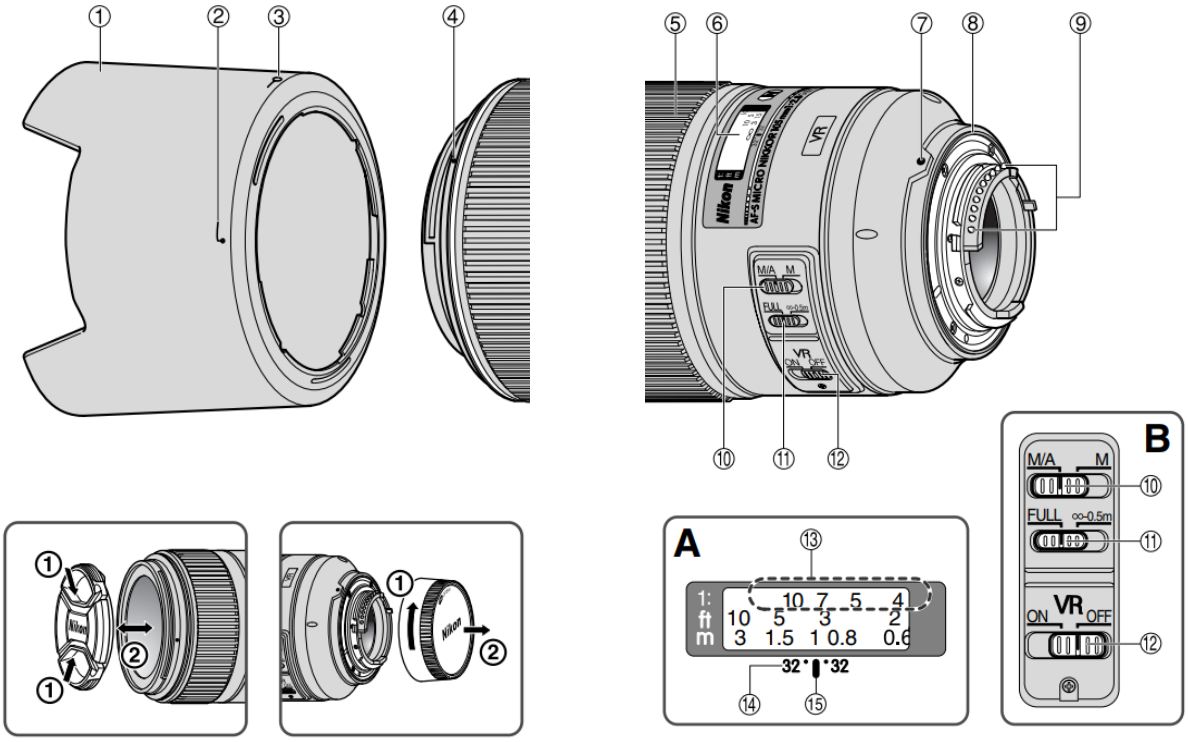

Figure A.3. Schematics of the Nikon 105mm micro-lens.

Table A.3. Controls and Displays of the Lens (in figure 3.11) used with the DSLR

1	Lens hood	9	CPU contacts
2	Lens hood attachment index	10	Focus mode switch
3	Lens hood setting index	11	Focusing limit switch
4	Lens hood mounting index	12	Vibration reduction ON/OFF switch
5	Focus ring	13	Reproduction ratio scale
6	Distance scale	14	Depth-of-field indicators
7	Mounting index	15	Distance index line
8	Lens mount rubber gasket		

Table A.4. Water/Decane Experiments.

Experiment	Total flow rate, Q_T (uL/min)	Water flow rate, Q_w (uL/min)	Decane (Oil) flow rate, Q_{nw} (uL/min)	Wetting-phase capillary number, Ca_w	Nonwetting-phase capillary number, Ca_{nw}
11	5.0	0.5	4.5	2.36×10^{-9}	1.94×10^{-8}
12	10.0	0.5	9.5	2.36×10^{-9}	4.09×10^{-8}
13	15.0	1.0	14.0	4.73×10^{-9}	6.03×10^{-8}
14	40.0	1.0	39.0	4.73×10^{-9}	1.68×10^{-7}
15	50.0	5.0	45.0	2.36×10^{-8}	1.94×10^{-7}
16	85.0	5.0	80.0	2.36×10^{-8}	3.45×10^{-7}
17	70.0	10.0	60.0	4.73×10^{-8}	2.59×10^{-7}
18	110.0	10.0	100.0	4.73×10^{-8}	4.31×10^{-7}
19	100.0	20.0	80.0	9.45×10^{-8}	3.45×10^{-7}
20	150.0	50.0	100.0	2.36×10^{-7}	4.31×10^{-7}
21	0.5	0.1	0.4	4.73×10^{-10}	1.72×10^{-9}
22	1.0	0.1	0.9	4.73×10^{-10}	3.88×10^{-9}
23	2.0	0.1	1.9	4.73×10^{-10}	8.19×10^{-9}
24	3.0	0.2	2.8	9.45×10^{-10}	1.21×10^{-8}
25	5.0	0.2	4.8	9.45×10^{-10}	2.07×10^{-8}
26	10.0	0.2	9.8	9.45×10^{-10}	4.22×10^{-8}
27	20.0	0.3	17.0	1.42×10^{-9}	7.33×10^{-8}
28	40.0	0.3	37.0	1.42×10^{-9}	1.60×10^{-7}
29	60.0	0.3	57.0	1.42×10^{-9}	2.46×10^{-7}
30	100.0	0.4	96.0	1.89×10^{-9}	4.14×10^{-7}
31	0.5	0.1	10.0	4.73×10^{-10}	4.31×10^{-8}
32	1.0	0.1	30.0	4.73×10^{-10}	1.29×10^{-7}
33	5.0	0.1	100.0	4.73×10^{-10}	4.31×10^{-7}
34	10.0	0.2	1.0	9.45×10^{-10}	4.31×10^{-9}
35	20.0	0.2	50.0	9.45×10^{-10}	2.16×10^{-7}
36	40.0	0.3	2.0	1.42×10^{-9}	8.62×10^{-9}
37	60.0	0.3	10.0	1.42×10^{-9}	4.31×10^{-8}
38	100.0	0.4	50.0	1.89×10^{-9}	2.16×10^{-7}
39	101.0	1.0	100.0	4.73×10^{-9}	4.31×10^{-7}
40	52.0	2.0	50.0	9.45×10^{-9}	2.16×10^{-7}
41	0.5	0.5	0.1	2.36×10^{-9}	4.31×10^{-10}
42	1.0	1.0	0.1	4.73×10^{-9}	4.31×10^{-10}
43	2.0	2.0	0.1	9.45×10^{-9}	4.31×10^{-10}
44	3.0	2.0	5.0	9.45×10^{-9}	2.16×10^{-8}
45	5.0	2.0	20.0	9.45×10^{-9}	8.62×10^{-8}
46	10.0	5.0	0.1	2.36×10^{-8}	4.31×10^{-10}
47	20.0	5.0	0.5	2.36×10^{-8}	2.16×10^{-9}
48	40.0	10.0	0.1	4.73×10^{-8}	4.31×10^{-10}
49	60.0	20.0	0.5	9.45×10^{-8}	2.16×10^{-9}
50	100.0	50.0	0.5	2.36×10^{-7}	2.16×10^{-9}
51	0.3	0.2	0.1	9.45×10^{-10}	4.31×10^{-10}
52	0.4	0.3	0.1	1.42×10^{-9}	4.31×10^{-10}
53	1.0	0.6	0.4	2.84×10^{-9}	1.72×10^{-9}

54	2.0	1.6	0.4	7.56×10^{-9}	1.72×10^{-9}
55	4.0	3.0	1.0	1.42×10^{-8}	4.31×10^{-9}
56	10.0	9.0	1.0	4.25×10^{-8}	4.31×10^{-9}
57	20.0	15.0	5.0	7.09×10^{-8}	2.16×10^{-8}
58	40.0	35.0	5.0	1.67×10^{-7}	2.16×10^{-8}
59	70.0	50.0	20.0	2.36×10^{-7}	8.62×10^{-8}
60	120.0	100.0	20.0	4.73×10^{-7}	8.62×10^{-8}
61	0.3	0.1	0.2	4.73×10^{-10}	8.62×10^{-10}
62	0.4	0.1	0.3	4.73×10^{-10}	1.29×10^{-9}
63	1.0	0.4	0.6	1.89×10^{-9}	2.59×10^{-9}
64	2.0	0.4	1.6	1.89×10^{-9}	6.90×10^{-9}
65	4.0	1.0	3.0	4.73×10^{-9}	1.29×10^{-8}
66	10.0	1.0	9.0	4.73×10^{-9}	3.88×10^{-8}
67	20.0	5.0	15.0	2.36×10^{-8}	6.47×10^{-8}
68	40.0	5.0	35.0	2.36×10^{-8}	1.51×10^{-7}
69	70.0	20.0	50.0	9.45×10^{-8}	2.16×10^{-7}
70	120.0	20.0	100.0	9.45×10^{-8}	4.31×10^{-7}

Table A.5. Water/Squalane Experiments.

Experiment	Total flow rate, Q_T (uL/min)	Water flow rate, Q_w (uL/min)	Squalane (Oil) flow rate, Q_{nw} (uL/min)	Wetting-phase capillary number, Ca_w	Nonwetting-phase capillary number, Ca_{nw}
11	0.3	0.2	0.1	9.42×10^{-10}	1.07×10^{-8}
12	0.4	0.3	0.1	1.41×10^{-9}	1.07×10^{-8}
13	1.0	0.6	0.4	2.83×10^{-9}	4.25×10^{-8}
14	2.0	1.6	0.4	7.53×10^{-9}	4.25×10^{-8}
15	4.0	3.0	1.0	1.41×10^{-8}	1.07×10^{-7}
16	10.0	9.0	1.0	4.24×10^{-8}	1.07×10^{-7}
17	20.0	15.0	5.0	7.07×10^{-8}	5.31×10^{-7}
18	40.0	35.0	5.0	1.65×10^{-7}	5.31×10^{-7}
19	70.0	50.0	20.0	2.36×10^{-7}	2.13×10^{-6}
20	120.0	100.0	20.0	4.72×10^{-7}	2.13×10^{-6}
21	0.3	0.1	0.2	4.72×10^{-10}	2.13×10^{-8}
22	0.4	0.1	0.3	4.72×10^{-10}	3.19×10^{-8}
23	1.0	0.4	0.6	1.88×10^{-9}	6.38×10^{-8}
24	2.0	0.4	1.6	1.88×10^{-9}	1.07×10^{-7}
25	4.0	1.0	3.0	4.72×10^{-9}	3.19×10^{-7}
26	10.0	1.0	9.0	4.72×10^{-9}	9.57×10^{-7}
27	20.0	5.0	15.0	2.36×10^{-8}	1.59×10^{-6}
28	40.0	5.0	35.0	2.36×10^{-8}	3.72×10^{-6}
29	70.0	20.0	50.0	9.42×10^{-8}	5.31×10^{-6}
30	120.0	20.0	100.0	9.42×10^{-8}	1.07×10^{-5}
31	5.0	0.5	4.5	2.36×10^{-9}	4.78×10^{-7}
32	10.0	0.5	9.5	2.36×10^{-9}	1.01×10^{-6}
33	15.0	1.0	14.0	4.72×10^{-9}	1.49×10^{-6}
34	40.0	1.0	39.0	4.72×10^{-9}	4.15×10^{-6}
35	50.0	5.0	45.0	2.36×10^{-8}	4.78×10^{-6}
36	85.0	5.0	80.0	2.36×10^{-8}	8.50×10^{-6}
37	70.0	10.0	60.0	4.72×10^{-8}	6.38×10^{-6}
38	110.0	10.0	100.0	4.72×10^{-8}	1.07×10^{-5}
39	100.0	20.0	80.0	9.42×10^{-8}	8.50×10^{-6}
40	120.0	50.0	100.0	2.36×10^{-7}	1.07×10^{-5}
41	0.5	0.1	0.4	4.72×10^{-10}	4.25×10^{-8}
42	1.0	0.1	0.9	4.72×10^{-10}	9.57×10^{-8}
43	2.0	0.1	1.9	4.72×10^{-10}	2.02×10^{-7}
44	3.0	0.2	2.8	9.42×10^{-10}	2.98×10^{-7}
45	5.0	0.2	4.8	9.42×10^{-10}	3.10×10^{-7}
46	10.0	0.2	9.8	9.42×10^{-10}	1.04×10^{-6}
47	20.0	0.3	17.0	1.41×10^{-9}	1.81×10^{-6}
48	40.0	0.3	37.0	1.41×10^{-9}	3.93×10^{-6}
49	60.0	0.3	57.0	1.41×10^{-9}	6.06×10^{-6}
50	100.0	0.4	96.0	1.88×10^{-9}	1.02×10^{-5}
51	0.5	0.1	10.0	4.72×10^{-10}	1.07×10^{-6}
52	1.0	0.1	30.0	4.72×10^{-10}	3.19×10^{-6}
53	5.0	0.1	100.0	4.72×10^{-10}	1.07×10^{-5}
54	10.0	0.2	1.0	9.42×10^{-10}	1.07×10^{-7}
55	20.0	0.2	50.0	9.42×10^{-10}	5.31×10^{-6}

56	40.0	0.3	2.0	1.41×10^{-9}	2.13×10^{-7}
57	60.0	0.3	10.0	1.41×10^{-9}	1.07×10^{-6}
58	100.0	0.4	50.0	1.88×10^{-9}	5.31×10^{-6}
59	101.0	1.0	100.0	4.72×10^{-9}	1.07×10^{-5}
60	52.0	2.0	50.0	9.42×10^{-9}	5.31×10^{-6}
61	0.5	0.5	0.1	2.36×10^{-9}	1.07×10^{-8}
62	1.0	1.0	0.1	4.72×10^{-9}	1.07×10^{-8}
63	2.0	2.0	0.1	9.42×10^{-9}	1.07×10^{-8}
64	3.0	2.0	5.0	9.42×10^{-9}	5.31×10^{-7}
65	5.0	2.0	20.0	9.42×10^{-9}	2.13×10^{-6}
66	10.0	5.0	0.1	2.36×10^{-8}	1.07×10^{-8}
67	20.0	5.0	0.5	2.36×10^{-8}	5.31×10^{-8}
68	40.0	10.0	0.1	4.72×10^{-8}	1.07×10^{-8}
69	60.0	20.0	0.5	9.42×10^{-8}	5.31×10^{-8}
70	100.0	50.0	0.5	2.36×10^{-7}	5.31×10^{-8}

Simulation Settings and Free Energy Lattice Boltzmann Params

```
1256                // LX  -  Total LX = 2* LX_geo + 2 * x_offset
764                 // LY  -  Total LY = 2* LY_geo + 2*y_offset
25                  // LZ  -  Total LZ = 2* LZ_geo + 2*z_offset
1000000000                  // nbEqStep: Number of total iterations
100000              // WriteStep: Save data every #infoStep iterations (for Output files)
1000                // infoStep: Calculate Average Velocities / Saturation every #infoStep
iterations
30                  // theta1 (expressed in degrees): Equil. contact angle for two phase flow
0.52198             // tauliquid: relaxation time for the “liquid” phase
0.52      // taugas: relaxation time for the “gas” phase
1.0                 // option_Relax_rates: Option for the relaxation rates in the MRT approx.
1.0                 // tau_p: relaxation time for the order parameter
2.0e-2              // kappa_p: kappa term in the free energy functional
3.08e-2             // -A and B: terms from the free energy functional
1.0                 // gama: \Gamma term related to the Mobility and Diffusivity
========== Driving the Fluid Flow ==========
0.0 0.0 0.0         // body force Fx, Fy, Fz
0.0 0.0 0.0         // initUX initUY initUZ : Initial Velocities
0                   // max_x_phase1: Phase 1 for x < max_x_phase1
1 0                 // Method of driving the fluid flow (1. Velocity BCs, 2. Pressure BCs) -
If both False, then Periodic BCs
2.5e-6 0.0 0.0      // velx_inlet, vely_inlet, velz_inlet: Case of Velocity Inlet BCs
0.0                 // +/- dif_density, i.e. density inlet = rho + dif_density, density
outlet = rho - dif_density
========== Variables When read_Geometry_from_File=true ==================
2448                // size_LX_input_file: Total size in x-direction of the input geometry
file
1528                // size_LY_input_file: Total size in y-direction of the input geometry
file
25                  // size_LZ_input_file: Total size in z-direction of the input geometry
file
1224                // LX_geo: size in x-direction I want to read from the input geometry
file
764                 // LY_geo: size in y-direction I want to read from the input geometry
file
25                  // LZ_geo: size in z-direction I want to read from the input geometry
file
16                  // x_offset: size of extra reservoir in the x-direction (to be added in
inlet & outlet)
0                   // y_offset: size of extra reservoir in the y-direction
0                   // z_offset: size of extra reservoir in the z-direction
========== Variables When restart_sim = true ====================
0                   // restart_sim: Restart simulation after t = t_restart (True=1, False=0)
18940000            // t_restart: Time simulation restarts
0 1                 // FileType_VTK >> FileType_Binary : Type of the input files if
restart_sim=True
32                  // n_bits_bin_files: Data type in bits if FileType_Binary=true
1 0                 // index_order_1_bin, index_order_2_bin // Index order (Filling order)
when reading the input files if FileType_Binary=true; index_order_1: z,y,x  index_order_2:
x,y,z
/project/QCCSRC/izacharo/drain_charact_TP_flow/tau_0.52/tau_0.52_M1e0/test_1_2b/rStart_4/
                    // Path for the Binary input files (density, concentration, velocity
files)
velx18940000.raw vely18940000.raw velz18940000.raw                                  // Velocity
input files
/project/QCCSRC/izacharo/drain_charact_TP_flow/tau_0.52/tau_0.52_M1e0/test_1_2b/rStart_4/nn18
940000.raw                      // Density file
/project/QCCSRC/izacharo/drain_charact_TP_flow/tau_0.52/tau_0.52_M1e0/test_1_2b/rStart_4/dd18
940000.raw                      // Concentration file
/project/QCCSRC/izacharo/drain_charact_TP_flow/tau_0.52/tau_0.52_M1e0/test_1_2b/rStart_4/velt
18940000.vtk                    // Velocity file
========== Other Variables - Type of Output Files ==========
0                   // choice_output_path: Save Output in the current directory (True=1) or
in a different path (False=0)
1                   // Binary_Output_files: Output data files in binary format
0                   // Matlab_Output_files: Matlab Output format (True=1, False=0)
1                   // Paraview_Output_files: Paraview Output format (True=1, False=0)
1                   // Concentration_output: Save the Concentration field
1                   // Density_output: Save the Density field
0                   // Pressure_output: Save the Pressure field
1                   // Velocity_output: Save the Velocity field
========== Simulation settings - Input Geometry ==========
1                   // read_Geometry_from_File: read the simulation Geometry from File
(True=1, False=0)
1 0                 // Geometry_Type_VTK >> Geometry_Type_Binary: Types of input Geometry
File (First VTK, Second Binary) (True=1, False=0)
8                   // n_bits: Data type in bits if Geometry_Type_Binary=true
1 0                 // index_order_1: z,y,x  index_order_2: x,y,z - Index order (Filling
order) when reading the input geometry file if Geometry_Type_Binary=true
1 0                 // ident_Solid/ident_Fluid: Value of Solid/Fluid nodes in input Geometry
File
0 0 0               // mirror in x-dir, y-dir, z-dir: mirror the geometry input file (True=1,
False=0)
```

```
1                   // reservoir: include extra reservoir in inlet and outlet (True=1,
False=0)
1                   // OutputGeometryFileVTKHeader
1                   // OutputGeometry_VTK_format: Output Simulation Geometry in VTK format
(Paraview)
4.21            // Resolution in microns
========== Simulation settings - Type of simulation ==========
0                   // Calculate_Abs_Permeability: Calculate Absolute Permeability (True=1,
False=0)
16 416              // Limits for Calculating Abs Perm when Velocity BCs (
x_lowerLimit_AbsPerm <= x < x_upperLimit_AbsPerm)
0 16                // Limits for Calc. Average Pressure in inlet - Used for AbsPerm when
Velocity BCs ( x_lowerLimit_Pres_Inlet <= x < x_upperLimit_Pres_Inlet)
416 432             // Limits for Calc. Average Pressure in outlet - Used for AbsPerm when
Velocity BCs ( x_lowerLimit_Pres_Outlet <= x < x_upperLimit_Pres_Outlet)
0                   // Calculate_Rel_Permeability: Calculate Relative Permeability (True=1,
False=0)
1                   // calculate_Saturation: Calculate Saturation Values (True=1, False=0) if
(t % infoStep ==0)
16 1240             // Limits for Calculating Average Velocities and Saturation (for two
phase flow) ( x_lowerLimit_Sat <= x < x_upperLimit_Sat )
0                   // Request_Sat_Converg: Stop the simulation if Saturation converges - for
two phase flow (True=1, False=0)
1e-3                // Stop_Cond_AbsRel_Conv: Stop Absolute Permeability Calculations when
the difference is smaller than this
========== Path Variables ==========
/export91/work/akr13/Geometry_files/Geometry_Ayo_2448x1528x25.vtk     // GeometryFile: Input
geometry
/export91/work/akr13/LB_sims/try_6/output_6/
                            // path_output: Output path if choice_output_path=False
========== Variables for Relative Permeability ==========
7.99731e+03 8.73423e+03 6.20664e+03     // Absolute Permeability (mD) of the rock sample in
x,y,z directions
/work/izacharo/calculate_Permeabilities/relative_permeabilities/multi_GPU/forced_drainage/ket
ton_forcedDrainage/ketton_ForcD
```

K100 GPU Script

```
#!/bin/sh
#PBS -N try_6
#PBS -l walltime=48:00:00
#PBS -l
select=1:ncpus=2:ngpus=2:mem=24GB:gpu_type=P100:mpiprocs=2:ompthreads=1

#! Mail to user when job terminate or abort
#PBS -m ae

export RUN=/export91/work/akr13/LB_sims/try_6/

cp $RUN/* $TMPDIR
copytmp

# Run
module load mpi
mpiexec $TMPDIR/Ayo_P_CX1_mod2_P100

copytmp

cp $TMPDIR/*  $RUN/)
```

American Physical Society
Reuse and Permissions License

22-Oct-2018

This license agreement between the American Physical Society ("APS") and Ayorinde Rufai ("You") consists of your license details and the terms and conditions provided by the American Physical Society and SciPris.

Licensed Content Information

License Number:	**RNP/18/OCT/008718**
License date:	22-Oct-2018
DOI:	10.1103/PhysRevLett.103.124502
Title:	Three Periods of Drying of a Single Square Capillary Tube
Author:	F. Chauvet et al.
Publication:	Physical Review Letters
Publisher:	American Physical Society
Cost:	USD $ 0.00

Request Details

Does your reuse require significant modifications: No

Specify intended distribution locations:	Worldwide
Reuse Category:	Reuse in a thesis/dissertation
Requestor Type:	Student
Items for Reuse:	Figures/Tables
Number of Figure/Tables:	2
Figure/Tables Details:	Evolution of bulk meniscus position z0 as a function of time. The thick solid line and the dashed line are for the square tube
Format for Reuse:	Electronic and Print
Total number of print copies:	Up to 1000

Information about New Publication:

University/Publisher:	Imperial College London
Title of dissertation/thesis:	Porous Media Drying and Two-phase Flow Studies Using Micromodels
Author(s):	Ayorinde K. Rufai
Expected completion date:	Nov. 2018

License Requestor Information

Name:	Ayorinde Rufai
Affiliation:	Individual
Email Id:	rufaiayo@gmail.com
Country:	United Kingdom